THE UNIVERSITY OF QUEENSLAND

AUSTRALIA

HYBRID ORGANIC-INORGANIC MOLECULAR TEMPLATED MEMBRANES FOR WATER DESALINATION

YEN THIEN CHUA

A thesis submitted for the degree of Doctor of Philosophy at

The University of Queensland in January 2015

School of Chemical Engineering

Abstract

The scarcity of fresh water resources has been of great concern for contemporary society, particularly against the backdrop of worsening climate change impacts and a growing global population. Desalination of saline water resources is one of the most feasible and effective technologies for fresh water production. Membrane-based desalination processes such as reverse osmosis (RO) have risen to prominence owing to their reduced energy intensity and compact footprint. However, extensive pre-treatment is required to perform RO on chemically and thermal aggressive waters, opening the door for alternative methods. In particular, membrane distillation (MD), a process which combines the benefits of both membrane and thermal technologies has received significant research interest in the last decade. Up till now, most studies on MD have focussed on the effect of operating parameters by using the commercial available polymeric membranes, which are designed for ultra- or microfiltration and may not be suitable for MD. New membrane materials and morphologies have not been extensively explored. The key target of this work therefore is to design a suitable membrane for MD by exploring the potential of hybrid organic-inorganic materials, specifically using silica-based (as inorganic) and carbon-based (as organic) materials.

Silica-based materials offer good chemical and thermal resistance, high porosity, and excellent versatility in forming various nano-sized morphologies. Unfortunately, most of the membrane-related work has focused on amorphous silica, which is sensitive to steam or water vapour and yields low water fluxes making it generally unsuitable for MD. The steam degradation can be controlled at MD relevant temperatures by incorporating organic moieties into the silica network. Meanwhile, the flux issues can be addressed by increasing porosity and pore size. This work demonstrates for the first time hybrid organic-inorganic mesoporous membranes with an ordered, narrow pore size distribution was developed by using soft-templating method and successfully applied to MD under a variety of operating conditions. Despite having a hydrophilic contact angle (i.e. < 90 °) and a pore size (2 nm) larger than hydrated salt ions (0.66-0.72 nm) which intuitively may lead to pore wetting, the membrane produced pure water (up to 13 L m^{-2} h^{-1}) with > 99 % salt rejection across an extreme range of salt concentrations (10-150 g L^{-1} NaCl) at moderate temperature (60 °C). This major finding was complimented by the fact that no concentration polarization was observed, with fluxes effectively unchanged across the entire range of salt concentrations.

Based on these results a model was proposed to explain how a hydrophilic, nanoporous membrane could operate effectively and with no observable pore wetting under vacuum MD. The model represents the second major contribution of the thesis and adapts the Lucas-Washburn equation for capillary pressure to nanopores. The model shows that the liquid/vapour interface is no longer formed in the pore entrance but shifted further into the pore channel due to the water intrusion (drawn by the capillary pressure) which balanced out by the vaporization of water from the liquid/water interface due to partial pressure difference. Crucially, fluid flow through the nanochannels experiences dramatically increased resistance, due to the sharp increase in the shear viscosity of water in nanoconfined spaces, preventing outright pore wetting. The impacts of pore size, membrane thickness, substrate thickness, concentration polarization, porosity, and contact angle on water flux and pore intrusion depth were tested using the model. The membrane hydrophilicity was found to impact on water flux and pore intrusion in a complex relationship with pore size. In order to elucidate this theory, organosilica membranes of different pore sizes and pore geometries were prepared; their performances were compared and found to be in broad agreement with the initial model.

In the second part of the thesis, a different strategy was trialled for the synthesis of hybrid organic-inorganic materials, which employs the triconstituent co-assembly method using two separate precursors for the organic and inorganic compounds and a structure directing agent. Unlike the organosilica membrane where carbon and silicon atoms are covalently bonded and homogeneously distributed in atomic scale, these new carbon-silica nanocomposites are comprised of carbon and silica networks that interact physically at the molecular level. The effects of silica content, carbonization temperature, types of surfactants and coating conditions on the formation and performance of the resulting membranes were evaluated. In the third major finding of the thesis, the results demonstrated that a carbon-silica nanocomposite could be a more economically viable and promising candidate in membrane development compared to the original organosilica membranes. Furthermore, the concept of carbon-silica nanocomposite membranes is novel in MD-based water desalination and this opens up a new development pathway for hybrid organic-inorganic membranes.

Declaration by author

This thesis is composed of my original work, and contains no material previously published or written by another person except where due reference has been made in the text. I have clearly stated the contribution by others to jointly-authored works that I have included in my thesis.

I have clearly stated the contribution of others to my thesis as a whole, including statistical assistance, survey design, data analysis, significant technical procedures, professional editorial advice, and any other original research work used or reported in my thesis. The content of my thesis is the result of work I have carried out since the commencement of my research higher degree candidature and does not include a substantial part of work that has been submitted to qualify for the award of any other degree or diploma in any university or other tertiary institution. I have clearly stated which parts of my thesis, if any, have been submitted to qualify for another award.

I acknowledge that an electronic copy of my thesis must be lodged with the University Library and, subject to the General Award Rules of The University of Queensland, immediately made available for research and study in accordance with the *Copyright Act 1968*.

I acknowledge that copyright of all material contained in my thesis resides with the copyright holder(s) of that material. Where appropriate I have obtained copyright permission from the copyright holder to reproduce material in this thesis.

Publications during candidature

Peer-reviewed papers

Y. T. Chua, C. X. C. Lin, F. Kleitz, X. S. Zhao and S. Smart, Nanoporous Organosilica Membrane for Water Desalination, Chem. Commun., 49, 2013, 4534-4536.

Y. T. Chua, G. Ji, G. Birkett, C. X. C. Lin, F. Kleitz and S. Smart, Nanoporous Organosilica Membrane for Water Desalination: Theoretical Study on the Water Transport, Journal of Membrane Science, 482, 2015, 56-66.

Y. T. Chua, C. X. C. Lin, F. Kleitz and S. Smart, Mesoporous Organosilica Membranes: Effects of Pore Geometry and Calcination Conditions on the Membrane Distillation Performance for Desalination, Desalination, 370, 2015, 53-62.

Y. T. Chua, C. X. C. Lin, F. Kleitz and S. Smart, Synthesis of Mesoporous Carbon-silica Nanocomposite Membranes using a Triconstituent Co-assembly Method, Journal of Materials Chemistry A, 3, 2015, 10480-10491.

Conference abstracts

Y. T. Chua, C. X. C. Lin, F. Kleitz and S. Smart, Ordered Mesoporous Silica Membrane for Desalination using Membrane Distillation. UQ Engineering Postgraduate Research Conference, 4th June 2012. (Oral presentation)

Y. T. Chua, C. X. C. Lin, F. Kleitz and S. Smart, Surfactant-tailored Mesostructured Silica Membranes for Water Desalination. The 7th Conference of Aseanian Membrane Society, Busan (Korea), 4-6th July 2012. (Poster presentation)

Y. T. Chua, C. X. C. Lin, F. Kleitz and S. Smart, Hybrid Organic-inorganic Mesoporous Membrane for Desalination using Vacuum Membrane Distillation. 3rd Early Career Researcher Membrane Symposium, Brisbane (Australia), 28-30th November 2012. (Oral presentation)

Y. T. Chua, C. X. C. Lin, F. Kleitz and S. Smart, Self-assembled Mesoporous Organosilica Membrane in Desalination via Vacuum Membrane Distillation. 1st International Conference on Desalination using Membrane Technology, Sitges (Spain), 7-10th April 2013. (Oral presentation)

Y. T. Chua, C. X. C. Lin, F. Kleitz and S. Smart, Synthesis of Mesoporous Carbon-Silica Nanocomposite Membrane for Water Desalination. UQ Engineering Postgraduate Research Conference, 11th June 2014. (Oral presentation)

Y. T. Chua, C. X. C. Lin, F. Kleitz, and S. Smart, Synthesis of Mesoporous Carbon-Silica Nanocomposite Membrane via Triconstituent Co-assembly Method for Water Desalination. 13th International Conference of Inorganic Membranes, Brisbane (Australia), 7-9th July 2014. (Oral presentation)

Publications included in this thesis

Y. T. Chua, C. X. C. Lin, F. Kleitz, X. S. Zhao and S. Smart, Nanoporous Organosilica Membrane for Water Desalination, Chem. Commun., 49, 2013, 4534-4536. – incorporated as Chapter 3.

Contributor	Statement of contribution
Author Yen Thien Chua (Candidate)	Designed experiments (80%) Analysed and interpreted data (70%) Wrote and edited paper (70%)
Author Chun Xiang Cynthia Lin	Designed experiments (10%) Analysed and interpreted data (10%) Wrote and edited paper (8%)
Author Freddy Kleitz	Analysed and interpreted data (10%) Wrote and edited paper (10%)
Author Xiu Song Zhao	Wrote and edited paper (2%)
Author Simon Smart	Designed experiments (10%) Analysed and interpreted data (10%) Wrote and edited paper (10%)

Contributions by others to the thesis

Contributions by Dr. Guozhao Ji and Dr. Greg Birkett from The University of Queensland in mathematical modelling and technical discussion which is reported in Chapter 4.

Contributions by Dr Ekaterina Strounina in NMR analysis for the material characterizations as parts of Chapter 3, 5-7.

Contributions by Dr Julius Motuzas in high resolution SEM imaging of membranes as parts of Chapter 7.

Statement of parts of the thesis submitted to qualify for the award of another degree

None

Acknowledgements

First of all, I wish to express my greatest gratitude to my supervisors Dr. Simon Smart, Prof. Freddy Kleitz and Dr. Chun Xiang Cynthia Lin for their endless support, encouragement and guidance throughout my PhD. Their experiences and dedications in scientific research as well as their positive personalities have immensely inspired and enlightened me.

Special thanks to Prof. Michael Yu and Dr. Tony Howes for their valuable comments and commitment as review panel members. I am also grateful to Prof. Joe da Costa for his valuable advices and kind generosity allowing me to work in his laboratory and to be a part of FIMLab group. Thanks to our previous and present postdocs Julius Motuzas, Christelle Yacou, Dana Marten, David Wang, Yen Tran, Xiwang Zhang and Chris Muller for their technical advices and knowledge sharing.

Many thanks to all the CMM staff, Graeme, Robyn, Anya, Kevin, Eunice, Ying Yu, Barry, Katia and Morgan for their friendliness and technical assistance. Thanks to our administrative staff who are always supporting and helpful. Thanks to Mr Bob Hannah and Peter Bleakley, Des Cameron from our workshop for their technical advices and assistance in fabricating my experimental test rig.

My thanks go to all the FIMLab members Ingrid, Gianni, Guozhao Ji, Liang, Diego, Ben, Aida, Muthia, Alice and Adi for knowledge sharing and those great memories in laboratory. I would also like to extend my thanks to all the members in Freddy's research group, especially Yen, Binh, Nima, Mahesh, Cao, François, Maxime and Justyna for your kind friendship during my stay in Canada. Special thanks to Tim Wu for those fruitful scientific and philosophical discussions. My buddies, Zheng Xing, Xiaoyu and Chris who are always supportive and lighten up my uni life, a simple thank you is not enough to express my gratefulness. Also thanks to all my friends in 102/103 who always give a great support and encouragement.

I wish to acknowledge The University of Queensland and Australian Research Council for their financial support.

Finally, I wish to thank my family and Sébastien for their unconditional love and constant support throughout my study; I would not have been able to complete this thesis without their continuous understanding and encouragement.

Keywords

Desalination, vacuum membrane distillation, nanoporous organosilica membrane, carbon-silica nanocomposites.

Australian and New Zealand Standard Research Classifications (ANZSRC)

ANZSRC code: 090404, Membrane and Separation Technologies, 80%
ANZSRC code: 100708, Nanomaterial, 20%

Fields of Research (FoR) Classification

FoR code: 0904, Chemical Engineering, 80%
FoR code: 1007, Nanotechnology, 20%

TABLE OF CONTENT

LIST OF FIGURES

LIST OF SUPPLEMENTARY FIGURES

LIST OF TABLES

LIST OF SUPPLEMENTARY TABLES

1 INTRODUCTION

1.1 Background

The ancient Greek philosopher, Thales of Miletus (c. 620 – 546 B.C.E.) once claimed that water is the nature, the *archê*, the originating principle [1]. His hypothesis that everything originated from and ultimately returns to water no longer bears scientific merit, yet the fact remains that water is one of the most vital elements for all forms of life on Earth. Fresh water is an indispensable part of global civilization in both urban and rural settings and for countless human activities including mining, agriculture, farming, energy generation, food processing and even recreation purposes. The industrialisation and population expansion of modern society combined with increasingly severe climate change impacts has made the scarcity of fresh water one of the great challenges of modern times and intensified the search for alternative water sources. In Australia, the driest inhabited continent, has varying rainfall (year to year), the need for searching fresh water resources particularly compelling. According to the National Water Commission, water supply within the country is still sufficient to cover the nation water consumption but certain regions are already experiencing in water security, in particular for agricultural and mining purposes [2].

Out of 1,386,000,000 km^3 of water that found on Earth, 97 % is saline, and majority of the fresh water is trapped in ice caps and glaciers, or groundwater, that requires energy for extraction [3]. Hence, desalination, a process of separating water from saline or brackish water, is perhaps the most crucial technology for continuously supplying fresh water. In general, desalination technologies can be categorised into 3 groups according to the primary mechanisms: (1) phase-change that involves heat, such as thermal distillation methods whereby the saline water is heated and evaporated to produce water vapour; (2) short-range (< ~ 1 nm) interactions with selective materials; and (3) long-range (> ~ 1 nm) electrostatic interactions as illustrated in Figure 1.1 [4, 5]. Due to their respective separation mechanisms, each technology has salinity range for which it is best suited, e.g. electrodialysis is limited to treating saline solutions of less than 5,000 ppm (5 g L^{-1}) total dissolved solids (TDS) [4]. By contrast, there is no upper limit to salinity for evaporative desalination. Reverse osmosis (RO) is currently considered the gold-standard in desalination technologies due to its lower energy consumption per cubic metre of fresh water product and its ability to reject monovalent ions, such as sodium and chloride [6] by

using dense polymeric membranes. It is the most applied technology globally and generally the first choice for new desalination plants, although its thermal and chemical resistance to harsh feed waters are low and it has an upper limit feed stream salinity of ~50,000 ppm (50 g L^{-1}) TDS [7]. Thermal technologies relying of phase change such as multi-stage flash (MSF) distillation and multi-effect distillation (MED) can effectively produce fresh water with 100 % salt rejection and very high water recovery rates but these technologies are highly energy and capital intensive in comparison to RO. In view of this, alternate desalination methods such as membrane distillation and pervaporation, which adapt both thermal technique and membranes, have grown in popularity in the research literature [8-13].

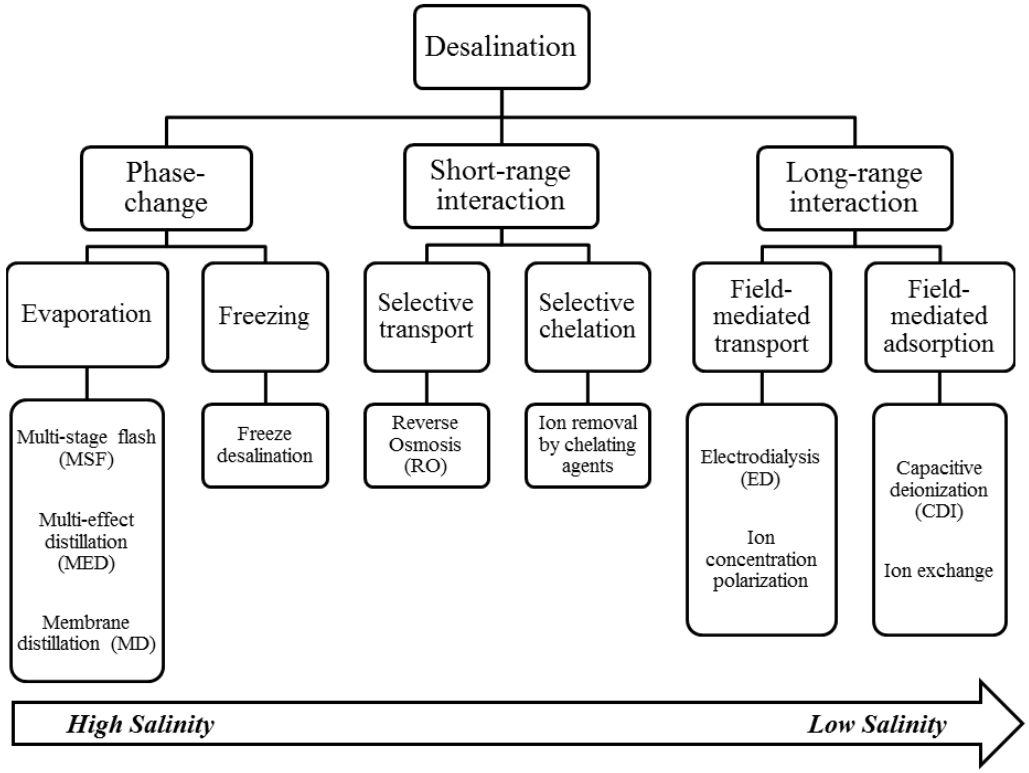

Figure 1.1 Overview of desalination processes with different separation mechanisms.

1.2 Membrane Distillation in Water Desalination

Membrane distillation (MD) is a separation process driven by a vapour pressure difference across the membrane, which is affected by different parameters but governed by the vapour pressure gradient across the membrane [14]. The history of MD dates back to the 1960s, but the success of RO and inappropriate membrane selection stifled the early MD work. In recent years, there has been a growing interest in MD due to its simple operational requirements and mild

operating conditions (close to ambient temperatures and pressures). In particular the advantages of MD over other conventional processes include: (1) operating at low temperatures (20 – 90 °C) which allows the utilization of low grade heat as exemplified by waste heat streams or solar thermal energy [15], (2) does not require high hydrostatic pressure as in RO, (3) 100% (theoretical) rejection of ions, macromolecules, colloids, cells, and all other non-volatile components, (4) less demanding membrane property requirements, (5) potential reduction in membrane fouling, and (6) process intensification through miniaturization of system design [14]. Furthermore, MD is highly feasible to form hybrid systems with other separation processes, such as ultrafiltration or RO due to its capability to treat highly saline solutions [14, 16]. Nevertheless, the MD process has not been fully commercialized due to several limitations, in particular, the lower permeating flux compared to RO, flux decay due to concentration and temperature polarization effects, pore wetting and intensive energy requirements [17]. Hence, despite the growth in MD research, there are still substantial gaps in understanding that should be addressed.

1.3 Motivation and Aims of this Research

The selection criteria for a good MD membrane is that it should exhibit high permeability, low thermal conductivity, good thermal stability, excellent chemical resistance and high liquid entry pressure (LEP) of water to avoid pore wetting. Most reported works have generally adopted commercially available polymeric membrane from hydrophobic materials like polytetrafluoroethylene (PTFE), polypropylene (PP) or polyvinylidene fluoride (PVDF). These membranes have pore size ranges from 0.1 to 1 μm and they are mainly used in microfiltration and ultrafiltration, which operate under different principles [18]. These hydrophobic membranes with large pores show high permeating water fluxes but are prone to bio-fouling and are susceptible to pore wetting. Part of the pore wetting problem arises from the relatively broad pore size distribution that comes from trying to improve the porosity and hence flux of the adapted MD membranes. Specifically, LEP is a function of pore size and hydrostatic pressure, so a broad pore size distribution increases the range of applied pressures which can cause pore wetting. Hence, an isoporous membrane with narrow pore size distribution (Figure 1.2) and optimised hydrophobicity is beneficial in enhancing membrane stability. **The first hypothesis is that the risk of pore wetting can be greatly reduced by employing a hydrophilic membrane with unconventionally small pores (< 20 nm) without sacrificing the performance.**

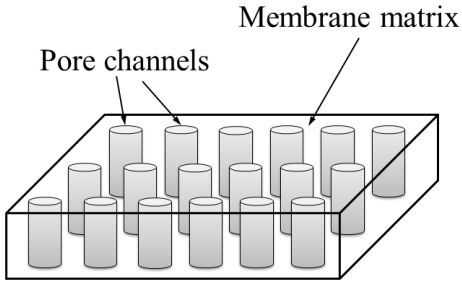

Figure 1.2 An illustrative diagram of isoporous membrane with pore channels of similar size.

Inorganic membranes, made of metals, metal oxides or elementary carbon with only a thin active layer supported by porous substrate are very promising in separation technologies owed to the better performance and chemical resistance [19]. Herein, this project focuses on the synthesis of porous silica-based membranes, which are highly versatile and easy to fabricate when compared to other inorganic membranes such as zeolites. Furthermore, the larger pore size can be tailored across mesoporous (2-50 nm; MD) range using surfactant-templating methods. Silica has comparable low thermal conductivity (~1.2 W m^{-1} K^{-1}) with PTFE (0.3 W m^{-1} K^{-1}) and this may further limit the conductive heat loss across the membrane. The major drawback of silica is its susceptibility to water attack and thus, modifications on the pore surface and within the silica matrix itself are typically required. Therefore, organic bridging siloxane network or incorporation of organic moieties within the silica matrix is typically employed to prevent the destruction of silica network. **It is therefore hypothesized that the incorporation of organic moieties in silica matrix will enhance the hydrothermal stability of the material.**

1.4 Key Contributions to the Field

This thesis has some key contributions to both the separation engineering and material science as follows:

- It is demonstrated for the first time that nanoporous organosilica membrane (pore size of 2 nm) with ordered pore structure produced pure water using vacuum membrane distillation with high and maintained permeation flux (13 L m^{-2} h^{-1}) across an extreme range of salt concentration (10-150 g L^{-1}) at moderate temperature (60 °C) with no observable pore wetting. The is significant because previous attempts using ceramic membranes suffered from low fluxes and/or flux decay and utilized either much larger or smaller pore sizes.

- A new mathematical model describing the transport of water through the unconventional, hydrophilic, nanoporous organosilica membrane was developed by adapting the Lucas-Washburn equation for water intrusion into the nanopores channel induced by capillary pressure. The model quantitatively describes the permeation flux under the impact of membrane physical properties, thermal and concentration polarization, membrane hydrophilicity and water shear viscosity in nanoconfined space.
- A new approach to preparing mesoporous carbon-silica nanocomposites is introduced. The carbon and silica networks were proven to interact physically (i.e. without covalent bonds) although the exact structure remained unclear. The evolution of the surface chemistry over temperature range of 600 to 900 °C, i.e. carbonization, proved counterintuitive with a decrease in the degree of condensation. This arose from the resorcinol-formaldehyde polymer releasing hydroxyl groups that in turn attack the adjacent siloxane bonds and consequently, reduces the silica condensation degree with more associated geminal and single silanols.
- Finally, this thesis shows that mesoporous polymer-silica nanocomposites membranes exhibit comparable results to the organosilica membrane with only a single coating layer and reduced pyrolysis temperature (450 °C). These membranes could be a more economically viable and functionally tunable for MD in comparison to organosilica membrane.

1.5 Thesis Structure

This thesis is written in accordance to the European style as endorsed by The University of Queensland, in which the relevant journal manuscripts are embedded as the body of the thesis. The thesis structure is presented as follows:

- Chapter 2 presents the critical literature review on (1) the fundamentals of the membrane distillation processes, (2) the material development of mesoporous membranes templated with surfactant and appropriate characterization methods, and (3) relevant knowledge gaps to be addressed by the thesis and the future perspectives of mesoporous membranes.
- Chapter 3 describes the preparation of nanoporous organosilica membrane with ordered pore structure and the evaluation of its performance in water desalination using vacuum membrane distillation process. This chapter was published in Chemical Communications.

- Chapter 4 investigates the transport phenomena of the organosilica membrane using mathematical model. This includes predicting and explaining correlation between the membrane properties to the permeation flux using the model. This chapter is under review for publication in the Journal of Membrane Science.
- Chapter 5 expands the studies of organosilica membranes to how different pore geometries and pore sizes impact the MD process. This chapter also discusses the effect of heat treatment on the membrane surface properties and performance.
- Chapter 6 presents the synthesis of mesoporous carbon-silica nanocomposite (CSN) membranes using a triconstituent organic-inorganic self-assembly method. The silica content on the CSN materials was varied, as was the heat treatment temperature to elucidate structure-property-performance relationships in VMD.
- Chapter 7 demonstrates the preparation of mesoporous polymer-silica nanocomposite derived from previous chapter by a single coating and evaluates the performances of membranes in water desalination using MD process.
- Finally, Chapter 8 presents the overall conclusions and recommendations for possible future works.

References

[1] D.R. Dicks, Thales, The Classical Quarterly (New Series), 9 (1959) 294-309.

[2] O. Barron, Desalination Options and their possible implementation in Western Australia: Potential Role for CSIRO Land and Water. , CSIRO: Water for a Healthy Country National Research Flagship, Canberra., CSIRO2006, pp. 4.

[3] J.E. McMahon, Water and Energy Interactions, 2013.

[4] T. Humplik, J. Lee, S.C. O'Hern, B.A. Fellman, M.A. Baig, S.F. Hassan, M.A. Atieh, F. Rahman, T. Laoui, R. Karnik, E.N. Wang, Nanostructured materials for water desalination, Nanotechnology, 22 (2011) 1-19.

[5] J.E. Miller, Review of Water Resources and Desalination Technologies, Sandia National Laboratories2003, pp. 3-54.

[6] L.F. Greenlee, D.F. Lawler, B.D. Freeman, B. Marrot, P. Moulin, Reverse osmosis desalination: Water sources, technology, and today's challenges, Water Research, 43 (2009) 2317-2348.

[7] DOW Water & Process Solutions - FILMTEC(TM) Reverse Osmosis Membranes, Technical Manual.

[8] H.J. Zwijnenberg, G.H. Koops, M. Wessling, Solar driven membrane pervaporation for desalination processes, Journal of Membrane Science, 250 (2005) 235-246.

[9] J. Zhang, N. Dow, M. Duke, E. Ostarcevic, J.-D. Li, S. Gray, Identification of material and physical features of membrane distillation membranes for high performance desalination, Journal of Membrane Science, 349 (2010) 295-303.

[10] Z. Xie, D. Ng, M. Hoang, T. Duong, S. Gray, Separation of aqueous salt solution by pervaporation through hybrid organic-inorganic membrane: Effect of operating conditions, Desalination, 273 (2011) 220-225.

[11] D. Winter, J. Koschikowski, M. Wieghaus, Desalination using membrane distillation: Experimental studies on full scale spiral wound modules, Journal of Membrane Science, 375 (2011) 104-112.

[12] P. Wang, M.M. Teoh, T.-S. Chung, Morphological architecture of dual-layer hollow fiber for membrane distillation with higher desalination performance, Water Research, 45 (2011) 5489-5500.

[13] M. Safavi, T. Mohammadi, High-salinity water desalination using VMD, Chemical Engineering Journal, 149 (2009) 191-195.

[14] K.W. Lawson, D.R. Lloyd, Membrane distillation, Journal of Membrane Science, 124 (1997) 1-25.

[15] F. Banat, R. Jumah, M. Garaibeh, Exploitation of solar energy collected by solar stills for desalination by membrane distillation, Renewable Energy, 25 (2002) 293-305.

[16] J.-P. Mericq, S. Laborie, C. Cabassud, Vacuum membrane distillation of seawater reverse osmosis brines, Water Research, 44 (2010) 5260-5273.

[17] F. Macedonio, E. Curcio, E. Drioli, Integrated membrane systems for seawater desalination: energetic and exergetic analysis, economic evaluation, experimental study, Desalination, 203 (2007) 260-276.

[18] A. Alkhudhiri, N. Darwish, N. Hilal, Membrane distillation: A comprehensive review, Desalination, 287 (2012) 2-18.

[19] H. Verweij, Inorganic membranes, Current Opinion in Chemical Engineering, 1 (2012) 156-162.

2 LITERATURE REVIEW

2.1 Introduction

This literature review covers the basic principles of membrane distillation (MD) for desalination and the synthesis of porous materials. Section 2.2 will first evaluate the difference between membrane configurations and respective transport mechanisms in membrane distillation. Followed by a critical review on reported works in MD and pervaporation using different inorganic membranes as well as distinguishing the difference between PV and vacuum MD processes, which has been the subject of some misconceptions (and are often used interchangeably) over the recent years [1]. The subsequent sections will then introduce the formation mechanisms of mesoporous materials by soft-templating methods, as well as the synthesis of carbon-silica nanocomposite materials. Finally, the future perspective of MD in desalination will also be discussed.

2.2 Fundamentals of Membrane Distillation

2.2.1 Membrane configurations

Membrane distillation (MD) is a thermal separation technology where the separation happens via a phase change across a non-selective, porous membrane used to control the liquid/vapour interface. In desalination it is a relatively immature technology compared to the conventional processes (distillation and RO) that shows promise owing to its lower operating pressures and temperatures, small vapour head space and ability to utilise low grade heat sources [2]. The driving force in MD is the vapour pressure gradient typically induced by the difference of transmembrane temperatures between the feed and permeate sides. The feed liquid is generally in contact with the membrane surface without penetrating into the dry pores, thus, a liquid/vapour interface is formed. In general, there are four main types of MD configurations as depicted in Figure 2.1: (i) DCMD (direct contact MD): where the permeate side of the membrane is in direct contact with cooled condensing liquid and a liquid/vapour interface is formed at each side of the membrane but the internal pore space remains vapour filled; (ii) AGMD (air-gap MD): where a cold condensing surface on the permeate side is separated from the membrane surface by a stagnant air gap (iii) SGMD (sweeping gas MD): where the vapour at the permeate

side is continuously swept away by cold inert gas and (iv) VMD (vacuum MD): where low pressure or near vacuum is applied on the permeate side [2-4]. Both SGMD and VMD require an external condenser unit which will increase the capital cost of such processes. Further the use of an external condenser may also increase the operating cost although it is unclear whether the additional cooling duty will exceed pumping and cooling requirements for DCMD systems, for example. However, VMD provides highest permeating flux due to the absence of concentration polarization layer at the permeate side and the largest transmembrane vapour pressure difference [3].

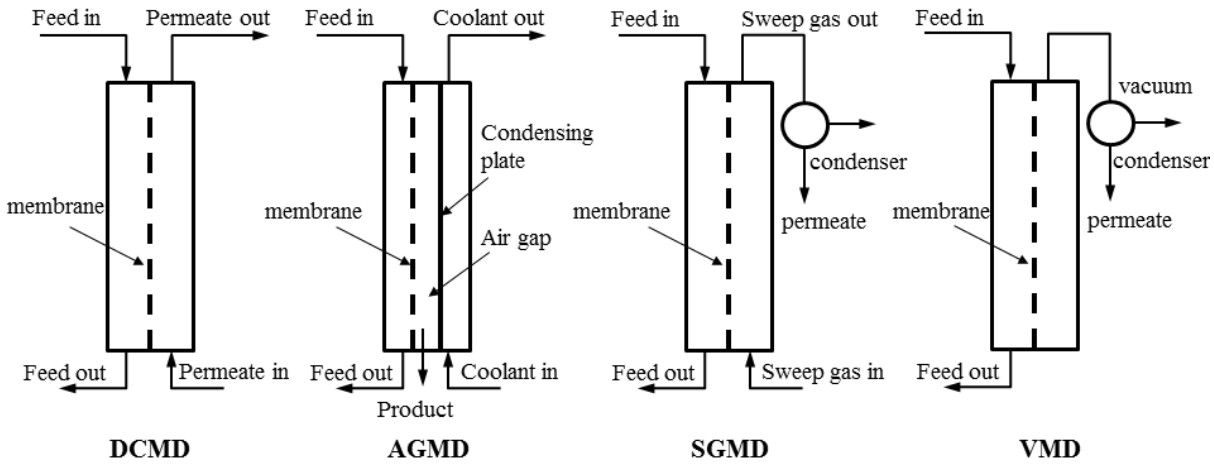

Figure 2.1 Different MD configurations: (from left) direct contact MD, air gap MD, sweep gas MD and vacuum MD [2]

In MD, the membrane only acts as physical barrier between the two phases with no permselectivity required. However, the pore must be kept dry to ensure only vapour and condensable gases pass through the pores. Transmembrane hydrostatic pressures exceeding the liquid entry pressure (LEP) or any surface active components within the solution that have direct contact with the membrane surface may also induce the loss of barrier of liquid/vapour interfaces at the pores. When this occurs, the pores filled with liquid or "wet out" and the separation performance of the membrane is significantly decreased. The LEP is defined by the equation as follows [5, 6]:

$$LEP = \frac{-2B\gamma_L \cos\theta}{r_{\max}} \tag{1}$$

Where B is a geometric factor determined by pore structure, γ_L the liquid surface tension, θ is the liquid/solid contact angle and $r_{\max}$ as the membrane's largest allowable pore size [6]. In order to

fulfil the LEP, hydrophobic membranes with pore size between 0.1-1.0 µm are essentially applicable in MD, except VMD that requires smaller pore sizes (less than 0.45 µm) due to the higher transmembrane pressure [2]. These figures may vary if the feed solutions contain different level of organic concentration, which might substantially alter the liquid surface tension [7]. Therefore, a hydrophobic membrane will not ensure a perfect dry pore considering microorganisms and organic compounds are ubiquitous in most salt water feeds.

2.2.2 Heat and mass transfer in MD

Transport phenomena in MD involve both heat and mass transfer, and whilst the overall concepts are effectively interchangeable regardless of the MD configuration, only VMD, as represented in Figure 2.2, is discussed herein. Three major steps are involved in heat transfer including: (i) heat transferred from the feed solution to the membrane surface across the thermal boundary layer inducing the temperature polarization effect. As consequence, bulk feed temperature T_{fb} is gradually decreased across the thermal feed boundary layer with thickness, δ_{ft} to feed side membrane surface temperature, T_{fm}; (ii) heat transport by conduction across both the membrane matrix of thickness, δ contributing to heat loss in MD; (iii) the latent heat of vaporization, ΔH and the heat loss accompanying mass transfer through the membrane pores. Similar steps are involved in mass transfer, although in this case the driving force is partial pressure difference as opposed to temperature.

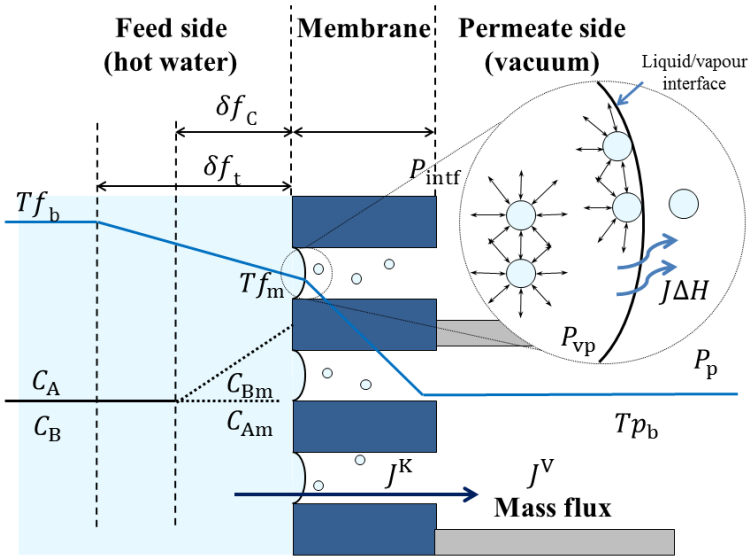

Figure 2.2 Temperature and concentration polarization in VMD

Concentration polarization is the mass transfer equivalent of temperature polarization and is mainly governed by the composition of the feed compound as well as its volatility. If there is only one single volatile compound, A in the feed side, then there will be no change of concentration in the bulk and membrane surface of the feed side, denoted as $C_{Ab} = C_{Am}$. On the contrary, if the feed solution contains non-volatile compound B (as is this case in desalination) this will eventually build up its concentration, C_{Bm}, on the membrane surface at the feed side inducing a mass boundary layer of thickness δ_{fc}, i.e., concentration polarization [2]. Mass transfer in MD is generally imposed by convective and diffusive transport of volatile species (gas phase) through the membrane pores. Three basic concepts known as Knudsen-diffusion, Poiseuille-flow (viscous flow), molecular-diffusion or some combinations between them are used to describe the transport mechanisms that related to resistance of membranes with different pore size. The governing mechanism can be determined by Knudsen number (Kn), which is defined as the ratio of the mean free path, λ, of the transported molecules to the pore size of membrane:

$$Kn = \frac{\lambda}{d_{\mathrm{p}}} \tag{2}$$

The mean free path, λ, is expressed as follows:

$$\lambda = \frac{k_B T}{\sqrt{2}\pi \overline{P} \sigma^2} \tag{3}$$

where, k_B is the Boltzmann constant, T as the absolute temperature, $\overline{P}$ as the mean pressure within the membrane pores and σ as the collision diameter (2.641 Å for water vapour) [3]. Given that the mean free path is governed by the mean pressure within the membrane pores, VMD with the lowest pressure applied at the permeate side gives the highest mean free path value.

Here, consider a membrane with uniform pore radius r. Knudsen flow dominates when r is less than 0.05λ [3] with the permeability of water vapour as follows:

$$B^K = \frac{2\varepsilon r}{3RT\tau\delta}\left(\frac{8RT}{\pi M}\right)^{1/2} \tag{4}$$

where ε is the membrane porosity, τ is the pore tortuosity, δ is the membrane thickness and M is the molecular weight.

When $0.05\lambda < r < 50\lambda$, transition flow will dominate and the permeability is expressed as,

$$B^T = \frac{1}{RT\delta}\left(\frac{2\varepsilon r}{3\tau}\left(\frac{8RT}{\pi M}\right)^{1/2} + \frac{\varepsilon r^2}{8\tau\eta}\overline{P}\right) \tag{5}$$

where, η is the viscosity of water vapour.

The mass transfer is driven by the vapour pressure difference across the membrane as follows [8],

$$J = C_{\mathrm{m}}\left(P_{\mathrm{fm}} - P_{\mathrm{intf}}\right) = C_{\mathrm{global}}\left(P_{\mathrm{Tfb}} - P_{\mathrm{Tpb}}\right) \tag{6}$$

where, C_{m} is the membrane mass transfer coefficient that is based on the membrane properties and gas condition within the pores, P_{fm} and P_{intf} are the vapour pressure at membrane feed and permeate sides, respectively, C_{global} is the global mass transfer coefficient that considers both boundary layer effects and membrane effects and P_{Tfb} and P_{Tpb} are the vapour pressure at the thermal boundary of feed side and permeate side, respectively. Comparing equation (6) to equation (4) and (5) gives the relationship of C_{m} to other parameters as,

$$C_{\mathrm{m}} \propto \frac{\varepsilon r}{\tau\delta} \tag{7}$$

It is more appropriate to assess the membrane performance by evaluating C_{m} values given that this coefficient is more independent of the effect of variations in operating temperature. However, C_{global} value has usually been assessed from experimental data due to the fact that C_{m} is more difficult to obtain [9]. As aforementioned, the heat transfer through a membrane is associated with heat conduction, Q_{c} across the membrane and the latent heat of vaporization (water), Q_{v}. Thus, the total heat transfer can be expressed as,

$$Q = Q_c + Q_v = -k_m\frac{dT}{dx} + J\Delta H_v \tag{8}$$

where, k_{m} is the thermal conductivity of the membrane, x is the distance across the membrane and J as the transmembrane flux. Here, the k_{m} value could be obtained from this equation,

$$k_{\mathrm{m}} = \varepsilon k_{\mathrm{g}} + (1-\varepsilon)k_{\mathrm{p}} \tag{9}$$

where, k_{g} is the thermal conductivity of the water vapour and k_{p} is the thermal conductivity of the material of the membrane.

Comparing to other membrane configurations, VMD has the advantages of low conductive heat loss, whereby the thermal boundary layer at the permeate side is negligible due to the applied vacuum [3, 10, 11]. Furthermore, mass transfer resistance is also greatly reduced due to the absence of air or other gases in the membrane pores, which might hinder the water vapour transport across the pore channel. In general, temperature polarization dominates the overall

mass transfer resistance more than concentration polarization and it becomes more significant for membranes with high fluxes [12]. Clever design of the membrane system by installing baffles or spacers in the membrane module to create turbulent flow [13, 14] and optimization of the operating conditions (feed temperature, cross flow velocity, enhanced condensation unit, etc.) is necessary to alleviate the heat and mass transfer resistances on the feed side.

2.2.3 Comparison of VMD and pervaporation

Pervaporation (PV) is a related technology, which also relies on volatile components evaporating across a membrane. However, the transport is more governed by the sorption equilibrium and mobility of water inside the membrane as opposed to MD [12, 15]. Notably, VMD process is commonly mistaken as pervaporation process due to the application of vacuum on the downstream or permeates side of the membrane. The main distinguishable characteristic of these two processes is that a dense and selective membrane is required in pervaporation, whereas VMD uses a porous and hydrophobic membrane as illustrated in Figure 2.3.

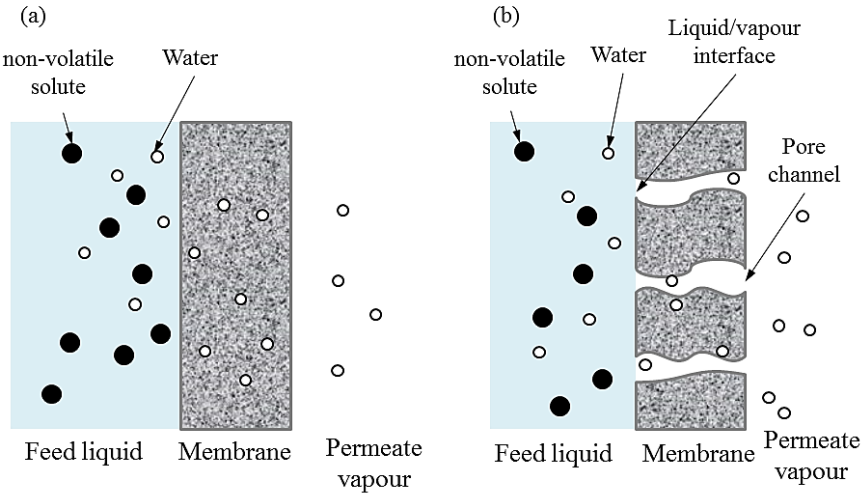

Figure 2.3 Mechanisms of mass transfer in pervaporation (a) and VMD (b) processes [1]

Mass transport in pervaporation is mainly governed by solution-diffusion mechanism through a dense polymeric membrane, whereby the selective permeation of water is determined by the (i) sorption of feed liquid molecules at the feed side of membrane, (ii) diffusion through the membrane matrix and (iii) desorption into vapour phase at the permeate side. Solubility and diffusivity of each component in the feed mixture play a major role in the separation process and the vaporization of the permeated component could be happening either on the feed or permeate

side of the membrane [1, 15]. Here, it is essential that the membrane to having high sorption sites for specific interactions with water either as dipole-dipole, hydrogen bonding, or ion dipole interactions. The last two interaction modes are stronger and thus, give a higher selectivity. When a multilayer of water molecules are adsorbed on the membrane surface, the diffusion channel becomes narrower and a "molecular sieve" effect will be created if the passage is smaller than the hydrated salt ion [15].

In VMD, a hydrophobic membrane with larger pores serves as physical barrier and molecular adsorption on membrane surfaces becomes negligible due to greater water-water interaction. The low water affinity of hydrophobic membrane in MD is exempted from the requirement of being permselective as in pervaporation. If the selected membrane has smaller pores than traditional MD membranes (<10 nm) but large enough to allow hydrated salt ions to pass and the material is not perfectly hydrophobic (contact angle < 90 °) then the exact transport mechanism is unclear. The membrane would not satisfy several criteria of the MD definition, nor would it be selective, ruling out pervaporation. Such cases highlight a gap in current knowledge and are explored experimentally and theoretically in Chapter 3 and 4 of this thesis.

2.2.4 State-of-the art of membrane development in MD-desalination

Hydrophobic polymeric membranes are widely used in MD but they can require extensive pre-treatment, wherein the membrane surface is functionalized by apolar or surface-active molecules to repel those components in the feed solution which can induce pore wetting [16]. To date, there is also an increasing interest in the hybrid membranes to improve their stability [17] and mechanical strength [18]. Hybrid organic-inorganic membranes have attracted some attention in this space in the quest to improve MD membranes. The inorganic component, typically a ceramic, improves chemical and thermal stability and allows operators to employ harsh anti-fouling measures not available to their polymeric counterparts. The organic part is typically used to induce or improve the hydrophobicity to minimise pore wetting. These hybrids can take the form of homogeneous composite, for example those formed from the organosilica precursor 1, 2-bis(triethoxysilyl)ethane (BTESE) were found to have improved hydrothermal stability [19-22]. Organosilica with alkyl or aromatic groups bridging the silica chain have been shown to strengthen the silica network to be more hydrolytically stable [21, 23]. Other attempts have focussed on the surface modification of a hydrophilic ceramic membrane to hydrophobic surface

by grafting the membrane with fluoroalkylsilanes (FAS) have also been reported [24-26]. Instead of using a common ceramic substrate for the FAS-grafting, Hendren and co-workers chose the anodic alumina disc, which has uniform cylindrical pores due to the anodization production process [27]. This in theory should reduce the tortuosity of the mass transport but the low permeating flux that was observed is believed to be due to the heat loss associated with the high thermal conductivity of alumina. Other than this, He et al. reported on partial-carbonization of polymeric (polyfurfuryl alcohol) membrane by using highly concentrated sulfonic acid [28]. The membrane has good stability against chlorine treatment but suffered low permeability [28]. However, this work shows the possibility of improving the membrane chemical resistance by using a low temperature approach and the benefits of tailoring the organic-inorganic components for better stability.

Table 2.1 lists the performances of a variety of polymeric and inorganic membranes used in MD and pervaporation for desalination studies. Hydrophobic membranes with large pores exhibit higher water fluxes, although a time-dependent decline in flux is observed when the salt concentration of feed solution increased [25]. In comparison to their polymeric counterparts (PVDF and PTFE), modified inorganic membranes (carbonized template membrane and hybrid) suffer from lower fluxes due to lower porosities and smaller pore sizes. For membranes with pore sizes within the meso- to nanopore region, the permeation fluxes are measured at 6-7 L m^{-2} h^{-1} at low feed temperature [29, 30]. However, the permeation fluxes are greatly influenced by MD configurations, membrane morphology, operating conditions (module set up, feed flow rate, transmembrane temperature difference etc.), membrane properties (pore size, porosity, thickness etc.) and thus, comparing the membrane performances based on reported fluxes may not be conclusive.

Table 2.1 Reported works on membrane distillation desalination using polymeric and inorganic membrane

Types of membrane	Pore Size, nm	Membrane morphology	Process module	Operating Conditions	Flux, L m^{-2} h^{-1}	Ref.
PVDF dual-layer	n/a	Hollow fiber	DCMD	50 °C, ΔT = 35 °C, 3.5 wt% NaCl	~ 30	[31]
PVDF	120-270	Hollow fiber	VMD	50 °C, distilled water	18	[32]
PTFE	200	Flat	DCMD	27.5 °C, distilled water	21.6	[33]
FAS-anodic Al_2O_3	200	Disk	DCMD	53 °C, ΔT= 35 °C, 0.6 wt% NaCl	8	[27]

FAS-Al_2O_3	700	Hollow fiber	VMD	50 °C, 40 Pa, 4 wt% NaCl	10	[25]
FAS-ZrO_2	50	Tubular	VMD	40 °C, 300 Pa,	7.5	[26]
FAS-TiO_2	5			3 wt% NaCl	6	
BTESE organosilica	~4.5	Tubular	Pervaporation	30 °C, < 266 Pa, 0.2 wt% NaCl	~3	[19]
Hybrid PVA/MA/Si	n/a	Flat	Pervaporation	22 °C, 800 Pa, 0.2 wt% NaCl	6.93	[29]
Carbonized template	0.5	Tubular	Pervaporation	25°C, 0.3-3.5 wt% NaCl	1.7-2.2	[34]
Silica	2-8	Tubular	Pervaporation	22 °C, 3.5 wt% NaCl	6.8	[30]

In short, many attempts on membrane development for MD are still ongoing, either to reach higher permeation flux or improve the membrane stability but there are still many unanswered questions. Essentially, a thorough understanding of the structure-property relationships for existing membranes and those outside typically consideration (e.g. d_p < 10 nm) is vital for future strategies in membrane design.

2.3 Silica Derived Membranes

Silica derived material are good candidates to be implemented as MD membrane, particularly due to its low thermal conductivity (~1.2 W m^{-1} K^{-1}) [35] and versatility to form any morphology and functionalization. The most commonly applied method for the synthesis of silica materials is via sol-gel method which involves a silicon alkoxide precursor for the formation of sol (a suspension of colloidal or polymeric particles in a liquid) that subsequently polymerizes and transforms into a macromolecule gel network. The process is generally based on the substitution of organic or inorganic ligands that are covalently bonded to the silicon atoms via hydrolysis (Eqn 10) and condensation (Eqn 11) reactions as described as follows [35]:

$$\equiv \text{Si-OR} + \text{H}_2\text{O} \xrightarrow{\text{hydrolysis}} \equiv \text{Si-OH} + \text{ROH} \quad (10)$$

$$\equiv \text{Si-OR} + \text{HO-Si} \equiv \xrightarrow{\text{alcohol condensation}} \equiv \text{Si-O-Si} \equiv + \text{R-OH} \quad (11)$$

$$\equiv \text{Si-OH} + \text{HO-Si} \equiv \xrightarrow{\text{water condensation}} \equiv \text{Si-O-Si} \equiv + \text{H}_2\text{O} \quad (12)$$

2.4 Mesoporous Materials with Controlled Pore Size and Pore Geometry

Porous materials with ordered pore structures were first developed and reported by Mobil researchers in the early 1990s [36, 37]. This had tremendous impact on materials science and engineering and lead to an explosion in mesostructured materials with tailorable pore size, pore geometries, shapes and functionalities. The remarkable porous structures were typically generated using soft matter, which are organic molecules or supramolecules (e.g. amphiphilic surfactants and biomacromolecules) as templates. Synthesis of the mesostructured silica in various forms such as particles [38-45], monoliths [46-49], fibers [50, 51] and thin films [46, 52-64] have been extensively studied using varying surfactants classified as cationic [50, 65], anionic [38, 58, 66-68], nonionic [46, 55, 69-71], amphoteric [42] or even combinations of them [72-76]. These materials with controllable structures and systematically tailored pore architectures show great potential in a myriad applications including catalysis, sensors, electronic devices, biology, nanodevices, and membrane separations [77-80]. Four principal approaches of synthesis strategies have been reported so far as shown in Figure 2.4:

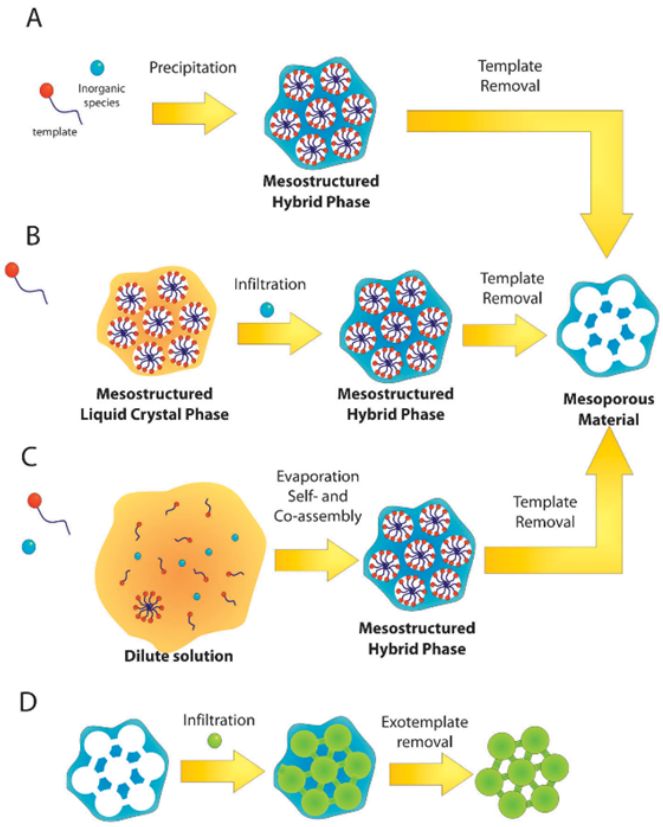

Figure 2.4 Main synthetic approaches for mesostructured materials: (A) Precipitation, (B) Liquid Crystal Templating (LCT), (C) Evaporation-Induced Self-Assembling (EISA) and (D) Exotemplating [81].

A. **Precipitation**. A mesophase with local order is formed via the cooperative assembly of the inorganic precursors and the supramolecular template. Both highly and locally ordered domains coexist during aging and thus, the inorganic hydrolysis and condensation needs to be controlled in order to obtain highly ordered pore systems. Nanoparticle formation can take place both in solution and in the interior of micelles, emulsions, or vesicles, leading to complex shaped materials [79]. This method is straightforward and mass produces mesostructured materials but is limited to the formation of particles/powders.

B. **Liquid crystal templating (LCT)**. This synthesis pathway involves true liquid crystal mesophases, in which high concentration of surfactants form mesostructures followed by attachment and condensation of inorganic precursors that grow on the liquid-crystal scaffolds [80]. However, the LCT is less feasible as the liquid crystal ordering could be easily disrupted by the addition of metal precursor or by the released alcohol during hydrolysis [81].

C. **Evaporation-induced self-assembly (EISA)**. A diluted mixture of the inorganic precursors and the supramolecular template are present and with the solvent evaporation that leads to more concentrated solution forming the inorganic-template hybrid mesophase. The inorganic phase is usually partially polymerized and is completed by aging under controlled humid conditions and heating. This method is highly versatile to form materials in the shape of thin films, aerosols and monoliths.

D. **Exotemplating**. This is a two-step route that using porous materials as hard template. After the addition of the precursor, the hard template/exotemplate is removed leaving the replica mesophase. This method is widely used in the formation of mesoporous carbon but involves higher cost due to the sacrificial hard template.

2.4.1 Self-assembling templates

Surfactants are amphiphilic compounds containing both hydrophobic groups (tails) and hydrophilic groups (head). In general, surfactants can be classified as cationic, anionic, nonionic and amphoteric depending on the head group present. At sufficiently high concentrations, surfactants will start to aggregate and self-assemble into higher ordered structures via non-

covalent interactions (hydrogen bonding, Van der Waals forces, electrostatic forces and π-π interactions) with no external intervention [82]. Micelles are formed in an aqueous medium when the surfactant concentration reaches the critical micelle concentration (CMC) and different structure of micelles can be obtained depending on its concentration. Figure 2.5 illustrates an example of the phase diagram of the cationic surfactant cetyltrimethylammonium bromide (CTAB, $C_{16}H_{33}N(CH_3)_3Br$) in water at varying concentrations and temperature. After exceeding the CMC the transformation of the mesophase from spherical micelle → cylindrical → 2-dimensional hexagonal array → cubic → lamellar liquid crystal occurs with increasing temperature and surfactant concentration. Surfactants with low CMC values (< 20 mg L^{-1}) yield ordered mesostructures, whereas large CMC values produce cubic mesostructures [83].

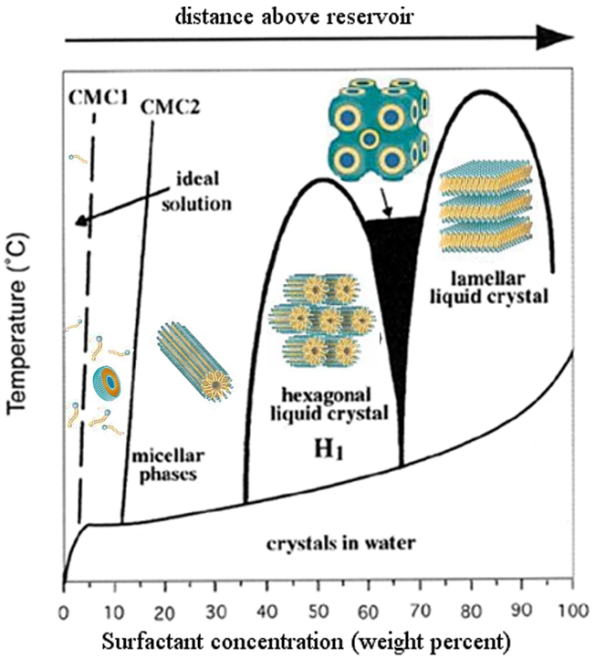

Figure 2.5 Schematic phase diagram of CTAB in water [82].

The type polar head group and hydrophobic chain length of the surfactant template determine the final mesostructure (lamellar, hexagonal or cubic phases) and the subsequent pore size [80]. The contemporary molecular descriptor for surfactant organization is the local effective surfactant packing parameter, $g = V/a_0 l$ (V is the total volume of the surfactant chains plus any co-solvent organic molecules between the chains, a_0 is the effective head group area at the micelle surface, and l is the kinetic surfactant tail length or the curvature elastic energy). An increase in g is associated with a decrease in surface curvature denoting the transition of the mesophase from a cubic to a lamellar structure as shown in Table 2.2. Huo et al. demonstrated that the phase

transition and mesostructure of the material could be predicted by referring to the *g* values of the surfactants correlated with the synthesis conditions (acidic/basic synthesis media)[84].

Table 2.2 The expected mesophase sequence as a function of the packing parameter

g	Mesophase
⅓	Cubic (*Pm*3*n*)
½	Hexagonal (*p*6*m*)
½ – ⅔	Cubic (*Ia*3*d*)
1	lamellar

Quaternary cationic surfactants, $C_nH_{2n+1}N(CH_3)_3Br$ (n = 8-22), have historically been the most studied due to their efficiency in providing ordered mesoporous structures [65, 85-87]. This is primarily because cationic surfactants have excellent solubility and a high critical micelle temperature making them easy to work with, but they are also typically toxic and expensive. Recently, nonionic surfactants, in particular, triblock copolymers have attracted more attention owing to the vast varieties in their chemical structure, lower price, nontoxicity, and biodegradability [80]. Similarly to the g value, the mesostructure of using nonionic surfactant could be predicted based on the hydrophilic/hydrophobic volume ratios (V_H/V_L) of the surfactant. For instance, triblock copolymer F127 (polyethylene oxide-polypropylene oxide-polyethylene oxide, PEO_{106}-PPO_{70}-PEO_{106}) with high V_H/V_L ratio has higher topological curvatures which favour the formation of cage-type cubic mesostructure [80].

2.4.2 Formation mechanisms of mesoporous thin films and membrane

The synthesis approach of ordered mesoporous silica thin films and membranes is slightly different from those employed to produce particles and monoliths. A versatile strategy suggested by Brinker and co-workers, the so-called evaporation-induced self-assembly (EISA) method [82], based on liquid crystal template pathway, is commonly adapted in the preparation of mesostructured silica thin films. Figure 2.6 illustrates the phenomena of EISA with different stages of film formation during the dip-coating. Beginning with the low degree of polymerization of the inorganic precursors in a volatile, weakly polar solvent; the film forms during the fast evaporation of the solvent (ethanol, HCl and water) (Stage 1). At Stage 2, the difference of relative humidity (RH) of environment (> 45 %) and the film (< 40 %) allows the

diffusion of water from the atmosphere into the film and the organic-inorganic mesophases begin to self-aggregate with continued drying (Stage 3). At this point, concentration of surfactant will increase and when beyond the CMC, liquid crystal phases will form. A phase transition from disorder-to-order is possible depending on the water content in the film and the RH. In the meantime, the inorganic precursors hydrolyse and cross-link, agglomerating on and around the liquid crystal template. Subsequently, the final mesostructure is formed as a result of further condensation releasing water that leads to volume contraction (Stage 4 and 5). In this case, the pH of the sol-gel solution was controlled at around the isoelectric point of silica at pH = 2 [88, 89].

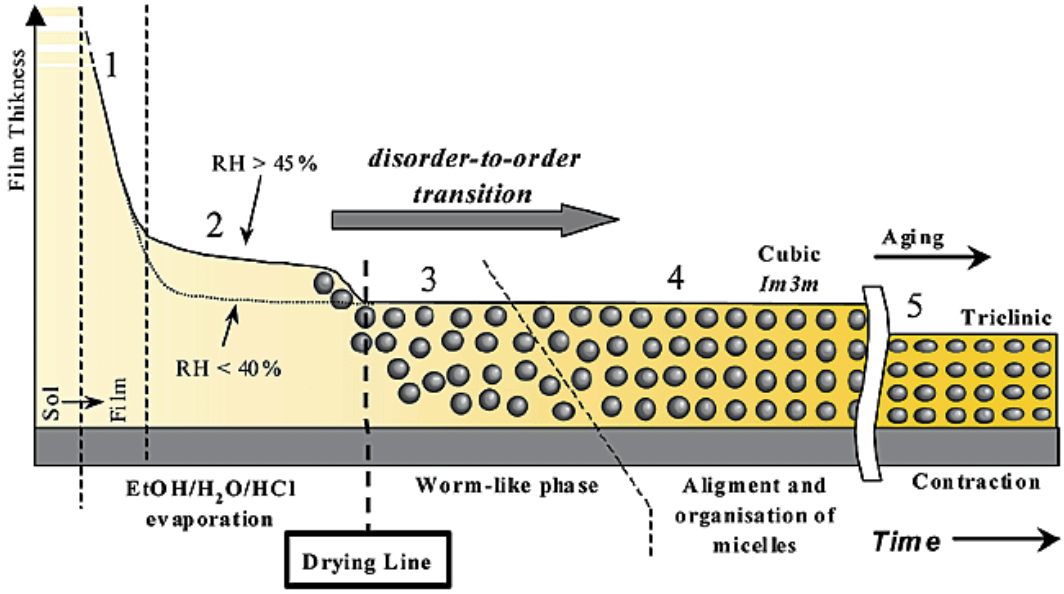

Figure 2.6 Scheme representing the stages of film formation during dip-coating [89].

Sanchez and co-workers have carried out extensive and comprehensive studies on the formation of mesostructured thin films by combining various techniques (^{29}Si NMR, *in situ* two-dimensional small angles X-ray scattering (2D-SAXS), *in situ* Fourier transform infrared (FTIR) spectroscopic ellipsometry, Karl Fischer water titration, transmission electron microscopy (TEM)) [60, 89-92]. The freshly deposited films are still prone to phase transition depending on the external conditions, e.g. environment humidity, convective air flow, evaporating rate and temperature. According to Grosso et al., the final structure in the film after evaporation experiences a crucial period namely, the modulable steady state (MSS), during which the water and the solvent contents of the film are in equilibrium with the environment allowing the rearrangement of the mesophases [92]. They demonstrated how one could modulate the film

mesostructure by tuning the relative humidity in the deposition chamber. In addition, the final mesostructures could also be influenced by the nature of surfactant [80], ratio of surfactant/inorganic precursors, hydrolysis and cross-linkage of inorganic precursors [91] and type of substrate [93].

Nevertheless, the deposited film is still not stable and requires further heat treatment for a higher degree of condensation and template removal. Herein, the film is highly likely to experience shrinkage in the direction normal to the substrate, which induces phase transition or strong distortion of the cell parameters. In this case, a distortion of the pore shape from spherical to ellipsoidal is possible and eventually the pore organization will also be disrupted. Figure 2.7 illustrates the mesophase transition induced by shrinkage of the deposited film after heat treatment [94].

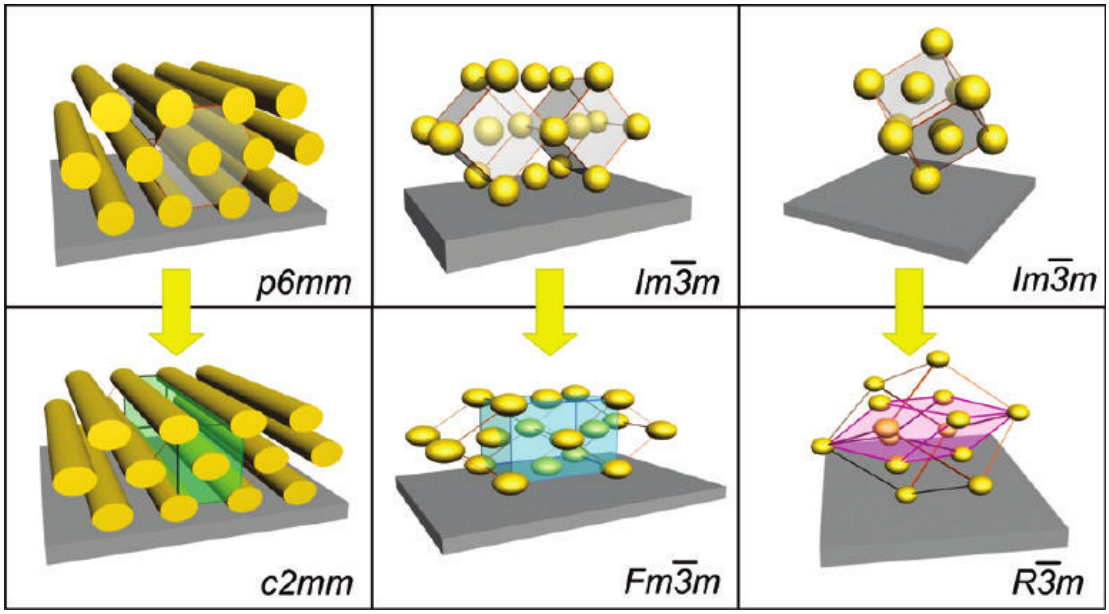

Figure 2.7 Mesophase transition in ordered mesoporous silica films [94]

Innocenzi et al. also discussed about other defects that commonly found in the formation of ordered structure mesoporous silica thin films on silicon wafer [94]. In particular, the mesophases tend to form a polycrystalline-like structure (Figure 2.8a), with random distribution of the ordered porous domains instead of a single crystal-like domain as shown in Figure 2.8b. Also, 2D-hexagonal mesostructures are more kinetically favour to align parallel to the substrate, which is not desired in the membrane separation. Other than this, Figure 2.8c shows the different mesostructures that coexist in the same film due to the different mesophase rearrangement

induced by varying solvent evaporation rate (from the film surface to the substrate). Falcaro et al. synthesized a defect-free hybrid MTES-TEOS silica thin film with a highly ordered tetragonal pore structure but still in a small range [95]. Hence, producing a defect-free highly ordered thin film/membrane is a substantial challenge not the least of which arises from the necessity of making thicker films for mechanical strength and the use of porous substrate with inherent defects and macrovoids.

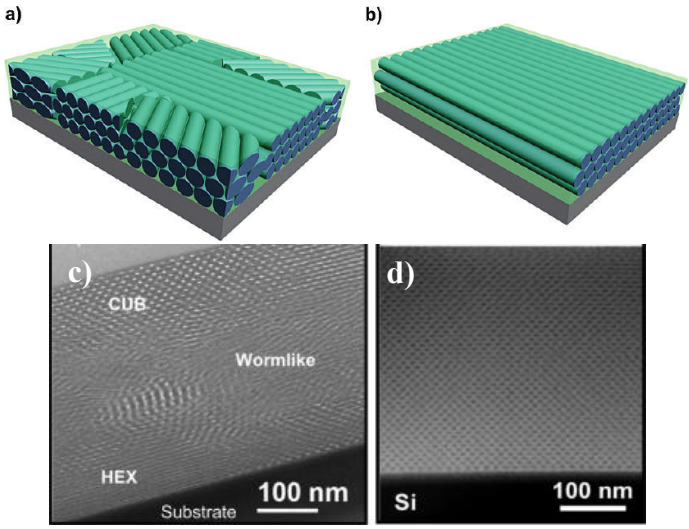

Figure 2.8 2D hexagonal ordered porous structure with (a) polycrystalline and (b) crystal-like domains[94]. TEM images of mesoporous silica with (c) mixture of hexagonal (HEX), wormlike and cubic (CUB) pore domains and (d) highly ordered tetragonal domain [95].

The applications of ordered mesoporous silica membranes vary from gas separation [96-99], filtration [100, 101] , ion transport in microfluidics [102] or even as intermediate layer for gas separation [103]. So far, there is no work reported on ordered pore structure silica membrane for desalination using membrane distillation process, which require membranes with narrow pore size distribution. Chowdhury et al. [100] and Nakagawa et al. [101] reported on synthesizing mesoporous silica membranes with hexagonal structures for ultrafiltration but the membrane hydrothermal stability was not further discussed. Recent research work on mesoporous inorganic membranes has begun to shift towards functionalization for specific applications, which will be further elaborated in the following section.

2.5 Functionalization of Mesoporous Silica Membrane

The mesoporous silica membranes possess ordered pore structures in an amorphous silica framework. Unfortunately, pure amorphous silica membranes have very limited hydrothermal stability and the maximum operating temperature in MD or pervaporation applications is only restricted to about 70 °C [104]. The pore surface of pure silica is enriched with hydroxyl groups (-OH), which provides a strong driving force for water sorption. Long term exposure in humid environment will eventually lead to cleavage of the siloxane bond (Si-O-Si) within the silica matrix and formation of silanol groups (Si-OH) from the reaction with water. The released silica moieties will be transported from high surface energy sites near nanopores to lower surface energy states, enlarging the large pores and blocking the nanopores [20]. It is therefore essential to functionalize the silica surface with organic groups to provide some shielding effect from water attack.

2.5.1 Modification by chemical interaction

Functionalization of mesoporous silica membrane with various organic groups to help protect the silica from hydrolytic attack could be conducted either on the silicate surface, pore walls or trapped within the pore channels [105]. Hybrid organic-inorganic silica membranes permit the modification of surface properties, such as hydrophilicity and hydrophobicity or chemical, physical, mechanical, and dielectric properties of its pore channels [106]. These membranes are generally synthesized via one-pot or post-grafting synthesis methods as illustrated in Figure 2.9.

a) Route (a) represents the post-grafting method, where the organic compound is incorporated by covalently binding to the inorganic walls after the synthesis of silica;
b) Route (b) shows the direct incorporation of organic compound into the inorganic matrix by co-condensation of siloxane and organosilane precursors (one-pot);
c) Route (c) uses bridged silsesquioxanes [$(RO)_3Si\text{-}R'\text{-}Si(OR)_3$] to produce organically modified mesoporous silica, known as periodic mesoporous organosilicas (PMO).

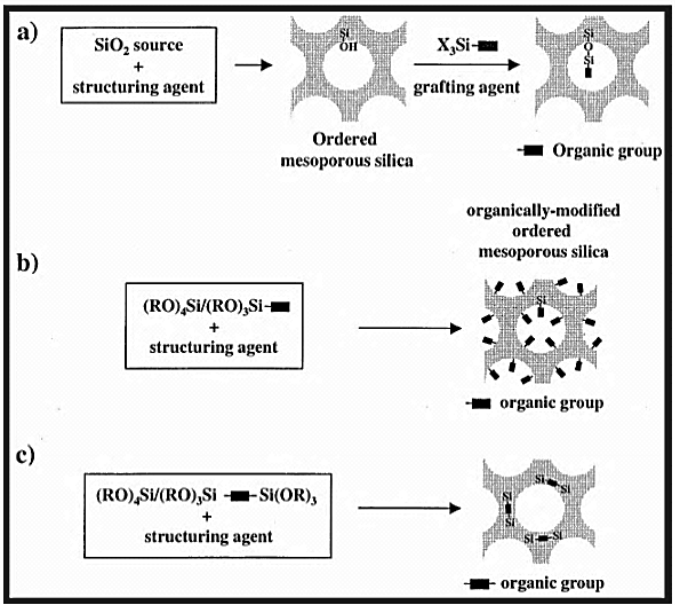

Figure 2.9 Incorporation of organic functions in mesoporous silica: (a) surface grafting of organic functions on the mesoporous walls by post-synthesis; (b) direct incorporation of organic functions by co-condensation of organosilanes or (c) bridging silsesquioxanes [106].

Extra care needs to be taken in the post-grafting synthesis method (Route a), which tends to have pore blocking due to the preferential reaction of organosilanes at the pore openings and the diffusion of molecules into the center of the pore [81]. In a membrane structure this would reduce the effective pore size and increase the tortuosity, compromising membrane performance. In comparison, the one-pot synthesis method with co-condensation of siloxane and organosiloxane precursors is beneficial in producing high modification ratios, homogeneous incorporation, and requires short preparation times but the choice of organosiloxane precursors is somewhat restricted by the synthesis conditions (alkaline media, hydrothermal synthesis and solvent extraction) [79]. Furthermore, this method allows the incorporation of different functional groups (e.g. phenyl, carboxylic, amine and fluorine species) with varying physico-chemical properties (e.g. hydrophobic, aromatic, acid/base) [107] into the silica matrix but the mesostructure ordering could be easily disturbed due to different hydrolysis-condensation rates [81]. Bridged silsesquioxanes are, however, more favourable in forming homogeneous organic-inorganic without the problem of pore blocking. The organic groups are embedded within the silica network, whereby organic bridges covalently with the silica ensures a stronger connection. However, the surface wettability of the material may not be much altered as compared to co-condensation and post-grafting methods. Different mesostructures and controlled morphologies

could be obtained by varying the R' group, either as alkyl groups $-(CH_2)_n-$ or aryl groups $-(C_6H_4)-$ [80].

2.5.2 Modification by physical interaction

Aside of chemical interaction, silica can also be physically modified by means of blending with polymer to produce composites. Unfortunately, a common trade-off problem for silica aerogel-polymer composites is the reduced mechanical strength (attributed to the polymer) and thermal stability (from silica) but these could be overcome when the inorganic phase is downsized to nanoscale (< 100 nm) to form nanocomposite [108]. Silica-polymer nanocomposite could be prepared by using conventional mixing process, such as melt kneading or solution blending, but these methods usually resulted in aggregation of silica particles [109] or the undesired interfacial void/gap between the silica phase and the polymer moieties [110]. Other interesting options so-called, *in situ* polymerization and sol-gel processes are able to produce homogeneous hybrids of two components with a high dispersion of silica due to its molecular level hybrids. However, the nanocomposites may undergo incomplete condensation of nano- or microscale silica structures due to the disruption of the polymer phase, and having difficulty of silica localization in the composite [111].

Recently, there are several approaches in producing nanocomposites either via nanocasting or co-assembly methods. Nanocasting is very similar to post-grafting except that there will only be physical interaction between the silica and polymer. Carbon precursors (furfuryl alcohol, sucrose, acenaphthene and mesophase pitch) are filled partially/completely into the ordered pore structure of the silica and different post treatments will be conducted to produce carbon-silica nanocomposites (pyrolysis in inert environment), mesoporous carbon (silica etching with hydrofluoric acid) or mesoporous silica (calcination in air to remove carbon) [112-114]. Nanocasting is effective in replicating the exact pore structure of the silica materials but the entire process is very time-consuming and there is a distinct lack of versatility for different morphologies. Following this, other efforts in simplifying the synthesis route to one-pot sol-gel synthesis method or so-called triconstituent co-assembly method was introduced by Zhao's group [115, 116]. In this method, three major components: thermoset resol as the organic precursor, silica source and surfactant were mixed together and allowed to co-assemble and form an ordered mesostructure (Figure 2.10).

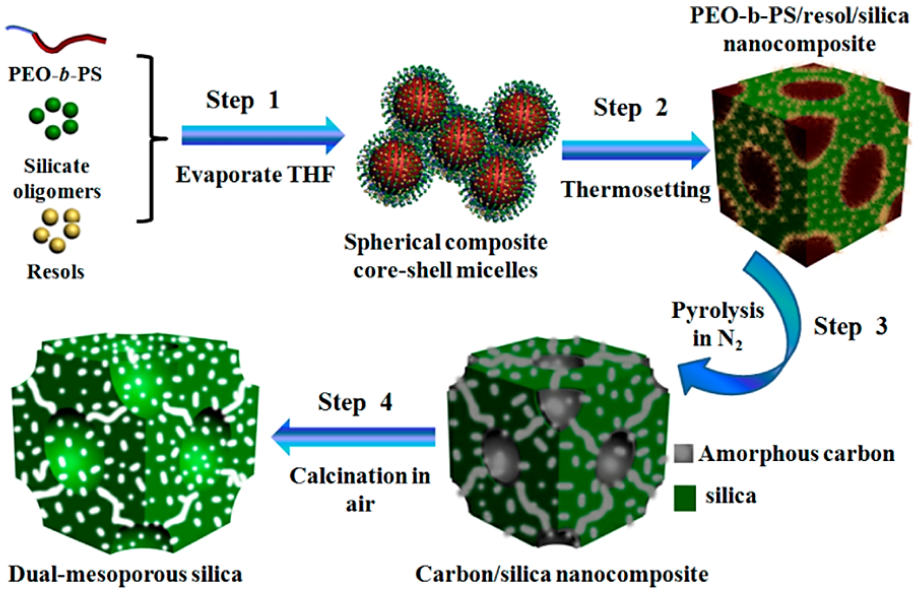

Figure 2.10 Formation process of 3D ordered mesoporous carbon/silica nanocomposites and the mesoporous silica [117]

Comparing to other carbon precursors, thermoset resol is more flexible in controlling the oligomer size and the resol network (benzene ring) is stronger and more hydrophobic than furfuryl alcohol. Due to the different polymerization rates of the silica and thermoset resol, it is quite challenging to produce highly ordered mesostructured nanocomposites without any phase separation. That being said, mesoporous carbon-silica nanocomposite thin films with varying silica content (38 to 56 wt%) have been prepared and silica was found to improve the adhesion of the thin film on the silicon wafer but the conductivity of the materials decreased at high silica content [116]. So far, all the reported works [117-119] used a pre-synthesized phenol-formaldehyde resol solution in order to ensure a complete polymerization of the polymer phase prior to the addition of inorganic phase. Also, the materials were carbonized at high temperatures (> 600 °C) for complete carbonization which can prove challenging for maintaining structural ability in the silica. Importantly, despite advances in carbon-silica nanocomposite materials, there have been few application based studies. There exists an opportunity therefore to examine the effectiveness of these materials as cheaper alternatives to organosilica membrane. Indeed, this facile and versatile synthesis method opens up a number of possible ways to produce materials of different morphologies (particles, films, monolith etc.) and some gaps remain in both the synthesis method improvement and suitable applications for the nanocomposites.

2.6 Research Gaps

Membrane distillation has promised much in desalination over recent decades mainly due to its reduced energy requirement compared to conventional thermal distillation method, compact footprint, simple operational requirements and zero liquid discharge ability. However, this technology still requires continuing research particularly in the understanding of membrane selection and technology improvement.

So far, most of the studies have focussed on hydrophobic membrane with pore size 0.1 to 1 μm as suggested in the membrane design criteria. According to the equation (1) for *LEP*, pore wetting can be prevented if the membrane has small pores but this is in direct trade-off with the permeation flux. Much of the literature has focussed on the permeating flux, larger pore sizes and preventing pore wetting; hence there is a scope for examining the problem from the other side of small pores, no risk of pore wetting but the need to increase flux. Templated silica-carbon composites are a logical step in examining the flux/pore wetting paradigm from the other side, yet the literature here is sparse. Indeed it would be of great interest to use a soft templating method to produce a membrane with an ordered pore structure for MD purposes and investigate the effect of pore size distribution on the separation performance. The concept of using soft-templated ordered mesoporous membranes with pores < 20nm is a fundamental component of this thesis. Hence this research gap is addressed extensively in Chapters 3 - 5 and to a lesser extent in Chapters 6 and 7.

Furthermore, there are also gaps in the study of transport mechanisms for such membranes operating in MD because despite the fact there are numerous works on understanding the behaviour of water in nanoconfined space in the area of micro- and nanofluidics, there is not yet any effort to merge this knowledge to improve the performance of MD. This research gap is addressed in Chapter 4 where the theory is directly applied to experimental membranes and again in Chapter 5 where the model is used to compare the effect of pore sizes.

Lastly, hybrid organic-inorganic membranes have been extensively studied but to date, there is no reported work on the synthesis of mesoporous carbon-silica nanocomposite membranes for MD purposes. It is believed the physical blending of two separate sols (organic and inorganic) could produce composites mixed at a molecular level. Thus, the particle aggregation and

macrophase separation could be prevented, which is beneficial in the formation of a thin, defect-free membrane and in turn offers a vast array of tailorable pore sizes and functionalities for the resultant membrane. This research gap is addressed through two different approaches in Chapters 6 and 7 of this thesis.

References

[1] M. Khayet, T. Matsuura, Chapter 12 - Vacuum Membrane Distillation, Membrane Distillation, Elsevier, Amsterdam, 2011, pp. 323-359.

[2] M.S. El-Bourawi, Z. Ding, R. Ma, M. Khayet, A framework for better understanding membrane distillation separation process, Journal of Membrane Science, 285 (2006) 4-29.

[3] M. Khayet, Membranes and theoretical modeling of membrane distillation: A review, Advances in Colloid and Interface Science, 164 (2011) 56-88.

[4] A. Alkhudhiri, N. Darwish, N. Hilal, Membrane distillation: A comprehensive review, Desalination, 287 (2012) 2-18.

[5] C. Cabassud, D. Wirth, Membrane distillation for water desalination: How to chose an appropriate membrane?, Desalination, 157 (2003) 307-314.

[6] K.W. Lawson, D.R. Lloyd, Membrane distillation, Journal of Membrane Science, 124 (1997) 1-25.

[7] A.C.M. Franken, J.A.M. Nolten, M.H.V. Mulder, D. Bargeman, C.A. Smolders, Wetting criteria for the applicability of membrane distillation, Journal of Membrane Science, 33 (1987) 315-328.

[8] Z. Ding, R. Ma, A.G. Fane, A new model for mass transfer in direct contact membrane distillation, Desalination, 151 (2003) 217-227.

[9] J. Zhang, J.-D. Li, M. Duke, Z. Xie, S. Gray, Performance of asymmetric hollow fibre membranes in membrane distillation under various configurations and vacuum enhancement, Journal of Membrane Science, 362 (2010) 517-528.

[10] K.W. Lawson, D.R. Lloyd, Membrane distillation. I. Module design and performance evaluation using vacuum membrane distillation, Journal of Membrane Science, 120 (1996) 111-121.

[11] S. Bandini, A. Saavedra, G.C. Sarti, Vacuum membrane distillation: Experiments and modeling, AIChE Journal, 43 (1997) 398-408.

[12] M. Khayet, T. Matsuura, Pervaporation and vacuum membrane distillation processes: Modeling and experiments, AIChE Journal, 50 (2004) 1697-1712.

[13] E. Curcio, E. Drioli, Membrane Distillation and Related Operations—A Review, Separation & Purification Reviews, 34 (2005) 35-86.

[14] M. Khayet, T. Matsuura, Chapter 9 - MD Membrane Modules, Membrane Distillation, Elsevier, Amsterdam, 2011, pp. 227-247.

[15] S.I. Semenova, H. Ohya, K. Soontarapa, Hydrophilic membranes for pervaporation: An analytical review, Desalination, 110 (1997) 251-286.

[16] H.J. Zwijnenberg, G.H. Koops, M. Wessling, Solar driven membrane pervaporation for desalination processes, Journal of Membrane Science, 250 (2005) 235-246.

[17] S.R. Chowdhury, J.E. ten Elshof, N.E. Benes, K. Keizer, Development and comparative study of different nanofiltration membranes for recovery of highly charged large ions, Desalination, 144 (2002) 41-46.

[18] X. Liu, Y. Peng, S. Ji, A new method to prepare organic-inorganic hybrid membranes, Desalination, 221 (2008) 376-382.

[19] R. Xu, J. Wang, M. Kanezashi, T. Yoshioka, T. Tsuru, Development of Robust Organosilica Membranes for Reverse Osmosis, Langmuir, 27 (2011) 13996-13999.

[20] H.L. Castricum, A. Sah, R. Kreiter, D.H.A. Blank, J.F. Vente, J.E. ten Elshof, Hydrothermally stable molecular separation membranes from organically linked silica, Journal of Materials Chemistry, 18 (2008) 2150-2158.

[21] H.L. Castricum, G.G. Paradis, M.C. Mittelmeijer-Hazeleger, R. Kreiter, J.F. Vente, J.E. ten Elshof, Tailoring the Separation Behavior of Hybrid Organosilica Membranes by Adjusting the Structure of the Organic Bridging Group, Advanced Functional Materials, 21 (2011) 2319-2329.

[22] J. Campaniello, C.W.R. Engelen, W.G. Haije, P.P.A.C. Pex, J.F. Vente, Long-term pervaporation performance of microporous methylated silica membranes, Chemical Communications, (2004) 834-835.

[23] R. Kreiter, M.D.A. Rietkerk, H.L. Castricum, H.M. van Veen, J.E. Ten Elshof, J.F. Vente, Evaluation of hybrid silica sols for stable microporous membranes using high-throughput screening, J. Sol-Gel Sci Technol, 57 (2011) 245-252.

[24] S.R. Krajewski, W. Kujawski, M. Bukowska, C. Picard, A. Larbot, Application of fluoroalkylsilanes (FAS) grafted ceramic membranes in membrane distillation process of NaCl solutions, Journal of Membrane Science, 281 (2006) 253-259.

[25] H. Fang, J.F. Gao, H.T. Wang, C.S. Chen, Hydrophobic porous alumina hollow fiber for water desalination via membrane distillation process, Journal of Membrane Science, 403–404 (2012) 41-46.

[26] S. Cerneaux, I. Struzynska, W.M. Kujawski, M. Persin, A. Larbot, Comparison of various membrane distillation methods for desalination using hydrophobic ceramic membranes, Journal of Membrane Science, 337 (2009) 55-60.

[27] Z.D. Hendren, J. Brant, M.R. Wiesner, Surface modification of nanostructured ceramic membranes for direct contact membrane distillation, Journal of Membrane Science, 331 (2009) 1-10.

[28] L. He, D. Li, G. Zhang, P.A. Webley, D. Zhao, H. Wang, Synthesis of Carbonaceous Poly(furfuryl alcohol) Membrane for Water Desalination, Industrial & Engineering Chemistry Research, 49 (2010) 4175-4180.

[29] Z. Xie, M. Hoang, T. Duong, D. Ng, B. Dao, S. Gray, Sol–gel derived poly(vinyl alcohol)/maleic acid/silica hybrid membrane for desalination by pervaporation, Journal of Membrane Science, 383 (2011) 96-103.

[30] M. Elma, C. Yacou, J. Diniz da Costa, D. Wang, Performance and Long Term Stability of Mesoporous Silica Membranes for Desalination, Membranes, 3 (2013) 136-150.

[31] P. Wang, M.M. Teoh, T.-S. Chung, Morphological architecture of dual-layer hollow fiber for membrane distillation with higher desalination performance, Water Research, 45 (2011) 5489-5500.

[32] S. Simone, A. Figoli, A. Criscuoli, M.C. Carnevale, A. Rosselli, E. Drioli, Preparation of hollow fibre membranes from PVDF/PVP blends and their application in VMD, Journal of Membrane Science, 364 (2010) 219-232.

[33] L. Martínez-Díez, F.J. Florido-Díaz, M.I. Vázquez-González, Study of evaporation efficiency in membrane distillation, Desalination, 126 (1999) 193-198.

[34] M.C. Duke, S. Mee, J.C.D. da Costa, Performance of porous inorganic membranes in non-osmotic desalination, Water Research, 41 (2007) 3998-4004.

[35] C.J. Brinker, G.W. Scherer, Sol-gel science: the physics and chemistry of sol-gel processing, Academic Press1990.

[36] J.S. Beck, J.C. Vartuli, W.J. Roth, M.E. Leonowicz, C.T. Kresge, K.D. Schmitt, C.T.-W. Chu, D.H. Olson, E.W. Sheppard, S.B. McCullen, J.B. Higgins, J.L. Schlenker, A new family of mesoporous molecular sieves prepared with liquid crystal templates, J. Am. Chem. Soc., 114 (1992) 10834-10843.

[37] C.T. Kresge, M.E. Leonowicz, W.J. Roth, J.C. Vartuli, J.S. Beck, Ordered mesoporous molecular sieves synthesized by a liquid-crystal template mechanism, Nature, 359 (1992) 710-712.

[38] C.-H. Tsai, J.L. Vivero-Escoto, I.I. Slowing, I.J. Fang, B.G. Trewyn, V.S.Y. Lin, Surfactant-assited controlled release of hydrophobic drugs using anionic surfactant templated mesoporous silica nanoparticles, Biomaterials, 32 (2011) 6234-6244.

[39] J.M. Rosenholm, C. Sahlgren, M. Linden, Towards multifunctional, targeted drug delivery systems using mesoporous silica nanoparticles - opportunities & challenges, Nanoscale, 2 (2010) 1870-1883.

[40] T. Ohkubo, T. Ogura, H. Sakai, M. Abe, Synthesis of highly-ordered mesoporous silica particles using mixed cationic and anionic surfactants as templates, Journal of Colloid and Interface Science, 312 (2007) 42-46.

[41] S.S. Mahajan, G. Subbarayan, B.G. Sammakia, Estimating thermal conductivity of amorphous silica nanoparticles and nanowires using molecular dynamics simulations, Physical Review E, 76 (2007) 056701.

[42] Y. Ma, L. Xing, H. Zheng, S. Che, Anionic−Cationic Switchable Amphoteric Monodisperse Mesoporous Silica Nanoparticles, Langmuir, 27 (2010) 517-520.

[43] C.H. Lee, S.H. Park, W. Chung, J.Y. Kim, S.H. Kim, Preparation and characterization of surface modified silica nanoparticles with organo-silane compounds, Colloids and Surfaces A: Physicochemical and Engineering Aspects, 384 (2011) 318-322.

[44] J.B. Joo, P. Kim, W. Kim, J. Kim, J. Yi, Preparation of mesoporous carbon templated by silica particles for use as a catalyst support in polymer electrolyte membrane fuel cells [Catal. Today 111 (2006) 171-175], Catal. Today, 151 (2010) 413.

[45] H. Fan, J. Gabaldon, C.J. Brinker, Y.-B. Jiang, Ordered nanocrystal/silica particles self-assembled from nanocrystal micelles and silicate, Chemical Communications, (2006) 2323-2325.

[46] X.-F. Zhou, C.-Z. Yu, J.-W. Tang, X.-X. Yan, D.-Y. Zhao, The effect of water content on the preparation of mesoporous monoliths and films, Microporous and Mesoporous Materials, 79 (2005) 283-289.

[47] H. Yang, Q. Lu, F. Gao, Q. Shi, Y. Yan, F. Zhang, S. Xie, B. Tu, D. Zhao, One-Step Synthesis of Highly Ordered Mesoporous Silica Monoliths with Metal Oxide Nanocrystals in their Channels, Advanced Functional Materials, 15 (2005) 1377-1384.

[48] H. Wei, Y. Lv, L. Han, B. Tu, D. Zhao, Facile Synthesis of Transparent Mesostructured Composites and Corresponding Crack-free Mesoporous Carbon/Silica Monoliths, Chemistry of Materials, 23 (2011) 2353-2360.

[49] N.A. Melosh, P. Lipic, F.S. Bates, F. Wudl, G.D. Stucky, G.H. Fredrickson, B.F. Chmelka, Molecular and Mesoscopic Structures of Transparent Block Copolymer−Silica Monoliths, Macromolecules, 32 (1999) 4332-4342.

[50] L. Zhou, G. Hong, L. Qi, Y. Lu, Seeding-Growth of Helical Mesoporous Silica Nanofibers Templated by Achiral Cationic Surfactant, Langmuir, 25 (2009) 6040-6044.

[51] P. Yang, D. Zhao, B.F. Chmelka, G.D. Stucky, Triblock-Copolymer-Directed Syntheses of Large-Pore Mesoporous Silica Fibers, Chemistry of Materials, 10 (1998) 2033-2036.

[52] D. Zhao, P. Yang, D. I. Margolese, G. D. Stucky, Synthesis of continuous mesoporous silica thin films with three-dimensional accessible pore structures, Chemical Communications, (1998) 2499-2500.

[53] X. Zhang, W. Wu, J. Wang, X. Tian, Direct synthesis and characterization of highly ordered functional mesoporous silica thin films with high amino-groups content, Applied Surface Science, 254 (2008) 2893-2899.

[54] A. Yildirim, H. Budunoglu, M. Yaman, M.O. Guler, M. Bayindir, Template free preparation of nanoporous organically modified silica thin films on flexible substrates, Journal of Materials Chemistry, 21 (2011) 14830-14837.

[55] B. Smarsly, A. Gibaud, W. Ruland, D. Sturmayr, C.J. Brinker, Quantitative SAXS Analysis of Oriented 2D Hexagonal Cylindrical Silica Mesostructures in Thin Films Obtained from Nonionic Surfactants, Langmuir, 21 (2005) 3858-3866.

[56] C. Sanchez, C. Boissière, D. Grosso, C. Laberty, L. Nicole, Design, Synthesis, and Properties of Inorganic and Hybrid Thin Films Having Periodically Organized Nanoporosity†, Chemistry of Materials, 20 (2008) 682-737.

[57] G.-S. Park, C.-W. Ahn, M.-W. Kim, Crystal Morphology of Mesoporous Silica Thin Films Synthesized by the Spin-Coating Method Using PEO–PPO–PEO Triblock Copolymer, Journal of the American Ceramic Society, 85 (2002) 2542-2544.

[58] A.D. Nikolov, D.T. Wasan, Ordered micelle structuring in thin films formed from anionic surfactant solutions: I. Experimental, Journal of Colloid and Interface Science, 133 (1989) 1-12.

[59] S.P. Naik, M. Ogura, H. Sasakura, Y. Yamaguchi, Y. Sasaki, T. Okubo, Phase and orientation control of mesoporous silica thin film via phase transformation, Thin Solid Films, 495 (2006) 11-17.

[60] A.A. Letailleur, F. Ribot, C. Boissière, J. Teisseire, E. Barthel, B. Desmazières, N. Chemin, C. Sanchez, Sol–Gel Derived Hybrid Thin Films: The Chemistry behind Processing, Chemistry of Materials, 23 (2011) 5082-5089.

[61] J. Köhler, J. Geserick, N. Hüsing, Mesostructured Silica Thin FilmsMaterials Syntheses, in: U. Schubert, N. Hüsing, R.M. Laine (Eds.), Springer Vienna2008, pp. 29-38.

[62] S.-B. Jung, H.-H. Park, Concentration-dependent mesostructure of surfactant-templated mesoporous silica thin film, Thin Solid Films, 494 (2006) 320-324.

[63] D. Grosso, A.R. Balkenende, P.A. Albouy, M. Lavergne, L. Mazerolles, F. Babonneau, Highly oriented 3D-hexagonal silica thin films produced with cetyltrimethylammonium bromide, Journal of Materials Chemistry, 10 (2000) 2085-2089.

[64] D. Grosso, A.R. Balkenende, P.A. Albouy, A. Ayral, H. Amenitsch, F. Babonneau, Two-Dimensional Hexagonal Mesoporous Silica Thin Films Prepared from Block Copolymers: Detailed Characterization and Formation Mechanism, Chemistry of Materials, 13 (2001) 1848-1856.

[65] K. Fontell, A. Khan, B. Lindstrom, D. Maciejewska, S. Phuang-Ngern, Phase Equilibria and Structures in Ternary Systems of a Cationic Surfactant (C16TABr or (C16TA)2SO4), alcohol, and water, Colloid & Polymer Science, 269 (1991) 727-742.

[66] J.-G. Wang, Q. Xiao, H.-J. Zhou, P.-C. Sun, D.-T. Ding, T.-H. Chen, Anionic surfactant-templated mesoporous silica (AMS) nano-spheres with radially oriented mesopores, Journal of Colloid and Interface Science, 323 (2008) 332-337.

[67] S. Shrivastava, J. Dey, Interaction of anionic surfactant with polymeric nanoparticles of similar charge, Journal of Colloid and Interface Science, 350 (2010) 220-228.

[68] S. Che, A.E. Garcia-Bennett, T. Yokoi, K. Sakamoto, H. Kunieda, O. Terasaki, T. Tatsumi, A novel anionic surfactant templating route for synthesizing mesoporous silica with unique structure, Nat Mater, 2 (2003) 801-805.

[69] D. Zhao, Q. Huo, J. Feng, B.F. Chmelka, G.D. Stucky, Nonionic Triblock and Star Diblock Copolymer and Oligomeric Surfactant Syntheses of Highly Ordered, Hydrothermally Stable, Mesoporous Silica Structures, Journal of the American Chemical Society, 120 (1998) 6024-6036.

[70] B. Tian, X. Liu, Z. Zhang, B. Tu, D. Zhao, Syntheses of High-Quality Mesoporous Materials Directed by Blends of Nonionic Amphiphiles under Nonaqueous Conditions, Journal of Solid State Chemistry, 167 (2002) 324-329.

[71] L. Chen, J. Xu, W.-H. Zhang, J.D. Holmes, M.A. Morris, Syntheses of complex mesoporous silicas using mixtures of nonionic block copolymer surfactants: Understanding formation of different structures using solubility parameters, Journal of Colloid and Interface Science, 353 (2011) 169-180.

[72] P. Somasundaran, E.D. Snell, E. Fu, Q. Xu, Effect of adsorption of non-ionic surfactant and non-ionic--anionic surfactant mixtures on silica--liquid interfacial properties, Colloids and Surfaces, 63 (1992) 49-54.

[73] R. Ryoo, S.H. Joo, J.M. Kim, Energetically Favored Formation of MCM-48 from Cationic−Neutral Surfactant Mixtures, The Journal of Physical Chemistry B, 103 (1999) 7435-7440.

[74] D. Li, X. Guan, J. Song, Y. Di, D. Zhang, X. Ge, L. Zhao, F.-S. Xiao, Highly efficient synthesis of ordered mesoporous silica materials with controllable microporosity using surfactant mixtures as templates, Colloids and Surfaces A: Physicochemical and Engineering Aspects, 272 (2006) 194-202.

[75] Y. Kaya, C. Aydiner, H. Barlas, B. Keskinler, Nanofiltration of single and mixture solutions containing anionics and nonionic surfactants below their critical micelle concentrations (CMCs), Journal of Membrane Science, 282 (2006) 401-412.

[76] X. Feng-Shou, Ordered mesoporous silica-based materials templated from fluorocarbon–hydrocarbon surfactant mixtures and semi-fluorinated surfactants, Current Opinion in Colloid & Interface Science, 10 (2005) 94-101.

[77] N.K. Raman, M.T. Anderson, C.J. Brinker, Template-based approaches to the preparation of amorphous, nanoporous silicas, Chem. Mater., 8 (1996) 1682-1701.

[78] Y. Shi, Y. Wan, D. Zhao, Ordered mesoporous non-oxide materials, Chemical Society Reviews, 40 (2011) 3854-3878.

[79] G.J.d.A.A. Soler-Illia, C. Sanchez, B. Lebeau, J. Patarin, Chemical Strategies To Design Textured Materials: from Microporous and Mesoporous Oxides to Nanonetworks and Hierarchical Structures, Chemical Reviews, 102 (2002) 4093-4138.

[80] Y. Wan, Zhao, On the Controllable Soft-Templating Approach to Mesoporous Silicates, Chemical Reviews, 107 (2007) 2821-2860.

[81] G.J.A.A. Soler-Illia, O. Azzaroni, Multifunctional hybrids by combining ordered mesoporous materials and macromolecular building blocks, Chemical Society Reviews, 40 (2011) 1107-1150.

[82] C.J. Brinker, Y. Lu, A. Sellinger, H. Fan, Evaporation-Induced Self-Assembly: Nanostructures Made Easy, Advanced Materials, 11 (1999) 579-585.

[83] C. Yu, J. Fan, B. Tian, G.D. Stucky, D. Zhao, Synthesis of Mesoporous Silica from Commercial Poly(ethylene oxide)/Poly(butylene oxide) Copolymers: Toward the Rational Design of Ordered Mesoporous Materials, The Journal of Physical Chemistry B, 107 (2003) 13368-13375.

[84] Q. Huo, D.I. Margolese, G.D. Stucky, Surfactant Control of Phases in the Synthesis of Mesoporous Silica-Based Materials, Chemistry of Materials, 8 (1996) 1147-1160.

[85] S.S. Park, J.H. Shin, D. Zhao, C.-S. Ha, Free-standing and bridged amine-functionalized periodic mesoporous organosilica films, Journal of Materials Chemistry, 20 (2010) 7854-7858.

[86] H.I. Lee, C. Pak, S.H. Yi, J.K. Shon, S.S. Kim, B.G. So, H. Chang, J.E. Yie, Y.-U. Kwon, J.M. Kim, Systematic phase control of periodic mesoporous organosilicas using Gemini surfactants, J. Mater. Chem., 15 (2005) 4711-4717.

[87] F. Kleitz, Ordered Mesoporous Materials, Handbook of Heterogeneous Catalysis, Wiley-VCH Verlag GmbH & Co. KGaA2008.

[88] P. Innocenzi, S. Costacurta, T. Kidchob, L. Malfatti, P. Falcaro, G. Soler-Illia, Mesoporous Thin Films: Properties and Applications
Sol-Gel Methods for Materials Processing, in: P. Innocenzi, Y.L. Zub, V.G. Kessler (Eds.), Springer Netherlands2008, pp. 105-123.

[89] E.L. Crepaldi, G.J.d.A.A. Soler-Illia, D. Grosso, F. Cagnol, F. Ribot, C. Sanchez, Controlled Formation of Highly Organized Mesoporous Titania Thin Films: From Mesostructured Hybrids to Mesoporous Nanoanatase TiO2, Journal of the American Chemical Society, 125 (2003) 9770-9786.

[90] C. Boissiere, D. Grosso, S. Lepoutre, L. Nicole, A.B. Bruneau, C. Sanchez, Porosity and Mechanical Properties of Mesoporous Thin Films Assessed by Environmental Ellipsometric Porosimetry, Langmuir, 21 (2005) 12362-12371.

[91] F. Cagnol, D. Grosso, G.J.d.A.A. Soler-Illia, E.L. Crepaldi, F. Babonneau, H. Amenitsch, C. Sanchez, Humidity-controlled mesostructuration in CTAB-templated silica thin film processing. The existence of a modulable steady state, Journal of Materials Chemistry, 13 (2003) 61-66.

[92] D. Grosso, F. Cagnol, G.J.d.A.A. Soler-Illia, E.L. Crepaldi, H. Amenitsch, A. Brunet-Bruneau, A. Bourgeois, C. Sanchez, Fundamentals of Mesostructuring Through Evaporation-Induced Self-Assembly, Advanced Functional Materials, 14 (2004) 309-322.

[93] A. Chougnet, C. Heitz, E. Sondergard, J.-M. Berquier, P.-A. Albouy, M. Klotz, Substrates do influence the ordering of mesoporous thin films, J. Mater. Chem., 15 (2005) 3340-3345.

[94] P. Innocenzi, L. Malfatti, T. Kidchob, P. Falcaro, Order−Disorder in Self-Assembled Mesostructured Silica Films: A Concepts Review, Chemistry of Materials, 21 (2009) 2555-2564.

[95] P. Falcaro, S. Costacurta, G. Mattei, H. Amenitsch, A. Marcelli, M.C. Guidi, M. Piccinini, A. Nucara, L. Malfatti, T. Kidchob, P. Innocenzi, Highly Ordered “Defect-Free” Self-Assembled

Hybrid Films with a Tetragonal Mesostructure, Journal of the American Chemical Society, 127 (2005) 3838-3846.

[96] B.A. McCool, N. Hill, J. DiCarlo, W.J. DeSisto, Synthesis and characterization of mesoporous silica membranes via dip-coating and hydrothermal deposition techniques, Journal of Membrane Science, 218 (2003) 55-67.

[97] P. Kumar, J. Ida, V.V. Guliants, High flux mesoporous MCM-48 membranes: Effects of support and synthesis conditions on membrane permeance and quality, Microporous and Mesoporous Materials, 110 (2008) 595-599.

[98] N. Nishiyama, D.H. Park, A. Koide, Y. Egashira, K. Ueyama, A mesoporous silica (MCM-48) membrane: preparation and characterization, Journal of Membrane Science, 182 (2001) 235-244.

[99] G. Xomeritakis, C.M. Braunbarth, B. Smarsly, N. Liu, R. Kohn, Z. Klipowicz, C.J. Brinker, Aerosol-assisted deposition of surfactant-templated mesoporous silica membranes on porous ceramic supports., Microporous and Mesoporous Materials, 66 (2003) 91-101.

[100] S.R. Chowdhury, A.M. Peters, D.H.A. Blank, J.E.t. Elshof, Influence of porous substrate on mesopore structure and water permeability of surfactant templated mesoporous silica membranes., Journal of Membrane Science, 279 (2006) 276-281.

[101] K. Nakagawa, H. Matsuyama, T. Maki, M. Teramoto, N. Kubota, Preparation of mesoporous silica membrane by solvent evaporation method for filtration application, Separation and Purification Technology, 44 (2005) 145-151.

[102] R.G. Juez, V. Boffa, D.H.A. Blank, J.E. ten Elshof, Preparation of self-supporting mesostructured silica thin film membranes as gateable interconnects for microfluidics, Journal of Membrane Science, 323 (2008) 347-351.

[103] K. Young Seok, K. Katsuki, Y. Seung Man, Microporous silica membrane synthesized on an ordered mesoporous silica sublayer, Chem. Mater., 15 (2003) 612-615.

[104] B.C. Bonekamp, R. Kreiter, J.F. Vente, Sol-gel approaches in the synthesis of membrane materials for nanofiltration and pervaporation, in: P. Innocenzi, Y.L. Zub, V.G. Kessler (Eds.) Sol-gel methods for materials processing - Focusing on materials for pollution control, water purification and soil remediation, Springer2008, pp. 47-65.

[105] A. Stein, B.J. Melde, R.C. Schroden, Hybrid Inorganic–Organic Mesoporous Silicates—Nanoscopic Reactors Coming of Age, Advanced Materials, 12 (2000) 1403-1419.

[106] P. Kumar, V.V. Guliants, Periodic mesoporous organic–inorganic hybrid materials: Applications in membrane separations and adsorption, Microporous and Mesoporous Materials, 132 (2010) 1-14.

[107] F. Cagnol, D. Grosso, C. Sanchez, A general one-pot process leading to highly functionalised ordered mesoporous silica films, Chemical Communications, (2004) 1742-1743.

[108] S. Yoda, M. Ohara, Y. Takebayashi, K. Sue, Y. Hakuta, T. Furuya, M. Yamada, K. Otake, A porous polymer-silica composite with a "vespula-like" structure for thermal insulating materials prepared via high pressure phase control, Journal of Materials Chemistry A, 1 (2013) 9620-9623.

[109] S. Takahashi, D.R. Paul, Gas permeation in poly(ether imide) nanocomposite membranes based on surface-treated silica. Part 1: Without chemical coupling to matrix, Polymer, 47 (2006) 7519-7534.

[110] H.B. Park, Y.M. Lee, Fabrication and Characterization of Nanoporous Carbon/Silica Membranes, Advanced Materials, 17 (2005) 477-483.

[111] H. Zou, S. Wu, J. Shen, Polymer/Silica Nanocomposites: Preparation, Characterization, Properties, and Applications, Chemical Reviews, 108 (2008) 3893-3957.

[112] J. Lee, J. Kim, T. Hyeon, Recent Progress in the Synthesis of Porous Carbon Materials, Advanced Materials, 18 (2006) 2073-2094.

[113] T.-W. Kim, R. Ryoo, K.P. Gierszal, M. Jaroniec, L.A. Solovyov, Y. Sakamoto, O. Terasaki, Characterization of mesoporous carbons synthesized with SBA-16 silica template, Journal of Materials Chemistry, 15 (2005) 1560-1571.

[114] K.P. Gierszal, M. Jaroniec, T.-W. Kim, J. Kim, R. Ryoo, High temperature treatment of ordered mesoporous carbons prepared by using various carbon precursors and ordered mesoporous silica templates, New Journal of Chemistry, 32 (2008) 981-993.

[115] R. Liu, Y. Shi, Y. Wan, Y. Meng, F. Zhang, D. Gu, Z. Chen, B. Tu, D. Zhao, Triconstituent Co-assembly to Ordered Mesostructured Polymer−Silica and Carbon−Silica Nanocomposites and Large-Pore Mesoporous Carbons with High Surface Areas, Journal of the American Chemical Society, 128 (2006) 11652-11662.

[116] L. Song, D. Feng, C.G. Campbell, D. Gu, A.M. Forster, K.G. Yager, N. Fredin, H.-J. Lee, R.L. Jones, D. Zhao, B.D. Vogt, Robust conductive mesoporous carbon-silica composite films with highly ordered and oriented orthorhombic structures from triblock-copolymer template co-assembly, Journal of Materials Chemistry, 20 (2010) 1691-1701.

[117] Y. Li, J. Wei, W. Luo, C. Wang, W. Li, S. Feng, Q. Yue, M. Wang, A.A. Elzatahry, Y. Deng, D. Zhao, Tricomponent Coassembly Approach To Synthesize Ordered Mesoporous Carbon/Silica Nanocomposites and Their Derivative Mesoporous Silicas with Dual Porosities, Chemistry of Materials, 26 (2014) 2438-2444.

[118] Q. Hu, R. Kou, J. Pang, T.L. Ward, M. Cai, Z. Yang, Y. Lu, J. Tang, Mesoporous carbon/silica nanocomposite through multi-component assembly, Chemical Communications, (2007) 601-603.

[119] C. Xue, B. Tu, D. Zhao, Evaporation-Induced Coating and Self-Assembly of Ordered Mesoporous Carbon-Silica Composite Monoliths with Macroporous Architecture on Polyurethane Foams, Advanced Functional Materials, 18 (2008) 3914-3921.

3 PREPARATION OF ALUMINA-SUPPORTED NANOPOROUS ORGANOSILICA MEMBRANE WITH ORDERED PORE STRUCTURE

Introduction

This chapter aims to demonstrate the concept of using an organosilica precursor, which has organic groups bridging two silicon atoms, with a surfactant, as soft template to produce a nanoporous membrane with narrow pore size distribution and ordered pore structure. The membrane performance was evaluated in water desalination by using vacuum membrane distillation process.

Contribution

It is demonstrated for the first time that a nanoporous organosilica membrane (pore size of 2 nm) with ordered pore structure produced pure water using vacuum membrane distillation with high and maintained permeation flux (13 L m^{-2} h^{-1}) across an extreme range of salt concentration (10-150 g L^{-1}) at moderate temperature (60 °C) with no observable pore wetting. This is significant because previous attempts using ceramic membranes suffered from low fluxes and/or flux decay and utilized either much larger or smaller pore sizes. This paper was published in Chemical Communications as:

Y. T. Chua, C. X. C. Lin, F. Kleitz, X. S. Zhao and S. Smart, Nanoporous Organosilica Membrane for Water Desalination, Chem. Commun., 49, 2013, 4534-4536.

Nanoporous Organosilica Membrane for Water Desalination

*Reproduced in part with permission from Yen Thien Chua, Chun Xiang Cynthia Lin, Freddy Kleitz, Xiu Song Zhao and Simon Smart, *Chem. Commun.*, 49, 2013, 4534-4536.

Abstract

Nanoporous organosilica membranes are successfully coated on porous alumina tubes and tested for desalination *via* membrane distillation. The membranes produced pure water (up to 13 L m^{-2} h^{-1}) across an extreme range of salt concentrations (10-150 g L^{-1} NaCl) at moderate temperatures (≤ 60 °C) without exhibiting the characteristic flux decay of competing materials.

3.1 Introduction

Water scarcity, brought about by population growth and industrialisation, is one of the major challenges facing contemporary societies; with desalination of brackish or sea water being the most effectively implemented solutions. Membrane distillation (MD) is a thermally driven, alternative process to conventional desalination technologies such as distillation and reverse osmosis (RO) [1]. The membrane in the MD process acts as a barrier to hold water at the pore entrance where it can form a liquid/vapour interface from which water can evaporate across, leaving the non-volatile salt behind [2]. MD offers several advantages such as being able to treat highly saline feed waters; reduced operating pressures in comparison to RO; and reduced operating temperatures and smaller vapour spaces compared to traditional distillation [3]. In particular, MD is often touted as a sustainable desalination solution due to its compact footprint and low grade heat requirements [2]. However, despite these benefits and the significant research efforts over the last decade, industrial acceptance of MD has been almost non-existent. The majority of this lack of acceptance stems from the sheer dominance of RO processes [4], membrane flux decay and the use of porous (0.2-0.7 μm), hydrophobic polymeric membranes [5] which are plagued by fouling and disruption of the liquid/vapour interface, which is more commonly called pore wetting [6]. Clearly, the development of new membrane materials that will overcome the flux, fouling and pore wetting limitations of current membrane materials are required. Nanoporous, inorganic materials that are chemically and thermally stable with

tailored, ordered pore sizes and shapes, and surface chemistry are an attractive membrane alternative [7-9].

Table 3.1 Reported work of polymeric and inorganic membranes for desalination via VMD

Membrane	Process[a]	Flux[b]	Rej.[c]	Ref.
Modified ZrO_2 (d_p=50 nm)	T_f = 40 °C; P_p = 0.3 kPa; 0.5 M NaCl;	7.49	96.1	Cerneaux et al.[10]
Modified TiO_2 (d_p =5 nm)	feed flow rate =210 L h^{-1}	6.08	99.5	
PTFE flat sheet (d_p =220 nm)	T_f = 48 °C; P_p = 4.5 kPa; 2.57 M TDS; Re = 3500	7.9	n/a	Mericq et al.[5]
Cobalt silica	T_f = 75 °C; P_p =8.8 kPa; 0.0017 M NaCl	1.8	> 99	Lin et al.[11]

[a] T_f, feed temperature; P_p, permeate pressure; Re, Reynolds number.

[b]Water permeate flux in L $m^{-2}hr^{-1}$. [c] Salt rejection in %.

Zeolite membranes have demonstrated initial promise [12], although long-term stability problems have raised concerns over their suitability [13]. Microporous silica-based membranes have also been investigated for liquid separations [14] including desalination [11, 15], but the reported fluxes are too low in comparison to RO (Table 3.1). Mesoporous silica-based membranes modified to include hydrophobicity [8], with high porosity and highly ordered, 3-dimensional pores seem a natural progression [16], but the complex task of producing thin-film membranes of usable size have severely limited their application.

Herein, we report the preparation of nanoporous organosilica thin-film membranes (~20 cm^2 in size) with highly ordered pores of around 2 nm in diameter, exhibiting outstanding desalination performance for synthetic salt solutions ranging from 0.17 to 2.57 M NaCl (10 (brackish water), 35 (sea water), 50 (brine), 75 and 150 g L^{-1} NaCl) for feed temperatures of 20, 40 and 60 °C using a vacuum MD (VMD) process. The organosilica membranes have good hydrothermal stability and provide adequate hydrophobicity to form a liquid/vapour interface. Furthermore, a well-ordered pore structure offers the advantages of reduced tortuosity and high porosity to facilitate a high water flux. To the best of our knowledge, the novel strategy of preparing a nanoporous organosilica membrane with a well-ordered, cubic pore structure for water desalination has never been reported. This work opens up a potentially scalable process for fabricating high-performance membranes for water desalination.

3.2 Results and Discussions

A well-ordered, porous organosilica membrane was synthesized *via* a soft-templating, sol-gel synthesis using the non-ionic, triblock copolymer surfactant Pluronic F68 ($EO_{80}PO_{30}EO_{80}$, (M_w = ~8,400 g mol^{-1}), Aldrich) as the structure directing agent, and 1, 2- bis(triethoxysilyl) ethane (BTESE, Aldrich, 96%) as the organic silica source. Both precursors were used as received. The membrane was fabricated *via* a standard dip-coating process, followed by calcination in air at 300 °C to remove the template. Detailed synthesis procedures are supplied in the electronic supporting information (ESI). Figure 3.1(a) shows a transmission electron microscope (TEM) image of the calcined sample. A well-ordered pore arrangement reflecting a body-centered cubic structure is observed [17]. This is expected as the Pluronic F68 has high EO/PO ratio of 2.7 (> 1.5), which favours the formation of a cubic structure [18]. Small angle X-ray scattering (SAXS) is presented in Figure 3.1(b), with a peak at 1.15 ° two theta, corresponding to an interplanar d-spacing of 7.68 nm. Nitrogen sorption analysis of this sample (Figure 3.1(c)) shows a type I isotherm with a corresponding pore size distribution centred at around 2 nm. The pore size was calculated using non-local density functional theory (NLDFT). The Brunauer-Emmett-Teller (BET) surface area of the sample was 310 m^2 g^{-1}, with a total pore volume of 0.18 cm^3 g^{-1}. Fourier Transform Infra-Red (FT-IR) spectroscopic characterisation of this sample was performed before and after calcination (Figure 3.1(d)). No significant peaks were observed between 1300-1500 cm^{-1} or 2800-3050 cm^{-1}, which are assigned to the C-H stretching and deformation modes of F68, respectively [19], indicating that the F68 copolymer template was removed by thermal treatment at 300 °C. Further analysis by ^{13}C MAS NMR did reveal that a small amount of surfactant remained within the pores as indicated by peaks at 63.5 and 70.8 ppm (Figure 3.1(e)). A prominent peak at 5.1 ppm is assigned to the resonance of carbon atoms covalently bonded to silicon (Si-CH_2-CH_2-Si) within the organosilica framework [20]. This also agreed with FTIR spectra in Figure 3.1(d) with the presence of absorption bands at 693 and 1,260 cm^{-1} indicating the retention of the Si-C-C-Si bonds [21]. ^{29}Si NMR spectra in Figure 3.1(f) shows that after calcination for surfactant removal, cleavage of some Si-C bonds was detected, as Q sites (between -90 to -120 ppm) were present alongside the condensed T^3 sites observed at -65.4 ppm. Thus the final membrane consisted of an ordered, porous framework of organic moieties, siloxane bridges and silanol groups, with a small amount of F68 surfactant template retained within the pores.

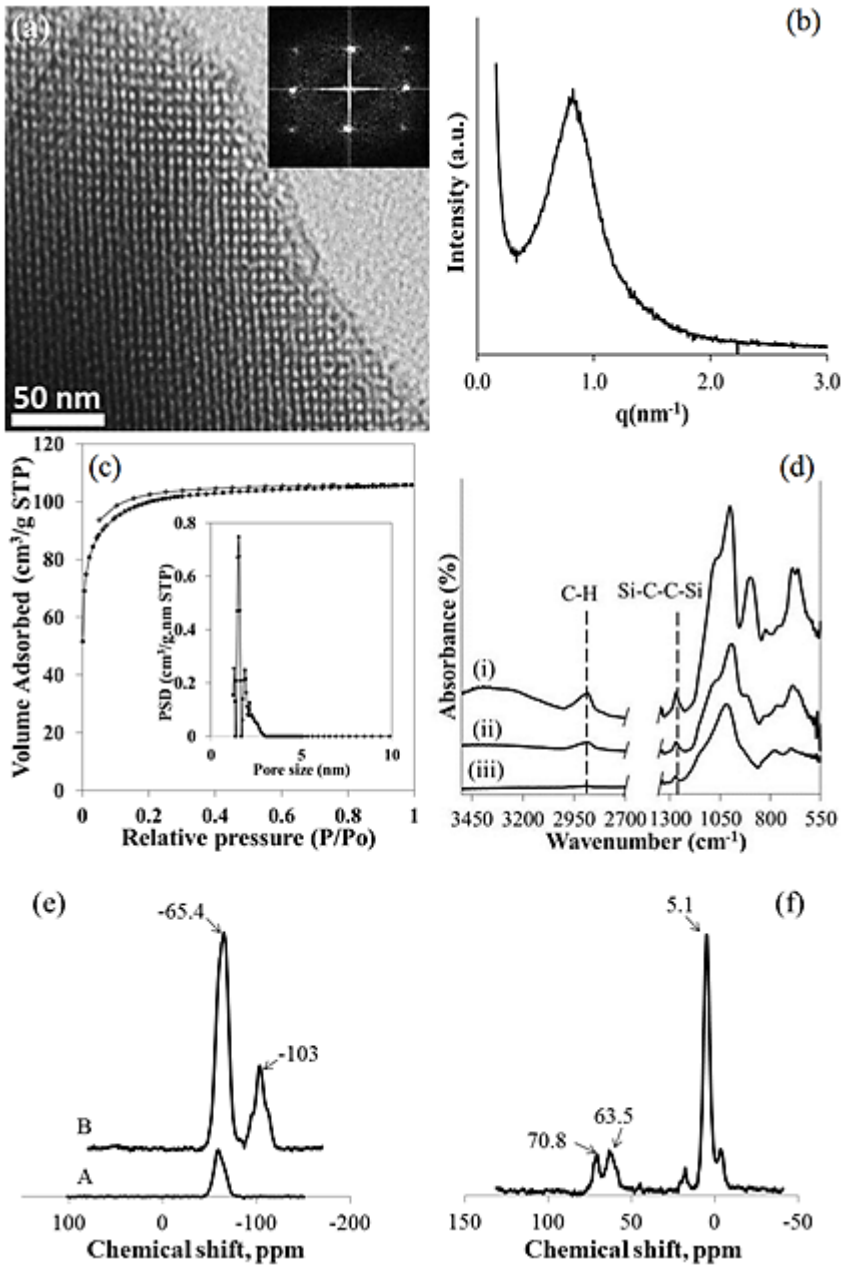

Figure 3.1 Material characterizations of the organosilica membrane (a) TEM image with inset showing the Fourier-transform diffraction pattern. (b) SAXS pattern of calcined sample with q = 4π(sinθ)/λ (λ = 0.1541 nm). (c) N_2 adsorption-desorption isotherm at -196 °C; filled symbols represent the adsorption branch and open symbols the desorption branch. Inset shows NLDFT pore size distribution calculated from the adsorption branch. (d) FT-IR spectra of the (i) as-synthesized, (ii) cured (150 °C for 12 hrs) and (iii) calcined (300 °C) organosilica sample. (e) ^{13}C NMR spectrum for calcined organosilica sample. (f) ^{29}Si MAS NMR spectra for calcined organosilica sample.

Membrane performance was assessed by evaluating the water flux (L m^{-2} h^{-1}) through the membrane and its salt rejection capabilities. The results shown in Figure 3.2 demonstrate

excellent salt rejection (> 99.9 %) and good water fluxes (up to L kg m^{-2} hr^{-1} at 60 °C). These fluxes are an order of magnitude larger than previously published results for silica-based membranes, for example we observed a 26 fold increase in water flux for the 150 g L^{-1} feed solution compared to the 0.5 L m^{-2} h^{-1} at 75 °C reported by Lin *et al.* [11]. Indeed, even against commercially available polymeric membranes run in a VMD setup these results compare very favorably (Table 3.1). It is also important to note here that the desalination trial was run almost continuously with only minute interruptions for changing the feed salinity. Thus, the membrane was tested for ~200 hours, without experiencing any flux decay. This is in stark contrast to previous attempts to use inorganic membranes (zirconia grafted with perfluoroalkyl groups) with MD where the flux decayed by up to 40 % in the first hour of testing [10].

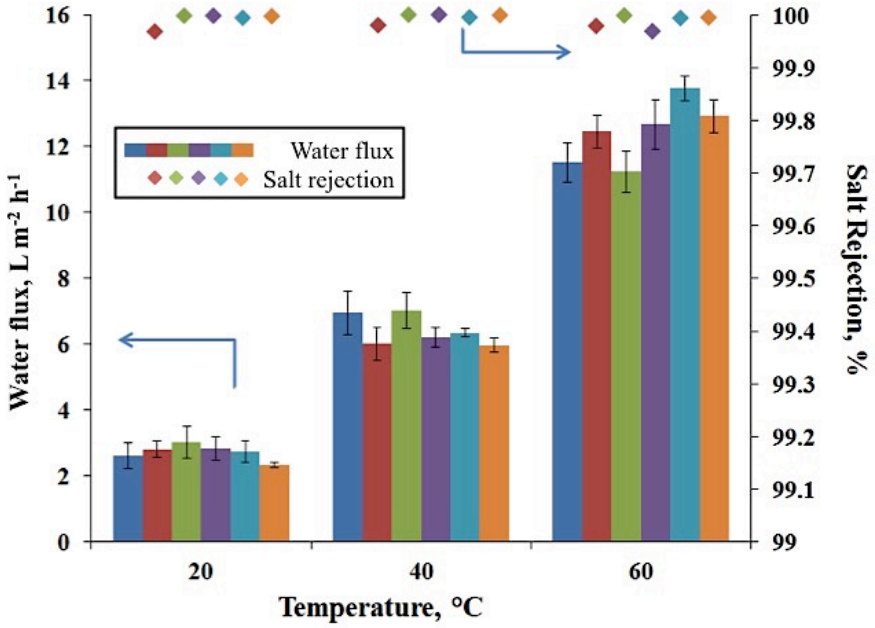

Figure 3.2 Membrane performance in VMD mode tested at feed water temperatures of 20, 40 and 60 °C. The water fluxes (shown on the left axis) are represented by the bar charts where the colour corresponds to the respective salt concentration in the feed water. Salt rejection values (shown on the right axis) are represented by solid diamond markers with the colour corresponding to the respective salt concentration in the feed. Error bars are defined as the confidence interval of the measured data.

Indeed a representative testing run (at feed concentration of 50 g L^{-1} (0.86 M NaCl) and temperature of 60 °C) shown in Figure 3.3 demonstrates the stability of the ordered, organosilica membrane. We hypothesized that the combination of the more hydrophobic organic moieties (-Si-C-C-Si-), the more hydrophilic siloxane/silanol framework and the well-

ordered 2 nm pores provided an appropriate combination of properties to maintain water flux without decay. In order to assess this we fabricated a pure silica membrane (*i.e.* a siloxane/silanol framework without organic moieties) with the same pore structure by using the Pluronic F68 template with the same synthesis condition except using tetraethylorthosilicate (TEOS, 98%, Aldrich) as the silicon source. In contrast to our organosilica membrane, the pure silica membrane with ordered pores suffered a dramatic drop of ~50 % in water flux through the membrane after 30 minutes. Furthermore the salt rejection decreased from 96.4 % to 70.3 % in this timeframe. These results suggest two things: firstly, the decrease in salt rejection indicates that the pure silica membrane was unable to sustain a liquid-vapour interface due to its more hydrophilic surface; secondly, the flux decayed through a build-up of salt within the membrane pores due to pore wetting and subsequent evaporation. Thus, rather than the high membrane flux and lack of flux simply being a function of the pore size, this result confirmed that it was the combination of more hydrophobic organic moieties with the well-ordered 2 nm pores that prevented pore wetting and maintained a good flux under all salt concentrations. All of these findings confirm that the new, organosilica membrane with a well-ordered micropore structure described in this study displays excellent potential for industrial applications.

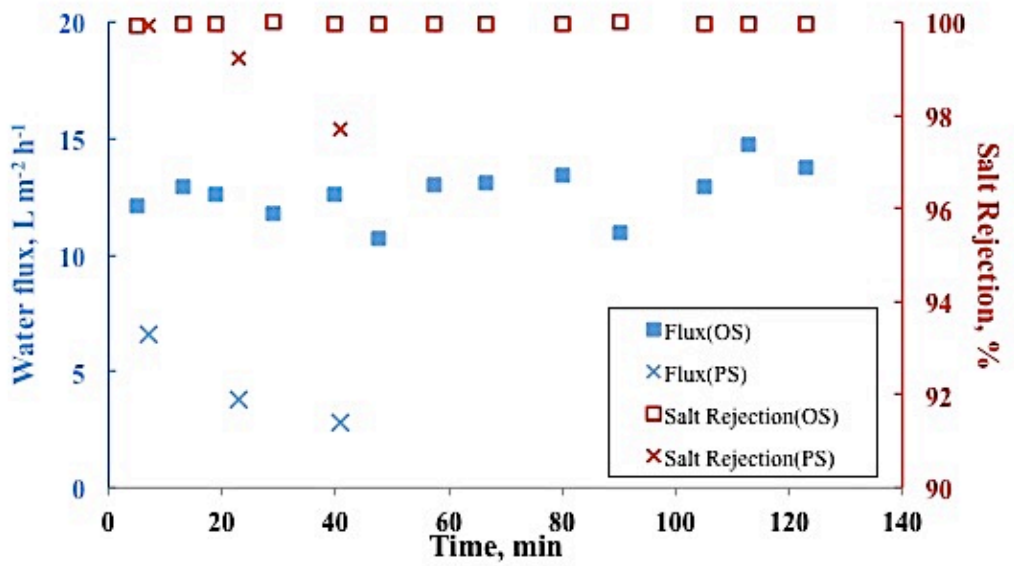

Figure 3.3 Comparison of organosilica (OS) membrane (square symbols) and pure silica (PS) membrane (cross symbols) in 50 g L^{-1} feed concentration run at 60°C. Filled symbols represent water fluxes and open symbols represent salt rejection.

3.3 Conclusions

In conclusion, a new organosilica membrane with well-ordered pores and a narrow pore size distribution centred around 2 nm, has successfully been synthesized *via* the soft templating route. Further, this study demonstrates that this new organosilica membrane is highly applicable and remarkably stable for desalination of a wide range of saline waters *via* membrane distillation producing 13 L m^{-2} h^{-1} at > 99.99 % rejection for 150 g L^{-1} brine. The organic moieties within the siloxane framework conferred enough hydrophobicity to the pore wall to form a liquid/vapour interface at the pore entrance, whilst the small pore size was crucial in preventing pore wetting. Further testing will focus on the effect of pore size, shape and hydrophobicity of the pore wall on membrane performance in order to elucidate the optimal membrane structure.

Acknowledgement

The authors would like to acknowledge funding from the Australian Research Council projects ARC-DP 110103440 and FT100100879. F.K. acknowledges the financial support from the Natural Sciences and Engineering Research Council of Canada (NSERC). Y.T.C. acknowledges The University of Queensland for providing an UQ International Scholarship. The authors acknowledge the facilities, and the scientific and technical assistance, of the Australian Microscopy & Microanalysis Research Facility at the Centre for Microscopy and Microanalysis, and Dr Ekaterina Strounina for the ^{29}Si and ^{13}C NMR technical help from the Centre of Advanced Imaging, The University of Queensland.

References

[1] M. Khayet, Membranes and theoretical modeling of membrane distillation: A review, Advances in Colloid and Interface Science, 164 (2011) 56-88.

[2] M.S. El-Bourawi, Z. Ding, R. Ma, M. Khayet, A framework for better understanding membrane distillation separation process, Journal of Membrane Science, 285 (2006) 4-29.

[3] K.W. Lawson, D.R. Lloyd, Membrane distillation, Journal of Membrane Science, 124 (1997) 1-25.

[4] Z. Steiner, J. Miao, R. Kasher, Development of an oligoamide coating as a surface mimetic for aromatic polyamide films used in reverse osmosis membranes, Chemical Communications, 47 (2011) 2384-2386.

[5] J.-P. Mericq, S. Laborie, C. Cabassud, Vacuum membrane distillation of seawater reverse osmosis brines, Water Research, 44 (2010) 5260-5273.

[6] M. Gryta, Fouling in direct contact membrane distillation process, Journal of Membrane Science, 325 (2008) 383-394.

[7] F. Kleitz, L.A. Solovyov, G.M. Anilkumar, S.H. Choi, R. Ryoo, Transformation of highly ordered large pore silica mesophases (Fm3m, Im3m and p6mm) in a ternary triblock copolymer-butanol-water system, Chemical Communications, (2004) 1536-1537.

[8] H.L. Castricum, A. Sah, R. Kreiter, D.H.A. Blank, J.F. Vente, J.E. ten Elshof, Hybrid ceramic nanosieves: stabilizing nanopores with organic links, Chemical Communications, (2008) 1103-1105.

[9] N. Liu, R.A. Assink, C.J. Brinker, Synthesis and characterization of highly ordered mesoporous thin films with -COOH terminated pore surfaces, Chemical Communications, 0 (2003) 370-371.

[10] S. Cerneaux, I. Struzynska, W.M. Kujawski, M. Persin, A. Larbot, Comparison of various membrane distillation methods for desalination using hydrophobic ceramic membranes, Journal of Membrane Science, 337 (2009) 55-60.

[11] C.X.C. Lin, L.P. Ding, S. Smart, J.C. Diniz da Costa, Cobalt oxide silica membranes for desalination, Journal of Colloid and Interface Science, 368 (2012) 70-76.

[12] M.C. Duke, J. O'Brien-Abraham, N. Milne, B. Zhu, J.Y.S. Lin, J.C. Diniz da Costa, Seawater desalination performance of MFI type membranes made by secondary growth, Separation and Purification Technology, 68 (2009) 343-350.

[13] M. Drobek, C. Yacou, J. Motuzas, A. Julbe, L. Ding, J.C. Diniz da Costa, Long term pervaporation desalination of tubular MFI zeolite membranes, Journal of Membrane Science, 415–416 (2012) 816-823.

[14] H.L. Castricum, G.G. Paradis, M.C. Mittelmeijer-Hazeleger, R. Kreiter, J.F. Vente, J.E. ten Elshof, Tailoring the Separation Behavior of Hybrid Organosilica Membranes by Adjusting the Structure of the Organic Bridging Group, Advanced Functional Materials, 21 (2011) 2319-2329.

[15] R. Xu, J. Wang, M. Kanezashi, T. Yoshioka, T. Tsuru, Development of Robust Organosilica Membranes for Reverse Osmosis, Langmuir, 27 (2011) 13996-13999.

[16] G.J.d.A.A. Soler-Illia, C. Sanchez, B. Lebeau, J. Patarin, Chemical Strategies To Design Textured Materials: from Microporous and Mesoporous Oxides to Nanonetworks and Hierarchical Structures, Chemical Reviews, 102 (2002) 4093-4138.

[17] C. Yacou, M.-L. Fontaine, A. Ayral, P. Lacroix-Desmazes, P.-A. Albouy, A. Julbe, One pot synthesis of hierarchical porous silica membrane material with dispersed Pt nanoparticles using a microwave-assisted sol-gel route, Journal of Materials Chemistry, 18 (2008) 4274-4279.

[18] D. Zhao, Q. Huo, J. Feng, B.F. Chmelka, G.D. Stucky, Nonionic Triblock and Star Diblock Copolymer and Oligomeric Surfactant Syntheses of Highly Ordered, Hydrothermally Stable, Mesoporous Silica Structures, Journal of the American Chemical Society, 120 (1998) 6024-6036.

[19] T. Asefa, M.J. MacLachlan, N. Coombs, G.A. Ozin, Periodic mesoporous organosilicas with organic groups inside the channel walls, Nature, 402 (1999) 867-871.

[20] S. Inagaki, S. Guan, Y. Fukushima, T. Ohsuna, O. Terasaki, Novel mesoporous materials with a uniform distribution of organic groups and inorganic oxide in their frameworks, Journal of the American Chemical Society, 121 (1999) 9611-9614.

[21] M.A. Wahab, Kim, II, C.-S. Ha, Hybrid periodic mesoporous organosilica materials prepared from 1,2-bis(triethoxysilyl)ethane and (3-cyanopropyl)triethoxysilane, Microporous and Mesoporous Materials, 69 (2004) 19-27.

Supplementary Information

Experimental Section

Preparation of nanoporous organosilica hybrid membranes

The organosilica hybrid membranes were prepared via the sol-gel method under acidic conditions. First, 1.0 g of BTESE was pre-hydrolysed in 1.26 g of ethanol with 0.61 g of 0.01 M hydrochloric acid (HCl, 37%, Aldrich) at 35 °C for one hour. Second, 0.28 g of non-ionic triblock copolymer surfactant Pluronic F68 was dissolved in ethanol under stirring for 2 hours. Finally, the two mixtures were combined under stirring to give a final molar ratio of 1 BTESE: 8.7 ethanol: 6 H_2O: 0.0022 HCl: 0.006 F68.

Dip-coating was carried out in a class 100 laminar flow cabinet to prevent from dust contamination on the membrane surface. The organosilica membrane was deposited by dip-coating the prepared sol as aforementioned on (a) glass slides (for TEM analysis sample) and (b) alumina substrate (PALL, length 100 mm, outer diameter 10 mm, thickness 1.7 mm, for desalination test) with titania as intermediate layer (pore size 5 nm) at a withdrawal speed of 10 cm min^{-1} and holding time of 1 min. After dip-coating, the membrane was dried in air overnight, and then cured at 150 °C for 12 hrs for the complete cross-linking and self-assembly of organosilica network before surfactant removal through calcination in air at 300 °C for 4 hrs with heating rate of 1 °C min^{-1}. The remaining sol was dried on a petri dish to form a thin layer and grinded for SAXS and N_2 adsorption analyses.

Characterization

Transmission electron microscopy (TEM) analysis was performed by JEOL JEM-1010 and JEM-2100 electron microscopes operated at accelerating voltage of 100 kV and 200 kV, respectively. TEM sample was prepared by scraping out the calcined thin films from glass slides, and mixed with ethanol to form slurry then dropped on holey carbon film coated Cu grid. The mesostructure of calcined organosilica membrane was investigated by small-angle X-ray scattering (SAXS) with lower starting angle of $2\theta < 0.5°$ using a Anton Paar 'SAXSess' which was equipped with both CCD and image plate detection. Fourier transform infrared spectroscopy was performed using a Shimadzu IRAffinity-1 FT-IR Spectrometer, from 4000-

500 cm^{-1} wavelength. Nitrogen adsorption and desorption isotherms were measured at 77 K using a Micromeritics Tristar 3020 analyzer. Prior to the adsorption measurements, the samples were outgassed under vacuum at 180 °C for 12 hrs. The mean pore size and pore size distribution were calculated from the adsorption branch of the isotherm using nonlocal density functional theory (NLDFT) method. The specific surface area was calculated by Brunauer-Emmett-Teller (BET) method and total pore volume was calculated by the amount of nitrogen adsorbed at $P/P_0 = 0.99$. ^{29}Si and ^{13}C nuclear magnetic resonance (NMR) were measured by a solid state Bruker Avance III spectrometer with a 7T (300 MHz for ^{1}H) magnet and a zirconia rotor, 4 mm, rotated at 7kHz. Thermogravimetric analysis (TGA) was performed using a Shimadzu TGA-50 with a temperature ramp rate of 1 °C min^{-1} to 700 °C under an air flow at 100ml min^{-1}. The surface morphology of the calcined membrane was observed using scanning electron microscopy (SEM; JCM-5000 Neo Scope, JEOL, Japan) in the secondary electron imaging mode with an acceleration voltage of 10 kV under high vacuum.

Performance test of organosilica membrane in desalination

Desalination test of organosilica and pure silica membrane were performed through a continuous flow system of vacuum membrane distillation (VMD) as shown in Figure S 3.1. Membrane module resembling shell-and-tube heat exchanger with varied temperature of feed solution was transported inside the tube lumen and vacuum of 80 mbar was applied at the shell side. Sodium chloride solution with varied concentrations (10, 35, 50, 75, 150 g L^{-1} of NaCl) was used as the feed solution that represent the range of brackish water (10 g L^{-1}), seawater (35 g L^{-1}) and brine solution (> 50 g L^{-1}) available in the natural environment. Effect of feed temperature to permeate flux was studied at 20, 40 and 60 °C. The feed and permeate conductivities were measured by a labCHEM CP conductivity meter, which was calibrated over a range of salt concentrations (0.1 to 150 g L^{-1}). The permeate flux through the membrane, F (L m^{-2} h^{-1}) was calculated by $F = m/A \cdot t$, where m is the mass of permeate collected, A as the membrane tube active area and t is the duration time of permeation test. Salt rejection, R (%) of the membrane was calculated by the following equation: $R = (C_f - C_p)/C_f \times 100\%$, where C_f and C_p were the feed and permeate concentrations (wt%), respectively.

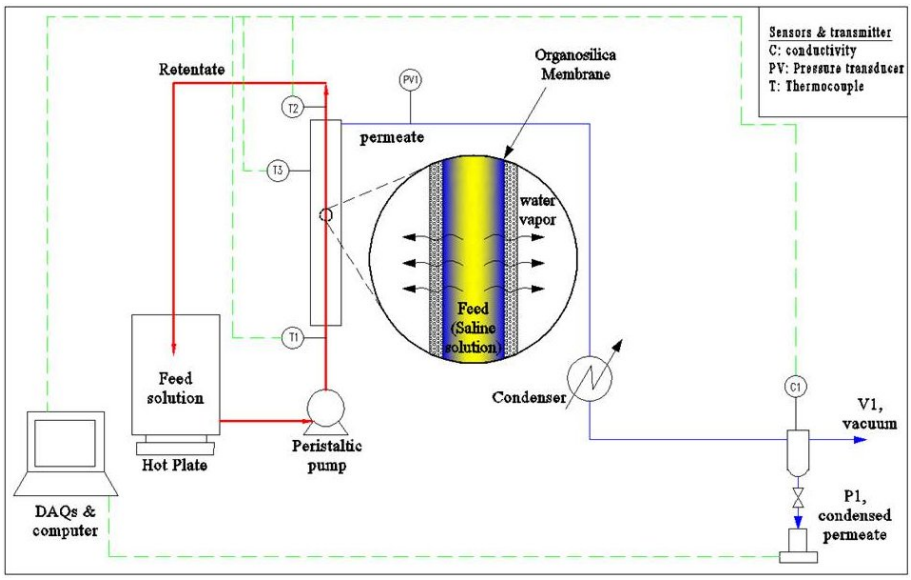

Figure S 3.1 Schematic diagram of vacuum membrane distillation test rig

A clear trade-off exists between surfactant removal and retention of organic moieties within the silica network as to completely remove the surfactant a calcination temperature of 400 °C would be required, as shown by thermogravimetric analysis (TGA) (Figure S 3.2); however a calcination temperature this high would have adversely affected the organosilica matrix. Indeed the TGA curve (Figure S 3.2) demonstrates that Si-C bonds gradually decomposed at around 320 °C suggesting that cleavage of a fraction of the Si-C bonds is unavoidable during surfactant removal.

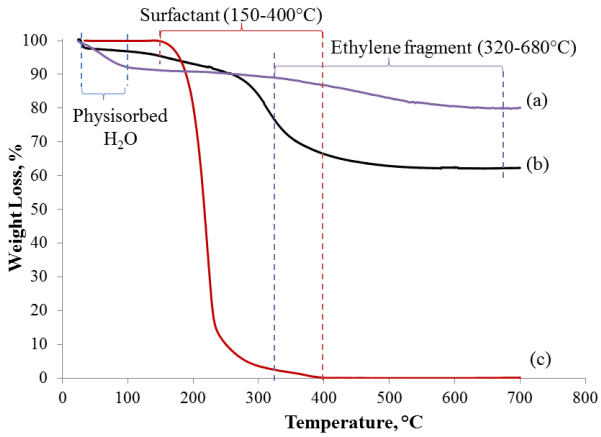

Figure S 3.2 TGA curve of the as-synthesized (a) organosilica without template; (b) organosilica templated with F68 and (c) pure Pluronic F68 as recorded under an air atmosphere.

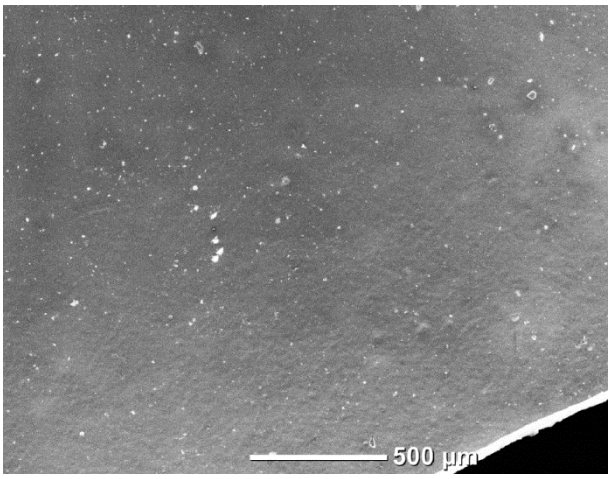

Figure S 3.3 SEM image of top plane view of organosilica membrane showing the large area of uniform coating without cracks or defects.

4 THEORETICAL STUDY ON THE WATER TRANSPORT IN NANOPOROUS ORGANOSILICA MEMBRANE

Introduction

The hydrophilic (contact angle < 90°), nanoporous organosilica membrane in the previous chapter showed excellent MD performance without pore wetting, with fluxes effectively unchanged across the entire range of salt concentrations. It is therefore vital to study the transport mechanism of water vapour in nanopores region and model the effect of membrane properties and operating parameters on the permeation fluxes.

Contribution

A new mathematical model describing the transport of water through the unconventional, hydrophilic, nanoporous organosilica membrane was developed by adapting the Lucas-Washburn equation for water intrusion into the nanopores channel induced by capillary pressure. The model quantitatively describes the permeation flux under the impact of membrane physical properties, thermal and concentration polarization, membrane hydrophilicity and water shear viscosity in a nanoconfined space. A version of this chapter has been published in the Journal of Membrane Science as:

> Y. T. Chua, G. Ji, G. Birkett, C. X. C. Lin, F. Kleitz and S. Smart, Nanoporous Organosilica Membrane for Water Desalination: Theoretical Study on the Water Transport, Journal of Membrane Science, 482, 2015, 56-66.

Nanoporous Organosilica Membrane for Water Desalination: Theoretical study on the water transport

*Reproduced in part with permission from Yen Thien Chua, Guozhao Ji, Greg Birkett, Chun Xiang Cynthia Lin, Freddy Kleitz and Simon Smart, *Journal of Membrane Science*, 482, 2015, 56-66.

Abstract

An unconventional nanoporous organosilica membrane has been tested in a vacuum membrane distillation (MD) process for water desalination. We propose a modified approach to understand the transport mechanism of water molecules through the nanopores of this membrane. The modified approach stems from the fact that the membrane has a hydrophilic surface (contact angle < 90 °) and so capillary pressure, which draws liquid water into the nanopore, must be considered when establishing the mathematical model. However, increased friction arising from the dramatic increase in shear viscosity of water in nano-confined spaces balances the capillary flow against the evaporative mass transport to avoid pore wetting. Notably, the liquid/vapour interface is no longer formed at the pore entrance as with a conventional hydrophobic membrane, but rather exists deeper in the pore channel as a consequence of capillary pressure. This was backed by experimental observations (no pore wetting) and SEM evidence which showed salt nucleation and growth existed only on the membrane surface, and did not infiltrate the membrane support layers. The impacts of pore size, membrane thickness, substrate thickness, concentration polarization, porosity, and contact angle on water flux and pore intrusion depth were tested using the model. Pore size was the most influential parameter with an > 80 % increase in permeation flux if the pore size increased from 2 to 3 nm at 60 °C. However, pore wetting is expected if d_p > 3.4 nm, particularly at low temperatures where the slower evaporation rate promoted greater pore intrusion. Concentration polarization was shown to be negligible which agreed well with experimentally observed water fluxes which remained relatively constant despite feed salinity increasing from 0 to 150 g L^{-1}. Lastly, the membrane hydrophilicity was found to impact on water flux and pore intrusion in a complex relationship with pore size. Ultimately, hydrophilic pores less than 3 nm in diameter offer a good combination of good water flux and minimal water intrusion suggesting that ordered mesoporous organosilica membranes have potential in MD applications.

Key words: membrane distillation, organosilica membrane, nano-confined viscosity

4.1 Introduction

Membrane distillation (MD) is a promising process for water desalination owing to its compact design and ability to process highly concentrated brines. It is a combined process that uses both thermal energy and membranes to produce fresh water and it has the potential to overcome some of the bottlenecks of conventional processes. Compared to traditional distillation, MD operates with a smaller vapour space, reducing unit operation size and works well with lower feed temperatures < 90 °C allowing low grade / waste heat to be utilized [1]. Furthermore, MD does not require extreme pressures of the reverse osmosis process [2], and is therefore able to treat highly concentrated brine solutions up to 300 g L^{-1} [3]. Many desalination studies that utilize MD have been reported using hydrophobic, polymeric membranes (e.g. polyvinylidene fluoride (PVDF) and polytetrafluoroethylene (PTFE)) with average pore size of 0.1 – 1.0 μm [4]. In such a system, a liquid/vapour interface or 'meniscus' is formed at the pore entrance, wherein only water will vaporize and transport across the membrane, leaving behind the non-volatile salts. The formation of this meniscus requires a hydrophobic membrane surface and that the transmembrane pressure is less than liquid entry pressure (LEP), (where LEP is expressed as $\Delta P = -2B\gamma_l \cos\theta / r_{max}$) a derivation from the Young-Laplace equation [5]. Should the transmembrane pressure exceed the LEP, liquid water will enter and then fill the pores (referred to as pore wetting), which renders the membrane incapable of separation. Typical performance requirements for MD membranes include a narrow pore size distribution, sufficient hydrophobicity, low tortuosity, high porosity, low thermal conductivity, good thermal stability and high fouling resistance [6]. As a result, most of the MD literature has focussed on increasing hydrophobicity, thermal stability and anti-fouling strategies [7-11].

Models for the transport mechanisms for different MD configurations, such as direct contact MD, air gap MD, sweep gas MD and vacuum MD, have been widely reported [10, 12-16]. In particular, vacuum MD (VMD) provides the highest water flux, establishing the highest vapour pressure gradient for a given operating temperature [6]. Unfortunately, VMD typically requires an external condenser and vacuum pump, which might increase the operating cost, although other options are available [17]. The larger transmembrane pressure in turn also implies a greater risk of pore wetting. Several groups have extensively studied the effect of operating parameters to the membrane performance [13, 14, 18-20]. For example, Imdakm and co-workers

investigated the effect of membrane pore interconnectivity on the permeate flux by using Monte-Carlo simulations [15], whereas Soukane and co-workers developed a model based on ballistic transport at the pore scale for VMD. Notably, there is no reported work using a hydrophilic, nanoporous membrane for study of transport mechanisms for a membrane with pore sizes smaller than 5 nm. Models do exist for liquid permeation in porous media for pores in this size range offering useful insight both from a mass transfer [21] and molecular dynamics perspective [22]. However, these either utilize surface diffusion or are computationally expensive, respectively which can hinder their applicability, especially under vacuum or non-isothermal conditions and there exists scope for a new approach. Our previous work described the application of a nanoporous, organosilica membrane in water desalination using VMD [23]. The membrane revealed promising water permeation fluxes and yet was unconventional where it exhibited: (1) much smaller pores (~ 2 nm) than the commonly tested polymeric membranes; (2) did not show any decline in permeation flux with the increment of salt concentration of the feed solution up to 150 g L^{-1}; and (3) no pore wetting was observed even though the membrane surface was not hydrophobic (contact angle < 90 °).

The advantages of our membrane come from its narrow pore size distribution, the combined benefits of hybrid organic and inorganic materials and thin active layer. The nanoporous membrane was prepared using the evaporation-induced self-assembly (EISA) pathway in the presence of a triblock copolymer surfactant as structure-directing agent, being the most versatile method thus far for producing thin mesoporous films [24, 25]. To accommodate the requirements of membrane properties in VMD, we selected 1, 2-bis(triethoxysilyl)ethane as the organosilica precursor for the membrane framework. The alkyl group bridging two silicon species within the matrix was reported to improve the hydrothermal stability of such hybrid silica membrane (preventing the enlargement of the pore or the densification of small pores), as well as providing some stress relaxation (reducing macroscopic cracking as observed in pure silica membranes) [26].

However, the organosilica membrane is not entirely hydrophobic due to the existence of silanol groups and the incorporation of alkyl species within the matrix instead of dangling on the pore walls (as in the case of post-grafting method). Thus, the intrusion of water into the pore channel in accordance to Hagen-Poiseuille equation is highly possible, which leads to the question of the contribution of water capillary pressure in hydrophilic pore channels. Therefore, a theoretical

examination of likely transport mechanisms for our membrane is necessary. The Lucas-Washburn equation is widely used in studying the capillary rise of water in the absence of gravitational field but its implementation in nanopores (microfluidics and nanofluidics) requires some modifications [27-30]. Another question that arises relates to the behaviour of water in nanoconfined spaces, in particular, to what extent is it valid to assume the continuum hydrodynamic properties of water hold, when examined in a nano-sized space. Ortiz-Young and co-workers performed experiments using AFM on the change of water shear viscosity in a confined space and reported a great increase of the viscous shear forces of nanoconfined water near hydrophilic surfaces compared to bulk water [31]. This information is particularly meaningful in explaining the water transport phenomena in our unconventional membrane. This contribution aims to assess the water transport in the confined nanopores (pore size ~ 2 nm) of the unconventional membrane by using a simple modelling approach followed by identifying future avenues of fundamental MD research based on the results.

4.2 Experimental

Desalination tests were conducted with an organosilica membrane using a continuous flow system (Figure S 4.1) of VMD as reported in our previous work [23]. The membrane module consists of a tubular membrane (PALL, length 100 mm, outer diameter 10 mm, thickness 1.7 mm) with feed solution was being transported into the tube lumen and vacuum (1.5 kPa) was applied at the shell side. The tests were carried out at varying feed temperature of 20, 40 and 60 °C and sodium chloride solution with various concentrations (10, 35, 50, 75, 150 g L^{-1} of NaCl). The permeate flux through the membrane, J (L m^{-2} h^{-1}) was calculated by $J = (1/A)\cdot(dm/dt)$, where m is the mass of permeate collected, A as the membrane tube active area and t is the time of permeation test. Salt rejection, R (%) of the membrane was calculated by the following equation: $R = (C_f - C_p)/C_f \times 100\%$, where C_f and C_p were the feed and permeate concentrations (wt %), respectively.

The substrate porosity was measured using a mercury porosimeter (Micromeritics, AutoPore IV 9500). The obtained mercury intrusion volume was then used to calculate the porosity of the material by $(\rho_S \times V_S)/(1+\rho_S \times V_S)$, where ρ_S (g cm^{-3}) is the material's density obtained from a gas pycnometer (Micromeritics, Accupyc II 1340) and V_S (mL g^{-1}) is the mercury intrusion volume. Surface wettability of the organosilica film coated on glass slide was examined by sessile drop

contact angle measurement. A water drop of about 1 µL on the surface at 10 different points was recorded using a contact angle system (Dataphysics, OCA20). The morphology of post-testing membrane was inspected using scanning electron microscopy (SEM). A JEOL JSM-6610 microscope at an accelerating voltage of 15 kV with electron source of LaB6 gun was used to perform the analysis on the sample. Prior to SEM analysis, the sample was coated with Iridium at sputtering current of 15 mA for 200 s.

4.3 Mathematical model of heat and mass transfer for water transport

In a typical VMD process using a hydrophobic membrane, a liquid/vapour interface is formed at the pore entrance as shown in Figure 4.1. This process involves both heat and mass transfer and has both thermal and concentration boundary layers with thickness δf_t and δf_c, respectively. Heat loss across the thermal boundary layer determines the water flux, owing to the evaporation rate depending on the feed side temperature at the membrane surface, Tf_m. With the phase change of water, this gives the difference of water vapour pressure, P_{vp} from the permeate pressure, P_p. Since this separation process is dealing with aqueous phase and non-volatile salt components, the salt concentration, C_{Bm} on the membrane phase increases with the evaporation of water (water concentration, C_{Am} is assumed to remain constant), forming a boundary layer of concentration polarization. Both thermal and concentration polarization affect the membrane flux and the rate limiting step for our unconventional membrane is yet to be determined.

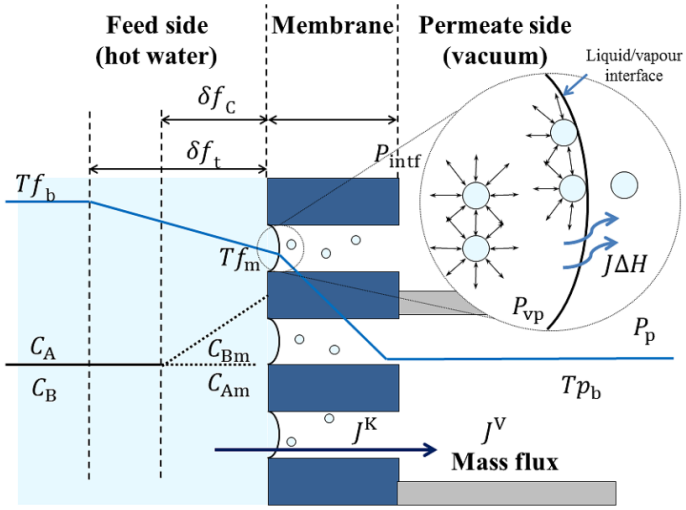

Figure 4.1 Schematic diagram of heat and mass transfer in VMD with thickness of membrane (navy blue), substrate (grey) and the thermal and concentration boundary layers not up to scaled.

The nanoporous membrane system in this study is an asymmetric configuration with a thin active layer on a porous ceramic substrate. Liquid is fed at the feed side, whilst at the permeate side, the transport of evaporated water vapour through the membrane pore channels and then the underlying substrate is considered as gas phase transport. The active layer of the membrane is comprised of mesopores, which are smaller than the typical pore sizes encountered in VMD [13] and larger than those encountered in pervaporation [32]. A mathematical model to simulate and validate the performance of the membrane in VMD was constructed using the following assumptions:

- the system is in steady-state
- only heat conduction is considered at the feed side liquid boundary layer
- only heat conduction is considered across the membrane
- interconnectivity of pore channels is not considered

From the mass transfer perspective, the entire system is divided into four main regions as shown in Figure 4.2:

(i) water transport from the bulk to the membrane pore entrance;

(ii) water transport in liquid phase from the pore entrance to the liquid/vapour interface;

(iii) transport of water vapour molecules from the liquid/vapour interface to the pore exit; and

(iv) transport of water vapour molecules from the pore exit, through the macroporous alumina substrate to vapour bulk under vacuum.

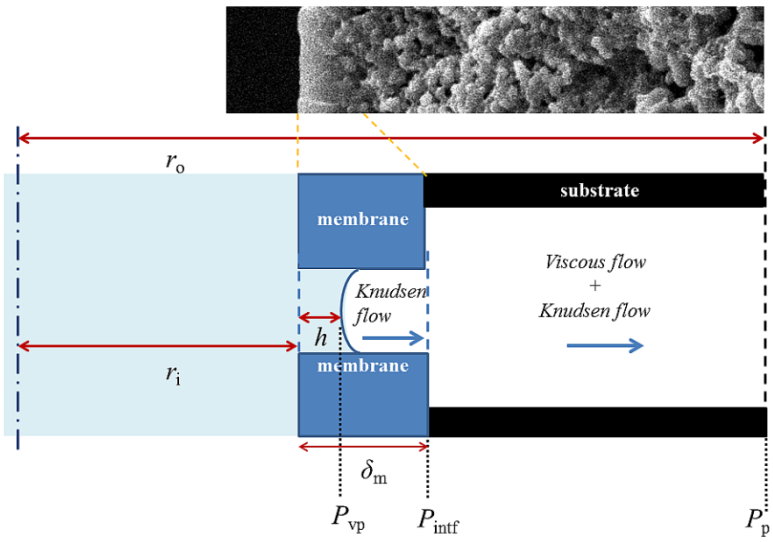

Figure 4.2 Schematic diagram of the mass transfer within the nanopores across the membrane to its substrate

4.3.1 Liquid phase flow through membrane pores

Since the membrane in this study is hydrophilic (Figure S4.2), it is expected that water will penetrate the membrane pores. However, the position of the liquid/vapour interface within the nanopore (or perhaps the macroporous support) is an unanswered question. Experimental observations from the previous work suggest that the membrane did not exhibit any pore wetting (i.e. the liquid water or crystallized salt was not observed on the permeate side of the membrane) even when tested for highly concentrated brines and higher feed temperatures of up to 60 °C. Water continuously evaporates from the interface due to the vapour pressure gradient. As there is no pore wetting observed, this implies the liquid/vapour interface lies at the position where the evaporation rate is in equilibrium with the liquid entry rate.

The Lucas-Washburn equation can be implemented to describe the capillary forces in nanopores, which has been widely used in microfluidics and nanofluidics. However, water properties have been found to greatly differ in confined space compared to the continuum dynamic flow regime, particularly in that the shear viscosity of water in a confined space (< 1 nm) could be in orders of magnitude higher than the classical continuum theory (about 70 Pa.s at room temperature for a silica surface) [31, 33]. Since the validity of macroscopic capillarity has been proven to be applicable down to meso- and nanoscale [29, 30], the Lucas-Washburn equation (eqn (1)) is used to express the capillary phenomena of water filling into the hydrophilic pore by defining the rise of liquid/vapour interface $h(t)$ over time t [27],

$$h(t) = \left(\frac{\gamma_l r_p \cos\theta}{2\eta_l} \right)^{1/2} \sqrt{t} \tag{1}$$

where, γ_l is liquid surface tension, r_p is pore radius, θ the contact angle between the liquid/vapour interface and the wall and η_l is the shear viscosity of liquid [31]. Solving the differential eqn (1) will give a term expressed in volumetric flux as,

$$J_{vol} = \frac{dh}{dt} = \frac{\gamma_l r_p \cos\theta}{4h\eta_l} \tag{2}$$

4.3.2 Gas phase flow in the active membrane layer

The transport mechanisms of gas or vapour within a porous material are routinely described by

viscous flow, Knudsen flow and activated diffusion depending on temperature, pressure and membrane pore size [34]. To investigate the transport of water vapour across the organosilica membrane, it is necessary to find the mean free path, λ, of the molecule within the membrane pores, which can be derived from eqn (3),

$$\lambda = \frac{k_B T}{\sqrt{2}\pi \bar{P} \sigma_i^2} \tag{3}$$

where, k_B is the Boltzmann constant, σ is the collision diameter (0.2641 nm for water vapour), $\bar{P}$ is the mean pressure within the membrane pores which is simply approximated by the average of vapour pressure and permeate pressure, and T is absolute temperature. The calculated mean free path as a function of temperature for a water vapour molecule is depicted in Figure 4.3.

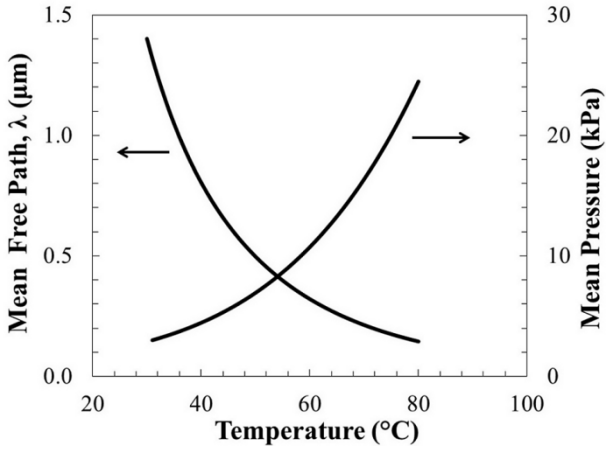

Figure 4.3 Mean free path of water vapour molecules and mean pressure at varying temperature

As shown in Figure 4.3, the value of mean free path is more than two magnitudes greater than the pore size of 2 nm, which implies that the vapour transportation in the membrane pores is in the Knudsen regime or activated diffusion regime. The pore size boundary between Knudsen flow and activated diffusion was firstly defined by Thornton et al. [35]; as when the molecule's kinetic energy is less than the absolute value of the pore wall potential, the transport is more likely to be governed by activated diffusion rather than Knudsen flow. Therefore, the potential distribution of a water vapour molecule in a 2 nm pore was calculated by using Lennard-Jones potential Figure 4.4. The Lennard-Jones parameters used in this work are listed in Table 4.1. The pores are assumed to be cylindrical and the pore wall is formed by silicon and carbon atoms with equal and uniform distribution. The interaction of the vapour molecule with the pore wall is a minimum (potential energy of 1.17×10^{-20} J) at a distance about 0.142 nm from the pore wall.

Table 4.1 Lennard-Jones parameters used in this work

Parameter	*Si*	*C*	*H_2O*
σ (nm)	0.280	0.340	0.264
ε/k_B (K)	492.7	36.0	809.1

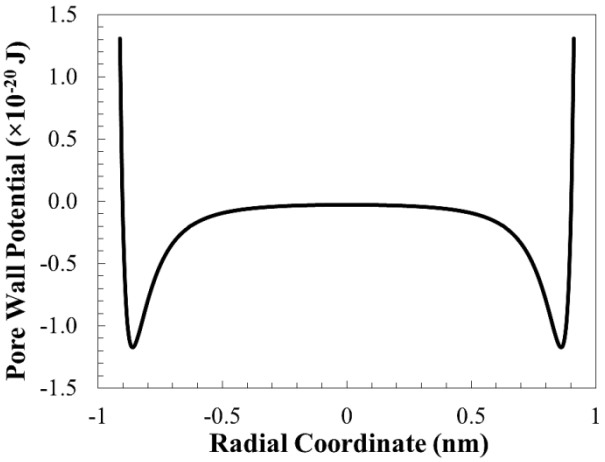

Figure 4.4 Potential distribution of a water vapour molecule in a 2 nm organosilica cylindrical pore given that the 0 coordinate is the center of the pore.

To determine the kinetic energy of a vapour molecule, it can be estimated by the classical kinetic theory by using eqn (4),

$$E_k = \frac{i}{2}kT \tag{4}$$

where, i is the freedom of the molecule, being 6 for H_2O. In this work, the experiment was carried out from 20 °C to 60 °C, which gives the kinetic energy of 1.214×10^{-20} J to 1.379×10^{-20} J. According to Thornton et al.'s definition, the vapour molecule kinetic energy is greater than the pore wall potential energy, implying that 2 nm is greater than the minimum pore size for Knudsen flow. Therefore, the transport of vapour molecule across the top layer is still considered to be Knudsen flow, as governed by eqn (5).

$$J^K = -\frac{2}{3}\frac{\varepsilon r_p}{\tau}\sqrt{\frac{8}{\pi RTM_i}}\frac{dP}{dr} \tag{5}$$

where, J^K is the flux in Knudsen flow, ε the porosity of the membrane, τ is pore tortuosity, M is the molecular weight of the transported species i.

Considering pressure at feed side as the vapour pressure, P_{vp}, and the pressure at the interface of membrane and substrate as, P_{if}, the flux across a membrane of thickness δ_m can be determined from eqn (5) as,

$$J^K = \frac{2}{3}\frac{\varepsilon r_p}{\tau}\sqrt{\frac{8}{\pi RTM_i}}\frac{P_{vp} - P_{if}}{\delta_m - h} \tag{6}$$

The vapour pressure of the NaCl solution, P_{vp} as a function of temperature and concentration can be calculated using the thermodynamic equations as reported by Sparrow et al. from 0 °C ≤ T ≤ 150 °C [36].

4.3.3 Mass transfer in the membrane support layer

From the data provided by manufacturer, the average pore size of the substrate is ~ 2 μm. Since the pore size is in the same magnitude of mean free path λ, so the flow must contain both viscous and Knudsen flow. A model superimposing Knudsen and viscous contributions is appropriate to describe the transport mechanism in the substrate. Assuming cylindrical pores, in the spirit of Dusty Gas Model (DGM) [37-39], the flow rate through the substrate can be expressed as,

$$F = -\frac{\varepsilon}{\tau}\left[\frac{97r_s}{R\sqrt{MT}}\frac{dP}{dr} + \frac{r_s^2 P}{8\eta_v RT}\frac{dP}{dr}\right]2\pi rL \tag{7}$$

where, L being the length of membrane, η_v being the viscosity of water vapour and r_s being the pore radius of substrate.

In a tubular substrate, the flux is not constant due to the fact that the flow is in the radial direction, but the flow rate remains constant. We will treat the flux at inner radius as the substrate flux as follows,

$$J = -\frac{\varepsilon}{\tau r_i \ln(r_o/r_i)}\left[\frac{97r_s}{R\sqrt{MT}}\left(P_{if} - P_p\right) + \frac{r_s^2 P}{16\eta RT}\left(P_{if}^2 - P_p^2\right)\right] \tag{8}$$

where, r_i is the inner radius of substrate and P_p being the permeate side pressure.

Other than this, we consider the pressure drop in our membrane module system, in which the vacuum pump system is located at a certain distance from our test rig. The permeate pressure is a function of flow rate, pipe radius and pipe length, whereas the pressure in the vacuum line follows the Hagen-Poiseuille equation [40, 41],

$$\frac{\mathrm{d}P}{\mathrm{d}l} = -\frac{8\eta_{\mathrm{v}} FRT}{\pi {r_{\mathrm{pp}}}^4 P} \tag{9}$$

$$\int_{P_{\mathrm{lm}}}^{P_{\mathrm{p}}} P\mathrm{d}P = -\frac{8\eta_{\mathrm{v}} FRT}{\pi {r_{\mathrm{pp}}}^4} \int_0^{L_{\mathrm{p}}} \mathrm{d}l \tag{10}$$

where, F is permeate flow rate, r_{pp} being radius of vacuum line, P_{lm} being the pressure of the vacuum pump and L_{p} as the length of the vacuum line from the rig to the pump.

$$P_{\mathrm{p}} = \sqrt{\frac{16\eta_{\mathrm{v}} FRT}{\pi r^4} l + {P_{\mathrm{lm}}}^2} \tag{11}$$

4.3.4 Heat transfer

As MD is a thermal process, heat transfer across the membrane involves:

(i) heat transport through the feed boundary layer with thickness δf_{t} (Figure 4.1),

(ii) heat transport through the membrane and substrate,

(iii) heat transport through the permeate boundary layer.

Due to the application of vacuum at the permeate side in VMD, the conductive heat loss across the permeate boundary layer can be neglected. A two-dimensional model has been designed with heat transfer in the bulk liquid along the membrane longitudinal direction z and radial coordinate r from the tube center ($r = 0$),

$$\frac{1}{r}\frac{\partial}{\partial r}\left(r\rho_{\mathrm{l}} u_{\mathrm{r}} T\right) + \frac{\partial}{\partial z}\left(\rho_{\mathrm{l}} u_{\mathrm{z}} T\right) = \frac{k_{\mathrm{l}}}{C_{\mathrm{p,\,l}}}\left[\frac{1}{r}\frac{\partial}{\partial r}\left(r\frac{\partial T}{\partial r}\right) + \frac{\partial}{\partial z}\left(\frac{\partial T}{\partial z}\right)\right] \tag{12}$$

where, k_{l} is thermal conductivity of liquid phase and $C_{\mathrm{p,l}}$ as the specific heat of water. The heat transfer at the interface of liquid and membrane is expressed as,

$$\frac{1}{r}\frac{\partial}{\partial r}\left(r\rho_{\mathrm{l}} u_{\mathrm{r}} T\right) + \frac{\partial}{\partial z}\left(\rho_{\mathrm{l}} u_{\mathrm{z}} T\right) = \frac{k_{\mathrm{l}}}{C_{\mathrm{p,\,l}}}\left[\frac{1}{r}\frac{\partial}{\partial r}\left(r\frac{\partial T}{\partial r}\right) + \frac{\partial}{\partial z}\left(\frac{\partial T}{\partial z}\right)\right] - \frac{Q}{C_{\mathrm{p,\,l}}}\frac{\partial A}{\partial V} \tag{13}$$

Heat loss Q can be derived by,

$$Q = \Delta \mathrm{H} \cdot J_{\mathrm{m}} \tag{14}$$

where ΔH is the enthalpy change of unit mass and J_{m} is the mass flux,

$$J_{\mathrm{m}} = \rho \cdot u_{\mathrm{r}} \tag{15}$$

In the substrate, the flow in the longitudinal direction z is negligible in relative to the flow in radial direction r. Thus, heat transfer across the substrate during water vaporization could be simplified into one-dimensional equation as,

$$\frac{1}{r}\frac{\partial}{\partial r}\left(r\rho_{\mathrm{v}}u_{\mathrm{r,v}}T\right)=\frac{k_{\mathrm{s}}}{C_{\mathrm{p,v}}}\frac{1}{r}\frac{\partial}{\partial r}\left(r\frac{\partial T}{\partial r}\right) \tag{16}$$

And substituting Eqn (15) into Eqn (16) gives,

$$\frac{1}{r}\frac{\partial}{\partial r}\left(rJ_{\mathrm{m}}T\right)=\frac{k_{\mathrm{s}}}{C_{\mathrm{p,v}}}\frac{1}{r}\frac{\partial}{\partial r}\left(r\frac{\partial T}{\partial r}\right) \tag{17}$$

where, $u_{\mathrm{r,v}}$ is the radial velocity in vapour phase, k_{s} is the thermal conductivity of vapour and substrate and $C_{\mathrm{p,v}}$ is the specific heat of vapour.

4.4 Results and Discussion

The properties of the organosilica membrane are listed in Table 4.1 with a narrow pore size distribution at around 2 nm as reported elsewhere [23]. This information was implemented in the mathematical model to data fit the experimental results. Contact angle measurement (Figure S 4.2) suggests the surface of organosilica membrane is hydrophilic.

Table 4.1 Properties of organosilica membrane and the alumina substrate

Properties	
BET surface area, $m^2\ g^{-1}$	310
Total pore volume (V_{p}), $cm^3\ g^{-1}$	0.18
Pore diameter (d_{p}), nm	2
Membrane thickness (δ_{m}), μm	1
Substrate manufacturer	PALL
Substrate material	Al_2O_3
Substrate inner diameter, mm	7
Substrate outer diameter, mm	10
Substrate porosity, %	25.7

The morphology of the organosilica membrane before and after the desalination tests was studied by SEM as shown in Figure 4.5. The fresh membrane (Figure 4.5(a)) has a smooth surface whereas the tested membrane was found to have bundles of salt crystals growing on the organosilica surface. Figure 4.5(d) shows the cross-sectional view of the organosilica membrane

and the substrate.

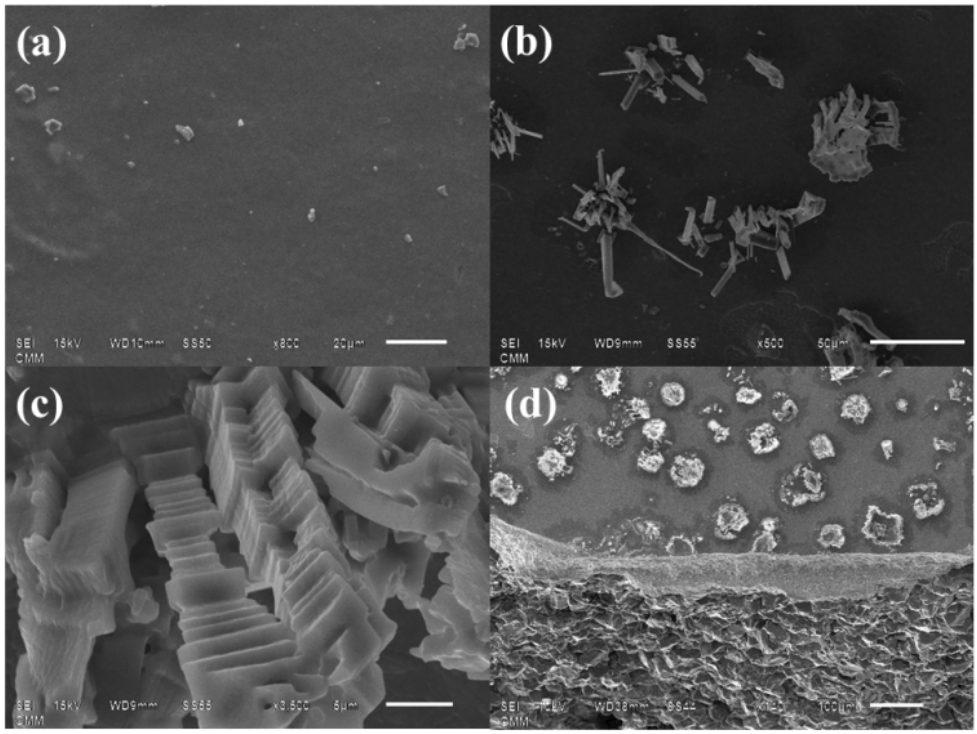

Figure 4.5 SEM images of the (a) fresh membrane before testing and (b) membrane after testing in desalination; (c) enlarged views of salt crystals growing from underneath membrane in island forms; (d) cross-sectional view of supported membrane (from top) organosilica membrane and salt crystals, titania layer, alumina substrate.

No salt crystals are observed on the alumina substrate, as shown in the enlarged boundary layer of the smaller alumina particles and larger alumina particles. It is quite interesting that the direction of growth and nucleation of the salt crystals was upward from the organosilica to air but not growing inside the membrane matrix. This could be explained by the nucleation of the salt ions happening only when the membrane is exposed to air, after desalination test has been stopped. It also provides strong evidence that the saline feed water did not pass through the active top layer of the membrane into the membrane substrate, and the capillary/evaporation equilibrium is reached inside the membrane layer.

4.4.1 Model validation

The established mathematical model was validated with the experimental data obtained from desalination tests over a range of salt concentrations and feed temperature as presented in Figure 4.6 [23].

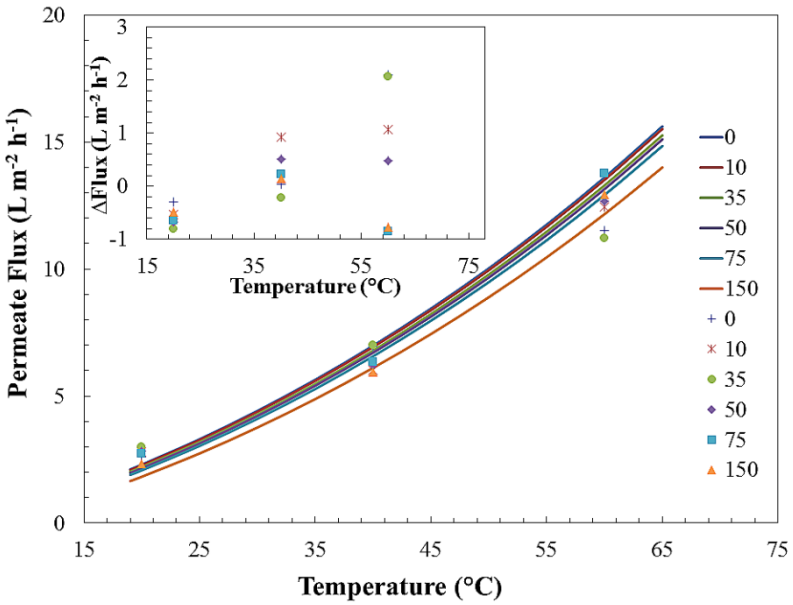

Figure 4.6 Plot of model fitting to the experimental data for salt concentrations from 0 to 150 g L^{-1} and temperatures from 20 – 60 °C. Symbols present the experimental data and curves represent the calculated values. Inset shows the variations of predicted values from model to the experimental data.

There are two important observations from Figure 4.6. The first is that the model and experimental data fit well with root mean square error below 0.78. The second is that the effect of salt concentration on the permeate flux is not significant, contrary to the findings of other studies utilizing inorganic membranes for MD or pervaporative desalination [42]. This is predominantly governed by the minor changes in P_{vp}, and thus driving forces, that occur as a result of changes in salt concentration [36].

Integration of the Lucas-Washburn equation yields the estimated distance the liquid phase travels into the pore channel, as presented in Figure 4.7. For the experimental conditions used in this study, the deepest distance the salt water travels into the membrane active layer is 470 nm at feed temperature of 20 °C. This value decreases as feed temperature increases, which is attributed to an increase in the evaporation rate relative to the liquid intrusion rate. Figure 4.7 implies that the water intrusion rate is more dominating when the feed temperature is lower, with the liquid/vapour interface shifted further into the membrane pores. It should be noted that the membrane has a thickness of ~1 μm which correlates well with the lack of pore wetting observed. The intriguing idea here is that the intrusion of more liquid water at lower temperatures has in a sense decreased the distance the water vapour must travel in the Knudsen region of the membrane, in effect decreasing the Knudsen resistance.

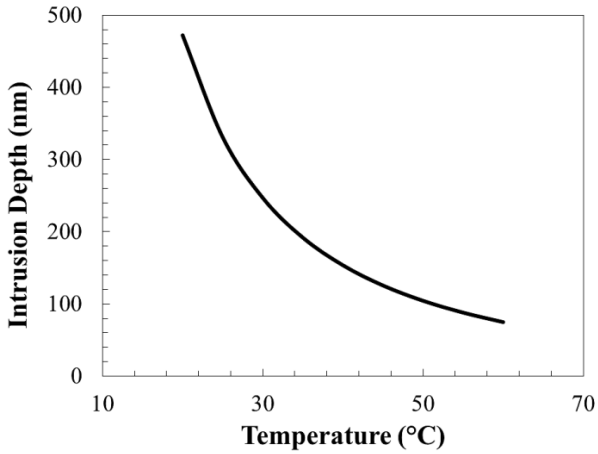

Figure 4.7 Water intrusion depth within a 2 nm nanopore channel at varying liquid temperatures.

4.4.2 Temperature Polarization

The temperature values across the membrane were measured at the feed side and permeate side by K-type thermocouples and these values were used to determine the heat loss across the membrane. Figure 4.8 presents the heat transfer profile of the system from the tube center (radial coordinate = 0) to the permeate side of membrane (outer surface) in a radial direction. Both of these points were experimentally measured (indicated as data points on Figure 4.8) and used as inputs for the modelled temperature profile (indicated by the lines on Figure 4.8). As the feed temperature increases, the thermal boundary layer becomes more severe. Most of the heat loss occurs in the thermal boundary layer, which is attributed to the vaporization of water. Indeed, the Nusselt number is approximated at 3.66 for fully developed laminar flow (Re = 250) in a tube with constant surface temperature [43], which confirms that convective heat transfer away from the membrane surface is only marginally larger than conductive hear transfer through the membrane itself. At low temperature, heat loss is very limited and almost negligible, suggesting the driving force is maintained by the low vapour pressure on the permeate side by means of the vacuum pump.

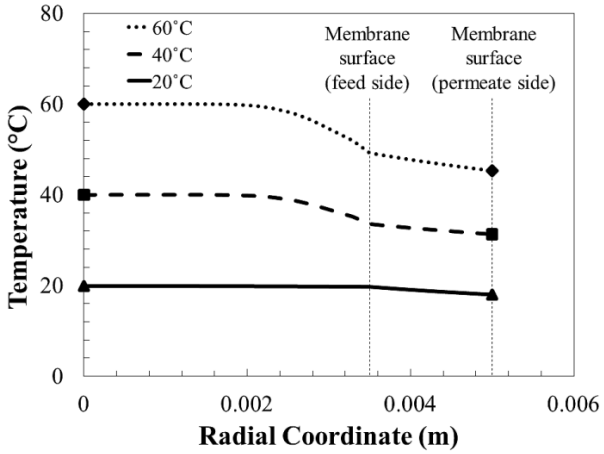

Figure 4.8 Heat transfer profile of the feed solution to the membrane at varying feed temperature from center of tube lumen (0 coordinate) to the permeate side of membrane (outer surface).

4.4.3 Concentration polarization

In MD, concentration polarisation (CP) has been found to influence membrane flux [4]. Here we are concerned with two types of concentration polarisation, namely external and internal CP. External CP occurs in the liquid phase on the membrane surface before entering the pore; whereas internal CP is defined as the concentration variation within the pore channel itself. From the macroscopic view, the flow within the membrane tube is laminar (Re = 250) which suggests the thickness of the boundary layer for external concentration polarization on the feed side (δf_c) should be further examined in line with the analysis of temperature polarization. However, in the case of external CP the Sherwood number ranges from 14-17 [43] which indicates that the convective mass transfer away from the membrane surface is more influential that the diffusive flow through the boundary layer. This in combination with the low sensitivity of vapour pressure to salt concentration [36], explains why the external CP is not a dominating factor in the mass transport.

However, the high cross flow velocity in the bulk solution does not affect the flow within the pore. Internal concentration polarization (ICP) on the other hand may lead to either a decline in flux or built-up of salt crystals if supersaturation of the saline feed is reached. It is necessary to understand the degree of ICP in our system. Figure 4.9 shows the penetration of liquid into the membrane pore until the liquid/vapour interface is reached. In the radial direction, the salt concentration increases due to evaporation of water; this permeate flow drives the salt from r_1 to

r_2 via advection. In the meantime, there is a diffusive flow in the opposite direction, driven by the salt concentration gradient between the pore (higher) and the bulk feed (lower) and allows the bulk concentration to be maintained in equilibrium.

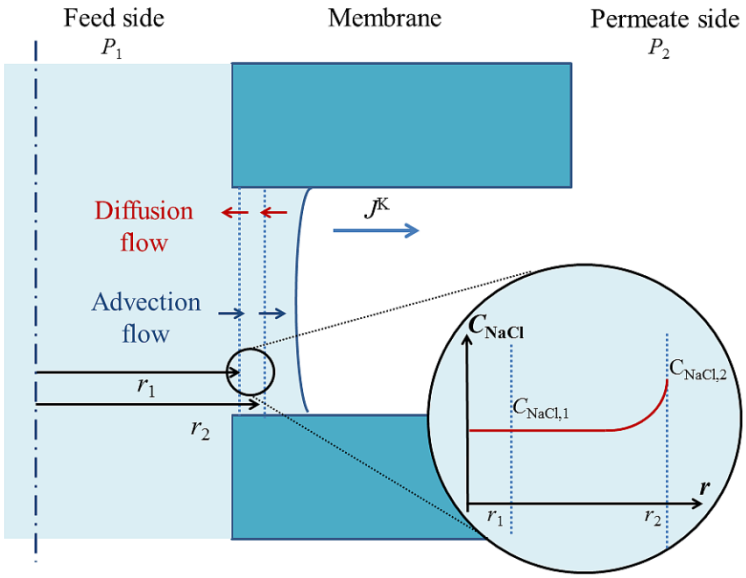

Figure 4.9 Internal concentration polarization inside the organosilica pore channel

Hence a mass balance for NaCl concentration can be performed,

$$Jx_2r_2 - Jx_1r_1 = D\left(\frac{\mathrm{d}c_{\mathrm{NaCl}}}{\mathrm{d}r}\right)_2 r_2 - D\left(\frac{\mathrm{d}c_{\mathrm{NaCl}}}{\mathrm{d}r}\right)_1 r_1 \tag{18}$$

where, D is diffusion coefficient of salt in water, x is the molar fraction of NaCl in water, C_{NaCl} is concentration of NaCl in water. If r_2 is approaching to r_1, eqn (18) can be re-written in derivative format as,

$$J\frac{\mathrm{d}(xr)}{\mathrm{d}r} = \frac{\mathrm{d}}{\mathrm{d}r}\left(Dr\frac{\mathrm{d}c_{\mathrm{NaCl}}}{\mathrm{d}r}\right) \tag{19}$$

If we assume the total concentration c is constant,

$$c_{\mathrm{NaCl}} = c \cdot x \tag{20}$$

$$J\frac{\mathrm{d}(xr)}{\mathrm{d}r} = Dc\frac{\mathrm{d}}{\mathrm{d}r}\left(r\frac{\mathrm{d}x}{\mathrm{d}r}\right) \tag{21}$$

$$Jx + Jr\frac{\mathrm{d}x}{\mathrm{d}r} = Dcr\frac{\mathrm{d}^2x}{\mathrm{d}r^2} + Dc\frac{\mathrm{d}x}{\mathrm{d}r} \tag{22}$$

Two boundary conditions are required to solve the second order derivative, given that

$$\begin{cases} r = r_i; x = x_0 \\ r = r_i; \dfrac{dx}{dr} = 0 \end{cases}$$

By solving the above equations, the ICP profile could be determined. Figure 4.10 represents the relationship of ΔC, where $\Delta C = C - C_0$ (C is the concentration along the intrusion depth and C_0 is the bulk concentration) to the intrusion depth at the highest salt concentration tested (150 g L^{-1} or 0.0441 mol m^{-3}) and feed temperatures of 20, 40 and 60 °C. As seen previously in Figure 4.10, the lowest temperature has the greatest intrusion depth due to the lower water evaporation rate. The further the liquid travels into the pore the greater the ICP. However, the real difference in the salt concentration is very small, on the order of picomoles m^{-3} compared to the bulk concentration of 0.0441 mol m^{-3}. To evaluate the sensitivity of the internal CP to temperature effects associated with back diffusion of salts, the diffusion coefficient D, was artificially increased and decreased by 3 orders of magnitude (Figure S4.3). The internal CP profile with pore depth also increased and decreased by 3 orders of magnitude; however the relative change in concentration remained negligible when compared to the total bulk concentration. It is therefore appropriate to neglect the ICP within the nanopores. This correlates well the lack of that flux decline and salt crystal formation in the membrane during operation.

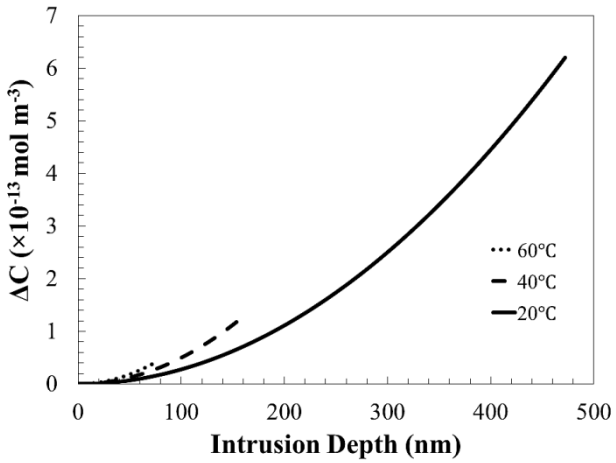

Figure 4.10 Profile of internal concentration polarization (ICP) in function of the depth of water intrusion in nanopores.

4.4.4 Effect of membrane properties

Given the fine balance between liquid intrusion and evaporation that exists within the pores, it is important to understand the effect of varying pore size, operating temperature and its likelihood

to undergo pore wetting. The change of water shear viscosity with the pore size has been taken into consideration during the simulation. These values were estimated based on the reported work from Riedo's group [31, 33]. Figure 4.11 shows the pore size effect on the intrusion depth of pure water into the pore channel and the water permeation flux at temperature of 20, 40 and 60 °C. Water intrudes deeper into the pore channel as pore size increases. This is to be expected as the water shear viscosity sharply reduces when the pore size increases, quickly approaching bulk water viscosity. The maximum allowable pore size for this type of organosilica membrane (at this active layer thickness) is at 3.4 nm but pore wetting is very likely to occur at 20 °C. This suggests that surface modification is necessary if a larger pore size is required to enhance the membrane permeation flux. Regarding future membrane design it is significant to note that enlarging the pore size by 50 % from 2 to 3 nm provides permeation flux enhancement of approximately 82 %, 49 % and 41 % at feed temperature of 20, 40 and 60 °C, respectively.

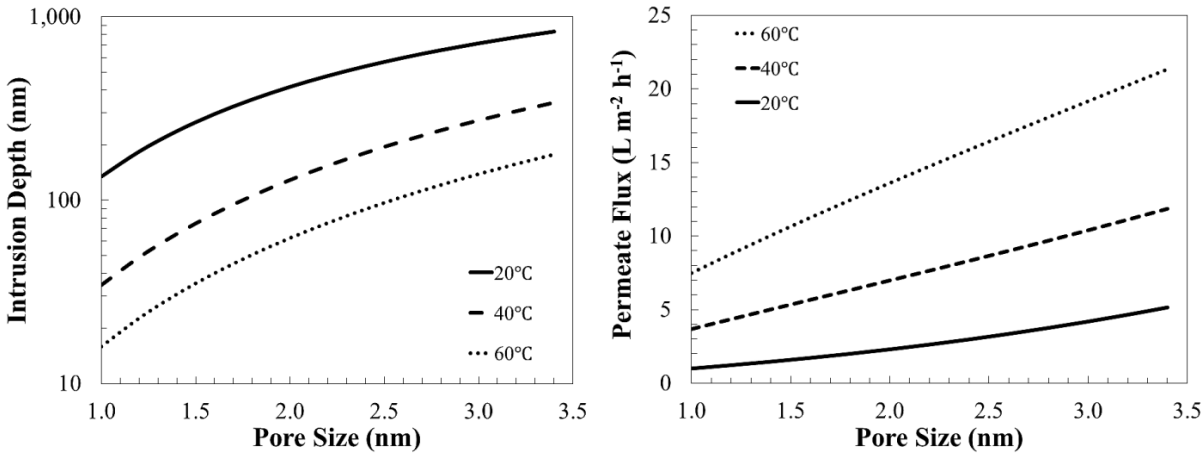

Figure 4.11 Effect of pore size to the liquid intrusion depth (left) and water permeation flux (right) at varying temperature

As for the membrane porosity, an increment of 50 % from 0.24 to 0.36 was found to improve the membrane water flux approximately 28 % irrespective with the change of feed temperature as can be seen in Figure 4.12. A 100 % improvement of membrane porosity to 0.4 may enhance the flux approximately 75 %. However, it is quite challenging to prepare a stable inorganic membrane with porosity of 0.4 as the mechanical strength of the membrane and its performance need to be balanced.

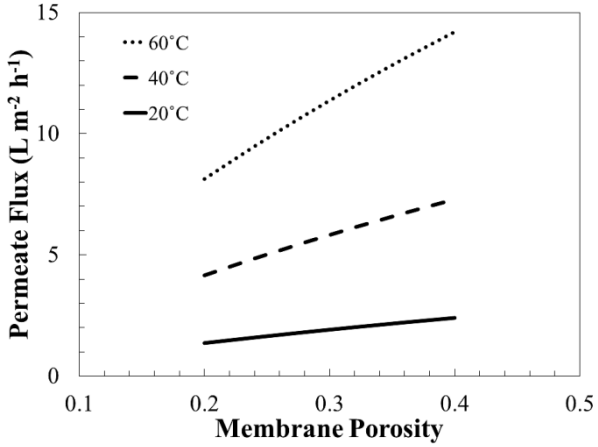

Figure 4.12 Effect of membrane porosity to the membrane permeation flux at varying feed temperature

Membrane thickness has a significant impact on the water permeation flux as presented in Figure 4.13. The flux was modelled for membranes with thickness from 500 nm up to 3 μm. An increase of approximately 27 % in the membrane water flux is observed when decreasing the membrane thickness from 1 to 0.5 μm at a feed temperature of 60 °C. However, fabricating a 500 nm thick, defect-free organosilica membrane with ordered pore structure is quite challenging and large performance gains are unlikely to be achieved here.

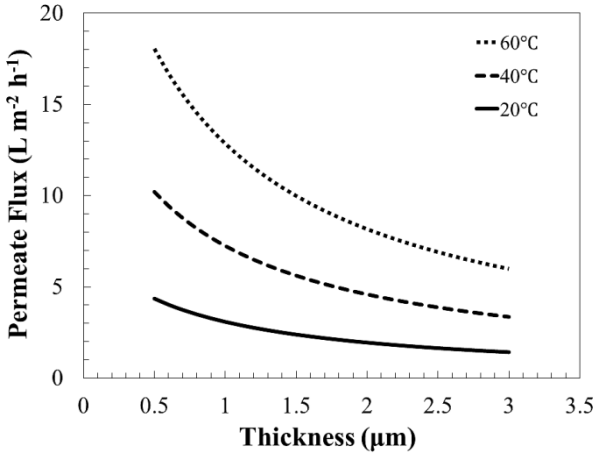

Figure 4.13 Effect of membrane thickness to water permeation flux

In comparison to membrane thickness, the effect of membrane support thickness on water flux is less intuitive as the primary function of the support is to provide mechanical strength. Further it is sometimes assumed that the large pore sizes of the membrane support do not significantly contribute to the overall transport resistance of the membrane, although this is not always the case [44]. Indeed, apportioning the resistance to flux through the membrane to either the top membrane layer or the membrane support reveals that the membrane support accounts for between ~20-30 % of the total resistance (Table S4.1). This indicates it is a useful target for

optimized design, although it should be noted that the support does not induce a significant pressure drop (Figure S4.4). Further to this Figure 4.14 shows that the flux could be improved approximately 15 % if the substrate thickness is reduced to 0.5 mm.

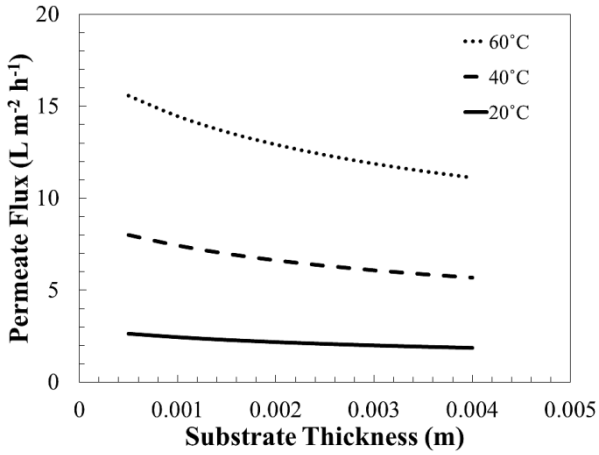

Figure 4.14 Effect of substrate thickness to water permeation flux at varying feed temperature

The model proposed here relies on the assumption that the liquid/vapour interface occurs at some point within the nanopore channel, specifically at the position where the evaporation rate is in equilibrium with the liquid entry rate. This is a delicate balance and necessitates a sensitivity analysis of the model parameters, as several were sourced from other studies or calibrated from experimental results. Given the importance of pore surface hydrophilicity/hydrophobicity (i.e. contact angle) in determining shear viscosity which in turn influences membrane flux and pore intrusion depth, these were further investigated with the results shown in Figure 4.15.

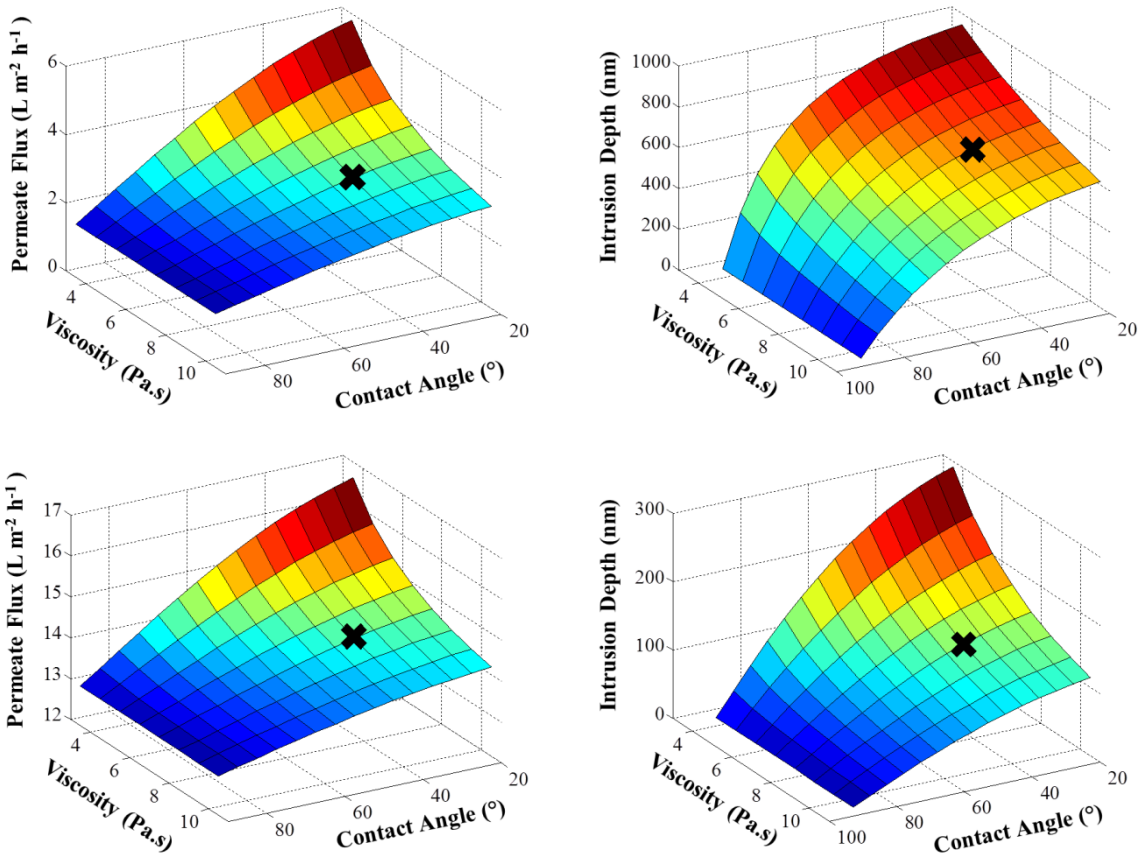

Figure 4.15 Effect of membrane surface hydrophilicity/hydrophobicity to water permeation flux and intrusion depth at 20 °C (top) and 60 °C (bottom).

It is important to note here that the surfaces presented in Figure 4.15 are continuous only for the purposes of analysing the parameters of the model and do not represent the physical system. Rather, the intent is to examine how an inaccurate estimate of contact or viscosity impacts of the predicted membrane flux and pore intrusion depth. To this end the values used in our study are marked on each surface to provide a visual indication of how sensitive the model is to these parameters. The results showed that for high values of shear viscosity (e.g. > 5 Pa.s) surface hydrophilicity had minimal impact on the overall membrane flux, which decreases as contact angle increases. On the other hand, contact angle significantly impacts on both membrane flux and pore intrusion depth at low shear viscosities (e.g. < 5 Pa.s), rapidly increasing pore intrusion depth in particular. The effects here are more pronounced at lower temperatures (e.g. 20 °C) as opposed to higher temperature (e.g. 60 °C). Assessing the region of interest for the membrane under investigation, it is clear that the degree of uncertainty in the contact angle and shear viscosity parameters does impact on the robustness of the overall model. Indeed, for the model, the success of the membrane in avoiding pore wetting during MD operation is predicated on a

value of shear viscosity for water that is several orders of magnitude greater than bulk water. There is a growing body of experimental evidence in the literature backing this assumption [45-48]. In turn, the experimental results combined with the model developed here indirectly support the idea that the shear viscosity of water is dramatically different in a nano-confined space. Indeed, there is no other explanation for the successful operation of the membrane and absence of pore wetting without it. However, greater accuracy for both the surface hydrophobicity and shear viscosity would certainly assist in further refining the model.

4.5 Conclusions

In conclusion, a mathematical model was established both to describe the water transport in a hydrophilic, nanoporous VMD system and to understand the influence of the membrane properties on the separation performance. The model corroborates well with the experimental data considering the heat transfer and heat loss across the membrane, as well as the change of water vapour pressure with the salt concentration. Despite the conventional wisdom that a hydrophobic membrane is considered a mandatory criteria in MD, the hydrophilic nanoporous membrane studied does not exhibit any pore wetting. This is mainly attributed to the confinement effects of the nanopore channels, which have dramatically increased the shear viscous force of water with respect to the hydrophilic pore wall. The model showed how the liquid/vapour interface is formed within the nanopores due to the opposing ‘forces’ of intrusion and evaporation. Indeed, despite vast differences in salt concentration and a liquid intrusion depth of up to 470 nm, negligible internal concentration polarization is observed within the confined nanospace. Increasing the pore size slightly enhanced the permeation flux but the trade-off was the increased risk of total pore wetting of the pore channel and membrane substrate. Similarly, the model found that a thin membrane is beneficial in inducing higher flux, particularly as the greatest resistance to water permeation is the Knudsen diffusion of the water vapour through the nanochannels. Indeed, it is now possible to predict the intrusion depth using the model developed here and thereby tailor the membrane thickness to minimise this resistance. However, the more dominant factor is the heat transfer across the membrane which can be reduced by choosing to make the membrane from a material with low thermal conductivity.

Acknowledgements

The authors would like to acknowledge funding from the Australian Research Council in the form of ARC-DP 110103440. F.K. thanks NSERC (Canada) and FQRNT (Province of Québec) for the financial support. Y.C. would like to acknowledge scholarship support from The University of Queensland in the form of the UQI International Scholarship. S.S. would like to acknowledge the Queensland Government Smart Futures Fellowship. The authors also thank Diego Schmeda for the analysis of the material porosimetry. The authors acknowledge the facilities, and the scientific and technical assistance, of the Australian Microscopy & Microanalysis Research Facility at the Centre for Microscopy and Microanalysis, The University of Queensland.

Abbreviation:

CP	Concentration polarization
EDX	Energy Dispersive X-ray Spectroscopy
EISA	Evaporation-induced self-assembly
LEP	Liquid entry pressure
MD	Membrane distillation
TP	Temperature polarization
VMD	Vacuum membrane distillation

Symbols:

$C_{p,l}$	Specific heat of water, J kg^{-1} K^{-1}
D	Diffusion coefficient
H	Enthalpy, J
J_m	Mass flux kg m^{-2} s^{-1}
k_B	Boltzmann constant, m^2 kg s^{-2} K^{-1}
k_l	thermal conductivity of liquid phase, J m^{-1} s^{-1} K^{-1}
k_s	thermal conductivity of vapour and substrate
r_s	pore radius of substrate, nm
$\bar{P}$	mean pressure within the membrane pores
Q	heat loss, J m^{-2}
T	absolute temperature, K

Greek symbols:

ε	porosity of membrane
δ	thickness
τ	tortuosity of membrane pore
γ	liquid surface tension
θ	contact angle
η	viscosity
λ	mean free path
σ	collision diameter
ρ	density

Subscript:

il	interlayer
if	interface
l	liquid phase
v	vapour phase

References

[1] K.W. Lawson, D.R. Lloyd, Membrane distillation, Journal of Membrane Science, 124 (1997) 1-25.

[2] T. Humplik, J. Lee, S.C. O'Hern, B.A. Fellman, M.A. Baig, S.F. Hassan, M.A. Atieh, F. Rahman, T. Laoui, R. Karnik, E.N. Wang, Nanostructured materials for water desalination, Nanotechnology, 22 (2011) 1-19.

[3] M. Safavi, T. Mohammadi, High-salinity water desalination using VMD, Chemical Engineering Journal, 149 (2009) 191-195.

[4] M.S. El-Bourawi, Z. Ding, R. Ma, M. Khayet, A framework for better understanding membrane distillation separation process, Journal of Membrane Science, 285 (2006) 4-29.

[5] A.C.M. Franken, J.A.M. Nolten, M.H.V. Mulder, D. Bargeman, C.A. Smolders, Wetting criteria for the applicability of membrane distillation, Journal of Membrane Science, 33 (1987) 315-328.

[6] M. Khayet, Advances in Colloid and Interface Science, 164 (2011) 56-88.

[7] S. Cerneaux, I. Struzynska, W.M. Kujawski, M. Persin, A. Larbot, Comparison of various membrane distillation methods for desalination using hydrophobic ceramic membranes, Journal of Membrane Science, 337 (2009) 55-60.

[8] M. Gryta, Fouling in direct contact membrane distillation process, Journal of Membrane Science, 325 (2008) 383-394.

[9] B. Li, K.K. Sirkar, Novel membrane and device for vacuum membrane distillation-based desalination process, Journal of Membrane Science, 257 (2005) 60-75.

[10] P. Wang, M.M. Teoh, T.-S. Chung, Morphological architecture of dual-layer hollow fiber for membrane distillation with higher desalination performance, Water Research, 45 (2011) 5489-5500.

[11] Z.D. Hendren, J. Brant, M.R. Wiesner, Surface modification of nanostructured ceramic membranes for direct contact membrane distillation, Journal of Membrane Science, 331 (2009) 1-10.

[12] C.A. Rivier, M.C. García-Payo, I.W. Marison, U. von Stockar, Separation of binary mixtures by thermostatic sweeping gas membrane distillation: I. Theory and simulations Journal of Membrane Science, 201 (2002) 1-16.

[13] M. Khayet, T. Matsuura, Pervaporation and vacuum membrane distillation processes: Modeling and experiments, AIChE Journal, 50 (2004) 1697-1712.

[14] S. Bandini, A. Saavedra, G.C. Sarti, Vacuum membrane distillation: Experiments and modeling, AIChE Journal, 43 (1997) 398-408.

[15] A.O. Imdakm, M. Khayet, T. Matsuura, A Monte Carlo simulation model for vacuum membrane distillation process, Journal of Membrane Science, 306 (2007) 341-348.

[16] H. Chang, J.-S. Liau, C.-D. Ho, W.-H. Wang, Simulation of membrane distillation modules for desalination by developing user's model on Aspen Plus platform, Desalination, 249 (2009) 380-387.

[17] A. Hausmann, P. Sanciolo, T. Vasiljevic, M. Weeks, M. Duke, Integration of membrane distillation into heat paths of industrial processes, Chemical Engineering Journal, 211-212 (2012) 378-387.

[18] J. Zhang, J.-D. Li, M. Duke, M. Hoang, Z. Xie, A. Groth, C. Tun, S. Gray, Modelling of vacuum membrane distillation, Journal of Membrane Science, 434 (2013) 1-9.

[19] K.W. Lawson, D.R. Lloyd, Membrane distillation. I. Module design and performance evaluation using vacuum membrane distillation, Journal of Membrane Science, 120 (1996) 111-121.

[20] A. Criscuoli, M.C. Carnevale, E. Drioli, Modeling the performance of flat and capillary membrane modules in vacuum membrane distillation, Journal of Membrane Science, 447 (2013) 369-375.

[21] K.-H. Lee, S.-T. Hwang, The transport of condensible vapors through a microporous vycor glass membrane, Journal of Colloid and Interface Science, 110 (1986) 544-555.

[22] T. Yoshioka, H. Nagasawa, M. Kanezashi, T. Tsuru, Micropore Filling Phase Permeation of a Condensable Vapor in Silica Membranes: A Molecular Dynamics Study, JOURNAL OF CHEMICAL ENGINEERING OF JAPAN, 46 (2013) 659-671.

[23] Y.T. Chua, C.X.C. Lin, F. Kleitz, X.S. Zhao, S. Smart, Nanoporous organosilica membrane for water desalination, Chemical Communications, 49 (2013) 4534-4536.

[24] D. Grosso, How to exploit the full potential of the dip-coating process to better control film formation, Journal of Materials Chemistry, 21 (2011) 17033-17038.

[25] Y. Wan, Zhao, On the Controllable Soft-Templating Approach to Mesoporous Silicates, Chemical Reviews, 107 (2007) 2821-2860.

[26] H.L. Castricum, A. Sah, R. Kreiter, D.H.A. Blank, J.F. Vente, J.E. ten Elshof, Hybrid ceramic nanosieves: stabilizing nanopores with organic links, Chemical Communications, (2008) 1103-1105.

[27] D.I. Dimitrov, A. Milchev, K. Binder, Capillary Rise in Nanopores: Molecular Dynamics Evidence for the Lucas-Washburn Equation, Physical Review Letters, 99 (2007) 054501.

[28] F. Caupin, M.W. Cole, S. Balibar, J. Treiner, Absolute limit for the capillary rise of a fluid, EPL (Europhysics Letters), 82 (2008) 56004.

[29] S. Gruener, T. Hofmann, D. Wallacher, A.V. Kityk, P. Huber, Capillary rise of water in hydrophilic nanopores, Physical Review E, 79 (2009) 067301.

[30] C. Bakli, S. Chakraborty, Capillary filling dynamics of water in nanopores, Applied Physics Letters, 101 (2012) -.

[31] D. Ortiz-Young, H.-C. Chiu, S. Kim, K. Voa-tchovsky, E. Riedo, The interplay between apparent viscosity and wettability in nanoconfined water, Nat Commun, 4 (2013) 1.

[32] C.X.C. Lin, L.P. Ding, S. Smart, J.C. Diniz da Costa, Cobalt oxide silica membranes for desalination, Journal of Colloid and Interface Science, 368 (2012) 70-76.

[33] T.-D. Li, J. Gao, R. Szoszkiewicz, U. Landman, E. Riedo, Structured and viscous water in subnanometer gaps, Physical Review B, 75 (2007) 115415.

[34] A.J. Burggraaf, Transport and separation properties of of membranes with gases and vapours, in: A.J. Burggraaf, L. Cot (Eds.) Fundamentals of Inorganic Membrane Science and Technology, Elsevier, Amsterdam, 1996, pp. 331-433.

[35] A.W. Thornton, T. Hilder, A.J. Hill, J.M. Hill, Predicting gas diffusion regime within pores of different size, shape and composition, Journal of Membrane Science, 336 (2009) 101-108.

[36] B.S. Sparrow, Empirical equations for the thermodynamic properties of aqueous sodium chloride, Desalination, 159 (2003) 161-170.

[37] R.B. Evans, G.M. Watson, E.A. Mason, Gaseous Diffusion in Porous Media. II. Effect of Pressure Gradients, The Journal of Chemical Physics, 36 (1962) 1894-1902.

[38] R.B. Evans, G.M. Watson, E.A. Mason, Gaseous Diffusion in Porous Media at Uniform Pressure, The Journal of Chemical Physics, 35 (1961) 2076-2083.

[39] X. Gao, M.R. Bonilla, J.C.D.d. Costa, S.K. Bhatia, The transport of gases in macroporous α-alumina supports, Journal of Membrane Science, 409–410 (2012) 24-33.

[40] G. Ji, G. Wang, K. Hooman, S. Bhatia, J.C. Diniz da Costa, Simulation of binary gas separation through multi-tube molecular sieving membranes at high temperatures, Chemical Engineering Journal, 218 (2013) 394-404.

[41] G. Ji, G. Wang, K. Hooman, S. Bhatia, J. da Costa, Scale-Up Design Analysis and Modelling of Cobalt Oxide Silica Membrane Module for Hydrogen Processing, Processes, 1 (2013) 49-66.

[42] M. Elma, C. Yacou, J. Diniz da Costa, D. Wang, Performance and Long Term Stability of Mesoporous Silica Membranes for Desalination, Membranes, 3 (2013) 136-150.

[43] F.P. Incropera, D.P. DeWitt, Fundamentals of heat and mass transfer, Wiley1996.

[44] R.M. de Vos, W.F. Maier, H. Verweij, Hydrophobic silica membranes for gas separation, Journal of Membrane Science, 158 (1999) 277-288.

[45] M. Antognozzi, A.D.L. Humphris, M.J. Miles, Observation of molecular layering in a confined water film and study of the layers viscoelastic properties, Applied Physics Letters, 78 (2001) 300-302.

[46] Y. Zhu, S. Granick, Viscosity of Interfacial Water, Physical Review Letters, 87 (2001) 096104.

[47] S.H. Khan, G. Matei, S. Patil, P.M. Hoffmann, Dynamic Solidification in Nanoconfined Water Films, Physical Review Letters, 105 (2010) 106101.

[48] M.P. Goertz, J.E. Houston, X.Y. Zhu, Hydrophilicity and the Viscosity of Interfacial Water, Langmuir, 23 (2007) 5491-5497.

Supplementary Information

Experimental Section

Performance test of organosilica membrane in desalination

The vacuum membrane distillation set-up comprises of a feed vessel, a peristaltic pump, a membrane module, condenser system, a vacuum pump and a data acquisition system. Feed solution under continuous stirring and heating was transferred into the tube lumen of membrane and recycled back to the vessel via the retentate line. Vacuum pressure at 1.5 kPa was applied at the shell side; permeate was collected and condensed in a cold trap. The temperature and pressure of the system were monitored by K-type thermocouples (Ø 1.5 mm) and pressure transducer (RS, -1 to 9 barG) and logged using the data acquisition (DAQ) system (Signal Express, NI).

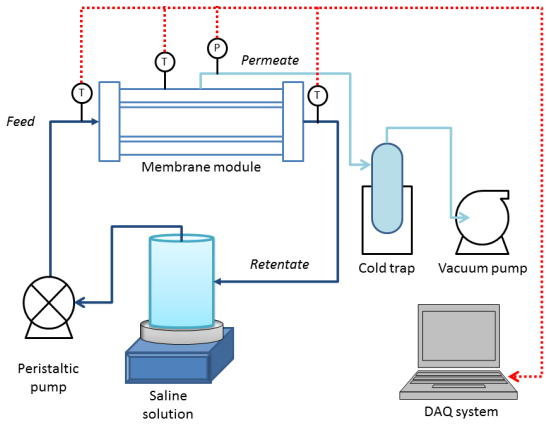

Figure S 4.1 Schematic diagram of vacuum membrane distillation test rig

Characterization

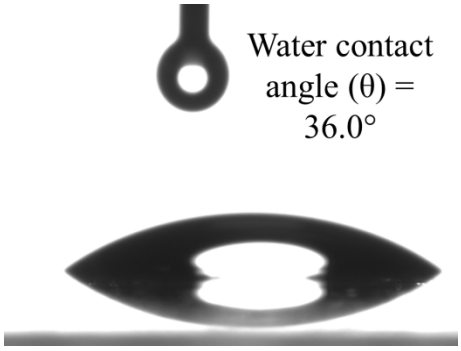

Figure S 4.2 Photographic image of water droplets on organosilica-coated glass slide.

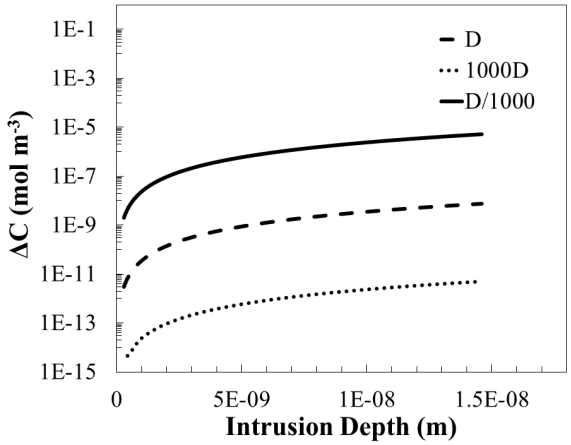

Figure S 4.3 Sensitivity analysis evaluating change in concentration inside the nanochannels by altering the diffusion coefficient and the intrusion depth.

Table S 4.1 Resistance proportion of top layer and substrate at different temperature

Resistance proportion	60 °C	40 °C	20 °C
Top layer (%)	78	77	69
Substrate (%)	22	23	31

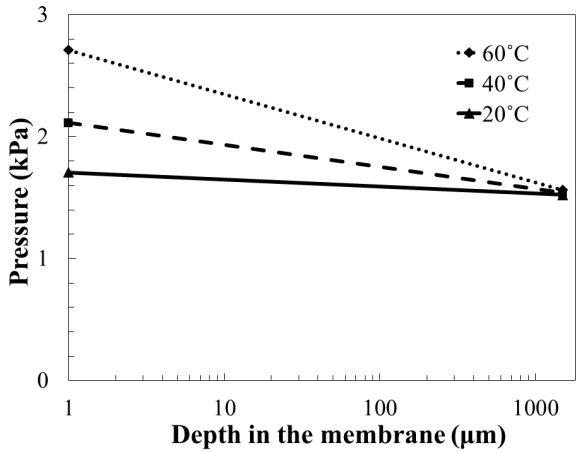

Figure S 4.4 Pressure profile within the membrane and support as a result of applied vacuum

5 Investigation on the Effect of Pore Geometry and Calcination Conditions on Membrane Performance

Introduction

The theoretical study in the previous chapter highlighted several means by which membrane properties could be altered to improve membrane flux without inducing pore wetting. This experimental chapter aims to further elucidate the effects of membranes pore geometry and their calcination conditions to membrane performance. Firstly, two surfactants of different molecular weight were employed to provide different pore sizes and pore structures. Secondly, the resultant membranes were either calcined in air or nitrogen to evaluate the role of Si-C-C-Si bonds, in particular their hydrophilicity, on the membrane performance in VMD.

Contribution

This work shows that, in accordance with literature, membrane pore size could be easily tailored by choosing surfactants of different molecular weights. Similarly, varying the calcination conditions will dictate the preservation of Si-C-C-Si bonds, suggesting that this covalent bond is very susceptible to cleavage under air calcination. Of note, however was the impact on membrane performance that these alterations to the pore size, geometry and surface chemistry had. Membranes with larger pore sizes yielded higher fluxes but the cage-like pores (arising from the use of F127 surfactant), combined with the hydrophilic surface, did not favour maintaining the liquid/vapour interface, compromising membrane stability. Secondly, neither heat treatment in air nor nitrogen fully decomposed either surfactant template, leaving some carbonaceous species on the pore wall which increased the tortuosity of the pore channel and decreased membrane flux well below theoretical predictions. The study highlighted how the model developed in the previous chapter could be improved by accommodating pore size distribution and percolation pathways to more accurately predict membrane performance. A version of this chapter has been published in Desalination as:

> Y. T. Chua, C. X. C. Lin, F. Kleitz and S. Smart, Mesoporous Organosilica Membranes: Effects of Pore Geometry and Calcination Conditions on the Membrane Distillation Performance for Desalination, Desalination, 370, 2015, 53-62.

Mesoporous Organosilica Membranes: Effects of Pore Geometry and Calcination Conditions on the Membrane Distillation Performance for Desalination

*Reproduced in part with permission from Yen Thien Chua, Chun Xiang Cynthia Lin, Freddy Kleitz and Simon Smart, *Desalination,* 370, 2015, 53-62

Abstract

Mesoporous organosilica membranes with different pore geometries and pore sizes (ranging from 2 to 12 nm) were synthesized using an evaporation induced self-assembly (EISA) method. The surfactants were removed under different calcination conditions (temperature and air/inert environment) so as to modify the surface chemistry of the final membrane. Nitrogen sorption results showed that the pore geometry and pore size of the organosilica materials could be tuned by using different types of triblock copolymer (Pluronic F68 and F127). The Si-C bond is well preserved after template removal under inert heat treatment condition, albeit a higher temperature is required for the decomposition of the polymer. However, none of the calcination conditions fully decomposed either surfactant template, leaving some carbonaceous species on the pore wall. In general, membranes with larger pore size gave higher water fluxes but the membrane stability with regards to pore wetting was suboptimal. The role of Si-C-C-Si bond and carbonized surfactant within the organosilica matrix was mainly in preventing hydrothermal degradation, but neither species significantly altered the bulk hydrophilicity/hydrophobicity of the membrane.

Keywords: Periodic organosilica membrane; mesoporous; pore geometry; membrane distillation.

5.1 Introduction

The increasing global water demand, driven by a rapid growing urbanised population and exacerbated by climate change and rising salinity levels, highlights the criticality of producing fresh water by desalination. Whilst much of this need can be met with existing reverse osmosis (RO) and thermal technologies, there is a growing interest and market for non-traditional desalination methods that can tackle unconventional waters. Membrane distillation (MD), is a

thermal based separation process driven by a vapour pressure difference across a membrane. As the push for zero-liquid discharge increases there has been a growing interest in MD for desalination due to its simple operational requirements and ability to operate under low temperatures (utilizing waste or solar heat) and low pressures [1].

MD membranes are typically porous, hydrophobic membranes that do not actively contribute to the separation process, rather the transport of vaporized water molecules through the membrane pores is governed by thermodynamics (operating temperature) and kinetic effects (diffusion of the components through the membrane) [2, 3]. As a result, most of the reported studies focus on commercially available membrane materials and the effect of membrane surface chemistry (beyond simply increasing hydrophobicity) and water affinity are rarely considered. However, the recognition that MD performance and stability (e.g. pore wetting) must improve to be commercial competitive with RO has seen a new range of membrane materials emerge including ceramics [4, 5] and carbon nanotubes [6] and morphologies [7, 8]. Of these ordered organosilica membranes have shown considerable promise [9].

Mesoporous materials [10, 11], with well-ordered pore structures of various pore geometries and synthesized from various inorganic precursors (silica, metal oxides, metals, carbon etc.), have been extensively studied over the last decades. The advantages of high porosity, surface area and narrow pore size distribution of these materials have demonstrated success in improving the performances in applications, such as adsorption [12, 13], drug delivery and catalysis [14, 15] and separation [16, 17]. Organosilica materials are hybrid organic and inorganic compounds integrated at the molecular level. They have demonstrated some fascinating properties such as morphology flexibility, versatility for different functionalities, ease of control in sol-gel synthesis and high chemical stability contributed by the inorganic silica framework [18]. Organosilica membranes and thin films are typically prepared by either co-condensation of organic containing precursor (e.g. methyltriethoxy silane, MTES) [19] with silica source (e.g. tetraethylorthosilicate, TEOS) or post-grafting of mesoporous silica [20].

Periodic mesoporous organosilica (PMO) is a well-studied subclass that is comprised of covalently-bonded organosilica scaffolds with well-distributed organic moieties within the silica matrix [21, 22]. However, despite the added versatility of an extremely narrow pore size distribution to minimise pore wetting, there have been very few applications of PMO to

membrane distillation. Previously, we showed that a PMO membrane synthesized from 1, 2-bis(triethoxysilyl) ethane (BTESE) and the non-ionic triblock copolymer surfactant Pluronic F68 gave excellent fluxes of up to 13 L m^{-2} h^{-1} across an extreme range of salt concentrations (10-150 g L^{-1} NaCl) at moderate temperatures (< 60 °C) [9]. In contrast to other MD work with inorganic materials, no concentration polarisation was observed as salt concentration increased [23, 24]. Importantly, no pore wetting was observed despite apparently possessing a hydrophilic surface, due in large part to the pore size regime used, which has opened further possibilities for PMO as MD membranes [Chapter 4]. Continuing the work from Chapter 4, we have synthesized PMO membranes of different pore sizes and geometries using triblock copolymers Pluronic F68 and F127 and evaluated their performances in vacuum membrane distillation (VMD). In contrast to the previous work we also adopted a new synthesis strategy by heat treating under both oxidising and inert atmospheres in an attempt to elucidate the impact of preserving or otherwise the Si-C bonds within the organosilica matrix.

5.2 Experimental Section

5.2.1 Preparation of periodic mesoporous organosilica membranes

The organosilica hybrid membranes were prepared via the sol-gel method under acidic conditions. First, triblock copolymer surfactant, either 0.28 g of Pluronic F68 ($PEO_{80}PPO_{30}PEO_{80}$, M_{wt} ~8,400 g $gmol^{-1}$, Aldrich) or 0.43 g Pluronic F127 ($PEO_{106}PPO_{70}PEO_{106}$, M_{wt} ~12,600 g $gmol^{-1}$, Aldrich), was dissolved in 2.8 ml ethanol and 0.01 M hydrochloric acid (HCl, 37%, Aldrich) at 35 °C under stirring for 1 hour. Then, 1.0 g of 1, 2-bis(triethoxysilyl) ethane (BTESE, 96 %, Aldrich) was added into the mixture and allowed to stir for 2 hours, giving the final molar ratio of 1 BTESE: 8.7 ethanol: 6 H_2O: 0.0022 HCl: 0.006 surfactant. The organosilica membrane was deposited by dip-coating the prepared sol on (a) glass slides (for TEM analysis) and (b) inner surface of an alumina substrate (PALL, length 100 mm, outer diameter 10 mm, thickness 1.7 mm, for desalination testing) with titania as intermediate layer (average pore size 5 nm as provided by manufacturer) at a withdrawal speed of 10 cm min^{-1} and holding time of 1 min. After dip-coating, the membrane was dried in air overnight, and then cured at 150 °C for 6 hrs for the complete cross-linking and self-assembly of the organosilica network. The remaining sol was dried on a petri dish to form a thin layer and grinded for further characterization analyses. Surfactant removal was then carried out through 2 hours heat treatment in air at 300 °C or nitrogen at 350 °C with heating rate of 1 °C min^{-1}. The

organosilica membranes obtained are denoted herein as PMO-*x*-*y*, where *x* is either 1 or 2, for Pluronic F68 and Pluronic F127, respectively, and *y* corresponds to the calcination conditions (*y* = 300A for membrane calcined in air at 300 °C and *y* = 350N for membrane pyrolysed in nitrogen at 350 °C).

5.2.2 Characterization

Transmission electron microscopy (TEM) analysis was performed by JEOL JEM-1010 and JEM-2100 electron microscopes operated at accelerating voltage of 100 kV and 200 kV, respectively. TEM sample was prepared by scraping out the calcined thin films from glass slides, and mixed with ethanol to form a slurry then dropped onto a carbon coated copper grid. Powder X-ray diffraction (PXRD) data were collected on a Bruker D8 Advance X-ray diffractometer with Cu-Kα radiation (λ = 0.154 nm). The voltage and the current were set to be 40 kV and 30 mA, respectively. The diffraction patterns were collected in the 2θ range of 0.5-10 ° at a scanning rate of 1 ° min^{-1}. Nitrogen adsorption and desorption isotherms were measured at 77K using a physisorption analyzer (Micromeritics, Tristar 3020). Prior to the adsorption measurements, the samples were outgassed under vacuum at 180 °C for 12 hr. The mean pore size and pore size distribution were calculated from the adsorption branch of the isotherm using the non-local density functional theory (NLDFT) method [25, 26]. The specific surface area was calculated by Brunauer-Emmett-Teller (BET) method at relative pressure of 0.05 – 0.2 and total pore volume was calculated by the amount of nitrogen adsorbed at P/P_0 = 0.97. ^{29}Si and ^{13}C nuclear magnetic resonance (NMR) were measured by a solid state Bruker Avance III spectrometer with a 7T (300 MHz for ^{1}H) magnet and a zirconia rotor, 4 mm, rotated at 7 kHz. Thermogravimetric analysis (TGA) was performed using a Differential Scanning Calorimeter/Thermogravimetric analyser (Mettler-Toledo, TGA/DSC 1) with a temperature ramp rate of 5 °C min^{-1} to 1,000 °C under air or nitrogen flow at 60 ml min^{-1}. The surface morphology of the calcined membrane was observed using scanning electron microscopy (SEM; JSM-6610, JEOL) in the secondary electron imaging mode with as acceleration voltage of 10 kV under high vacuum. Sessile drop contact angle measurement was performed by Dataphysics OCA20 at dosing rate of 5 μL s^{-1} and dosing volume of 1 μL.

5.2.3 Performance test of organosilica membrane in desalination

Performance tests of the organosilica membranes were conducted on a continuous flow system of vacuum membrane distillation (VMD) that consists of a feed vessel, membrane module and condenser unit. Saline solution was fed to membrane tube lumen by a peristaltic pump at a flow rate of 5 L hr^{-1} and the retentate was circulated back to the feed vessel. Vacuum (absolute pressure of 1.5 kPa) was applied at the permeate side and water vapour was condensed by coolant at - 20 °C and collected in a cold trap. Sodium chloride solution with varied concentrations (10, 35, 50, 75, 150 g L^{-1} of NaCl) was used as the feed solution to represent the range of brackish water (10 g L^{-1}), seawater (35 g L^{-1}) and brine solution (> 50 g L^{-1}) available in the natural or industrial environment. The effect of feed temperature on permeate flux was studied at 25, 40 and 60 °C. The feed and permeate conductivities were measured by a labCHEM CP conductivity meter, which was calibrated over a range of salt concentrations (0.1 to 150 g L^{-1}). The permeate flux through the membrane, F (kg m^{-2} hr^{-1}) was calculated by $F = m/A \cdot t$, where m is the mass of permeate collected, A as the membrane tube active area and t is the duration time of permeation test. Salt rejection, R (%) of the membrane was calculated by the following equation: $R = (C_f - C_p)/C_f \times 100\%$, where C_f and C_p were the feed and permeate concentrations (wt %), respectively.

5.3 Results and Discussion

5.3.1 Characterization

The low angle PXRD diffraction patterns in Figure 5.1 show that all the calcined organosilica materials exhibit only one distinct peak, with the exception of the PMO-2-350N sample which has a well-resolved peak at $2\theta = 0.56°$ and a secondary one at 1.16°. These XRD results strongly suggest that all the calcined organosilica materials had an ordered pore structure, regardless of the surfactant template or calcination conditions. Samples calcined in air did possess a smaller *d*-spacing and hence unit cell compared to those pyrolysed in nitrogen. Kleitz *et al.* found that the *d*-spacing value of SBA-3 decreased more intensely with direct calcination compared to the sample with template removal via solvent extraction prior to calcination [27]. They suggested that the lattice shrinkage might be due to either the higher effective temperature of sample (due to heat released from the exothermic surfactant decomposition reaction) compared to the bulk oven temperature or the effect of successive condensation of the framework [27]. Therefore, the

highly exothermic reactions (surfactant decomposition and Si-C cleavage) in air (as shown in DSC results in Figure 5.5) imply the rapid oxidation of surfactant in air leads to the sudden contraction and impacts the structural rearrangement of the framework.

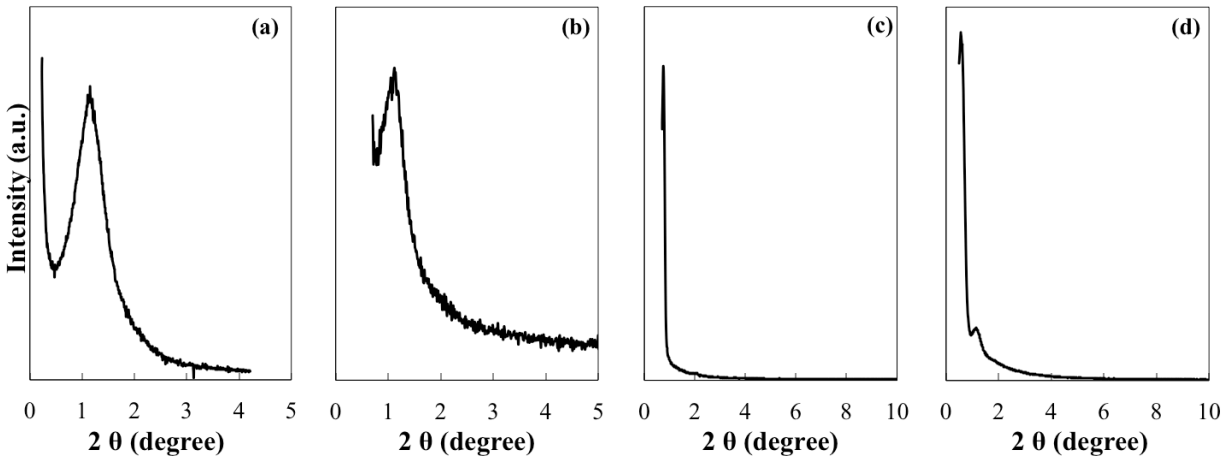

Figure 5.1 Low angle PXRD patterns of (a) PMO-1-300A, (b) PMO-1-350N, (c) PMO-2-300A and (d) PMO-2-350N.

The TEM images, shown in Figure 5.2, are in agreement with the XRD data with all samples exhibiting long range order. For samples PMO-2-300A and PMO-2-350N this took the form of cage-like cubic pores, whereas the PMO-1-300A and PMO-1-350N samples exhibited a distorted orthogonal pore structure derived from body-centered cubic geometry [9]. This is reasonable as F127 has a longer EO chain that favours aggregation into globular structures which result in larger cage-like pores [28, 29].

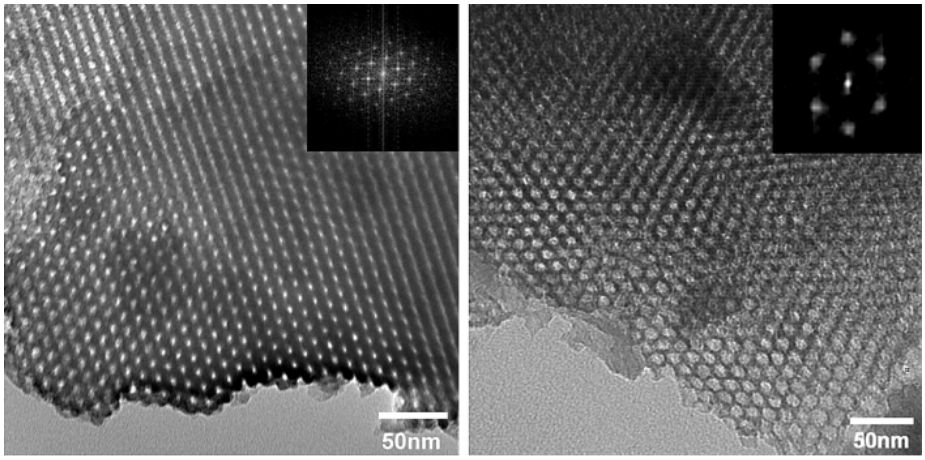

Figure 5.2 TEM images of well-ordered organosilica (left) PMO-2-300A and (right) PMO-2-350. Insets show the Fourier transform diffraction patterns.

Nitrogen physisorption isotherms of the organosilica samples are shown in Figure 5.3. The use of F68 produces an organosilica matrix with smaller pores showing a type I isotherms which is indicative of a microporous material. Organosilica materials templated with F127, however, reveal an isotherm (type IV isotherm with H2 hysteresis) similar to SBA-16 silica. This is a typical isotherm for mesostructured materials with cage-like pores of a spherical geometry. A steep capillary condensation step is observed for both samples with similar closure point of the hysteresis loop at relative pressure of $P/P_0 = 0.45$, implying the pore structure is well ordered and a good degree of uniformity of the cage dimension [28].

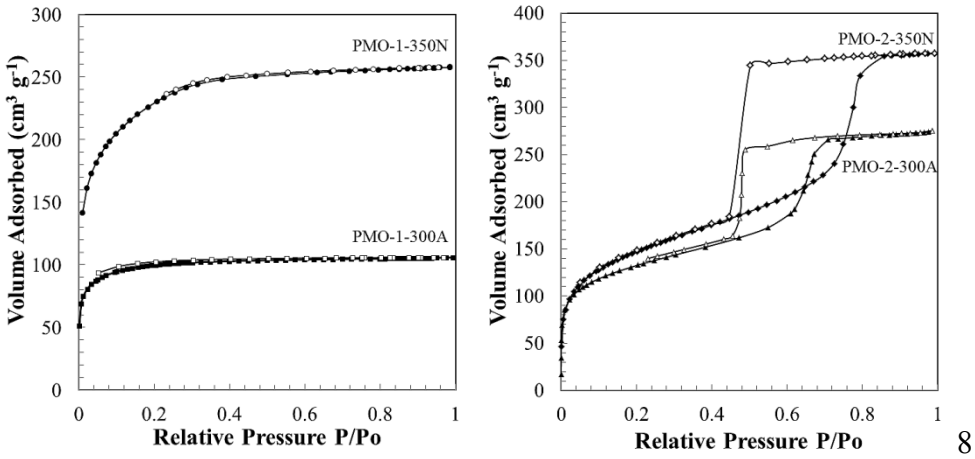

Figure 5.3 Nitrogen adsorption-desorption isotherms of (left) PMO-1-300A (square), PMO-1-350N (circle), (right) PMO-2-300A (triangle) and PMO-2-350N (diamond).

Non-local density functional theory (NLDFT) methods were employed for the characterization of gas adsorption, with calculation based on kernel for adsorption of nitrogen at -196 °C in silica with cylindrical pore geometry. The pore size distribution (PSD) (Figure 5.4 (a)) of PMO-1-300A and PMO-1-350N are centered at 2.0 nm and 2.4 nm, respectively with a fitting error below 0.434 %. In contrast to the organosilica templated with F68, PMO-2-300A and PMO-2-350N display type H2 hysteresis. In that particular case, the kernel of N_2 adsorption in spherical pore geometry (adsorption branch) had to be employed for the pore size determination. This is critical, in particular for pores with window sizes smaller than 5 nm, as the instability of the meniscus and fluid cavitation during desorption will most likely provide an unreliable window size analysis [28]. The pore size distributions were calculated based on the kernel for adsorption of nitrogen at -196 °C in silica with a combination of cylindrical and spherical pore geometry. Both PMO-2-300A and PMO-2-350N in Figure 5.4 (b) show a major peak in their pore size distribution at 9.1 and 12.9 nm and fitting error 0.63% and 0.56%, respectively.

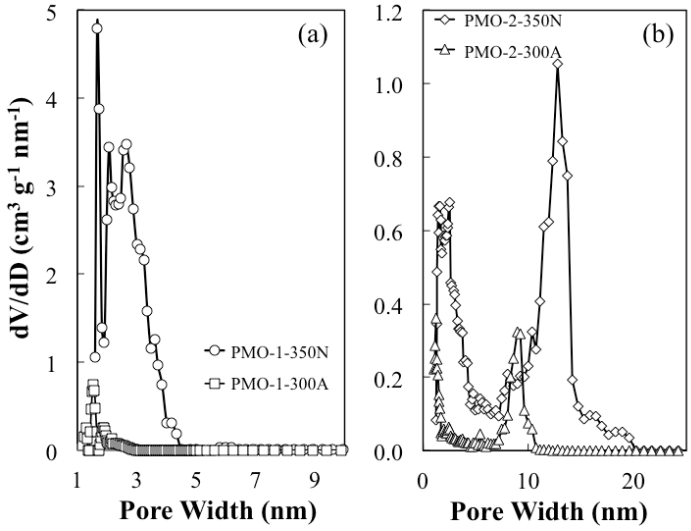

Figure 5.4 Pore size distribution (PSD) curves of the (a) PMO-1-300A (square) and PMO-1-350N (circle) calculated from the nitrogen physisorption isotherms at -196°C using the NLDFT model based on N_2 sorption in silica with cylindrical pore geometry. PSD for (b) PMO-2-300A (triangle) and PMO-2-350N (diamond) are calculated from the nitrogen physisorption isotherms at -196 °C using the NLDFT model based on N_2 adsorption in silica with combination of cylindrical and sphere pore geometry.

Table 5.1 shows the overall physicochemical properties of the organosilica materials. It is interesting to discover that samples pyrolysed in an inert environment tend to form larger pores, with higher BET surface area. In addition, there is another population of pore size within the micropore region (complementary pores), which is formed due to the removal of EO groups of the triblock copolymer after heat treatment [30]. The pore wall thickness of the organosilica materials are calculated considering cubic unit cell. PMO-1-300A and PMO-1-350N have similar pore wall thickness and they are thicker than those templated with F127. PMO-2-300A has the thinnest pore wall with thickness of 5.2 nm, led by the contraction of the entire organosilica matrix as a result of strong oxidation of the organic templating species from the hybrid mesophase precursor under high temperature and an air atmosphere.

Table 5.1 Physicochemical properties of organosilica material

Sample	S_{BET}, m^2/g	V_p, cm^3/g	D_p (NLDFT), nm	Complementary pores, nm	*d*-spacing value, nm	Unit cell, a_0, nm	Wall thickness, T_{wall}, nm

PMO-1-300A	310	0.18	2.0	-	7.6	10.7	7.3
PMO-1-350N	808	0.40	2.4	1.5	8.0	11.3	7.4
PMO-2-300A	468	0.43	9.1	1.1	11.7	16.5	5.2
PMO-2-350N	529	0.55	12.9	2.0	16.0	22.6	6.7

*Calculation method for cubic unit cell $a_0 = d \times \sqrt{2}$ and pore wall thickness $T_{wall} = \sqrt{3}a_o/2\text{-}D_p$ based on *bcc* structure [31]

The decomposition of the surfactants in air and nitrogen was investigated by thermal gravimetric analysis. Figure 5.5 shows the weight loss of the organosilica materials and the heat flow as measured by the differential scanning calorimeter (DSC). Surfactants decompose in both air and nitrogen at temperatures ranging from 150 to 400 °C. For the F68 sample calcined in air, a total weight loss of 40.7% was measured with 27.7 % loss at temperature range of 150 to 400 °C, which is greater than the weight of surfactant (21.8 %). The onset of the major weight loss occurred at 350 °C. Only one broad exothermic peak is formed at ~ 370 °C and it was therefore not possible to distinguish distinct temperatures either for the surfactant decomposition or the Si-C bond cleavage. Under nitrogen heat treatment, the F68 surfactant appeared to decompose at a higher temperature compared to oxidation in air, with the onset of major weight loss occurring at 420 °C. In this case, DSC analysis showed two distinct exothermic peaks at 367 °C which is related to the pyrolysis of the surfactant and at 460 °C related to further poly-condensation of organo-siloxane network. In comparison, the F127 surfactant decomposed at lower temperatures in both air and nitrogen atmospheres. In air, the onset of major weight loss occurred at 300 °C whilst the single exothermic peak appeared at 310 °C, although there was a small shoulder at ~ 250 °C which suggests greater demarcation of the surfactant decomposition and Si-C bond cleavage temperatures. Likewise in N_2, the onset of major weight loss occurred at 380 °C about 80 °C higher than in air. The DSC trace however was markedly different with only one exothermic peak present at 430 °C and an endothermic peak present at 390 °C which could be attributed to the removal of stronger bounded HCl, water and surfactant [27, 32], compared with the 2 exothermic peaks seen with F68. The lowered decomposition temperature is consistent with the more open pore network seen for F127 templated samples, which provides less resistance to the gaseous decomposition products as they leave the matrix. Importantly, the TGA investigation implies that the calcination temperatures chosen for this study (300 °C in air and 350 °C in N_2) do not carry significant risk of Si-C bond cleavage and should leave the organosilica network intact. On the downside, it does appear that a fraction of both surfactants

remains within their respective samples regardless of the calcination atmosphere and may contribute to lowering the pore volume available for water transport.

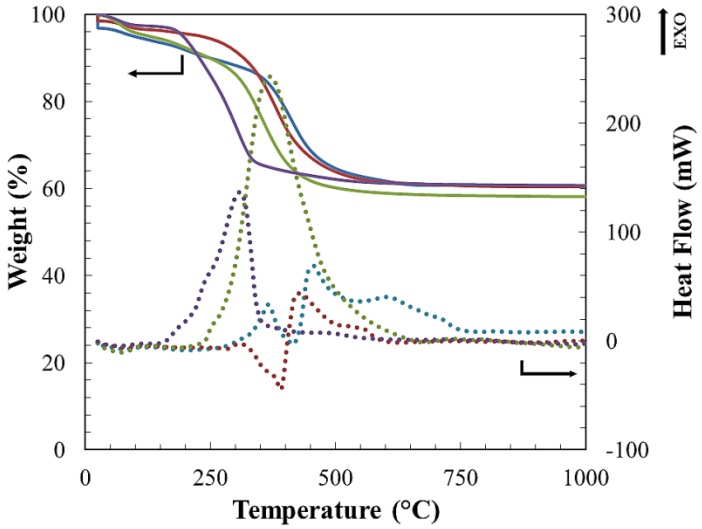

Figure 5.5 TGA/DSC curves of organosilica materials templated with F68 and F127 (solid lines correspond to TGA curves and dotted lines correspond to DSC curves) analysed in air (F68 in green and F127 in purple) and nitrogen (F68 in blue and F127 in red) environment with upward direction corresponds to exothermic peak.

The magic angle spinning nuclear magnetic resonance (MAS NMR) results show that both organic and inorganic moieties remain in the mesostructure framework (Figure 5.6). ^{13}C cross-polarization (CP) NMR spectra (Figure 5.6, left) confirmed the Si-C-C-Si bonds [33] remain in all samples either calcined in air or nitrogen with a strong resonance at 5 ppm [34]. The peaks at 60-70 ppm correspond to the carbon in the surfactants [35] corroborating the TGA evidence that the removal of surfactant from the samples by calcination is incomplete at calcination temperatures of 300-350 °C. The ^{29}Si CP-NMR spectra (Figure 5.6, right) confirmed that the Si-C bonds remain intact in all samples with a peak observed at around -62 ppm. There are three populations of trifunctional silicon species, T sites within this broad peak, with T^1 ($R'Si(OH)_2(OSi)$) at signal -51 ppm, T^2 ($R'Si(OH)(OSi)_2$) at signal -58 ppm and T^3 ($R'Si(OSi)_3$) at signal -65 ppm [33]. The T^3 species yields the major peak followed by T^2 resonance with only trace amounts of the T^1 species, indicating the higher degree of framework cross-linking. However, both samples calcined in air, PMO-1-300A and PMO-2-300A have slight cleavage of Si-C-C-Si bonds with peaks present at -101 ppm, which assigned to the presence of tetrafunctional silicon, Q species (SiO_4) [36]. This is further confirmed with the appearance of a

signal at -4.2 ppm in the ^{13}C NMR spectra which corresponds to a terminal methyl group that could result from after the cleavage of Si-C-C-Si bonds [37].

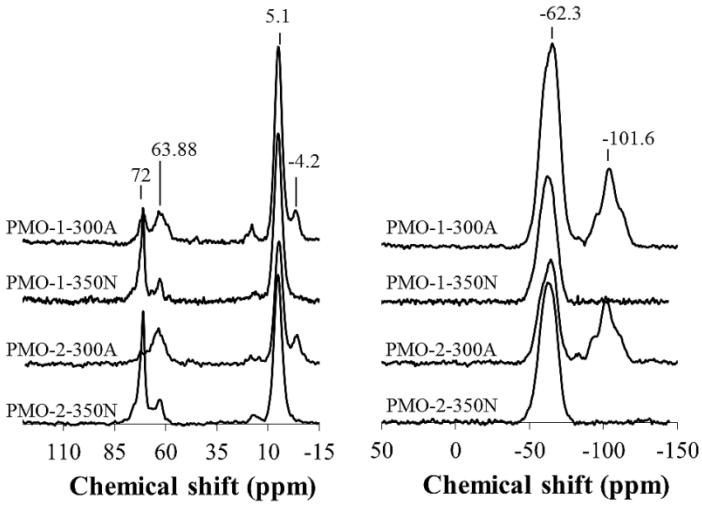

Figure 5.6 ^{13}C CP MAS NMR (left) and ^{29}Si MAS NMR (right) spectra of organosilica materials (from top to bottom) PMO-1-300A, PMO-1-350N, PMO-2-300A and PMO-2-350N.

The morphology of the organosilica membranes were examined using SEM as shown in Figure 5.7. The substrate is an asymmetric ceramic tube consisting of an α-alumina support and titania interlayer. Uniform, defect free membrane layers can be clearly observed on the titania interlayers, without any visible infiltration into the substrate layer. The average thickness of the organosilica membrane is about 1 µm as measured from the SEM image (Inset, Figure 5.7).

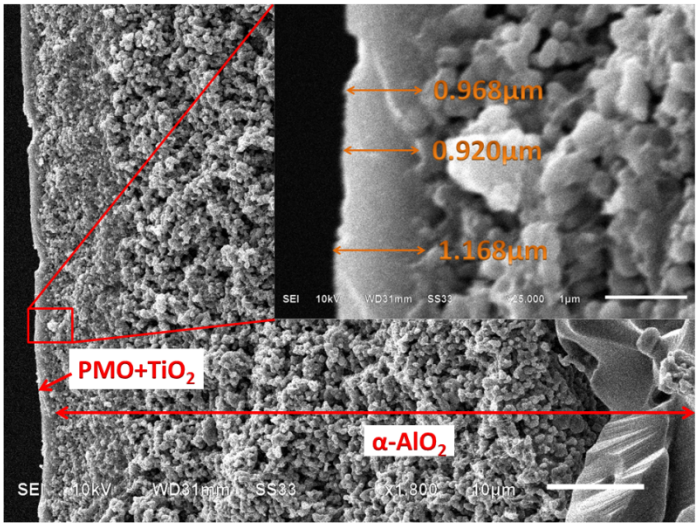

Figure 5.7 SEM image of the cross-sectional view of the organosilica membrane (PMO-1-350N) and alumina substrate with titania interlayer. Inset shows the organosilica membrane as active skin with average thickness of ~1 µm.

The contact angle measurement (Figure 5.8) was performed to give a preliminary idea if the heat treatment under an inert environment altered the hydrophobicity of the organosilica membrane materials. The contact angle was increased by ~ 35-40 % for both F68 and F127 templated organosilica films when the calcination atmosphere was replaced with nitrogen. It is interesting to observe that the thin films are macroscopically hydrophilic in comparison to conventionally MD membranes. However, it is important to note that this method is only suitable for determining the macroscopic surface hydrophobicity and may not be representative of the surface chemistry within the pore channels.

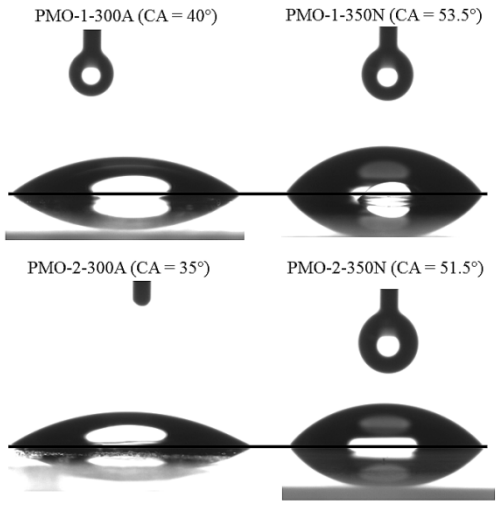

Figure 5.8 Contact angle (CA) for one layer of organosilica films coated on glass slides.

5.3.2 Membrane performance

Membrane performance is commonly evaluated based on the permeating water flux and the salt rejection. However, the ability of the membrane to maintain a liquid/vapour interface (i.e. avoid pore wetting) is another important factor in the membrane distillation process. Figure 5.9 shows the overall performances of PMO-1-300A, PMO-1-350N, PMO-2-300A and PMO-2-350N as tested for pure water and a synthetic saline (NaCl) solution of 10 and 35 g L^{-1} at feed water temperatures of 20 to 60 °C. Throughout the performances tests of all membranes, the salt rejection was 99.9 % for all membranes which agrees well with the theoretical MD rejection. There is no significant difference in membrane performance at ambient temperature; regardless of the templating surfactant or calcination atmosphere. However, at higher feed water temperatures, and therefore higher driving force, the effect of pore size becomes more significant.

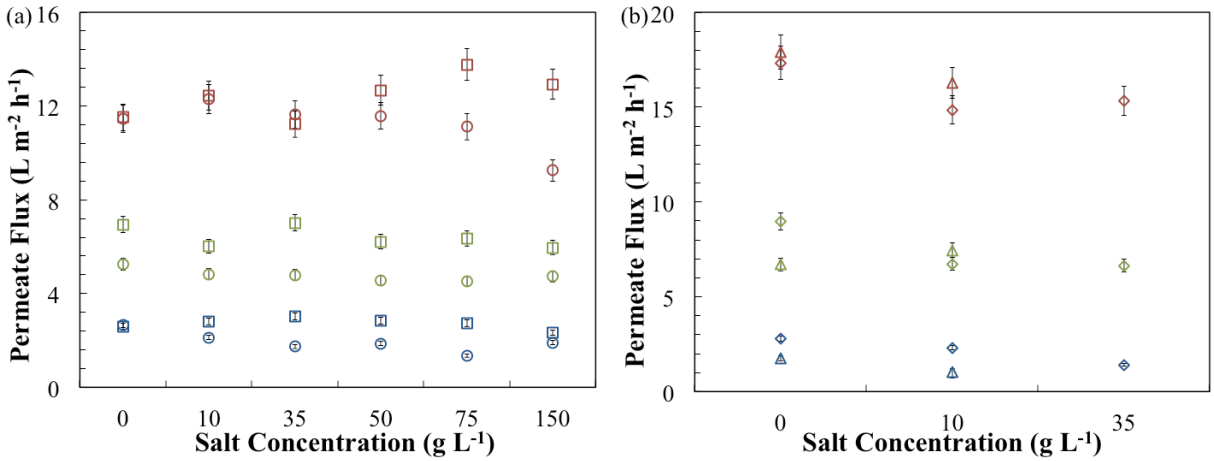

Figure 5.9 Comparison of water permeation fluxes of organosilica membranes (a) PMO-1-300A (square) and PMO-1-350N (circle); (b) PMO-2-300A (triangle) and PMO-2-350N (diamond) tested in pure water (0 g L^{-1}) and NaCl solution (10-150 g L^{-1}) at feed temperatures of 20 °C (blue), 40 °C (green) and 60 °C (red).

Membranes templated with F68 have similar permeation fluxes for pure water regardless of the calcination atmosphere, although as the salt feed concentration increases the PMO-1-300A membrane frequently has a greater flux than the PMO-1-350N membrane. These results are counterintuitive when considering the pore size analysis in Table 5.1, where the PMO-1-350N sample has both a wider pore size and larger pore volume than the PMO-1-300A membrane. On the other hand, the contact angle is more hydrophobic for the PMO-1-350N sample, which can in theory, act to counterbalance the larger, more open pore network to some extent. The models of different pore geometries are illustrated in Figure 5.10, comparing the cubic pore network and large cage-like pore network of sample PMO-1-300A/350N and PMO-2-300A/350N, respectively. Applying all these parameters to our previously established model [see Chapter 4] we obtain a predicted flux for the PMO-1-350N samples that is approximately twice that of the PMO-1-300A membrane (Figure 10). Instead the experimentally determined flux is in average 6 % smaller than the PMO-1-300A membrane across the range of feed water temperatures and salt concentrations tested. There several possible explanations for the lack of agreement between the theoretical model and the experimental results. Firstly, the average pore size and pore volume determined by sorption analysis provides no indication of the tortuosity of the material in question. It is clear from the NMR and TGA analysis that some of the carbonised surfactant remains in the pore network of the PMO-1-350N sample, which may impact on the percolation pathway for a permeating water molecule (Figure 5.10a). This is not the case for the PMO-1-

300A membrane where the surfactant is removed through oxidation in air (Figure 5.10c). Utilising the theoretical model, the tortuosity would need to approximately double to offset the larger pore size and greater pore volume. Secondly, the pore size analysis is not able to determine the location of the complementary pores which may serve to act as bottlenecks in the larger PMO network (Figure 5.10c). Thirdly, the model considers only an average pore size and not a pore size distribution, which given the dramatic differences in Figure 5.4 is clear and area for future model development, although it remains outside the scope of this study. Lastly, the sorption analysis is conducted on powdered xerogels which may have different structures to the final membrane, although in such analyses the trends tend to remain even if the absolute values are not comparable [38].

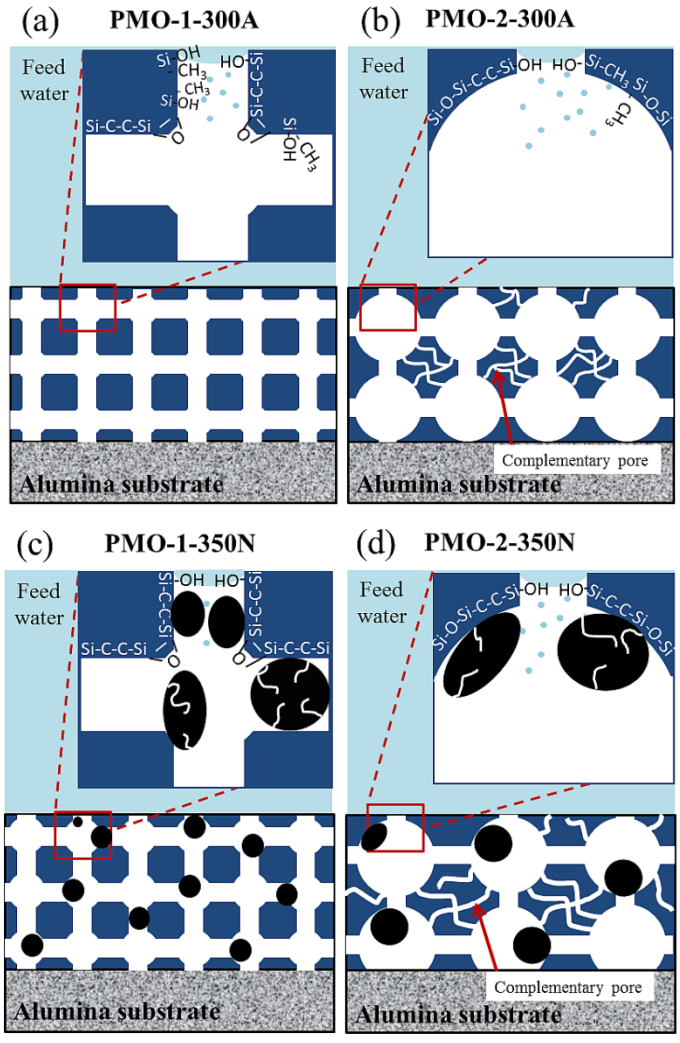

Figure 5.10 Pore structure for PMO-1-300A/350N and PMO-2-300A/350N with white colour area as pores network, bottom area represents the porous alumina substrate. Insets show the liquid/vapour interface at the pore entrance and the evaporation of water to water vapour molecules (blue spheres), both PMO-1-350N and PMO-2-350N have some remaining carbonized surfactant on pore walls with micropores (dark patches).

For membranes templated with the larger F127 triblock copolymer, greater permeating water flux was observed at temperatures of 40 and 60 °C. For pure water the PMO-2-300A membrane showed significant improvement (55 % greater water flux) over those obtained by other membranes at a feed temperature of 60 °C. This flux, however, dropped 9.1 % when it was tested in NaCl solution of 10 g L^{-1}. The flux decay continued until salt formation was observed on permeate side of the membrane at NaCl > 35 g L^{-1}, which indicates the occurrence of pore wetting in this membrane. Similarly, the PMO-2-350N membrane experienced pore wetting for salt feed concentrations > 35 g L^{-1}. As shown in Figure 5.10b, PMO-2-300A has the largest pore size, the highest pore volume and the thinnest pore walls, all of which suggest a shorter pathway that bridges two cages and a window that it too wide to maintain a liquid/vapour interface. Combined with the higher water affinity provided by its more hydrophilic surface, this all serves to increase the risk of rupture of the liquid/vapour interface, allowing the saline solution to flow into the pore network. The flux decay of PMO-2-300A could be attributed to the instability of its liquid/vapour interface, in which water intrusion into the pore channels occurs and due to the cage-like pore structure, the preservation of the liquid/vapour interface becomes more complex. Further, the continuing evaporation of water leaves behind non-volatile salt particles, which accumulate in the pores, decreasing flux and membrane performance.

5.4 Conclusions

Organosilica membranes were successfully synthesized by using triblock copolymer Pluronic F68 and F127 to yield different pore sizes, ranging from 2 – 10 nm, and pore geometries, cubic and cage-like cubic mesophases, respectively. The surface chemistry of the organosilica membranes heat treated under different atmospheres was slightly altered, and it was confirmed that calcination in air will inevitably lead to some cleavage of Si-C bonds. However, neither heat treatment fully decomposed either surfactant template, leaving some carbonaceous species on the pore wall which in the case of the PMO-1-350N and PMO-2-350N samples increased the tortuosity of the pore channel and decreased membrane flux. F127 templated membranes possessed larger pore sizes which yielded higher fluxes but the cage-like pores, combined with the hydrophilic surface, did not favour in maintaining the liquid/vapour interface, compromising membrane stability. Indeed, salt deposits on the permeate side of membrane surface at higher feed saline concentrations suggest the PMO-2 series of organosilica membranes possess a much

larger risk of pore wetting. Therefore the membrane properties and surface chemistry need to be well designed and balanced to ensure a high permeation flux, perfect salt rejection and no pore wetting within the system.

Acknowledgement

The authors would like to acknowledge funding from the Australian Research Council projects ARC-DP 110103440. Y.C. would like to acknowledge The University of Queensland for providing an UQI International Scholarship. F.K. acknowledges financial support from the Natural Sciences and Engineering Research Council of Canada (NSERC). S.S. would like to acknowledge the Queensland Government Smart Futures Fellowship. The authors acknowledge the facilities, and the scientific and technical assistance, of the Australian Microscopy & Microanalysis Research Facility at the Centre for Microscopy and Microanalysis, and Dr Ekaterina Strounina for the ^{29}Si and ^{13}C NMR technical help from the Centre of Advanced Imaging, The University of Queensland.

Abbreviation

EISA	Evaporation induced self-assembly
NLDFT	Non-local density functional theory
PMO	Periodic mesoporous organosilica
SEM	Scanning electron microscopy
TEM	Transmission electron microscopy
TGA	Thermal gravimetric analysis
VMD	Vacuum membrane distillation
VLE	Vapour liquid equilibrium
XRD	X-ray diffraction

References

[1] S. Al-Obaidani, E. Curcio, F. Macedonio, G. Di Profio, H. Al-Hinai, E. Drioli, Potential of membrane distillation in seawater desalination: Thermal efficiency, sensitivity study and cost estimation, Journal of Membrane Science, 323 (2008) 85-98.

[2] M. Khayet, Advances in Colloid and Interface Science, 164 (2011) 56-88.

[3] C.A. Rivier, M.C. García-Payo, I.W. Marison, U. von Stockar, Separation of binary mixtures by thermostatic sweeping gas membrane distillation: I. Theory and simulations Journal of Membrane Science, 201 (2002) 1-16.

[4] S. Cerneaux, I. Struzynska, W.M. Kujawski, M. Persin, A. Larbot, Comparison of various membrane distillation methods for desalination using hydrophobic ceramic membranes, Journal of Membrane Science, 337 (2009) 55-60.

[5] A. Larbot, L. Gazagnes, S. Krajewski, M. Bukowska, K. Wojciech, Water desalination using ceramic membrane distillation, Desalination, 168 (2004) 367-372.

[6] L.F. Dumée, K. Sears, J. Schütz, N. Finn, C. Huynh, S. Hawkins, M. Duke, S. Gray, Characterization and evaluation of carbon nanotube Bucky-Paper membranes for direct contact membrane distillation, Journal of Membrane Science, 351 (2010) 36-43.

[7] R. Thomas, E. Guillen-Burrieza, H.A. Arafat, Pore structure control of PVDF membranes using a 2-stage coagulation bath phase inversion process for application in membrane distillation (MD), Journal of Membrane Science, 452 (2014) 470-480.

[8] P. Peng, A.G. Fane, X. Li, Desalination by membrane distillation adopting a hydrophilic membrane, Desalination, 173 (2005) 45-54.

[9] Y.T. Chua, C.X.C. Lin, F. Kleitz, X.S. Zhao, S. Smart, Nanoporous organosilica membrane for water desalination, Chemical Communications, 49 (2013) 4534-4536.

[10] C.T. Kresge, M.E. Leonowicz, W.J. Roth, J.C. Vartuli, J.S. Beck, Nature, 359 (1992) 710-712.

[11] J.S. Beck, J.C. Vartuli, W.J. Roth, M.E. Leonowicz, C.T. Kresge, K.D. Schmitt, C.T.-W. Chu, D.H. Olson, E.W. Sheppard, S.B. McCullen, J.B. Higgins, J.L. Schlenker, A new family of mesoporous molecular sieves prepared with liquid crystal templates, J. Am. Chem. Soc., 114 (1992) 10834-10843.

[12] P.J. Lebed, J.-D. Savoie, J. Florek, F. Bilodeau, D. Larivière, F. Kleitz, Large pore mesostructured organosilica-phosphonate hybrids as highly efficient and regenerable sorbents for uraniium sequestration, Chemistry of Materials, 24 (2012) 4166-4176.

[13] Z. Sun, Y. Deng, J. Wei, D. Gu, B. Tu, D. Zhao, Hierarchically ordered macro-/mesoporous silica monolith: Tuning macropore entrance size for size-selective adsorption of proteins, Chemistry of Materials, 23 (2011) 2176-2184.

[14] J. Shang, W. Li, Y. Zhu, Structure and photocatalytic characteristics of TiO2 film photocatalyst coated on stainless steel webnet, Journal of Molecular Catalysis A: Chemical, 202 (2003) 187-195.

[15] Y. Li, Z.-Y. Fu, B.-L. Su, Hierarchically structured porous materials for energy conversion and storage, Advanced Functional Materials, 22 (2012) 4634-4667.

[16] B. Platschek, A. Keilbach, T. Bein, Mesoporous structures confined in anodic alumina membranes, Advanced Materials, 23 (2011) 2395-2412.

[17] P. Kumar, V.V. Guliants, Microporous and Mesoporous Materials, 132 (2010) 1-14.

[18] N. Mizoshita, T. Tani, S. Inagaki, Syntheses, properties and applications of periodic mesoporous organosilicas prepared from bridged organosilane precursors, Chemical Society Reviews, 40 (2011) 789-800.

[19] B. Smarsly, G. Xomeritakis, K. Yu, N. Liu, H. Fan, R.A. Assink, C.A. Drewien, W. Ruland, C.J. Brinker, Microstructural characterization of polystyrene-block-poly(ethylene oxide)-templated silica films with cubic-ordered spherical mesopores, Langmuir, 19 (2003) 7295-7301.

[20] A. Calvo, M. Joselevich, G.J.A.A. Soler-Illia, F.J. Williams, Chemical reactivity of amino-functionalized mesoporous silica thin films obtained by co-condensation and post-grafting routes, Microporous and Mesoporous Materials, 121 (2009) 67-72.

[21] Ö. Dag, C. Yoshina-Ishii, T. Asefa, M.J. MacLachlan, H. Grondey, N. Coombs, G.A. Ozin, Oriented periodic mesoporous organosilica (PMO) film with organic functionality inside the channel walls, Advanced Functional Materials, 11 (2001) 213-217.

[22] S.S. Park, C.-S. Ha, High-quality free-standing and oriented periodic mesoporous organosilica films grown without a solid substrate at the air-water interface, Chemical Communications, 0 (2004) 1986-1987.

[23] C.X.C. Lin, L.P. Ding, S. Smart, J.C. Diniz da Costa, Cobalt oxide silica membranes for desalination, Journal of Colloid and Interface Science, 368 (2012) 70-76.

[24] M. Elma, C. Yacou, J. Diniz da Costa, D. Wang, Performance and Long Term Stability of Mesoporous Silica Membranes for Desalination, Membranes, 3 (2013) 136-150.

[25] F. Kleitz, F.o. Bérubé, R.m. Guillet-Nicolas, C.-M. Yang, M. Thommes, Probing Adsorption, Pore Condensation, and Hysteresis Behavior of Pure Fluids in Three-Dimensional Cubic Mesoporous KIT-6 Silica, The Journal of Physical Chemistry C, 114 (2010) 9344-9355.

[26] M. Thommes, Physical Adsorption Characterization of Nanoporous Materials, Chemie Ingenieur Technik, 82 (2010) 1059-1073.

[27] F. Kleitz, W. Schmidt, F. Schüth, Calcination behavior of different surfactant-templated mesostructured silica materials, Microporous and Mesoporous Materials, 65 (2003) 1-29.

[28] F. Kleitz, T. Czuryszkiewicz, L.A. Solovyov, M. Lindén, X-ray structural modeling and gas adsorption analysis of cagelike SBS-16 silica mesophases prepared in a F127/Butanol.H2O system, Chemistry of Materials, 18 (2006) 5070-5079.

[29] F. Kleitz, T.-W. Kim, R. Ryoo, Phase Domain of the Cubic Im3̄m Mesoporous Silica in the EO106PO70EO106−Butanol−H2O System, Langmuir, 22 (2005) 440-445.

[30] A. Galarneau, H. Cambon, F. Di Renzo, R. Ryoo, M. Choi, F. Fajula, Microporosity and connections between pores in SBA-15 mesostructured silicas as a function of the temperature of synthesis, New Journal of Chemistry, 27 (2003) 73-79.

[31] P.I. Ravikovitch, A.V. Neimark, Density Functional Theory of Adsorption in Spherical Cavities and Pore Size Characterization of Templated Nanoporous Silicas with Cubic and Three-Dimensional Hexagonal Structures, Langmuir, 18 (2002) 1550-1560.

[32] J. Ryczkowski, J. Goworek, W. Gac, S. Pasieczna, T. Borowiecki, Temperature removal of templating agent from MCM-41 silica materials, Thermochimica Acta, 434 (2005) 2-8.

[33] S. Inagaki, S. Guan, Y. Fukushima, T. Ohsuna, O. Terasaki, Novel mesoporous materials with a uniform distribution of organic groups and inorganic oxide in their frameworks, Journal of the American Chemical Society, 121 (1999) 9611-9614.

[34] Y. Lu, H. Fan, N. Doke, D.A. Loy, R.A. Assink, D.A. LaVan, C.J. Brinker, Evaporation-induced self-assembly of hybrid bridged silsesquioxane film and particulate mesophases with integral organic functionality, J. Am. Chem. Soc., 122 (2000) 5258-5261.

[35] T. Asefa, M.J. MacLachlan, N. Coombs, G.A. Ozin, Periodic mesoporous organosilicas with organic groups inside the channel walls, Nature, 402 (1999) 867-871.

[36] M. Ide, M. El-Roz, E. De Canck, A. Vicente, T. Planckaert, T. Bogaerts, I. Van Driessche, F. Lynen, V. Van Speybroeck, F. Thybault-Starzyk, P. Van Der Voort, Quantification of silanol sites for the most common mesoporous ordered silicas and organosilicas: total versus accessible silanols, Physical Chemistry Chemical Physics, 15 (2013) 642-650.

[37] T. Asefa, M.J. MacLachlan, H. Grondey, N. Coombs, G.A. Ozin, Metamorphic channels in periodic mesoporous methylenesilica, Angewandte Chemie International Edition, 39 (2000) 1808-1811.

[38] C.J. Brinker, A.J. Hurd, P.R. Schunk, G.C. Frye, C.S. Ashley, Review of sol-gel thin film formation, Journal of Non-Crystalline Solids, 147-148 (1992) 424-436.

Supplementary Information

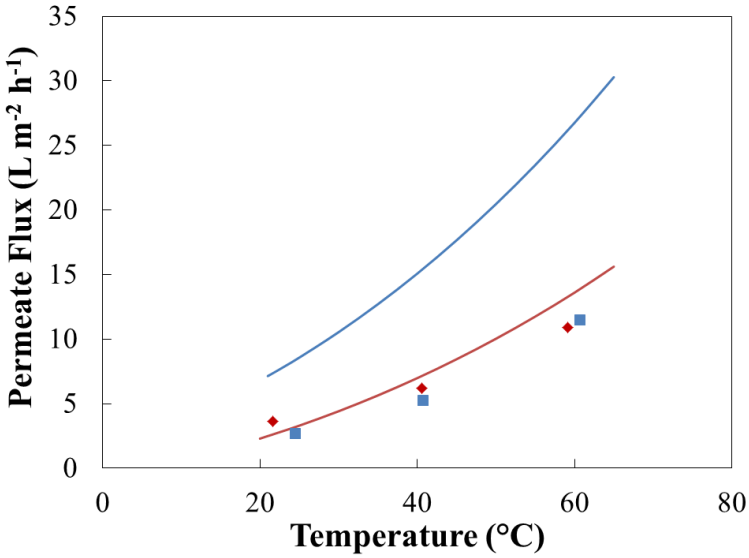

Figure S 5.1 Comparison of experimental (symbols) and calculated (solid lines) water permeate flux by using mathematical model for PMO-1-300A (red) and PMO-1-350N (blue)

6 SYNTHESIS OF MESOPOROUS CARBON-SILICA NANOCOMPOSITE MEMBRANES USING A TRI-CONSTITUENT CO-ASSEMBLY METHOD

Introduction

Building on the lessons learned in the previous chapter around membrane pore size, geometry and surface chemistry, this study reports on a different strategy to produce hybrid organic-inorganic membranes. In the organosilica membranes described in Chapters 3-5, the carbon is covalently bonded with silicon and homogeneously embedded in the membrane matrix, and the option for altering the material hydrophobicity is limited. The new strategy physically blended two separate sols, of organic and inorganic precursors, which could be mixed homogeneously at molecular level, without chemical bonding between them. The subsequent membranes were characterized and their performance evaluated under VMD.

Contribution

The work demonstrates that the modified triconstituent co-assembly method is a viable synthesis route in producing mesoporous carbon-silica nanocomposite membranes. One of the major findings is the understanding of the evolution of carbon and silica species with carbonization temperature, which was studied by using FTIR and ^{29}Si NMR methods. In particular, the evolution of the surface chemistry over temperature range of 600 to 900 °C, i.e. carbonization, proved counterintuitive with a decrease in the degree of silica condensation. This arose from the resorcinol-formaldehyde polymer releasing hydroxyl groups that in turn attack the adjacent siloxane bonds and consequently, reduces the silica condensation degree with more associated geminal and single silanols. Membranes performance was comparable with the organosilica membrane in Chapter 3-5, suggesting that the carbon-silica nanocomposite membranes are suitable for MD. This work is published in Journal of Material Chemistry A as:

> Y. T. Chua, C. X. C. Lin, F. Kleitz and S. Smart, Synthesis of Mesoporous Carbon-silica Nanocomposite Membranes using a Triconstituent Co-assembly Method, Journal of Materials Chemistry A, 3, 2015, 10480-10491.

Synthesis of mesoporous carbon-silica nanocomposite membranes using a triconstituent co-assembly method

*Reproduced in part with permission from Yen Thien Chua, Chun Xiang Cynthia Lin, Freddy Kleitz and Simon Smart, *Journal of Materials Chemistry A*, 3, 2015, 10480-10491.

Abstract

A direct synthesis method is introduced to prepare mesoporous carbon-silica nanocomposite (CSN) membranes. Unlike the intricate and expensive nanocasting method, this triconstituent co-assembly method is a one-pot synthesis method using Pluronic F127 as templating agent with a hybrid organic-inorganic matrix formed by tetraethylorthosilicate (TEOS), resorcinol and formaldehyde. The silica content is varied in the polymer solution to investigate the material properties, stability of the nanocomposite mesostructured and membrane performance in vacuum membrane distillation (VMD). The CSN materials are carbonised under nitrogen at temperatures of 600-900 °C without any significant lattice shrinkage, demonstrating excellent stability. They possess a highly ordered pore structure with moderate BET surface area (430-550 m^2 g^{-1}) and narrow pore size distribution at around 5.5-7.6 nm. The NLDFT model provides a better fit for the pore size calculation suggesting that the pore wall of the CSN may enriched with silica rather than carbon. Based on the FTIR and NMR analyses, there is no covalent bond between the carbon and silica networks, but the carbon compound was counterintuitively found to affect the condensation degree of the silica. Raising the temperature from 700 to 900 °C leads to further condensation of the carbon network, which in turn releases hydroxyl or water groups that inadvertently attack the adjacent siloxane bond. The CSN membranes performed well in VMD with water permeation flux up to 12 L m^{-2} h^{-1} and salt rejection > 99 %. This work shows that a different strategy of modifying silica-based membrane has been successfully applied for the desalination of saline waters through VMD.

Keywords: Carbon-silica nanocomposites, vacuum membrane distillation, tri-constituent co-assembly

6.1 Introduction

The depletion of fresh water resources through population growth, rising salinity levels and climate change impacts means that desalination becomes a critical technology to produce fresh water, not only for drinking water but also to treat water for industrial, agricultural and farming use. There are numerous mature processes (e.g. multi-flash distillation, reverse osmosis, electro-dialysis etc.) implemented at a global scale across a wide range of markets targeting different salinity, acidity and organic contaminant levels. Membrane distillation (MD) is a combination of membrane and thermal technologies wherein a porous membrane acts as a liquid entry barrier allowing only evaporating vapour to permeate. MD offers some advantages over existing RO and thermal technologies including a reduced vapour space and unit operation size and milder operating pressures [1, 2]. Further it offers the possibility of low grade heat or renewable energy [3] integration and could potentially be used to treat extreme saline waters (> 200 g L^{-1} total dissolved solids (TDS)) [4] thereby operating under zero liquid discharge regimes. Lastly, there is potentially less membrane fouling [5] due to its non-pressure driven process.

There are several criteria for the membrane design in MD; in particular, membranes with a tunable pore size, narrow pore size distribution and high hydrophobicity are frequently cited as desirable [2, 6, 7]. Whilst much of the literature and commercialisation attempts have focused on existing microfiltration (MF) or ultrafiltration (UF) membranes, newer techniques such as electrospinning [8] and modified hollow fibres [9] have continued to expand the field. Yet none have the control necessary to produce the much sought after narrow pore size distribution. By contrast, the soft-templating method is a simple and viable approach to produce organic [10-12] or inorganic membranes [13-15] with an ordered pore structure and tunable pore size. Surfactant is used as the sacrificial templating agent or porogen, and the pore size can be tailored by varying the surfactant concentration, type of surfactant, pH, or other synthesis conditions [16]. Our previous work reported that periodic mesoporous organosilica (PMO) membranes applied to a vacuum MD process proved to be quite promising, by demonstrating a water permeation flux of about 12 L m^{-2} h^{-1} at a feed water temperature of 60 °C [17]. Subsequent work demonstrated that due to the nanoporous nature of the PMO and behaviour of water in nanoconfined spaces, the hydrophobic criteria of conventional MD membranes was unnecessary [Chapter 4], although the pore size control needed to be very fine [Chapter 5]. Despite this, the presence of alkyl groups bridging two silicon atoms within the organosilica precursor was still influential in

membrane flux and was also necessary to prevent the water attack on siloxane bonds and played a significant role in prevent membrane degradation.

Another strategy for improving the stability of the silica network and control pore size and surface chemistry is to incorporate carbon into the silica network by physical blending of the carbon and silica precursors. The main advantage of using this synthesis method is the homogeneous blend of both organic and inorganic precursors without aggregation of silica nanoparticles [18] or compromising on the mechanical strength and thermal resistance [19]. In this paper, we prepared the mesoporous carbon-silica nanocomposite (CSN) membrane using a triconstituent co-assembly method adapted from the work of Zhao's [20] and Lu's [21] groups with triblock copolymer as the templating agent, TEOS as silica source and resorcinol as the carbon precursor (Figure 6.1).

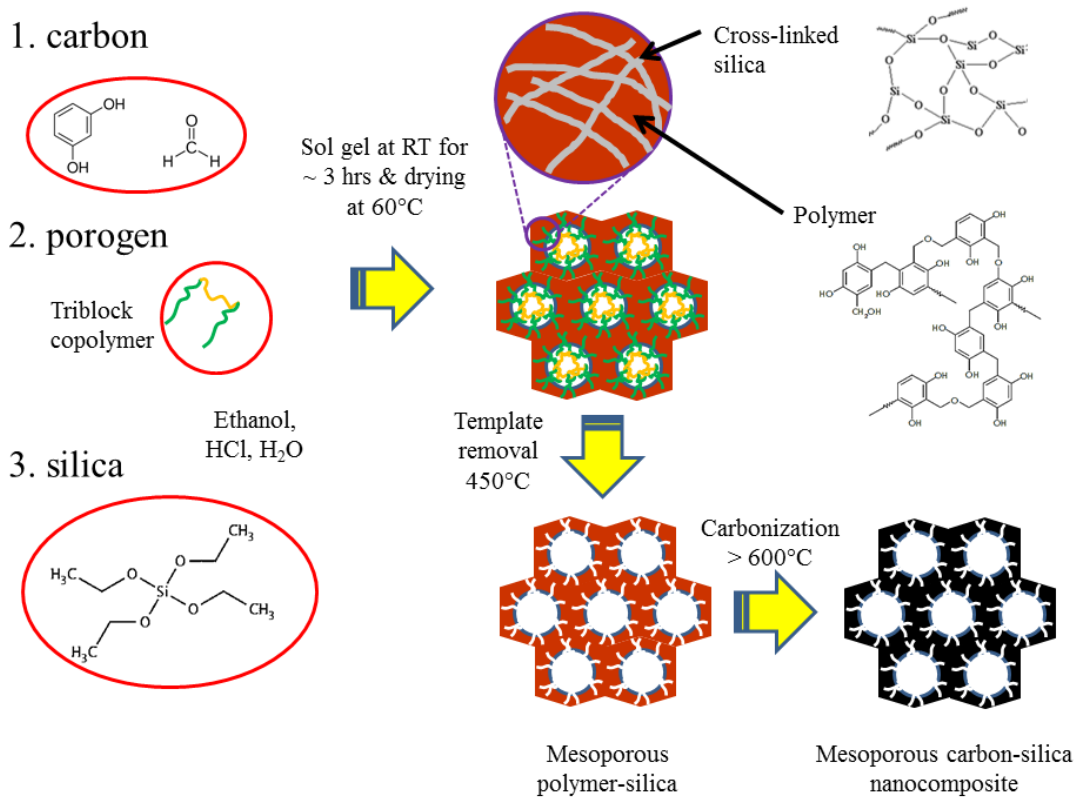

Figure 6.1 Schematic diagram of the formation of mesoporous carbon-silica nanocomposite materials using tri-constituents co-assembly method.

The advantage of this method is a better control of the pore ordering induced by the electrostatic interaction between the surfactant and polymer [22]. In order to reduce the reaction time and adapt the resulting solution for dip-coating, precursors with more hydroxyl groups, such as resorcinol ($C_6H_4(OH)_2$) and phloroglucinol ($C_6H_3(OH)_3$), as well using highly acidic solutions have been utilised to increase the polymerization rate [23, 24]. The incorporation of silica in to the carbon framework is believed to enhance the rigidity, thermal and mechanical properties of the mesostructure [25]. Liu et al. reported that there is no chemical bonding between the silicates and nanosized resols, instead they are homogeneously aggregate, intercalate and cross-linking to form a "reinforced concrete-steel" framework [20]. One of the advantages of the CSN materials is that the hydrophilic/hydrophobic balance could be easily tuned by adjusting the silica/carbon molar ratio [25, 26].

Here, we prepare mesoporous CSN membranes with varying silica content and evaluate their performance in vacuum membrane distillation (VMD) based desalination.

6.2 Experimental

6.2.1 Synthesis of carbon-silica nanocomposite

A triconstituent co-assembly method, using resorcinol, TEOS and surfactant, was applied to prepare the CSN materials following a typical sol-gel process under highly acidic conditions. First, non-ionic triblock copolymer Pluronic F127 ($PEO_{106}PPO_{70}PEO_{106}$, M_{wt} ~12,600 g $gmol^{-1}$, Aldrich) of 4.1 g was dissolved in 9 ml of ethanol and 1 ml of 0.2 M hydrochloric acid (HCl, 37 %, Aldrich) under stirring at room temperature for one hour to complete dissolution. A certain amount of TEOS was then added drop wise to the acidic ethanol solution. In the meantime, 1.1 g of resorcinol was dissolved with a mixture of ethanol and 3 M hydrochloric acid in another polypropylene bottle. After stirring for 30 mins, 1.3 g of formaldehyde was added to the resorcinol mixture with continuous stirring for 30 min to form resol solution. Finally, the resol solution was added into the copolymer mixture solution to give a final molar ratio of $C_6H_4(OH)_2$: CH_2O: TEOS: ethanol: H_2O: HCl: polymer as 1: 1.6: *x*: 19.3: 16.7: 0.62: 0.03-0.04 (where *x* represents 2.5, 3.7 and 6.2. Please refer Table S6.1, ESI). The final solution was allowed to mix under vigorous stirring for another 2 hours.

6.2.2 Preparation of mesoporous carbon-silica nanocomposite membranes

The CSN membranes were prepared by dip-coating method, which was carried out in a class 100 laminar flow cabinet to prevent dust contamination on the membrane surface. The CSN membrane was deposited onto an alumina substrate with zirconia as intermediate layer (PALL, length 100 mm, outer diameter 10 mm, thickness 1.7 mm, for desalination test) at a withdrawal speed of 10 cm min^{-1} and holding time of 1 min. After dip-coating, the membrane was dried in air and 60 °C, each time overnight, and then cured at 150 °C for 6 hrs for the complete cross-linking and self-assembly of organic-inorganic network. Subsequently, surfactant removal was conducted through heat treatment at 450 °C for 2 hours followed by carbonization for 1 hour (at various temperatures) with heating rate of 1 °C min^{-1} under nitrogen flow. The dip-coating and carbonization steps were repeated four times until the membrane is leak-proof in water test. The resulting carbon-silica nanocomposite is denoted as CSi_xY (Y is the carbonization temperature ranging from 600 to 900 °C).

6.2.3 Characterization of mesoporous carbon-silica nanocomposites

Thermal gravimetric analysis (TGA) was performed using a Differential Scanning Calorimeter/Thermogravimetric analyser (Mettler-Toledo, TGA/DSC 1). Samples were heated in a platinum pan with a temperature ramp rate of 5 °C min^{-1} to 1,000 °C under an air flow at 60 ml min^{-1}. The pore structure of the nanocomposite materials was observed using transmission electron microscopy (TEM) (JEOL, JEM-1010 and JEM-2100). TEM samples were prepared by mixing the finely ground CSi_xY samples with ethanol to form slurry, then dropped onto a carbon film coated Cu grid. Powder X-ray diffraction (PXRD) data were collected on a Bruker D8 Advance X-ray diffraction instrument (Karlsruhe, Germany) with Cu-Kα radiation (λ = 0.154 nm). The voltage and the current were set to be 40 kV and 40 mA, respectively. The diffraction patterns being collected in the 2θ range of 0.5-10 ° at a scanning rate of 1 ° min^{-1}. Nitrogen adsorption-desorption isotherms were measured at 77 K using a physisorption analyzer (Micromeritics, Tristar 3020). Prior to the adsorption measurements, the samples were outgassed under vacuum at 200 °C for 12 hr. The specific surface area was calculated by Brunauer-Emmett-Teller (BET) method at range from 0.05 to 0.2 of relative pressure. Total pore volume was obtained by the amount of nitrogen adsorbed at P/P_0 = 0.97. Cumulative pore volumes and pore size distribution were determined from the adsorption branch of the isotherm using

Quantachrome Autosorb iQ 2.02 software (Quantachrome Instruments, USA). Non-local density functional theory (NLDFT) model based on silica adsorbent with cylindrical pores and quenched solid density functional theory (QSDFT) model based on carbon with slit/cylindrical pores, were used to calculate the pore size of the materials [27]. Attenuated total reflection – Fourier transform infrared (ATR-FTIR) spectroscopy was performed using a Shimadzu IRAffinity-1 spectrometer and data was recorded in transmission mode, in the range from 4000-550 cm^{-1} and resolution of 4 cm^{-1}. Prior to FTIR measurement, the samples were dried overnight in vacuum oven at 70 °C. Peak deconvolution of the FTIR spectra was performed using Fityk software version 0.9.4 based on Gaussian fitting (R-squared equals to 0.99). Solid state cross-polarization magic-angle spinning (CP-MAS) ^{13}C nuclear magnetic resonance (NMR) spectrum and single pulse with high proton decoupling (SP-hpdec) ^{29}Si were measured by a solid state Bruker Avance III spectrometer with a 7T (300 MHz for ^{1}H) magnet and a zirconia rotor, 4 mm, rotated at 7kHz.

6.2.4 Test of membrane performance in water desalination

The performances of mesoporous CSN membranes in water desalination were assessed in a vacuum membrane distillation process. The experimental set-up included a feed vessel, peristaltic pump, membrane module, condenser unit, vacuum pump and data logging system connected to computer. The temperature of feed solution was set at 25, 40 and 60 °C and the feed water was a synthetic saline solution (NaCl) with concentrations varying from 0 to 35 g L^{-1}. The feed was introduced into membrane module at a flow rate of 5 L h^{-1} and circulated back into the feed vessel. This feed flow rate corresponded to a cross flow velocity of 1.38×10^{-6} m^3 s^{-1} and Reynolds number of 250, placing the system in the laminar flow regime. Vacuum (1.5kPa) was applied at the permeate side and water vapour was condensed and collected in the cold trap at temperature -15 °C. Each membrane was tested in pure water as a control test, followed by subsequent tests which increased the salt water feed concentration and temperature. The feed and permeate conductivities were measured by a labCHEM CP conductivity meter. Type-K thermocouples were placed in the system to measure the temperature of feed inlet, feed outlet and permeate side. The weight of permeate (m) was measured and applied in the calculation of permeate flux, J (L m^{-2} h^{-1}), in which $J = m/A \cdot t$, where A as the membrane active area and t is the duration time of the sample collected in the permeation test. Salt rejection, R (%) of the membrane was determined by $R = (C_f - C_p)/ C_f \times 100$ %, where C_f and C_p are the feed and permeate concentrations (g L^{-1}), respectively. Performances of different membranes are

compared based on the global mass transfer coefficient, C_g (L m^{-2} h^{-1} Pa^{-1}), in which $C_g = J/(P_{Tf} - P_{Tp})$, where P_{Tf} and P_{Tp} is the water partial pressure at feed side and permeate side, respectively.

6.3 Results and Discussion

Figure 6.2 presents the results of the thermal gravimetric analysis and differential scanning calorimetry (TGA/DSC) of the three CSN samples ($CSi_{2.5}$, $CSi_{3.7}$ and $CSi_{6.2}$) under an air atmosphere to a maximum temperature of 1000 °C. The major weight loss is attributed to surfactant decomposition and is observed between 400 - 600 °C. Complete combustion of the carbon above 600 °C yields the silica content. There are two main regions of activity on the DSC trace, both exothermic, which occur within the temperature regions of 200 – 400 °C and 400 – 600 °C. There mainly correspond to the removal of surfactant and the oxidation of carbonaceous material within the nanocomposite, respectively. Interestingly, instead of the expected single oxidation step for the oxidation of triblock copolymer [28], all samples present a shoulder at ~250 °C and another two peaks within the temperature of 300 – 400 °C. This suggests a multi-step degradation process for the surfactant oxidation which has been previously observed for meso and microporous materials [29]. Despite the appearance of several smaller peaks and shoulders, the main exothermic peak at ~350 °C is sharp and narrow. By contrast the final oxidation process is characterised by a series of broad peaks beyond 400 °C which suggests a complex, multi-stage process [28].

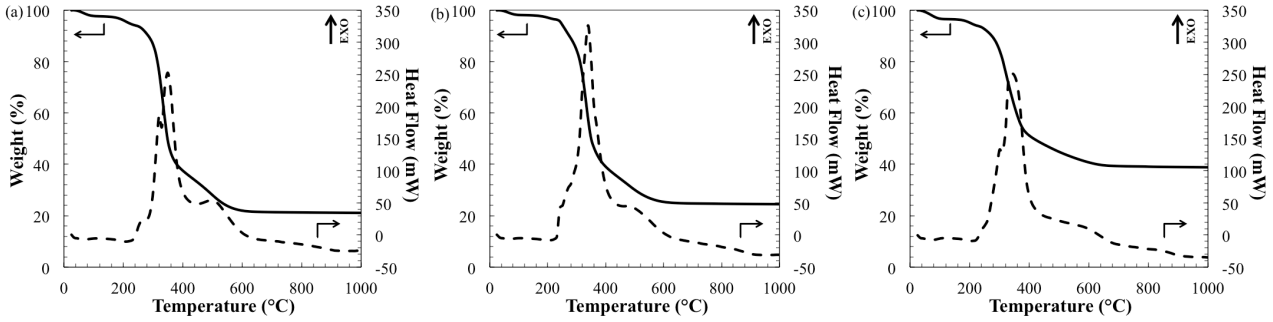

Figure 6.2 TGA/DSC curves of carbon-silica nanocomposites (a) $CSi_{2.5}$, (b) $CSi_{3.7}$ and (c) $CSi_{6.2}$ under air flow with solid lines represent the weight loss and dotted lines correspond to heat flow.

To better understand the surfactant removal process and subsequent carbonization of the resol, the three CSN samples ($CSi_{2.5}$, $CSi_{3.7}$ and $CSi_{6.2}$) were subjected to thermal gravimetric analysis and differential scanning calorimetry (TGA/DSC) under a nitrogen atmosphere to a maximum

temperature of 1000 °C. As shown in Figure 6.3, the surfactant is clearly being decomposed at higher temperature (~400 °C) which is also associated with a prominent endothermic peak on the DSC trace [30]. There is a gradual weight loss shown on the TGA curve from 600 °C onwards which is coupled with an endothermic peak in the DSC curve at around ~ 660 °C. Even though the measured heat flows here are not significantly different to those measured under an air atmosphere, it is clear that the weight loss beyond 600 °C is associated with two endothermic reactions corresponding to the cleavage of C-O bonds (200~300 kJ mol^{-1}) and C-H bonds (400~500 kJ mol^{-1}) and the formation of C-C bond [31]. In contrast to the report by Lin and Ritter that resorcinol-formaldehyde carbon xerogel did not exhibit any significant weight loss after 750 °C under N_2 flow [32], these CSN samples experienced a gradual weight loss above 600 °C, with about ~20 wt% carbon remaining within the silica framework. This additional carbon content could be associated to the densification of the carbon xerogels (cleavage of C-H bond to form C-C bond) and the continuous condensation of the silica matrix with increasing carbonization temperature, both of which may delay the carbon decomposition.

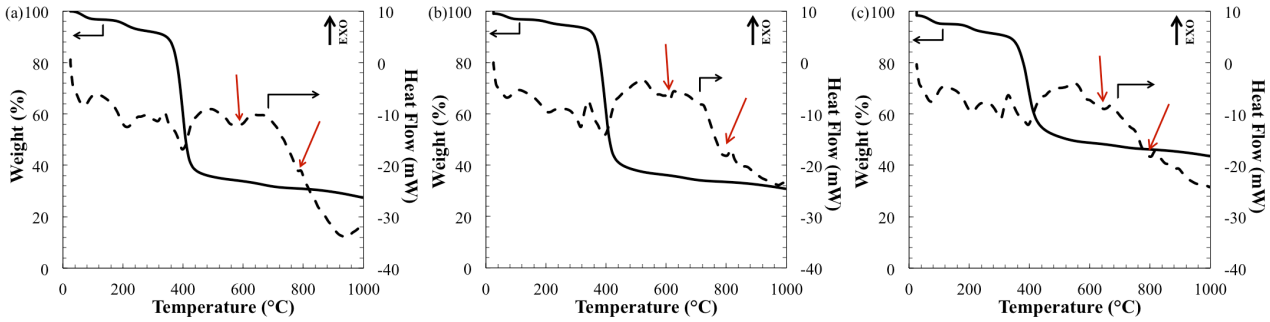

Figure 6.3 TGA/DSC curves of carbon-silica nanocomposite (a) $CSi_{2.5}$, (b) $CSi_{3.7}$ and (c) $CSi_{6.2}$ under nitrogen flow with solid lines correspond to weight loss and dotted lines correspond to heat flow.

The TEM images in Figure 6.4 demonstrate that the CSN materials maintained an ordered mesoporous pore network even at carbonization temperatures as high as 900 °C. Whilst pore size is best determined through sorption techniques, it can be clearly seen that $CSi_{3.7}700$ sample has the largest pore size (Figure 6.4e), whereas $CSi_{6.2}700$ has the smallest (Figure 6.4f). This is due to the fact that the surfactant to total precursors molar ratio double for $CSi_{3.7}700$ compared to $CSi_{6.2}700$.

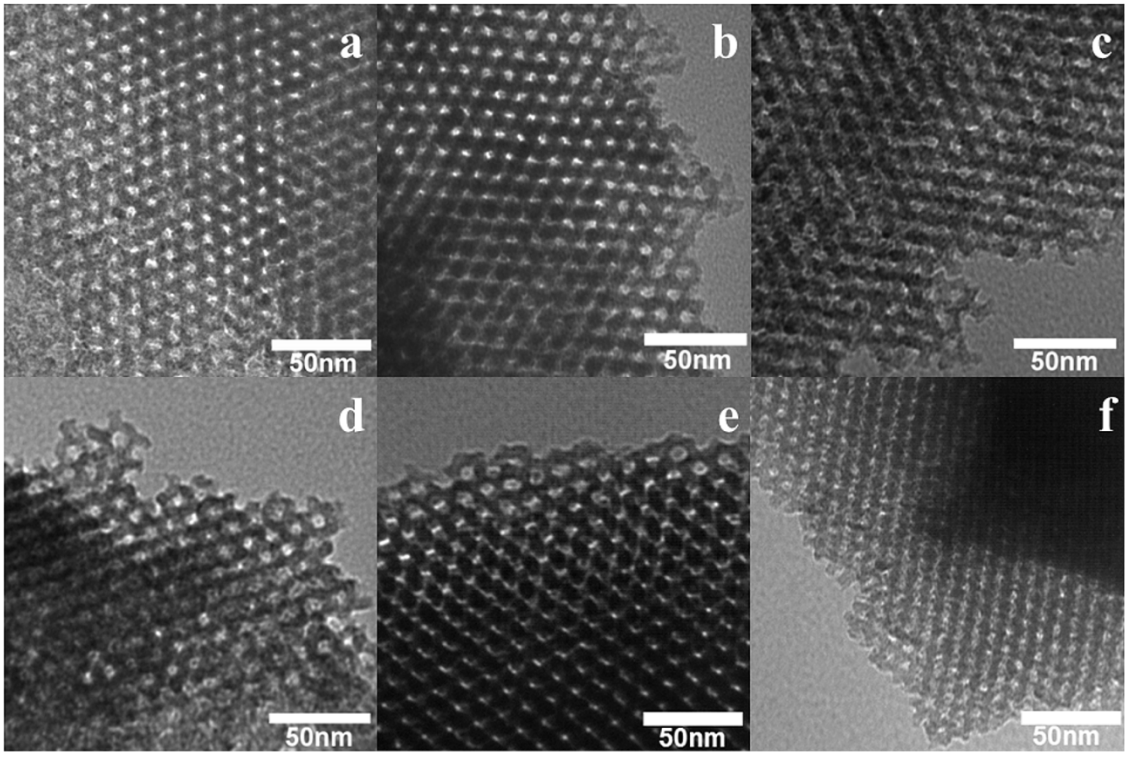

Figure 6.4 TEM images of carbon-silica nanocomposite $CSi_{2.5}$ carbonized at (a) 600, (b) 700, (c) 800 and (d) 900°C, (e) $CSi_{3.7}$700 and (f) $CSi_{6.2}$700.

Low angle powder X-ray diffraction was performed on the mesoporous CSN materials to observe their mesostructure. Figure 6.5 (a) shows the XRD plots of $CSi_{2.5}$ series that was carbonized from 600 to 900 °C. Noticeably each sample exhibits a distinct peak at the same position which corresponds to a d-spacing value, a reflection of interplanar distance, of ~ 10.5 nm. Despite the elevated temperature, the materials possess good mesostructural resilience without suffering any lattice shrinkage, which is in good agreement with the TEM results (Figure 4a-d). Both $CSi_{3.7}$700 and $CSi_{6.2}$700 exhibited higher intensity peaks at 0.83° and 0.9° 2θ, respectively, compared to $CSi_{2.5}$700 (Figure 6.5 (b)). This could be implied that silica helps in reinforcing the carbon network and maintaining the mesostructure after surfactant removal. However, in addition to demonstrating a high degree of long range order for the primary peak (same position as $CSi_{2.5}$ series) the $CSi_{3.7}$700 sample also exhibited two secondary peaks at 1.4° and 1.6° 2θ. $CSi_{6.2}$700 has the smallest lattice size given the primary peak was detected at higher 2θ, which is in agreement with the TEM analysis. The broad nature of this peak, in comparison to the sharp peak for the $CSi_{3.7}$700 sample indicates a lower degree of pore ordering. The low angle XRD results show that a higher silica content and appropriate amount of surfactant are essential in providing better ordering of the mesostructured in the CSN matrix.

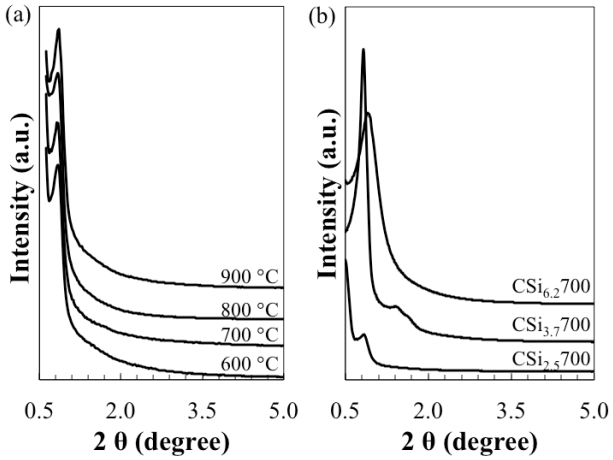

Figure 6.5 Powder XRD diffraction patterns of (a) $CSi_{2.5}$ carbonized at 600, 700, 800 and 900 ºC and (b) combination of $CSi_{2.5}$700, $CSi_{3.7}$700 and $CSi_{6.2}$700.

Figure 6.6 (left) shows the nitrogen physisorption isotherms of $CSi_{2.5}$ with different carbonization temperatures, whilst Figure 6.6 (right) shows the isotherms for CSN samples carbonized at 700 °C for varying silica contents. All of the 7 samples exhibit type IV isotherm with pronounced capillary condensation, which is typical for mesoporous material (pore size of 2 to 50 nm) [33]. Table 6.1 presents the overall physicochemical properties of the CSN as obtained from nitrogen physisorption measurement and XRD analysis. As the temperature increases from 600 to 900 °C, the mesostructure of the nanocomposite is maintained with similar isotherm curve (Figure 6.6, left). The hysteresis loops slightly deviate from the ideal H1 type at lower carbonization temperature but appear to be more conspicuous with a steeper capillary condensation step for the $CSi_{2.5}$900 sample. Indeed, the higher temperature and longer duration of carbonization may allow the organic moieties to undergo further dehydrogenation and condensation (see FTIR analysis below and in Figure 6.8), thus, reducing pore blocking/percolation effects as resulting in type H2 hysteresis [34]. The carbonization temperature at 700 °C produces nanocomposites with highest BET surface area and pore volume, and further pyrolysis leads to mesostructural densification. Overall, the mesostructure of the nanocomposite is quite stable considering the lattice shrinkage is 0.003 nm $°C^{-1}$.

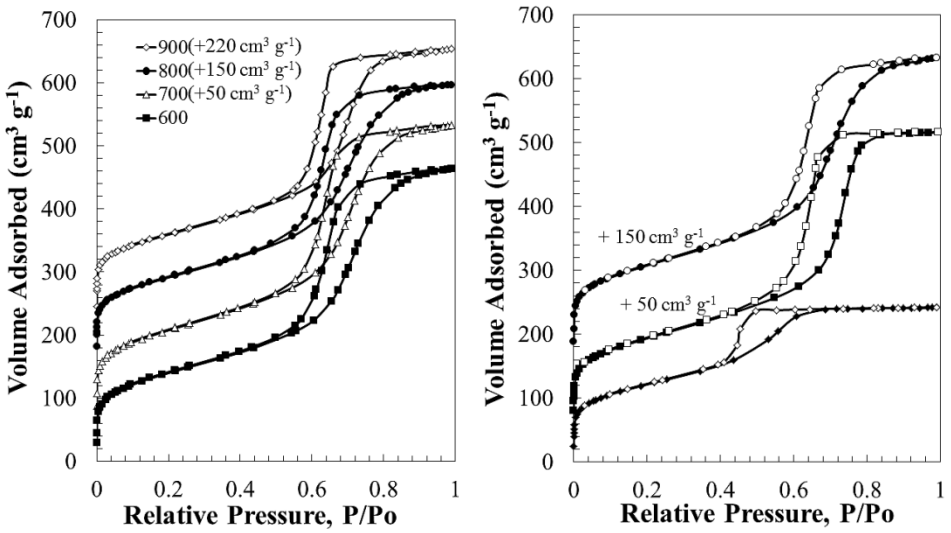

Figure 6.6 Nitrogen adsorption-desorption isotherms of (left) $CSi_{2.5}$ samples carbonized at 600 °C (square), 700 °C (triangle), 800 °C (circle) and 900 °C (diamond); (right) Isotherms of $CSi_{6.2}$700, $CSi_{3.7}$700 and $CSi_{2.5}$700 from bottom to top.

In contrast to the marginal changes induced by carbonization temperature, varying the silica content had a dramatic impact on the isotherms of the CSN samples. In the case of the $CSi_{6.2}$700 sample, with the highest silica content but lowest surfactant to carbon molar ratio, the N_2 isotherm is fundamentally different from both the $CSi_{2.5}$700 and $CSi_{3.7}$700 samples (Figure 6.5, right). The isotherm remains of type IV but the hysteresis loop is more aptly described as type H2 rather than the type H1 seen for the other two samples. Due to the lower concentration of surfactant, $CSi_{6.2}$700 has smaller pore size which shifts the capillary condensation step to a lower relative pressure in the isotherm [34]. Similarly, the relatively small capillary condensation step suggests that the material has a smaller pore volume than its counterparts. In comparison, the $CSi_{3.7}$700 sample reveals a steeper adsorption and desorption branch with a better resolved H1-type hysteresis loop, indicating it has a higher degree of pore order, which is in line with the XRD results.

Table 6.1 Physicochemical properties of carbon-silica nanocomposite materials

	Unit cell[a], nm	S_{BET}[b], $m^2\ g^{-1}$	V_{NLDFT}[c], $cm^3\ g^{-1}$	D_{NLDFT}[d], nm
$CSi_{2.5}600$	12.1	498	0.70	7.0
$CSi_{2.5}700$	12.4	556	0.73	7.0
$CSi_{2.5}800$	12.1	500	0.67	6.8
$CSi_{2.5}900$	11.9	492	0.64	6.8
$CSi_{3.7}700$	12.4	509	0.70	7.6
$CSi_{6.2}700$	11.2	431	0.36	5.5

[a] The unit cell parameter a is calculated from $a = 2/\sqrt{3} \times d_{hkl}$, where d_{hkl} is the d-spacing value obtained from XRD data.

[b] S_{BET}, BET specific area calculated from the volume of N_2 adsorbed in the relative pressure range from 0.05 to 0.2.

[c] V_{NLDFT}, total pore volume calculated by the NLDFT method based on adsorption branch of silica with cylindrical pore models.

[d] D_{NLDFT}, pore width calculated by similar method as V_{NLDFT}.

Cumulative pore volume and pore size distributions for all the CSN samples calculated from the adsorption branch of N_2 isotherms are presented in Figure 6.7. The NLDFT method based on the kernel for silica with cylindrical pore geometry was implemented as this model gives a better fit with the measured data. For comparison, the respective cumulative pore volume and pore size distributions obtained from QSDFT method based on carbon adsorbent with slit/cylindrical pore model is also presented in Figure S6.1 (see ESI). The curve of cumulative pore volume represents the volume fraction of pores at different width [35]. Two populations of pore width attributed to the mesopores and intrawall pores (~ 1 nm) could be observed from the cumulative pore volume plots. A narrow distribution of pore size averaging 7.0 nm is observed for the $CSi_{2.5}600$ and $CSi_{2.5}700$ samples. However, there is a slight shrinkage of the material at higher carbonization temperatures (800 and 900 °C) which results in a pore size reduction of 3 %. However, the pore size distribution becomes narrower at higher carbonization temperatures, implying a higher degree pore ordering. For $CSi_{3.7}700$ with higher silica content, the cumulative pore volume plot reveals a steep slope and a sharp peak in the pore size distribution which is consistent with both the TEM and XRD analysis. In contrast, $CSi_{6.2}700$ shows two peaks in the region of 2 to 7 nm. Figure S6.1 (see ESI) compares the pore size distributions as calculated by NLDFT and QSDFT. The major difference between the two methods is that the QSDFT calculates a greater fraction of micropores than the NLDFT. Crucially, the fact that the NLDFT

offers a better fitting for the CSN materials strongly suggests that the pores are predominantly cylindrical and that the pore surface is most likely enriched with silica.

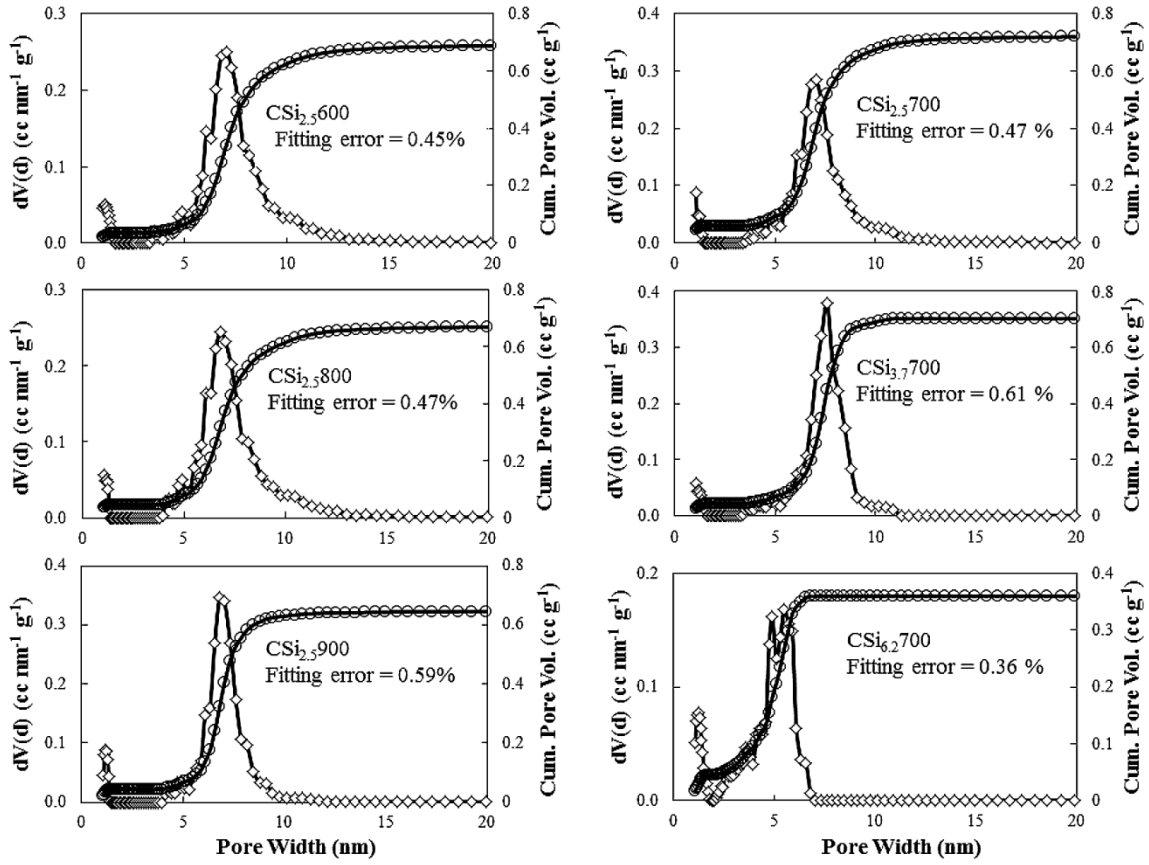

Figure 6.7 Cumulative pore volume and pore size distribution of nanocomposite materials calculated using NLDFT based on adsorption branch of silica with cylindrical pore model.

The functional groups of the CSN materials were determined using ATR-FTIR analysis. Figure 6.8 displays the thermal evolution of the functional groups within the $CSi_{2.5}$ sample from pre-carbonization up to the highest carbonization temperature of 900 °C. After carbonization, the peaks at 2882 and 1345 cm^{-1} corresponding to the surfactant (polyethylene glycol) are no longer visible which, when taken in conjunction with the TEM analysis, confirms that the heat treatment was sufficient to remove the templating agent. The spectra of CSN materials are comprised of several bands associated with both carbon and silica functional groups. All samples possess peaks in the low frequency regions of ~796 and ~1080 cm^{-1} and a shoulder peak at ~950 cm^{-1} that assigned to the vibrational modes of silica [36]. The organic groups are represented by peaks at 1465 – 1615 cm^{-1} and importantly they are still visible at high carbonization temperatures. The band at 1465 cm^{-1} is assigned to C-H bending of an aliphatic bridge structure,

which is not bonded to Si [37, 38], whereas, the aromatic structure of the organic component confirmed with C=C ring stretching at ~1600 cm^{-1}[38, 39].

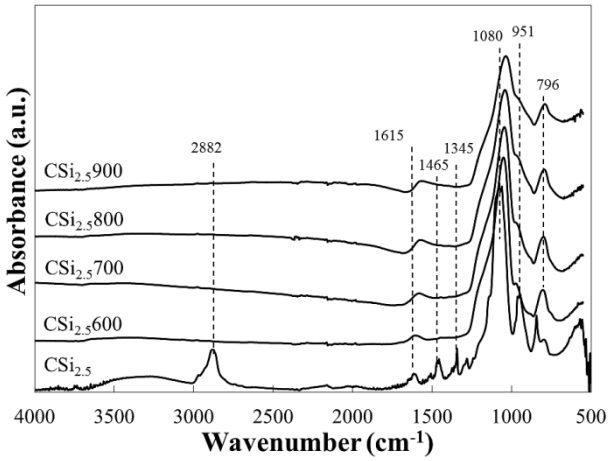

Figure 6.8 ATR-FTIR spectra of pre-carbonized $CSi_{2.5}$, and $CSi_{2.5}$ carbonized at 600, 700, 800 and 900 ºC.

Different vibration modes of Si-O-Si within the peaks at region 900 – 1200 cm^{-1} are quantified by deconvoluting the peaks as represented in Figure 6.9 (left) for the $CSi_{2.5}700$ sample. Two major peaks at ~1040 cm^{-1} (peak 4) and ~1140 cm^{-1} (peak 2) assigned to the transverse-optical (TO) and longitudinal-optical (LO) mode of the anti-symmetric stretching vibration mode, respectively [36]. A densified silica material mainly consists of 6-fold silica rings (Figure 6.10, right) but 4-fold silica rings (Figure 6.10, left) may be retained within the matrix as a result of incomplete hydrolysis-condensation reaction during the sol-gel process or defects of the silica microstructure [40]. Each peak (6-fold silica ring) has its respective shoulder at slightly higher wavenumber corresponding to the equivalent modes but of 4-fold siloxane rings (peak 1 and 3, respectively) [41]. Most noticeably, the band at 1040 cm^{-1} (peak 4) is shifted to lower wavelengths as the carbonization temperature is increased. This could be related to the enhancement of silica porous structure [41] and greater transformation of 6-fold siloxane ring to the 4-fold structure [40]. The residual silanol (Si-OH) group is obtained at ~ 950 cm^{-1} (peak 5) with another vibration mode contributed by $Si\text{-}O^-$ open rings in silica network at ~ 910 cm^{-1} (peak 6) [42]. The ratio of peak area associated with the Si-OH vibration band to the most dominant anti-symmetric Si-O-Si band (TO mode at 1040 cm^{-1}) is evaluated as shown in Figure 6.9 (right). The analysis suggests there is an increase in the amount of silanol species as the carbonization temperature increases. However, as the temperature exceeds 800 °C, the ratio tends to plateau. Since the TO vibration mode (peak 4) shifted to lower wavenumber at higher

carbonization temperature, the ratio of silanol to the total siloxane components was evaluated. Both plots of $SiOH/SiOSi_{1040}$ and $SiOH/SiOSi_{total}$ show a similar trend, albeit the overall silanol to siloxane ratio is considered reasonable even with the existence of carbonaceous moieties [41]. The peak area ratio of 4-fold silica ring (both ν_1(LO) and ν_3(TO), refer to Table S6.2, ESI) to 6-fold silica ring (both ν_2(LO) and ν_4(TO), refer to Table S6.2, ESI) is also presented in Figure 6.9 (right) to evaluate the transformation of the silica microstructure. As carbonization temperature increases, the 6-fold silica ring appears open to form either 4-fold silica ring or open SiO^-. This explains why the peak area of the region 900 – 950 cm^{-1} increases, suggesting an increase in defects in the silica microstructure as the sample carbonization temperature is increased.

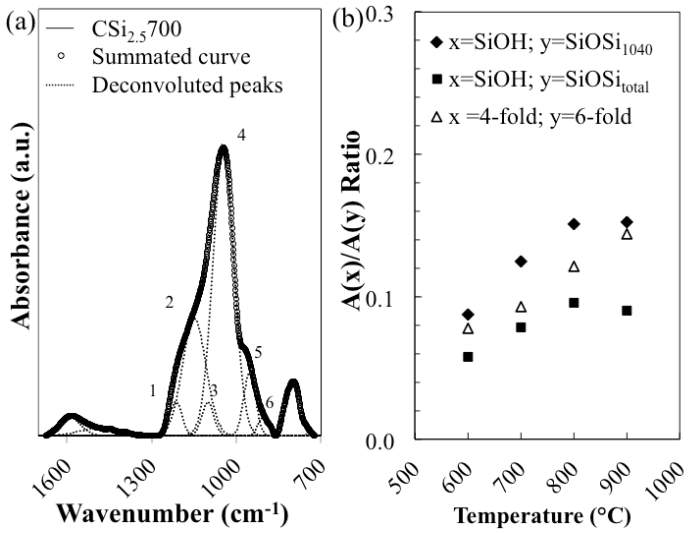

Figure 6.9 (a) Deconvoluted peaks of $CSi_{2.5}700$ with 6 components. (b) Plots of the peak area (A) ratio of SiOH to (TO) Si-O-Si (~ 1,040 cm^{-1}) (square), peak area ratio of SiOH to total siloxane (diamond) and ratio of 4-fold to 6-fold silica ring.

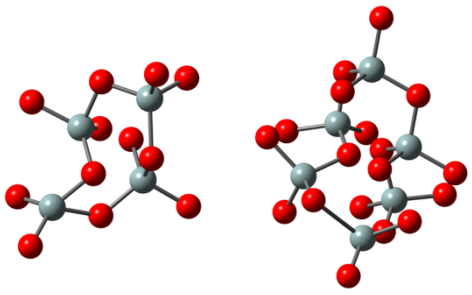

Figure 6.10 Images of (left) 4-fold and (right) 6-fold silica ring type clusters with silicon atom (grey) and oxygen atom (red).

By increasing the silica content, the intensity of C=C band (~ 1600 cm^{-1}) is significantly decreased as displayed in Figure 6.11 (left). On the other hand, the ratio of silanol to the most dominant siloxane band (~1040 cm^{-1}) is well maintained below 0.15 as depicted in Figure 6.11 (right). However, the ratio of 4-fold to 6-fold silica rings is found to increase with increasing silica content. Of note, the ratio doubled in $CSi_{6.2}700$ as compared to $CSi_{2.5}700$ where the silica content was half as much. This suggests that the transformation of 4-fold to 6-fold silica ring may not be significantly influenced by the existence of carbonaceous compound.

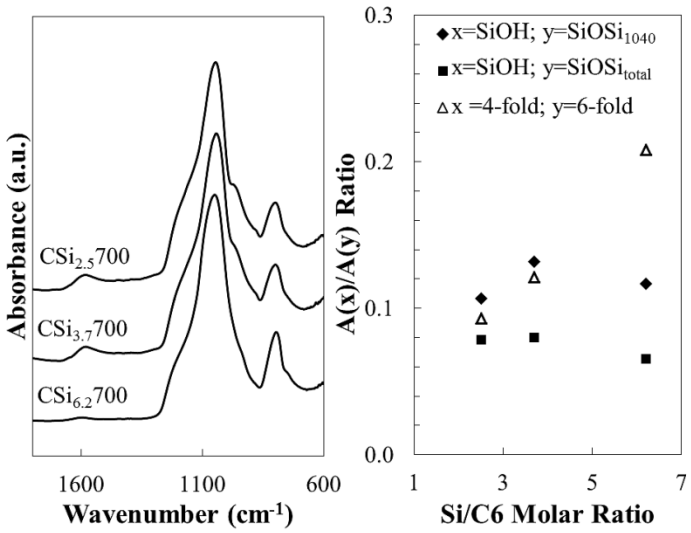

Figure 6.11 ATR-FTIR spectra of mesoporous carbon-silica nanocomposite materials of different TEOS to resorcinol molar ratio (left) and the ratio of Si-OH/Si-O-Si and the ratio of four-fold to six-fold silica ring (right).

In order to understand the interaction between the silica network and the carbonaceous framework the $CSi_{2.5}700$ sample was examined using single pulse ^{29}Si MAS NMR and ^{13}C NMR and the results are shown in Figure 6.12. One important message from the ^{29}Si NMR spectrum is that the silica and carbon network do not chemically bond since there are no T species (-50 to -65 ppm) detected in ^{29}Si NMR [43]. Furthermore, the ^{13}C NMR shows no trace of Si-CH_3 species which are usually observed around -5 ppm [37, 44] further confirming the absence of Si-C bonds. However, a high degree of condensation of the silica network is evidenced with the high fraction of Q^4 ($Si(OSi)_4$) species suggesting a highly condensed silica network. The ^{13}C NMR spectra reveal the evolution of carbon species with the carbonization temperature (Figure 6.12, right). Both aromatic and aliphatic hydrocarbon species derived from the pyrolysed phenolic carbon network [20, 37] were detected at high (100-150 ppm) and low (15-60 ppm)

chemical shifts, respectively. The aromatic carbon with –OH groups (151 ppm) remains for the $CSi_{2.5}600$ sample, but this compound is no longer present when the carbonization temperature is increased, suggesting that the carbonization is virtually complete at 700 °C. Likewise, the intensity of the major peak at 126 ppm decreases drastically after 600 °C with little difference between $CSi_{2.5}800$ and $CSi_{2.5}900$.

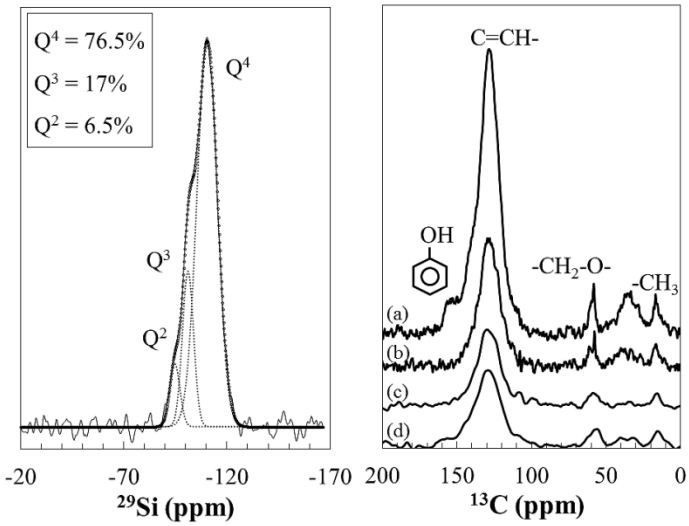

Figure 6.12 The spectra of ^{29}Si MAS NMR of $CSi_{2.5}700$ with deconvoluted peaks correspond to Q^2, Q^3 and Q^4 species (left) and ^{13}C NMR for (a) $CSi_{2.5}600$, (b) $CSi_{2.5}700$, (c) $CSi_{2.5}800$ and (d) $CSi_{2.5}900$ (right).

The amount of geminal, Q^2 ($(SiO)_2Si(OH)_2$) and single, Q^3 ($(SiO)_3SiOH$), silanols within the silica matrix were quantified by ^{29}Si NMR as presented in Table 6.2. In general, the surface functional groups are dominated by single silanols with only a small amount of geminal silanol species detected in the CSN materials, albeit in samples with a considerable degree of condensation. The ratio of Q^2 to Q^4 resonance peak areas obtained from the deconvoluted peaks show a similar trend as obtained from the ATR-FTIR analysis (Figure 6.9), whereby the total silanol groups increases as the material is carbonized at higher temperatures. The degree of condensation for the $CSi_{2.5}$ sample peaks at 700 °C, but begins to decline with increasing carbonization temperature. An apparent transformation of Q^3 species to Q^2 and Q^4 species at 700 °C is observed as the carbonization temperature increases from 600 °C to 900 °C. For pure silica gels, the silica undergoes further condensation as the temperature increases with a reduction in Q^3 and Q^2 species. However, the observation here suggesting that the presence of carbon moieties has inevitably interrupted the silica microstructure. One could postulate that at 700 °C, cleavage of chemical bond between the aromatic carbon and hydroxyl group (-OH) leads to the

formation of free –OH groups and pyrolyzed carbon. The liberated –OH groups may form hydrogen bonds with the adjacent siloxane bonds, rehydrating the fully condensed silica surface (Q^4 sites) via water adsorption followed by dissociative chemisorption [45]. This leads to the cleavage of siloxane bond in Q^4 and an increase in Q^2 and Q^3 species.

Table 6.2 The ^{29}Si NMR quantification data of Q^2, Q^3 and Q^4 species of the CSN

Material	Q^3/Q^4	Q^2/Q^4	Total SiOH $(2Q^2+Q^3)/(Q^2+Q^3+Q^4)$	Condensation degree $Q^4/(Q^2+Q^3+Q^4)$
$CSi_{2.5}600$	**0.36**	**0.04**	**0.31**	**0.71**
$CSi_{2.5}700$	**0.22**	**0.08**	**0.30**	**0.77**
$CSi_{2.5}800$	**0.52**	**0.10**	**0.44**	**0.62**
$CSi_{2.5}900$	**0.52**	**0.07**	**0.41**	**0.63**

Thin film membranes were synthesized using a carbonization temperature of 700 °C to see the structure-property relationships associated with varying the silica content in the CSN materials. Specifically, the performances of the CSN membranes were assessed in a vacuum membrane distillation process and the results are presented in Figure 6.13. In general, the water permeation flux increases with feed temperature, signifying that, as with all MD processes, the temperature driven vapour pressure gradient is the dominant driving force. The influence of salt concentration had minimal impact on the membranes performance, except for the $CSi_{3.7}700$ membrane, where a significant drop in flux is observed with increasing feed concentration. To better understand the performance of the membranes they are compared based on the calculated global mass transfer coefficient, C_g as displayed in Figure 6.13d. As the temperature increases, the C_g values decline which is likely associated with several factors. The first points to an increase in temperature polarisation at the feed side, as the small Re number (250) and associated laminar flow makes temperature polarization significant for the module used in this study [Chapter 4]. This impacts the driving force, making the actual vapour pressure difference smaller than the apparent vapour pressure difference if only the bulk conditions are considered. In addition, previous modelling of nanoporous membranes indicates that the main rate limiting step is the transport of water through the nanopores in the vapour phase. This transport is governed by Knudsen diffusion and as the viscosity of the water vapour rises with respect to the increase in

temperature within the pore channel, it will negatively impact on the global mass transfer coefficient.

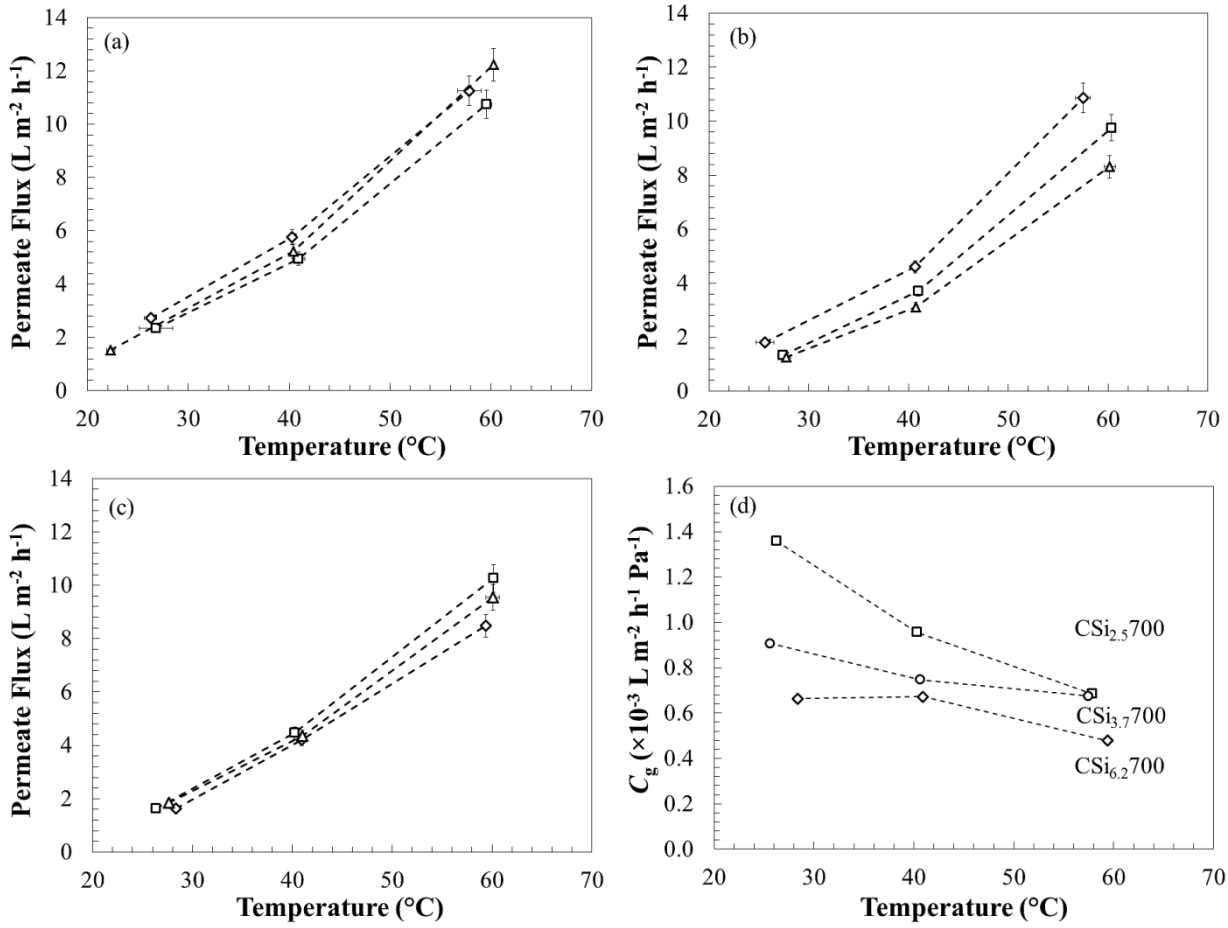

Figure 6.13 Water vapour permeation fluxes of (a) $CSi_{2.5}700$, (b) $CSi_{3.7}700$ and (c) $CSi_{6.2}700$ at feed concentration of 0 (diamond), 10 (square) and 35 g L^{-1} NaCl (triangle). (d) Plots of global mass transfer coefficient, C_g of each membrane with respect to the feed temperature.

$CSi_{2.5}700$ seems to outperform the other membranes, most likely as it has the largest pore volume, although its performance is less dominant at higher feed water temperatures. $CSi_{3.7}700$ has the largest pore size (7.6 nm), and its global mass transfer coefficient suffers the least with increasing temperature; however, it carries the risk of pore wetting. Indeed, salt deposits were observed on the permeate surface at a feed water temperature of 25 °C and a concentration of 35 g L^{-1} of NaCl. This pore wetting behaviour was not observed for either of the other membranes tested, regardless of salt concentration or feed water temperature. Interestingly, the membrane performance of $CSi_{2.5}700$ is comparable to the nanoporous organosilica membrane (Figure 6.14) as reported in our previous work [17]. The similar performances of both these membranes

despite having different porosities and different pore sizes is evidence of the complex relationship of water flux with the membrane thickness, pore size and membrane surface chemistry, which require further investigation. These results also provide good evidence that these CSN materials could be a good candidate as a more cost-effective material compared to organosilica MD membranes.

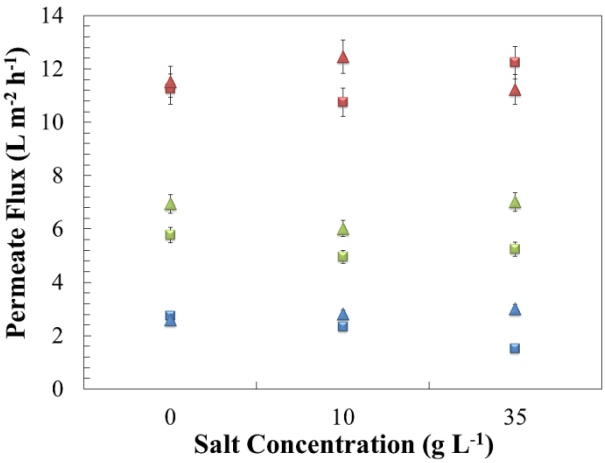

Figure 6.14 Comparison of membranes performances for organosilica membrane (triangle) and $CSi_{2.5}700$ (square) over feed temperature 25 (blue), 40 (green) and 60 °C (red).

In order to have better understanding, the structures of two different materials are illustrated in Figure 6.15. For organosilica, the two carbon atoms that form bridges between silicon atoms are believed to improve the hydrothermal stability of silica matrix [46]. Meanwhile, the structure of CSN resembles two individual networks of silica and carbon that are intercalated physically without any chemical bonding. The enlargement of larger pores and closure of smaller pores due to water attack as commonly observed in pure silica matrix could be prevented [47] with the presence of carbon moieties in the silica matrix. Whilst the pore wall seems to be enriched with silica as deduced from NLDFT model and sorption analysis, it is believed that the pyrolysed carbon acts to prevent the migration of mobile silanols by intermittently appear in the pore wall. Meanwhile, the silica scaffold behaves as steel-in-concrete reinforcing for the carbon network and assists in preserving the mesostructure of the nanocomposite [20]. This study proved that carbon-silica nanocomposites could be an alternative candidate for VMD membrane, given that the CSN precursors are far less expensive than organosilica precursors. However, the carbon-silica molar ratio and other physico-chemical properties of the membrane need to be optimised to improve the membrane stability and enhance its water separation performance.

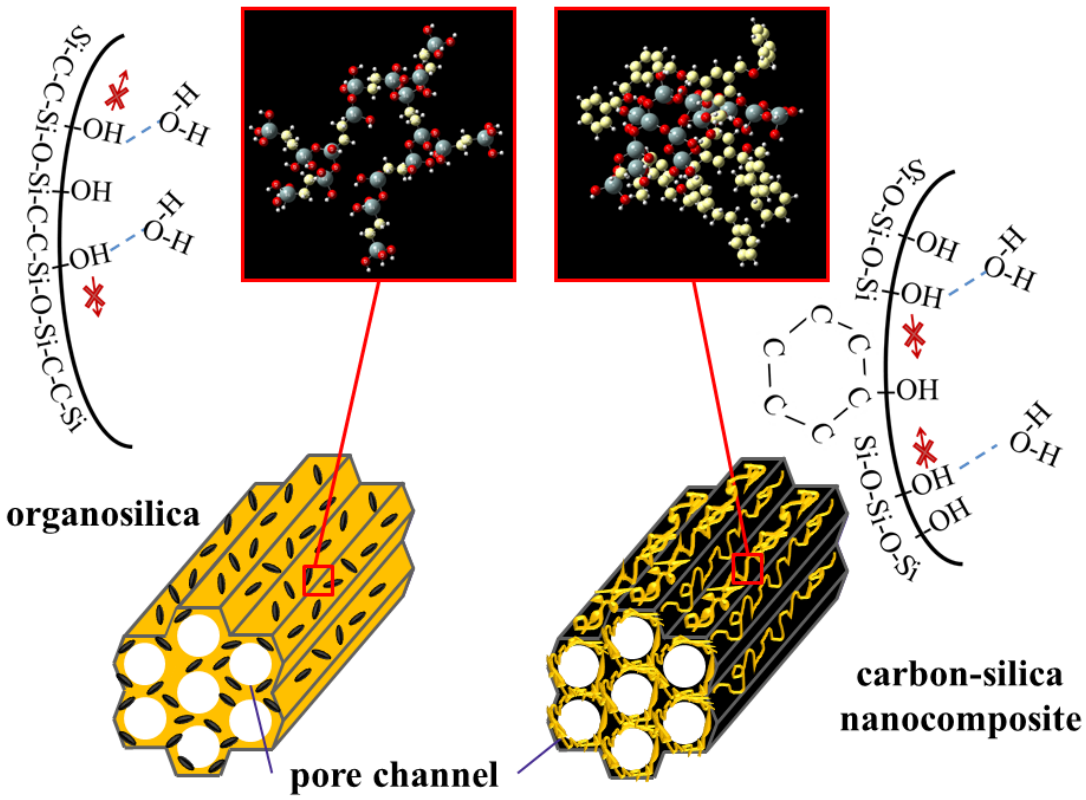

Figure 6.15 Schematic structure of the ordered pore in organosilica and carbon-silica nanocomposite materials (yellow area as silica matrix and black area represents carbon moieties). Insets depict the interaction between carbon and silica in the materials with silicon (grey), carbon (yellow), oxygen (red) and hydrogen (white).

6.4 Conclusion

Mesoporous CSN membrane were successfully fabricated using a modified synthesis route, which is faster and easier than the comparable nanocasting method for periodic mesoporous organosilica. The nanocomposite lattice structure is stable with silica content as low as 44 wt% and the highly ordered mesoporous structure was preserved even when carbonized at temperatures as high as 900 °C. In a critical difference with conventional organosilica membranes there is no evidence of any chemical bonding or interaction between the silica and carbon network as analysed by NMR and FTIR. Rather the phenolic network of the carbon framework remains intact as does the highly ordered and condensed silica framework. However, increasing the carbonization temperature from 700 to 900 °C promotes the release of hydroxyl

groups from the carbon which in turn attacks adjacent siloxane bonds, inducing more hydrolysis of the silica surface. This impacts on the surface chemistry and functional groups present but does not appear to induce significant structural reorganization of the silica network. Therefore, one may deduce that the pyrolysed carbon in this case protects the silica from water attach but not contribute any significant alteration in water transport. Membrane performance was dominated by the variation in pore volume of the membranes, but pore size was a significant factor in pore wetting. Temperature polarization was a significant factor at feed temperatures of 60 °C. The VMD performance of the CSN membranes is quite comparable with similar organosilica membranes suggesting that it could be a suitable, lower cost alternative to organosilica in inorganic/organic membrane manufacture.

Acknowledgement

The authors would like to acknowledge funding from the Australian Research Council projects ARC-DP 110103440. Y.C. would like to acknowledge The University of Queensland for providing an UQI International Scholarship. F.K. acknowledges financial support from the Natural Sciences and Engineering Research Council of Canada (NSERC). S. S. would like to acknowledge the Queensland Government Smart Futures Fellowship. The authors acknowledge the facilities, and the scientific and technical assistance, of the Australian Microscopy & Microanalysis Research Facility at the Centre for Microscopy and Microanalysis, and Dr Ekaterina Strounina for the ^{29}Si and ^{13}C NMR technical help from the Centre of Advanced Imaging, The University of Queensland.

References

[1] T. Humplik, J. Lee, S.C. O'Hern, B.A. Fellman, M.A. Baig, S.F. Hassan, M.A. Atieh, F. Rahman, T. Laoui, R. Karnik, E.N. Wang, Nanostructured materials for water desalination, Nanotechnology, 22 (2011) 1-19.

[2] M.S. El-Bourawi, Z. Ding, R. Ma, M. Khayet, A framework for better understanding membrane distillation separation process, Journal of Membrane Science, 285 (2006) 4-29.

[3] H.J. Zwijnenberg, G.H. Koops, M. Wessling, Solar driven membrane pervaporation for desalination processes, Journal of Membrane Science, 250 (2005) 235-246.

[4] M. Safavi, T. Mohammadi, High-salinity water desalination using VMD, Chemical Engineering Journal, 149 (2009) 191-195.

[5] A.M. Alklaibi, N. Lior, Membrane-distillation desalination: Status and potential, Desalination, 171 (2005) 111-131.

[6] M. Khayet, Membranes and theoretical modeling of membrane distillation: A review, Advances in Colloid and Interface Science, 164 (2011) 56-88.

[7] A. Alkhudhiri, N. Darwish, N. Hilal, Membrane distillation: A comprehensive review, Desalination, 287 (2012) 2-18.

[8] L.D. Tijing, J.-S. Choi, S. Lee, S.-H. Kim, H.K. Shon, Recent progress of membrane distillation using electrospun nanofibrous membrane, Journal of Membrane Science, 453 (2014) 435-462.

[9] X. Yang, R. Wang, L. Shi, A.G. Fane, M. Debowski, Performance improvement of PVDF hollow fiber-based membrane distillation process, Journal of Membrane Science, 369 (2011) 437-447.

[10] W.A. Phillip, B. O'Neill, M. Rodwogin, M.A. Hillmyer, E.L. Cussler, Self-Assembled Block Copolymer Thin Films as Water Filtration Membranes, ACS Applied Materials & Interfaces, 2 (2010) 847-853.

[11] X. Qiu, H. Yu, M. Karunakaran, N. Pradeep, S.P. Nunes, K.-V. Peinemann, Selective Separation of Similarly Sized Proteins with Tunable Nanoporous Block Copolymer Membranes, ACS Nano, (2012).

[12] M. Zhou, T.J. Kidd, R.D. Noble, D.L. Gin, Supported Lyotropic Liquid-Crystal Polymer Membranes: Promising Materials for Molecular-Size-Selective Aqueous Nanofiltration, Advanced Materials, 17 (2005) 1850-1853.

[13] V.V. Guliants, M.A. Carreon, Y.S. Lin, Ordered mesoporous and macroporous inorganic films and membranes, Journal of Membrane Science, 235 (2004) 53-72.

[14] C. Sanchez, C. Boissière, D. Grosso, C. Laberty, L. Nicole, Design, Synthesis, and Properties of Inorganic and Hybrid Thin Films Having Periodically Organized Nanoporosity†, Chemistry of Materials, 20 (2008) 682-737.

[15] D. Zhao, P. Yang, B.F. Chmelka, G.D. Stucky, Multiphase Assembly of Mesoporous−Macroporous Membranes, Chemistry of Materials, 11 (1999) 1174-1178.

[16] C.J. Brinker, Y. Lu, A. Sellinger, H. Fan, Evaporation-Induced Self-Assembly: Nanostructures Made Easy, Advanced Materials, 11 (1999) 579-585.

[17] Y.T. Chua, C.X.C. Lin, F. Kleitz, X.S. Zhao, S. Smart, Nanoporous organosilica membrane for water desalination, Chemical Communications, 49 (2013) 4534-4536.

[18] S. Takahashi, D.R. Paul, Gas permeation in poly(ether imide) nanocomposite membranes based on surface-treated silica. Part 1: Without chemical coupling to matrix, Polymer, 47 (2006) 7519-7534.

[19] S. Yoda, M. Ohara, Y. Takebayashi, K. Sue, Y. Hakuta, T. Furuya, M. Yamada, K. Otake, A porous polymer-silica composite with a "vespula-like" structure for thermal insulating materials prepared via high pressure phase control, Journal of Materials Chemistry A, 1 (2013) 9620-9623.

[20] R. Liu, Y. Shi, Y. Wan, Y. Meng, F. Zhang, D. Gu, Z. Chen, B. Tu, D. Zhao, Triconstituent Co-assembly to Ordered Mesostructured Polymer−Silica and Carbon−Silica Nanocomposites and Large-Pore Mesoporous Carbons with High Surface Areas, Journal of the American Chemical Society, 128 (2006) 11652-11662.

[21] Q. Hu, R. Kou, J. Pang, T.L. Ward, M. Cai, Z. Yang, Y. Lu, J. Tang, Mesoporous carbon/silica nanocomposite through multi-component assembly, Chemical Communications, (2007) 601-603.

[22] F. Zhang, Y. Meng, D. Gu, Yan, C. Yu, B. Tu, D. Zhao, A Facile Aqueous Route to Synthesize Highly Ordered Mesoporous Polymers and Carbon Frameworks with Ia3̄d Bicontinuous Cubic Structure, Journal of the American Chemical Society, 127 (2005) 13508-13509.

[23] C. Liang, S. Dai, Synthesis of Mesoporous Carbon Materials via Enhanced Hydrogen-Bonding Interaction, Journal of the American Chemical Society, 128 (2006) 5316-5317.

[24] T.-Y. Ma, L. Liu, Z.-Y. Yuan, Direct synthesis of ordered mesoporous carbons, Chemical Society Reviews, 42 (2013) 3977-4003.

[25] M. Si, D. Feng, L. Qiu, D. Jia, A.A. Elzatahry, G. Zheng, D. Zhao, Free-standing highly ordered mesoporous carbon-silica composite thin films, Journal of Materials Chemistry A, 1 (2013) 13490-13495.

[26] C. Xue, B. Tu, D. Zhao, Evaporation-Induced Coating and Self-Assembly of Ordered Mesoporous Carbon-Silica Composite Monoliths with Macroporous Architecture on Polyurethane Foams, Advanced Functional Materials, 18 (2008) 3914-3921.

[27] É. Gagnon-Thibault, D. Cossement, R. Guillet-Nicolas, N. Masoumifard, P. Bénard, F. Kleitz, R. Chahine, J.-F. Morin, Nanoporous ferrocene-based cross-linked polymers and their hydrogen sorption properties, Microporous and Mesoporous Materials, 188 (2014) 182-189.

[28] F. Kleitz, W. Schmidt, F. Schüth, Calcination behavior of different surfactant-templated mesostructured silica materials, Microporous and Mesoporous Materials, 65 (2003) 1-29.

[29] B.P. Ladewig, Y.H. Tan, C.X.C. Lin, K. Ladewig, d.C.J.C. Diniz, S. Smart, Preparation, characterization and performance of templated silica membranes in non-osmotic desalination, Materials, 4 (2011) 845-856.

[30] J. Ryczkowski, J. Goworek, W. Gac, S. Pasieczna, T. Borowiecki, Temperature removal of templating agent from MCM-41 silica materials, Thermochimica Acta, 434 (2005) 2-8.

[31] C. Lin, J.A. Ritter, Effect of synthesis pH on the structure of carbon xerogels, Carbon, 35 (1997) 1271-1278.

[32] C. Lin, J.A. Ritter, Carbonization and activation of sol–gel derived carbon xerogels, Carbon, 38 (2000) 849-861.

[33] K.S.W. Sing, Reporting physisorption data for gas/solid systems with special reference to the determination of surface area and porosity (Recommendations 1984), Pure and Applied Chemistry1985, pp. 603.

[34] F. Kleitz, F.o. Bérubé, R.m. Guillet-Nicolas, C.-M. Yang, M. Thommes, Probing Adsorption, Pore Condensation, and Hysteresis Behavior of Pure Fluids in Three-Dimensional Cubic Mesoporous KIT-6 Silica, The Journal of Physical Chemistry C, 114 (2010) 9344-9355.

[35] N.V. Reichhardt, R. Guillet-Nicolas, M. Thommes, B. Klosgen, T. Nylander, F. Kleitz, V. Alfredsson, Mapping the location of grafted PNIPAAM in mesoporous SBA-15 silica using gas adsorption analysis, Physical Chemistry Chemical Physics, 14 (2012) 5651-5661.

[36] A. Bertoluzza, C. Fagnano, M. Antonietta Morelli, V. Gottardi, M. Guglielmi, Raman and infrared spectra on silica gel evolving toward glass, Journal of Non-Crystalline Solids, 48 (1982) 117-128.

[37] V. Jousseaume, A. Zenasni, L. Favennec, G. Gerbaud, M. Bardet, J.P. Simon, A. Humbert, Comparison Between E-beam and Ultraviolet Curing to Perform Porous a-SiOC : H, Journal of The Electrochemical Society, 154 (2007) G103-G109.

[38] L. Song, D. Feng, C.G. Campbell, D. Gu, A.M. Forster, K.G. Yager, N. Fredin, H.-J. Lee, R.L. Jones, D. Zhao, B.D. Vogt, Robust conductive mesoporous carbon-silica composite films with highly ordered and oriented orthorhombic structures from triblock-copolymer template co-assembly, Journal of Materials Chemistry, 20 (2010) 1691-1701.

[39] H. Preiss, L.-M. Berger, M. Braun, Formation of black glasses and silicon carbide from binary carbonaceous/silica hydrogels, Carbon, 33 (1995) 1739-1746.

[40] P. Innocenzi, Infrared spectroscopy of sol–gel derived silica-based films: a spectra-microstructure overview, Journal of Non-Crystalline Solids, 316 (2003) 309-319.

[41] A. Fidalgo, L.M. Ilharco, The defect structure of sol–gel-derived silica/polytetrahydrofuran hybrid films by FTIR, Journal of Non-Crystalline Solids, 283 (2001) 144-154.

[42] A. Chmel, E.K. Mazurina, V.S. Shashkin, Vibrational spectra and deffect structure of silica prepared by non-organic sol-gel process, Journal of Non-Crystalline Solids, 122 (1990) 285-290.

[43] M. Ide, M. El-Roz, E. De Canck, A. Vicente, T. Planckaert, T. Bogaerts, I. Van Driessche, F. Lynen, V. Van Speybroeck, F. Thybault-Starzyk, P. Van Der Voort, Quantification of silanol sites for the most common mesoporous ordered silicas and organosilicas: total versus accessible silanols, Physical Chemistry Chemical Physics, 15 (2013) 642-650.

[44] S. Inagaki, S. Guan, Y. Fukushima, T. Ohsuna, O. Terasaki, Novel mesoporous materials with a uniform distribution of organic groups and inorganic oxide in their frameworks, Journal of the American Chemical Society, 121 (1999) 9611-9614.

[45] C.J. Brinker, G.W. Scherer, Sol-gel science: the physics and chemistry of sol-gel processing, Academic Press1990.

[46] H.L. Castricum, A. Sah, R. Kreiter, D.H.A. Blank, J.F. Vente, J.E. ten Elshof, Hydrothermally stable molecular separation membranes from organically linked silica, Journal of Materials Chemistry, 18 (2008) 2150-2158.

[47] M.C. Duke, d.C.J.C. Diniz, D.D. Do, P.G. Gray, G.Q. Lu, Hydrothermally robust molecular sieve silica for wet gas separation, Adv. Funct. Mater., 16 (2006) 1215-1220.

Supplementary Information

Experimental

Table S 6.1 Compositions of carbon and silica precursors and surfactant for the synthesis of CSN

	Resorcinol	Formaldehyde	TEOS	F127	F127/(Si+C)
$CSi_{2.5}$	1	1.6	2.47	0.0326	0.0094
$CSi_{3.7}$	1	1.6	3.70	0.0429	0.0094
$CSi_{6.2}$	1	1.6	6.17	0.0326	0.0045

Results and Discussion

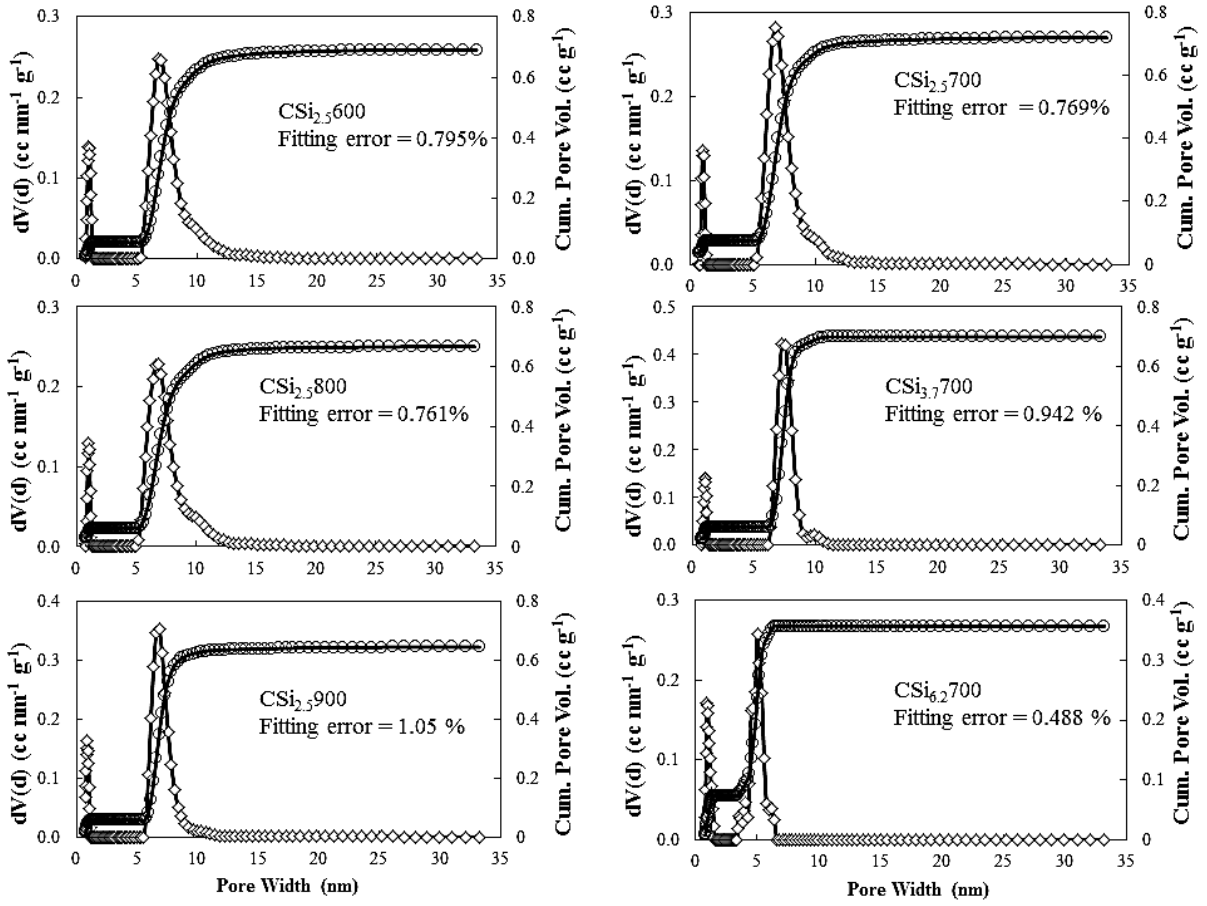

Figure S 6.1 Nitrogen sorption cumulative pore volumes (right axes) and pore size distributions (left axes) of the $CSi_{2.5}$, $CSi_{3.7}$ and $CSi_{6.2}$ samples calculated using QSDFT method based on adsorption branch of carbon adsorbent with slit/cylindrical pore model.

Table S 6.2 Deconvoluted results of Si-O-Si band in Gaussian components

Sample	$CSi_{2.5}600$	$CSi_{2.5}700$	$CSi_{2.5}800$	$CSi_{2.5}900$
ν_1 (LO) (cm^{-1})	1222.82	1214.06	1206.23	1198.93
FWHM (cm^{-1})	44.0463	50.1722	54.9779	54.8409
***A* (%)**	2.33	3.43	4.45	4.50
ν_2(LO) (cm^{-1})	1164.33	1149.21	1137.87	1128.9
FWHM (cm^{-1})	98	98	98	97.199
***A* (%)**	23.38	22.96	24.04	22.72
ν_3(TO) (cm^{-1})	1120.36	1101.04	1088.32	1080.92
FWHM (cm^{-1})	50	50	50	50
***A* (%)**	3.99	3.36	4.40	5.68
ν_4(TO) (cm^{-1})	1053.67	1045.84	1038.61	1032.03
FWHM (cm^{-1})	86	88	88	88
***A* (%)**	58.06	49.99	49.00	47.85
***A*(4-fold)/*A*(6-fold) (%)**	7.76	9.31	12.11	14.42

**A* is the integrated area under the specific deconvoluted peak of each component. FWHM is full width half maximum of the peak. ν is the frequency of each mode.

7 STRUCTURE-PERFORMANCE RELATIONSHIP OF POLYMER-SILICA NANOCOMPOSITES MEMBRANE IN WATER VAPOUR TRANSPORT

Introduction

In the previous chapter, the study of mesoporous carbon-silica nanocomposite membranes was focussed on nanocomposites with high silica content, high carbonization temperature and larger pore sizes. This chapter will investigate low silica content, polymer/silica nanocomposites with smaller pore sizes under VMD. The motivation for this was two-fold. Firstly, it is clear that the exceptional performance see in Chapter 3 cannot be improved upon simply by increasing the pore size, without significant alteration of the membrane surface chemistry. The lack of performance stability and flux improvement in Chapters 5 and 6 are evidence of this. Therefore a higher carbon content is desirable to further alter the surface chemistry whilst increasing pore size. Secondly, the membrane synthesis procedure can be improved by reducing the coating time which is best achieved by reducing the number of membrane coats. Therefore, the sol viscosity in this work was increased relative to the previous chapter by reducing the ethanol content, which should reduce the sol infiltration into the substrate. However, high viscosity usually leads to thicker membrane and therefore, a slower withdrawal rate of substrate was applied during the dip-coating process. Low thermal treatment was also introduced to remove the surfactant but retain other functional groups within the polymer matrix of the nanocomposites. The correlation between membrane structure and silica content to the separation performance was evaluated in VMD over a range of feed temperature (25-60 °C) and salt concentrations (0 – 150 g L^{-1}).

Contribution

The main contribution of this work is the successful demonstration of the membrane preparation procedures, in which a single layer, defect-free membrane was produced in only one coat. The performance of the subsequent membranes was comparable, in terms of flux and global mass transfer coefficient to Chapters 5 and 6, although greater stability over a wide range of salt concentrations was observed. These membranes show great potential for further VMD work through further tailoring of the pore size, geometry and surface chemistry.

Structure-performance relationship of polymer-silica nanocomposite membranes in water vapour transport

Abstract

Mesoporous polymer-silica nanocomposite membranes were prepared via a simple one-pot synthesis approach utilizing a triconstituent co-assembly of resorcinol-based polymer (organic precursor), tetraethylorthosilicates (inorganic precursor) and triblock-copolymer Pluronic F68 (surfactant). The membrane materials were calcined at lower temperatures (450 °C) than traditional carbon-silica nanocomposites to preserve many of the polymeric functional groups. The nitrogen physisorption analysis showed that different micro- and mesoporous networks could be obtained for the nanocomposites by varying silica content. In particular, pore volume decreased dramatically as silica content reduced. Both Fourier-transformed infrared (FTIR) and nuclear magnetic resonance (NMR) analyses confirmed that there was no covalent bonding between the polymer matrix and the reinforcing silica. A single layer, defect-free, and well adhered membrane is formed on the porous alumina substrate as observed under the scanning electron microscopy (SEM). Membrane performance was tested in a vacuum membrane distillation process for water desalination. The membrane with the second highest silica content, $CSi_{1.2}$ outperformed the other membranes with the highest water vapour permeation flux (up to 14 L m^{-2} h^{-1}) and good stability across a range of feed water salt concentrations (0-150 g L^{-1} NaCl).

Keywords: Mesoporous polymer-silica nanocomposites; triconstituent co-assembly; membrane distillation; desalination.

7.1 Introduction

Desalination is an increasingly important technology for fresh water production. Reverse osmosis (RO) currently dominates the global market for new seawater desalination plants due to its lower energy requirements, smaller plant footprint and reduced capital expenditure (CapEx) compared to traditional thermal techniques [1]. However, RO is unsuited to treating chemically or thermally aggressive feed waters or highly saline brines (total dissolved solids (TDS) > 50 g

L^{-1}) and hence there is an opportunity for alternate desalination technologies in emerging markets [2]. Membrane distillation (MD) is a desalination process which combines thermal distillation with a membrane so as to utilise low grade heat sources such as waste heat or renewable energy sources but in a smaller plant footprint. In theory this should allow MD to treat a vast array of feed waters and brines but at a lower CapEx than conventional thermal techniques. There is also the potential to integrate MD with RO for high water recoveries in zero liquid discharge applications.

Thin film nanocomposite membrane with a thin-film layer supported on porous substrate have been extensively studied for reverse osmosis (RO) and nanofiltration (NF) processes due to its high water flux, high solute rejection, minimum membrane fouling and excellent mechanical strength [3-7]. These materials are usually a mix of hydrophobic (e.g. PDVF) and hydrophilic (e.g. silica nanoparticles) properties and therefore lack of interest in MD. However, nanocomposite membranes have attracted more attraction in MD but the efforts were still focusing on improving the hydro/superhydrophobicity of the material surface [8, 9].

Nanocomposites are materials composed of a matrix, for example an organic polymer and a nanofiller, for example inorganic nanoparticles whose dimensions are < 100 nm. The idea being that the addition of the filler phase to the matrix will improve the overall performance either through transference of the nanofillers specific functionality or through synergistic effects arising from the matrix/filler interactions. Such materials have been receiving significant attention over the last three decades due to the explosion in nanomaterials research which has produced a fantastic array of nanofillers with extraordinary properties (e.g. rigidity, thermal and/or chemical stability, optical transparency etc.) [10]. There are numerous synthesis routes for the nanocomposites in particular, ways to introduce the polymer (either as a precursor or a preformed polymer) and inorganic phase (either as monomer or preformed nanostructure of different morphologies) in different forms and sequences [11]. Several studies reported on the nanocomposite membrane systems for applications in gas [12-16] or liquid separation [6, 17-19] and found that the incorporation of nanoparticles (silica, zeolite etc.) in a polymer matrix could enhance the permeability and selectivity compared to the pure polymer membrane. Nevertheless, challenges remain in these materials with well-known problems such as formation of voids or defects during the dewetting of the polymer-inorganic interface [13, 20] and agglomeration of nanoparticles within the polymer matrix [11].

The *in situ* sol-gel method is another approach for the synthesis of nanocomposite material, wherein organic polymer and silica sol are mixed together during the sol-gel process to form a single homogeneous phase [10]. Essentially, a low molecular weight resol is chosen as the polymer matrix which could ensure a homogeneous aggregation with the inorganic phase, in which the silica serves as a "reinforced-steel bar" and the polymer resin serves as the "concrete" [21]. Further, there are several reported works even incorporated surfactants into the mixture of polymer and silica sol as a self-assembling, pore directing agent in a process known as triconstituent co-assembly [21-23]. In this method, pre-polymerized phenol-formaldehyde resol forms a hydrogen bond with surfactant and pre-hydrolyzed silica sol. The viscosity is adjustable by varying the amount of solvent (e.g. ethanol) for different morphologies, such as monoliths [23], thin films [21, 24] and particles [25]. This method is advantageous to produce several types of products either: 1) mesoporous polymer-silica nanocomposites (only surfactant is removed by thermal treatment > 450 °), 2) mesoporous carbon-silica nanocomposites (carbonization > 600 °C under inert gas flow), 3) mesoporous silica (calcination in air) and 4) mesoporous carbon (silica removal by hydrofluoric acid treatment). So far, most of the reported works have focussed on high temperature thermal treatment methods (i.e. products 2, 3 and 4) and no attempt has been reported for testing mesoporous polymer-silica nanocomposite membranes in water desalination. Herein, we prepare a series of mesoporous polymer-silica nanocomposite (PSN) membranes with varying silica content using the triconstituent co-assembly method. The membrane preparation was be simplified to only one coating layer that required a single low temperature thermal treatment (450 °C) for removing the surfactant. The idea being that the low temperature may result in incomplete polymerization of the polymer matrix and some organic functional groups could be retained. The impact of these organic functional groups and the subsequent pore sizes and geometries on the membrane performance (water transport) will be evaluated in vacuum membrane distillation (VMD).

7.2 Experimental

7.2.1 Materials and Characterization

The polymer-silica nanocomposites are prepared by using the triconstituent co-assembly method, whereby resorcinol-based resol was used as the organic precursor, tetraethylorthosilicate (TEOS) as the inorganic precursor and surfactant Pluronic F68 as the structure directing agent. This

method resembles a sol-gel process, with the combination of two individually polymerized sols, a silica sol and the resol in the presence of surfactant micelles. First, a certain amount of non-ionic triblock copolymer F68 ($PEO_{78}PPO_{30}PEO_{78}$, M_{wt} ~8400 g $gmol^{-1}$, Aldrich) was dissolved in the mixture of 3 ml ethanol and 1 ml of 0.2 M hydrochloric acid (HCl, 37 %, Aldrich) solution under vigorous stirring for one hour to complete dissolution. In the meantime, 1.1 g of resorcinol was added into 3M HCl ethanolic solution at room temperature. After stirring for 30 minutes, 1.3 g of 37 % formaldehyde was added into the resorcinol solution to initiate the polymerization reaction. TEOS was then introduced into the surfactant mixture, followed by the addition of resol solution under vigorous stirring for 2 hours. The final molar ratios of the components were resorcinol: formaldehyde: TEOS: F68: ethanol: H_2O: HCl as 1: 1.6: 0.05-2.5: 0.0095-0.03: 12: 16.66: 0.62. The ratio of F68 to the total precursors (resorcinol and TEOS) was kept at 0.009.

The membrane was prepared by a dip-coating process in a class 100 laminar flow cabinet. A tubular alumina substrate with a titania interlayer on the inner surface (PALL, length 100 mm, outer diameter 10 mm, thickness 1.7 mm) was dip-coated with the as-synthesized sol at a holding time of 1 minute and withdrawal rate of 2 cm min^{-1}. The membrane was allowed to remain at room temperature overnight, followed by drying at 60 °C for 12 hrs. Prior to carbonization in nitrogen, the membranes were vacuumed dried for 20 minutes, then heat treated at 150 °C for 6 hrs and finally 450 °C for 4 hrs at a ramping rate of 1 °C min^{-1}.

Thermogravimetric analysis (TGA) was performed using a Differential Scanning Calorimeter/Thermogravimetric analyser (Mettler-Toledo, TGA/DSC 1) with a temperature ramp rate of 2 °C min^{-1} to 1,000 °C under air flow at 60 ml min^{-1}. The pore structure of the nanocomposite materials was observed using transmission electron microscopy (TEM) (JEOL, JEM-1010). TEM samples were prepared by mixing the finely ground PSN samples with ethanol to form slurry, which was then added dropwise to a carbon film coated Cu grid. The surface morphology of the coated membranes was inspected by using scanning electron microscopy (SEM) (JEOL, JSM-7100F), in which sample was coated with Iridium at 15 mA for 45 sec using a Baltek coater. Powder X-ray diffraction (PXRD) data were collected on a Bruker D8 Advance X-ray diffraction instrument (Karlsruhe, Germany) with Cu-Kα radiation (λ = 0.154 nm). The voltage and the current were set to be 40 kV and 40 mA, respectively. The diffraction patterns being collected in the 2θ range of 0.5-10 ° at a scanning rate of 1 ° min^{-1}. Nitrogen adsorption-desorption isotherms were measured at 77 K using a physisorption analyzer (Micromeritics,

Tristar 3020). Prior to the adsorption measurements, the samples were outgassed under vacuum at 200 °C for 12 hr. The specific surface area was calculated by Brunauer-Emmett-Teller (BET) method at range from 0.05 to 0.2 of relative pressure. Total pore volume was obtained by the amount of nitrogen adsorbed at $P/P_0 = 0.97$. Cumulative pore volumes and pore size distribution were determined from the adsorption branch of the isotherm using Quantachrome Autosorb iQ 2.02 software (Quantachrome Instruments, USA). For comparison purposes, non-local density functional theory (NLDFT) model based on silica adsorbent with cylindrical pores and quenched solid density functional theory (QSDFT) model based on carbon adsorbent with slit/cylindrical pores, were used to calculate the pore size of the materials. Attenuated total reflection – Fourier transform infrared (ATR-FTIR) spectroscopy was performed using a Shimadzu IRAffinity-1 spectrometer and data was recorded in transmission mode, in the range from 4000-550 cm^{-1} at a resolution of 4 cm^{-1}. Prior to FTIR measurement, the samples were dried overnight in vacuum oven at 70 °C. Peak deconvolution of the FTIR spectra was performed using Fityk software version 0.9.4 based on Gaussian fitting ($R^2 = 0.99$). Solid state cross-polarization magic angle spinning (CP-MAS) ^{13}C nuclear magnetic resonance (NMR) spectrum and single pulse with high power decoupling (SP-hpdec) ^{29}Si spectrum were measured on a Bruker Avance III spectrometer with a 7T (300 MHz for ^{1}H) magnet using 4 mm zirconia rotor rotated at 7kHz.

7.2.2 Desalination Test

The mesoporous polymer-silica nanocomposite membranes were tested for water desalination using a vacuum membrane distillation process. The experimental set-up was comprised of a feed vessel, peristaltic pump, membrane module, condenser unit, vacuum pump and data logging system connected to computer. Type-K thermocouples were installed in the membrane module to measure the temperature of feed inlet and retentate outlet, as well as the permeate side temperature. The temperature of feed solution was set at 25, 40 and 60 °C with different NaCl concentration ranging from 0 to 150 g L^{-1}. Each experiment was conducted for about 3 hours (with steady state reached within 5 min); starting from the lowest salt concentration and lower feed temperature. The feed was introduced into membrane module at a flow rate of 5 L h^{-1} and circulated back into the feed vessel. Vacuum (1.5 kPa) was applied at the permeate side and water vapour was condensed and collected in the cold trap at a temperature of -15 °C. The feed and permeate conductivities were measured by a labCHEM CP conductivity meter. The weight of permeate (m) was measured and applied in the calculation of permeate flux, J (L m^{-2} h^{-1}), in

which $J = m/A \cdot t$, where A as the membrane active area and t is the duration time of the sample collected in the permeation test. Salt rejection, R (%) of the membrane was determined by $R = (C_f - C_p)/ C_f \times 100$ %, where C_f and C_p are the feed and permeate concentrations, respectively. Performances of different membranes are compared based on the global mass transfer coefficient, C_g (L m^{-2} h^{-1} Pa^{-1}), in which $C_g = J/(P_{Tf} - P_{Tp})$, where P_{Tf} and P_{Tp} is the bulk water partial pressure at feed side and permeate side, respectively.

7.3 Results and Discussion

Nitrogen adsorption-desorption isotherms for the polymer-silica nanocomposites are presented in Figure 7.1. All samples exhibit a typical type IV isotherm that corresponds to a mesoporous (pore size 2 to 50 nm) material in accordance to the IUPAC classification [26]. There is also a significant content of micropores based on the rapid uptake of N_2 adsorbed at low relative pressure ($10^{-5} \leq P/P_0 \leq 10^{-1}$). The hysteresis loop, however, evolves a more pronounced capillary condensation step as the silica content of the PSN samples increases. In general, the hysteresis loops are of type H2 but it is clear that the width of the hysteresis loop decreases with increasing silica. Sample $CSi_{2.5}$ shows an isotherm characteristic of the typical cage-like or ink-bottle pores with a steep desorption step. By contrast, the hysteresis loop of $CSi_{1.2}$ resembles a transition from H2 to H3 type, only closing at high relative pressures. This is attributed to the presence of non-rigid aggregates of plate-like particles associated with slit-like pores [27]. Both $CSi_{0.5}$ and $CSi_{0.05}$ do not exhibit a proper hysteresis closure point, with the desorption branch running parallel to the adsorption branch at low relative pressure. This is also attributed to the swelling of non-rigid porous structures, due to the relatively concentration of polymer [26, 28]. Clearly, the silica content of the PSN is essential in rigidifying the structure, preserving its mesostructure, as well as enhancing the samples mesoporosity.

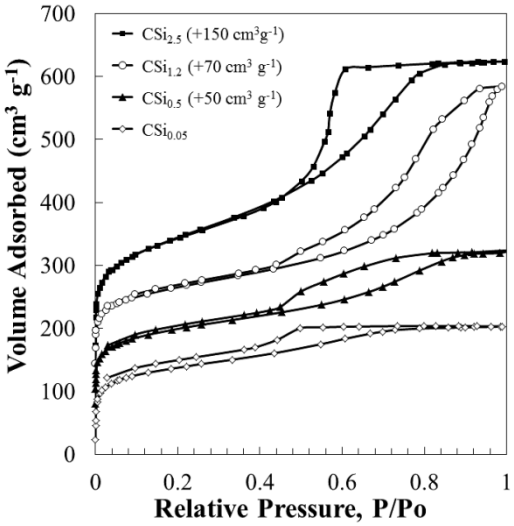

Figure 7.1 Nitrogen physisorption isotherms of polymer-silica nanocomposites in which $CSi_{2.5}$, $CSi_{1.2}$ and $CSi_{0.5}$ are each offset 150, 70 and 50 cm^3 g^{-1}, respectively, for clarity purposes.

The calculated BET specific surface area and pore volume of the samples are listed in Table 7.1. $CSi_{2.5}$ shows the greatest BET specific surface area and pore volume among all the samples, which is likely due to its highest silica content compared to the other PSN samples. Indeed, a reduction pore volume is observed as the silica content decreases, suggesting that the material becomes denser and less porous. Therefore, in addition to enhancing the mesostructured, silica also plays an important role in maintaining the microporous structure of the nanocomposites [22].

Table 7.1 Physicochemical properties of polymer-silica nanocomposites

Sample	S_{BET} [a], m^2 g^{-1}	V_{QSDFT} [b], cm^3 g^{-1}	D_{QSDFT} [c], nm
$CSi_{2.5}$	695	0.70	0.9/4.8-8.0
$CSi_{1.2}$	504	0.60	0.8/[d]
$CSi_{0.5}$	516	0.40	0.8/3.0-12.0
$CSi_{0.05}$	474	0.29	0.8/4.6

[a] S_{BET}, BET specific area calculated from the volume of N_2 adsorbed in the relative pressure range from 0.05 to 0.2. [b] V_{QSDFT}, total pore volume calculated by the QSDFT method based on carbon adsorbent with slit-like and cylindrical pore models. [c] D_{QSDFT}, pore width calculated by similar method as V_{QSDFT}. [d] Broad mesopores distribution

Pore size distribution of the PSN is calculated using quenched solid density functional theory (QSDFT) methods based on a carbon adsorbent utilizing a slit/cylindrical pore model [28]. The NLDFT method based on a silica adsorbent with cylindrical pores was also applied to the same

isotherms for comparison purposes and the values of fitting error for both methods are presented in Figure S7.1 and S7.2. For almost all PDN samples the QSDFT model gives a better fit suggesting that the material is enriched with carbon and consists of both slit-like (micropores) and cylindrical shaped mesopores. However, the $CSi_{0.05}$ sample, which incidentally had the lowest silica content, was better suited by the NLDFT model. This was attributed to phase separation between the silica and polymer sols, as was observed following dip-coating. The lateness of this observation in the membrane production process indicates that the phase separation is very slow and unlikely to dramatically impact on membrane formation. However, it also implies that caution should be used in drawing conclusions form material characterization of the heat treated powder. From the plots of cumulative pore volume as in Figure 7.2 (left), all materials exhibit pore sizes in both the micropore and mesopore regions. This is evidenced by the immediate increase in cumulative pore volume at pore size < 2 nm. In $CSi_{2.5}$, micropores are observed well below 2 nm whilst the majority of pore volume is associated with the mesopores which are distinctly observed within the range of 4 to 8 nm. The $CSi_{1.2}$ sample shows far less demarcation between micro- and mesopores with ~ 30 % of pore volume associated with micropores but a very wide distribution of pore sizes above 3 nm. Given that the $CSi_{1.2}$ sample exhibits a H3 hysteresis loop, the calculated pore size distribution and total pore volume might not be reliable [27]. Both $CSi_{0.5}$ than $CSi_{0.05}$ samples exhibit a significant fraction of micropores (between 40 – 50 % total pore volume) but $CSi_{0.5}$ exhibits a much wider mesopores size distribution. By contract the $CSi_{0.05}$ sample has a significant peak centered around 4.5 nm.

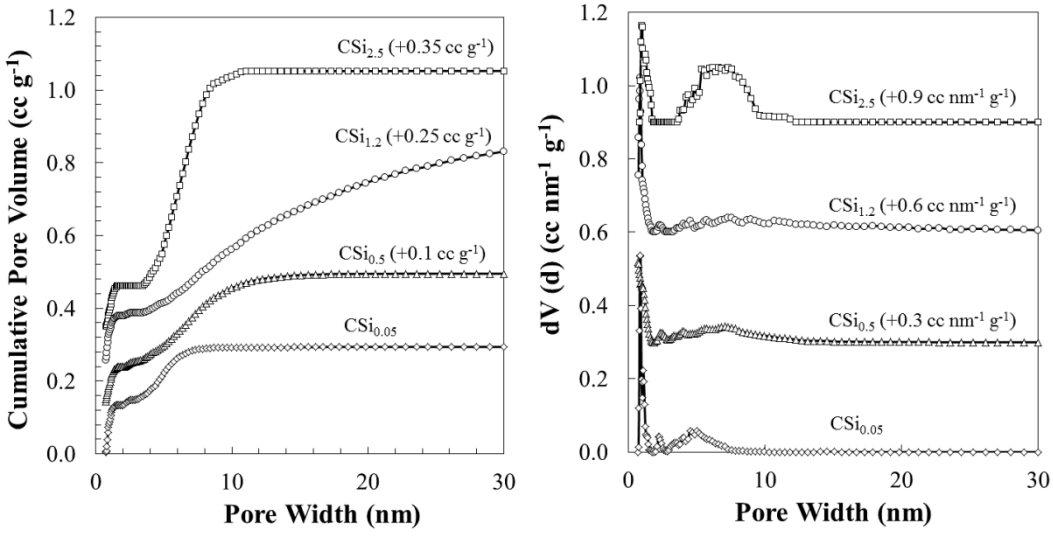

Figure 7.2 Plots of cumulative pore volume of the material calculated by QSDFT method based on the adsorption branch of carbon adsorbent with slit/cylindrical pores model. Curves for $CSi_{0.5}$, $CSi_{1.2}$ and $CSi_{2.5}$ were offset for better visualisation (values shown in blanket).

TEM images of the PSN materials are displayed in Figure 7.3. Overall, it appears that these materials randomly aggregate into a wormlike mesophase with noticeable mesopores. However, the materials appear to get denser and more amorphous as the silica content decreases. Indeed, it is difficult to distinguish mesopores in the $CSi_{0.05}$ sample (Figure 7.3 far right) as compared to the $CSi_{2.5}$ sample (Figure 7.3 far left). The formation of wormlike mesostructures in the materials was attributed to the different polymerization rate of the resorcinol-formaldehyde resol and the silica network [29, 30]. In order to further characterize the mesophase, low angle X-ray diffraction was performed on the PSN powders, which confirmed the disordered mesophase in all samples (Figure S7.3a, ESI). No peak was detected within the 2θ range of 0.5 to 10 °. Figure S7.3b presents the wide angle diffraction patterns of the materials from 10 to 80 °. Two weak and broad peaks detected at 22 ° and 40 ° which is a strong indication of amorphous carbon [31], suggesting the resorcinol-formaldehyde resin has partially carbonized at 450 °C.

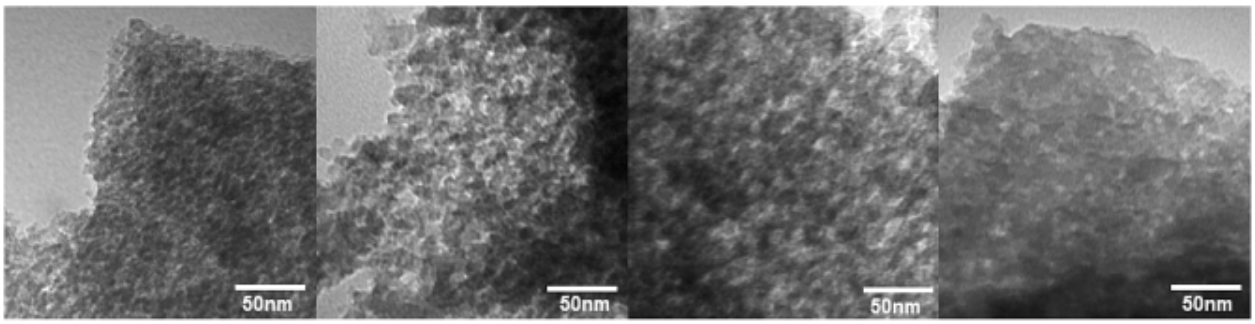

Figure 7.3 TEM images of polymer-silica nanocomposite of $CSi_{2.5}$, $CSi_{1.2}$, $CSi_{0.5}$ and $CSi_{0.05}$ with decreasing silica content (from left to right).

Figure 7.4 reports the XPS spectra of the polymer-silica nanocomposites with oxygen, carbon and silicon the main elements observed (O 1s, C 1s and Si 2p). The variation in the carbon to silicon ratio calculated from the XPS is in good agreement with the theoretical molar ratio based on precursor adding during synthesis.

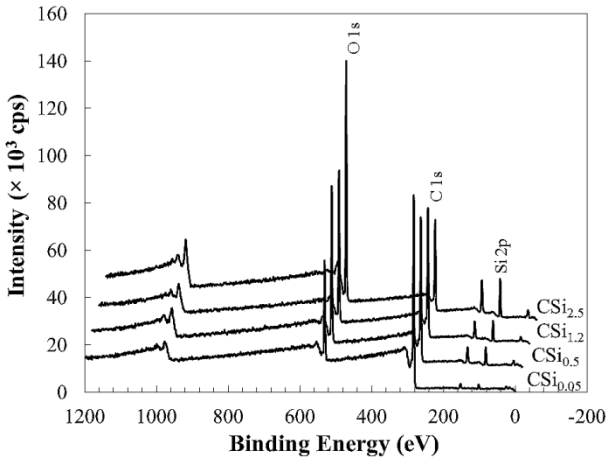

Figure 7.4 XPS spectra of polymer-silica nanocomposite for $CSi_{0.05}$ (blue), $CSi_{0.5}$ (red), $CSi_{1.2}$ (green) and $CSi_{2.5}$ (purple). The spectra for $CSi_{0.5}$, $CSi_{1.2}$ and $CSi_{2.5}$ are offset vertically and laterally for clarity purposes.

FTIR spectra for the inorganic and hydrocarbon species within the polymer-silica nanocomposites are shown in Figure 7.5 (a). A prominent peak corresponding to the characteristic absorption for the Si-O-Si skeletal vibration is visible at 1100-1000 cm^{-1}. Due to the pre-treatment of the material under vacuum, only a slight but very broad peak is seen at ~3700 cm^{-1}, indicating only a trace amount of free silanol groups (-OH) on the material surface [32]. No absorption bands corresponding to methyl groups ($-CH_3$) or methylene bridges ($-CH_2-$) were detected in region 3200-2700 cm^{-1}, suggesting that heat treatment at 450 °C had partially carbonized the nanocomposite. This is further evidenced by the presence of peaks at 1615-1580 cm^{-1} (peak I) and 1510-1450 cm^{-1} (peak II) which correspond to a C=C-C aromatic ring stretch, as well as bands at 900-670 cm^{-1} assigned to C-H out-of-plane bending [33]. A weak band, associated with C-H in-plane bending, is observable in the 1225-950 cm^{-1} region; however, it is insignificant in comparison to the silica related peaks present. As such, only Si-OH and Si-O-Si species are considered in the region of 1250-900 cm^{-1} as shown in the peak deconvolution presented in Figure 7.5 (b). In general, two anti-symmetric stretching modes for Si-O-Si, namely, transverse-optical (TO) and longitudinal-optical (LO) are observed at ~1060 cm^{-1} and ~1190 cm^{-1}, respectively. However, both peaks have been shifted to higher wavenumbers as the carbon content increases. In particular, there is a shift of 34 cm^{-1} for LO mode of $CSi_{2.5}$ to $CSi_{0.05}$. According to Gallardo et al. [34], the peak shift to higher wavenumbers indicates a reduction in porosity, which is in line with the physisorption results. The implication here is that the presence of a significant amount of organic moieties has disrupted the silica structure at both the meso- and micropore scale which is in good agreement with the sorption and XRD data [35].

Due to the large reduction of silica content, the ratio of peak areas for silanol (peak 4) to siloxane (peak 3) also decreases as depicted in Figure 7.5 (c). The trend was confirmed by calculating the ratio of silanol peak area to the total siloxane peak area (sum of area for peaks 1, 2 and 3). To further evaluate the differences in the silica microstructure, the ratio of 4-member siloxane rings (peak 2) to 6-member siloxane rings (peak 1 and 3) was calculated and presented in Figure 7.5c [35]. The ratio of 4-member to 6-member siloxane rings increases with increasing carbon content. The implication is that the presence of the polymer may impact the microstructural of silica by hindering the condensation of silica [35].

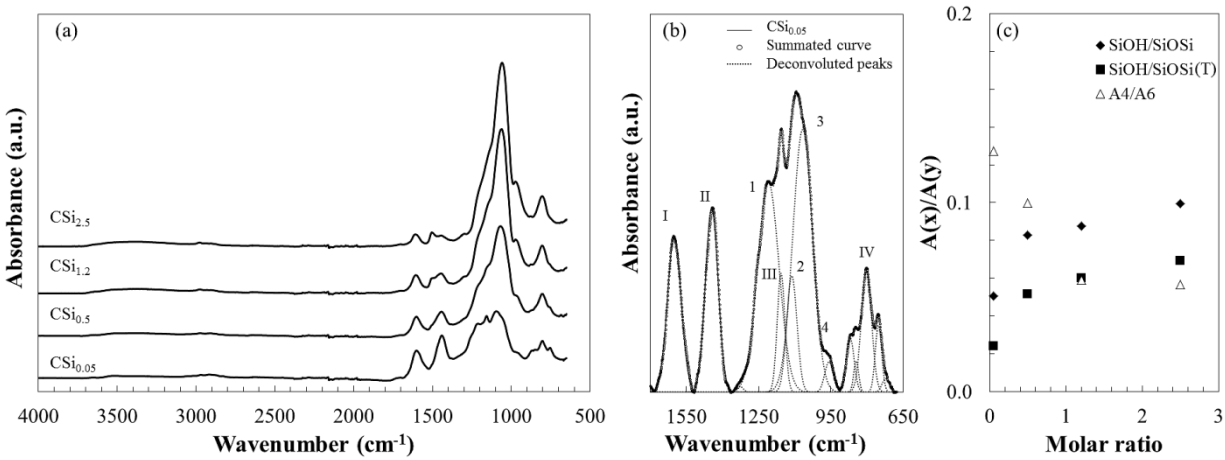

Figure 7.5 (a) ATR-FTIR spectra of polymer-silica nanocomposite, (b) representative deconvoluted FTIR spectrum of $CSi_{0.05}$ where peaks I, II, III & IV correspond to polymers and peaks 1, 2, 3 & 4 correspond to silica species and, (c) ratio of integrated peak area of SiOH/SiOSi, SiOH/SiOSi (total) and 4-fold to 6-fold siloxane rings corresponding to molar ratio of TEOS to resorcinol from 0.05 to 2.5.

^{13}C CP MAS NMR was performed to qualitatively assess the covalent bonding of the heat-treated resorcinol-formaldehyde resin within the polymer-silica nanocomposites as shown in Figure 7.6. A broad peak at 103.6-120.8 ppm is assigned to the mixture of substituted and unsubstituted C_2 and C_4 carbons of resorcinol, whereas peaks for C_5 appeared at around 128 ppm [36]. Peaks at 151.5 ppm are assigned to C_1 and C_3 carbons of the resorcinol rings with mono- (157.4-156.1 ppm), di- (155.0-153.8 ppm), and trisubstituted (152.0-151.1 ppm) methylene bridges (i.e. $-CH_2$, $-CH_2OH$ or $-CH_2O(CH_2O)_xH$) observed [36, 37]. As the peak assigned to C_1 and C_3 carbons of resorcinol (159.6 ppm) is not visible, one may infer that all resorcinol rings have been transformed into the form of substituted resorcinol rings. Peaks at lower chemical shift

are usually assigned to the aliphatic carbon of the methylene bridges or the substituent groups. This includes –CO, -CH_2 and –CH_3 substituent groups detected at around 59, 30 and 16.8 ppm, respectively.

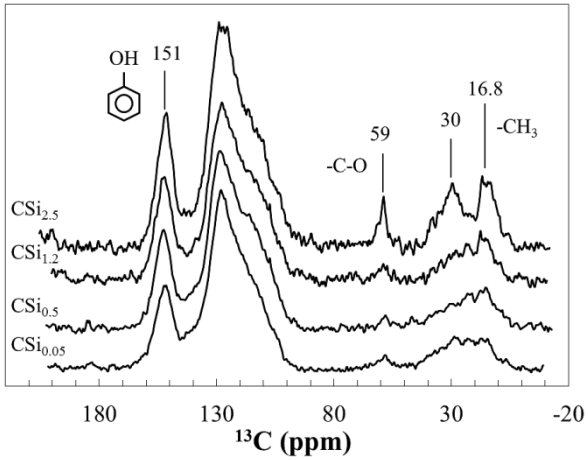

Figure 7.6 ^{13}C CP MAS NMR spectra of polymer-silica $CSi_{0.05}$, $CSi_{0.5}$, $CSi_{1.2}$ and $CSi_{2.5}$ (from bottom to top).

Figure 7.7a presents the ^{29}Si NMR spectra of the materials with the only signals detected in the region of -90 to -120 ppm, which are commonly associated with Q species. There is no evidence of bonding between the silica and carbon networks, highlighted by the absence of T species, which are usually found at -50 to -65 ppm [38]. This is in good agreement with the result from ^{13}C NMR spectra with no peak detected at -5 ppm, which corresponds to a Si-C bond. Three peaks corresponding to Q^2 ($Si(OH)_2(OSi)_2$), Q^3 ($SiOH(OSi)_3$) and Q^4 ($Si(OSi)_4$)[39] are obtained from the peak deconvolution as depicted in Figure 7.7b. The integrated area of the respective chemical shift of each signal is plotted in Figure 7.7c. All samples exhibit a similar trend in the amount of Q species present. The silica structure appears relatively uncondensed with only around 60 % of the bonding associated with fully condensed Q^4 sites. The relatively low polymerization of the siloxane network is most likely due to the low thermal treatment temperature rather than interruption induced by the presence of the resorcinol.

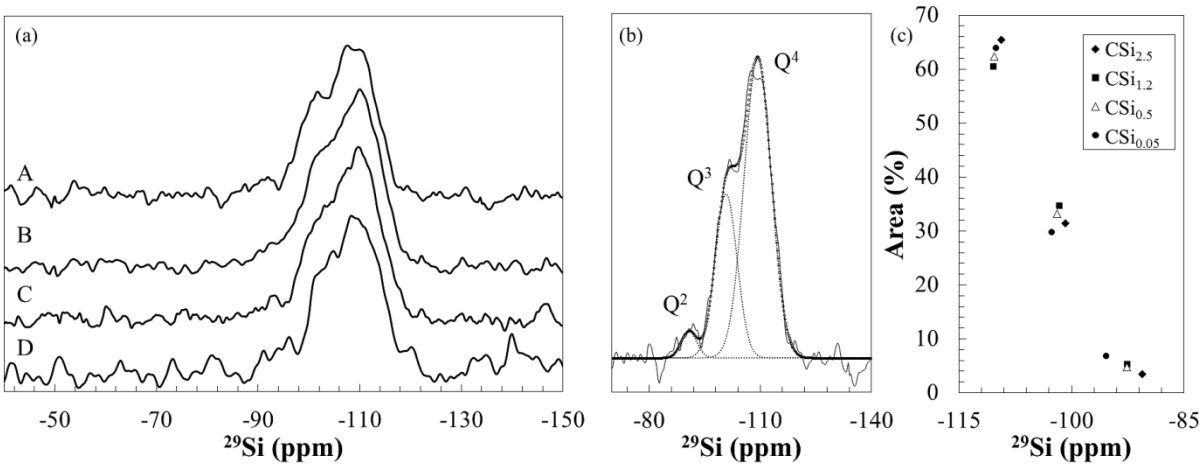

Figure 7.7 (a) ^{29}Si NMR spectra of $CSi_{2.5}$ (trace A), $CSi_{1.2}$ (trace B), $CSi_{0.5}$ (trace C) and $CSi_{0.05}$ (trace D). (b) Peak deconvolution of ^{29}Si NMR spectrum for Q^2, Q^3 and Q^4 species. (c) Percentage of integrated analytical area obtained for each deconvoluted peak of Q species.

The morphology of the membranes produced from the PSN materials was inspected using FE-SEM and presented in Figure 7.8. The cross-sectional view shows that the α-alumina substrate is comprised of an asymmetric structure of coarse α-alumina particles of descending grain size from the outer surface to the inner tube surface (bottom to top as in Figure 7.8, I-III a). With the exception of the $CSi_{0.05}$ membrane the dense layer formed on top of the alumina support is the superimposition of the polymer-silica nanocomposite membrane and the titania intermediate layer (Figure 7.8, I-II b). There is some slight infiltration could be observed for $CSi_{2.5}$ and $CSi_{0.5}$, but this does not impose any mass transfer resistance on the α-alumina layer, given that the porosity in the alumina layer is still visible. In the case of the $CSi_{0.05}$ membrane there are two well-distinguished dense layers observable which correspond to the membrane and the titania intermediate layer, respectively (Figure 7.8, III-b). Membrane thickness was estimated from Figure 7.8 (I-III c) and found that increased silica content was associated with thicker membranes. For example the $CSi_{2.5}$ membrane is ~ 415 nm thick whereas the $CSi_{0.05}$ membrane has a membrane thickness of ~ 590 nm. In general, the membrane layer was uniform as seen in Figure 7.8, I-III d; however, Figure 7.8 (I-III e-f) shows evidence of α-alumina on the surface of both the $CSi_{2.5}$ and $CSi_{0.5}$ membranes signifying the infiltration of the sol into the porous substrate. Furthermore, some defects were observable for both these membranes; however, as the SEM analysis was conducted post-testing it is unclear if the defects were present prior to testing thereby influencing the membrane performances. By contrast the $CSi_{0.05}$ membrane had a very smooth surface associated with the lack of PSN infiltration into the support.

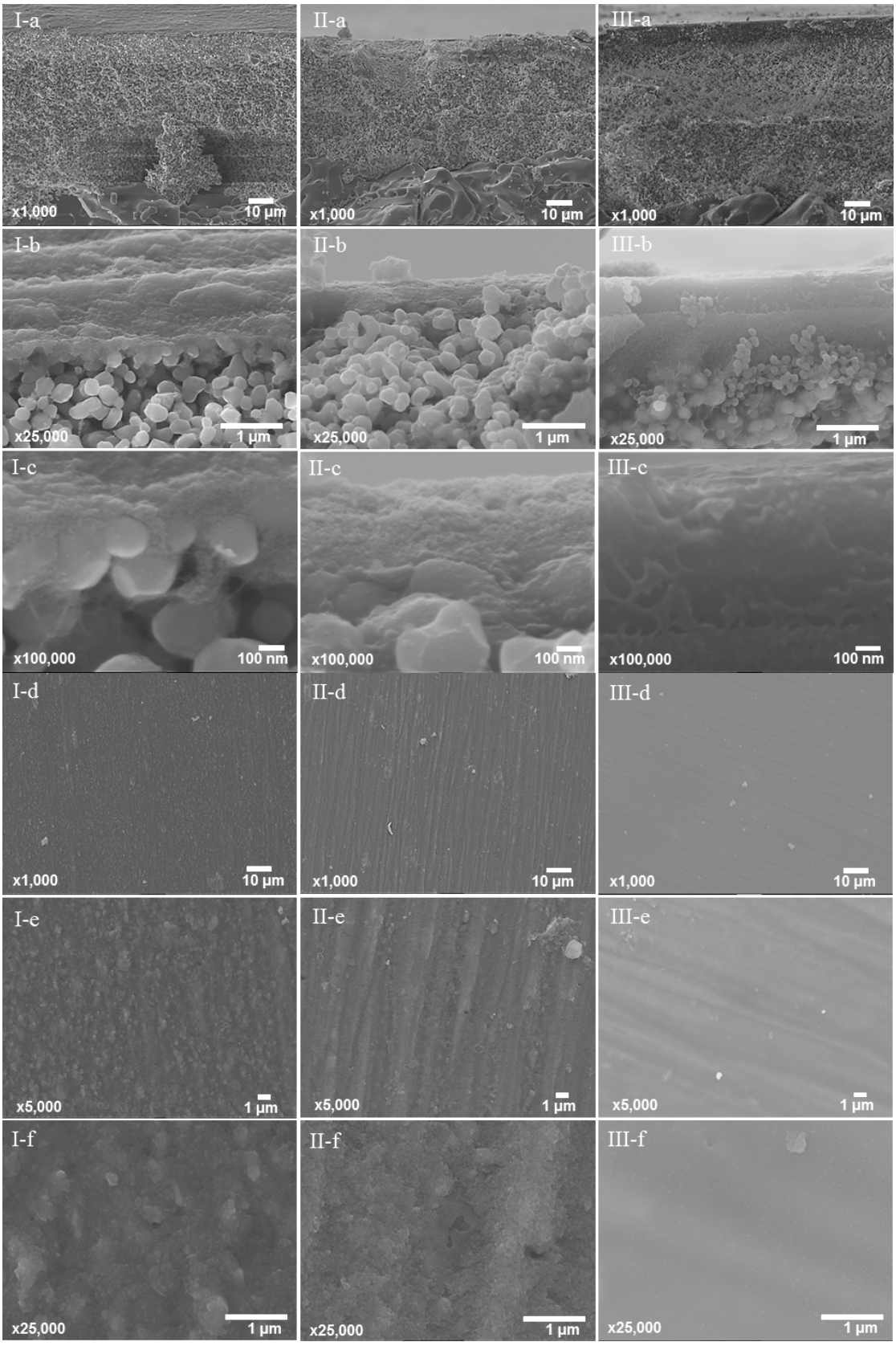

Figure 7.8 FE-SEM images of (I-a to c) cross-sectional view and (I-d to f) surface morphology of $CSi_{2.5}$; (II-a to c) cross-sectional view and (II-d to f) surface morphology of $CSi_{0.5}$; (III-a to c) cross-sectional view and (III-d to f) surface morphology of $CSi_{0.05}$.

Membrane desalination performance was evaluated by the water vapour flux permeating across the membrane and the salt rejection of the permeate itself. All membranes were initially tested using RO water as a control with feed temperatures increasing from 25 to 40 and 60 °C. Overall, the membrane flux performance could be classified into two groups based upon the silica content. Membranes with a higher silica content such as $CSi_{2.5}$ and $CSi_{1.2}$ also yielded higher fluxes (of 10 – 14 L m^{-2} h^{-1}), whereas membranes with a lower silica content such as $CSi_{0.5}$ and $CSi_{0.05}$, displayed lower fluxes of 5 – 6.5 L m^{-2} h^{-1} (approximately 50 % less) at a feed temperature of 60 °C (Figure 7.9). Interestingly, the water permeation flux of all membranes is almost identical at a feed temperature 25 ± 3 °C at ~ 1 L m^{-2} h^{-1}, and the differences became more obvious as the feed temperature increased.

The membranes were then tested with synthetic (i.e. NaCl in RO water) solutions for NaCl concentrations ranging from 10-150 g L^{-1}. At brackish and seawater concentrations, all membranes exhibit virtually no loss of flux across the range of feed water testing temperatures. This has been observed previously for mesoporous organosilica membranes of similar pore sizes, but vastly different pore geometries and surface chemistry to these PSN materials [40]. Nevertheless, the influence of the feed water salt concentration became apparent when exceeded 50 g L^{-1}, with a significant drop in flux for all membranes except $CSi_{1.2}$, which recorded no reduction in flux until the feed water salt concentration reached 150 g L^{-1} when flux dropped ~ 50 % at a feed temperature of 60 °C. It is noteworthy to mention that all membranes gave > 99 % salt rejection, in all cases. However, once the flux dropped and the membrane testing was discontinued, salt formation was observed on the membrane surface at permeate side. The high salt rejection that was observed despite the salt build up is an artefact of the experiment set-up, where an external condenser was used and non-volatile salt crystals are unlikely to be collected in the cold trap. The combination of observations strongly implies the $CSi_{2.5}$, $CSi_{0.5}$ and $CSi_{0.05}$ membranes had experienced pore wetting. In each case the failure of the membrane is attributed to the presence of larger mesopores > 4 nm as calculated by the QSDFT model.

However, unlike the other membranes, no salt deposit was observed on the permeate surface of the $CSi_{1.2}$ membrane, even after flux decay. Further, the flux decay only occurred at the final testing point of 60 °C and 150 g L^{-1}, which is suggestive of structural failure of the membrane rather than pore wetting. Indeed, examining a plot of permeate flux as a function of temperature

(Figure S7.4), it is clear that the high salt concentration (150 g L^{-1}) at 60 °C is an outlier, even if we consider the possible impacts of concentration polarization.

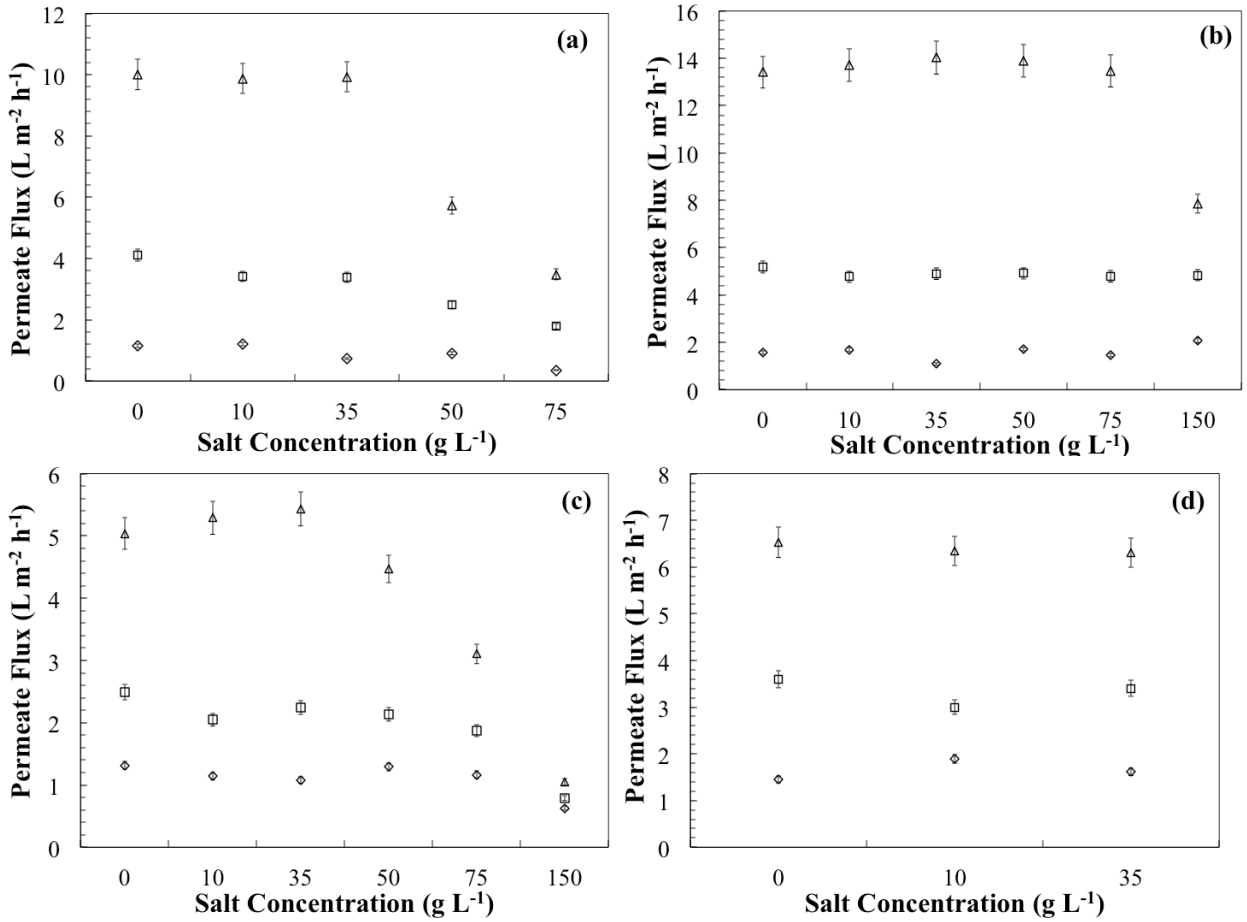

Figure 7.9 Permeate fluxes of membranes (a) $CSi_{2.5}$, (b) $CSi_{1.2}$, (c) $CSi_{0.5}$ and (d) $CSi_{0.05}$ tested at varying salt concentration (clockwise from top left) and feed temperature at 25 (diamond), 40 (square) and 60 °C (triangle).

The performance of the membranes was further compared based on their global mass transfer coefficient, C_g as shown in Figure 7.10 for fresh water only. As previously, there are two general trends in Figure 7.10, which are grouped into high ($CSi_{2.5}$ and $CSi_{1.2}$) and low silica content ($CSi_{0.5}$ and $CSi_{0.05}$), respectively. For the high silica content membranes, the C_g curves resemble the transition region between Knudsen and molecular diffusion as previously investigated by Ding et al. [41], which implies a combination of transport mechanisms often referred to as parallel transport. For the low silica content membranes, the global mass transfer coefficient declined with the feed temperature indicating that the water vapour transport is mainly in accordance with the Knudsen diffusion model. Despite operating in the Knudsen regime which

should produce a higher C_g than molecular diffusion, both $CSi_{0.5}$ and $CSi_{0.05}$ membranes possess smaller pore volumes which substantially contributes to smaller C_g values.

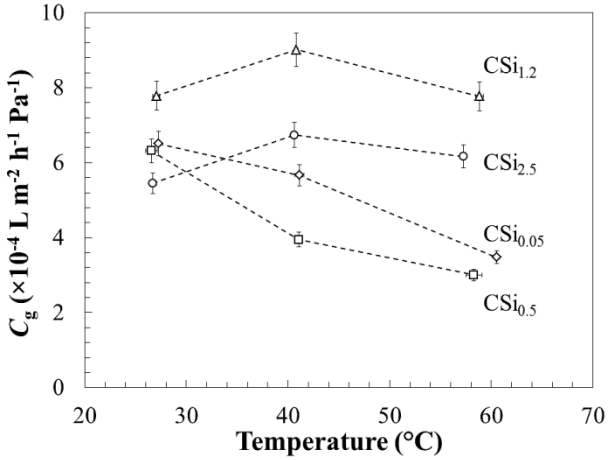

Figure 7.10 Global mass transfer coefficient of membranes with varying silica content correspond to varying temperature of fresh water.

Importantly the analysis of the global mass transfer coefficient reveals that additional factors influence the membrane water flux that remain unaccounted for. In particular the fresh water flux at room temperature was almost identical for all membranes yet the C_g values varied up to 50 % in some cases (e.g. $CSi_{2.5}$ compared to $CSi_{1.2}$). Therefore, in order to investigate how the membrane permeability was affected by varying the silica content, the membrane thickness was eliminated by calculating and comparing the activation energy of all the membranes. This approach was considered appropriate given that all membranes had a substantial quantity of micropores (Figure 7.2 right). Details on how the activation energy was calculated can be found in the supplementary information; whilst Figure 7.11 shows the representative Arrhenius plots of $CSi_{2.5}$ for the estimation of apparent activation energy, E_{aa} and activation energy for permeation, E_p.

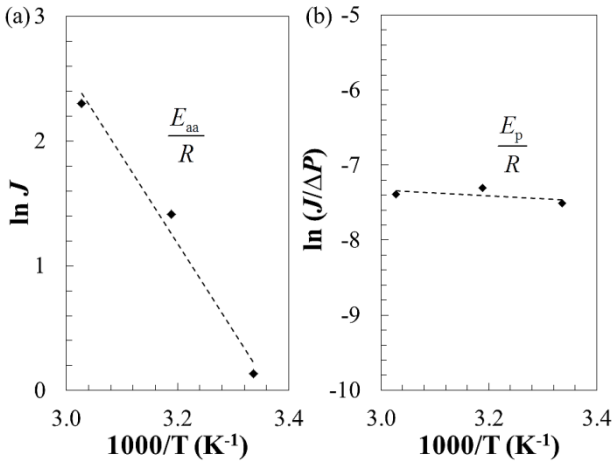

Figure 7.11 Arrhenius plots of (a) permeation flux and (b) partial pressure-normalised permeation flux for $CSi_{2.5}$ in fresh water at varying feed temperature.

Table 7.2 summarizes the E_{aa} and E_p values obtained from the Arrhenius plots and Eqn (2) (ESI) for comparison purposes. The E_p values obtained from Figure 7.11b are far smaller than the E_p values calculated from Figure 7.11a. This is anticipated as the ΔP used in the calculation of E_p values (Table 7.2, column 2) is overestimated, in which the vapour pressure of membrane surface is hard to determine. However, it is obvious that the highest activation energy for permeation, E_p belong to the membrane with the highest silica content. Negative E_p values are obtained for low silica membrane indicating that the ΔH_S (negative for exothermic sorption process) dominates in the permeation process (Eqn (3), ESI). In other words, the activation energy of diffusion E_D is more dominant in the water vapour permeation for high silica membrane, e.g. $CSi_{1.2}$ and $CSi_{2.5}$. This increased water affinity is presumably the result of more silanol groups present in the silica as opposed to the polymeric component.

Table 7.2 Estimated apparent activation energy and activation energy for permeation

	E_{aa}, kJ mol^{-1}	E_p[a], kJ mol^{-1}	E_p[b], kJ mol^{-1}
$CSi_{0.05}$	37.19	-15.94	-5.29
$CSi_{0.5}$	34.94	-19.24	-7.54
$CSi_{1.2}$	55.76	1.66	13.28
$CSi_{2.5}$	58.16	3.19	15.68

[a] E_p value obtained from plot of ln ($J/\Delta p$) versus 1/T.

[b] E_p value obtained from Eqn (2) with $\Delta H_{V,\,60\,^\circ C}$ = 42.48 kJ mol^{-1}.

7.4 Conclusions

The attempt to produce single-layer polymer-silica nanocomposite membranes from a triconstituent co-assembly method proved successful. The lower carbonization temperature (450 °C) than seen in Chapter 6 lead to the incomplete condensation of silica with NMR showing a majority Q^3 sites. This homogenised with a partially carbonized polymer where some organic functional groups were preserved. The nitrogen sorption analysis using QSDFT and NLDFT models suggested a bimodal pore size distribution where the pore wall could be a combination of silica enriched with organic moieties. The aggregation of the organic and inorganic network is physically and homogeneously distributed down to nanoscale without any covalent bond as evidence by XPS and NMR. The thickness of membrane formed on the porous substrate was found to increase with the carbon content in the dip-coating sol, and some phase separation was observed for sols with very high carbon content. From the water permeation test, membranes with high silica content yielded higher water fluxes, with the $CSi_{1.2}$ demonstrating the best flux and stability until the final at a feed temperature 60 °C and extreme salt concentration of 150 g L^{-1}. The membranes were further analysed for global mass transfer coefficients and activation energy with the $CSi_{1.2}$ membrane yielding the highest C_g value, despite a positive E_{aa} and E_p. The negative flux decreasing impacts of having a positive activation energy appeared to be offset by having a high pore volume in comparison to the other samples. Although the poor performance of the $CSi_{2.5}$ membrane which also possessed these qualities suggests there are other complex factors involved in improving membrane flux and avoiding pore wetting.

Acknowledgement

The authors would like to acknowledge funding from the Australian Research Council projects ARC-DP 110103440. Y.C. would like to acknowledge The University of Queensland for providing an UQI International Scholarship. F.K. acknowledges financial support from the Natural Sciences and Engineering Research Council of Canada (NSERC). S. S. acknowledges support from the Queensland Government Smart Futures Fellowship Scheme. The authors acknowledge the facilities, and the scientific and technical assistance, of the Australian Microscopy & Microanalysis Research Facility at the Centre for Microscopy and Microanalysis, Dr Julius Motuzas for the SEM images and Dr Ekaterina Strounina for the ^{29}Si and ^{13}C NMR technical help from the Centre of Advanced Imaging, The University of Queensland.

References

[1] N. Ghaffour, T.M. Missimer, G.L. Amy, Technical review and evaluation of the economics of water desalination: Current and future challenges for better water supply sustainability, Desalination, 309 (2013) 197-207.

[2] U.K. Kesieme, N. Milne, H. Aral, C.Y. Cheng, M. Duke, Economic analysis of desalination technologies in the context of carbon pricing, and opportunities for membrane distillation, Desalination, 323 (2013) 66-74.

[3] D. Li, H. Wang, Recent developments in reverse osmosis desalination membranes, Journal of Materials Chemistry, 20 (2010) 4551-4566.

[4] C. Klaysom, S.-H. Moon, B.P. Ladewig, G.Q.M. Lu, L. Wang, The Influence of Inorganic Filler Particle Size on Composite Ion-Exchange Membranes for Desalination, The Journal of Physical Chemistry C, 115 (2011) 15124-15132.

[5] J. Huang, K. Zhang, K. Wang, Z. Xie, B. Ladewig, H. Wang, Fabrication of polyethersulfone-mesoporous silica nanocomposite ultrafiltration membranes with antifouling properties, Journal of Membrane Science, 423–424 (2012) 362-370.

[6] J. Yin, E.-S. Kim, J. Yang, B. Deng, Fabrication of a novel thin-film nanocomposite (TFN) membrane containing MCM-41 silica nanoparticles (NPs) for water purification, Journal of Membrane Science, 423–424 (2012) 238-246.

[7] E.M.V. Hoek, A.K. Ghosh, X. Huang, M. Liong, J.I. Zink, Physical–chemical properties, separation performance, and fouling resistance of mixed-matrix ultrafiltration membranes, Desalination, 283 (2011) 89-99.

[8] A. Razmjou, E. Arifin, G. Dong, J. Mansouri, V. Chen, Superhydrophobic modification of TiO2 nanocomposite PVDF membranes for applications in membrane distillation, Journal of Membrane Science, 415–416 (2012) 850-863.

[9] L. Dumée, V. Germain, K. Sears, J. Schütz, N. Finn, M. Duke, S. Cerneaux, D. Cornu, S. Gray, Enhanced durability and hydrophobicity of carbon nanotube bucky paper membranes in membrane distillation, Journal of Membrane Science, 376 (2011) 241-246.

[10] H. Zou, S. Wu, J. Shen, Polymer/Silica Nanocomposites: Preparation, Characterization, Properties, and Applications, Chemical Reviews, 108 (2008) 3893-3957.

[11] P. Hajji, L. David, J.F. Gerard, J.P. Pascault, G. Vigier, Synthesis, structure, and morphology of polymer–silica hybrid nanocomposites based on hydroxyethyl methacrylate, Journal of Polymer Science Part B: Polymer Physics, 37 (1999) 3172-3187.

[12] T.-H. Bae, J. Liu, J.S. Lee, W.J. Koros, C.W. Jones, S. Nair, Facile High-Yield Solvothermal Deposition of Inorganic Nanostructures on Zeolite Crystals for Mixed Matrix Membrane Fabrication, Journal of the American Chemical Society, 131 (2009) 14662-14663.

[13] S. Takahashi, D.R. Paul, Gas permeation in poly(ether imide) nanocomposite membranes based on surface-treated silica. Part 1: Without chemical coupling to matrix, Polymer, 47 (2006) 7519-7534.

[14] X. Hu, H. Cong, Y. Shen, M. Radosz, Nanocomposite Membranes for CO2 Separations: Silica/Brominated Poly(phenylene oxide), Industrial & Engineering Chemistry Research, 46 (2007) 1547-1551.

[15] L. Li, T. Wang, Q. Liu, Y. Cao, J. Qiu, A high CO2 permselective mesoporous silica/carbon composite membrane for CO2 separation, Carbon, 50 (2012) 5186-5195.

[16] H.B. Park, Y.M. Lee, Fabrication and Characterization of Nanoporous Carbon/Silica Membranes, Advanced Materials, 17 (2005) 477-483.

[17] J. Dulebohn, P. Ahmadiannamini, T. Wang, S.-S. Kim, T.J. Pinnavaia, V.V. Tarabara, Polymer mesocomposites: Ultrafiltration membrane materials with enhanced permeability, selectivity and fouling resistance, Journal of Membrane Science, 453 (2014) 478-488.

[18] M.L. Lind, D. Eumine Suk, T.-V. Nguyen, E.M.V. Hoek, Tailoring the Structure of Thin Film Nanocomposite Membranes to Achieve Seawater RO Membrane Performance, Environmental Science & Technology, 44 (2010) 8230-8235.

[19] Z. Xie, M. Hoang, T. Duong, D. Ng, B. Dao, S. Gray, Sol–gel derived poly(vinyl alcohol)/maleic acid/silica hybrid membrane for desalination by pervaporation, Journal of Membrane Science, 383 (2011) 96-103.

[20] S.G. Kim, J.H. Chun, B.-H. Chun, S.H. Kim, Preparation, characterization and performance of poly(aylene ether sulfone)/modified silica nanocomposite reverse osmosis membrane for seawater desalination, Desalination, 325 (2013) 76-83.

[21] L. Song, D. Feng, C.G. Campbell, D. Gu, A.M. Forster, K.G. Yager, N. Fredin, H.-J. Lee, R.L. Jones, D. Zhao, B.D. Vogt, Robust conductive mesoporous carbon-silica composite films with highly ordered and oriented orthorhombic structures from triblock-copolymer template co-assembly, Journal of Materials Chemistry, 20 (2010) 1691-1701.

[22] R. Liu, Y. Shi, Y. Wan, Y. Meng, F. Zhang, D. Gu, Z. Chen, B. Tu, D. Zhao, Triconstituent Co-assembly to Ordered Mesostructured Polymer−Silica and Carbon−Silica Nanocomposites and Large-Pore Mesoporous Carbons with High Surface Areas, Journal of the American Chemical Society, 128 (2006) 11652-11662.

[23] Z. Wang, A. Stein, Morphology Control of Carbon, Silica, and Carbon/Silica Nanocomposites: From 3D Ordered Macro-/Mesoporous Monoliths to Shaped Mesoporous Particles†, Chemistry of Materials, 20 (2007) 1029-1040.

[24] M. Si, D. Feng, L. Qiu, D. Jia, A.A. Elzatahry, G. Zheng, D. Zhao, Free-standing highly ordered mesoporous carbon-silica composite thin films, Journal of Materials Chemistry A, 1 (2013) 13490-13495.

[25] Q. Hu, R. Kou, J. Pang, T.L. Ward, M. Cai, Z. Yang, Y. Lu, J. Tang, Mesoporous carbon/silica nanocomposite through multi-component assembly, Chemical Communications, (2007) 601-603.

[26] K.S.W. Sing, Reporting physisorption data for gas/solid systems with special reference to the determination of surface area and porosity (Recommendations 1984), Pure and Applied Chemistry1985, pp. 603.

[27] M. Thommes, Physical Adsorption Characterization of Nanoporous Materials, Chemie Ingenieur Technik, 82 (2010) 1059-1073.

[28] É. Gagnon-Thibault, D. Cossement, R. Guillet-Nicolas, N. Masoumifard, P. Bénard, F. Kleitz, R. Chahine, J.-F. Morin, Nanoporous ferrocene-based cross-linked polymers and their hydrogen sorption properties, Microporous and Mesoporous Materials, 188 (2014) 182-189.

[29] Z.M. Wang, K. Hoshinoo, K. Shishibori, H. Kanoh, K. Ooi, Surfactant-Mediated Synthesis of a Novel Nanoporous Carbon−Silica Composite, Chemistry of Materials, 15 (2003) 2926-2935.

[30] Z. Wang, A. Stein, Morphology Control of Carbon, Silica, and Carbon/Silica Nanocomposites: From 3D Ordered Macro-/Mesoporous Monoliths to Shaped Mesoporous Particles†, Chemistry of Materials, 20 (2007) 1029-1040.

[31] Z. Wu, W. Li, Y. Xia, P. Webley, D. Zhao, Ordered mesoporous graphitized pyrolytic carbon materials: synthesis, graphitization, and electrochemical properties, Journal of Materials Chemistry, 22 (2012) 8835-8845.

[32] M.L. Hair, Hydroxyl groups on silica surface, Journal of Non-Crystalline Solids, 19 (1975) 299-309.

[33] J. Coates, Interpretation of infrared spectra, a practical approach, Encyclopedia of analytical chemistry, (2000).

[34] J. Gallardo, A. Durán, D. Di Martino, R.M. Almeida, Structure of inorganic and hybrid SiO2 sol–gel coatings studied by variable incidence infrared spectroscopy, Journal of Non-Crystalline Solids, 298 (2002) 219-225.

[35] A. Fidalgo, L.M. Ilharco, The defect structure of sol–gel-derived silica/polytetrahydrofuran hybrid films by FTIR, Journal of Non-Crystalline Solids, 283 (2001) 144-154.

[36] M.G. Kim, L.W. Amos, E.E. Barnes, Investigation of a resorcinol–formaldehyde resin by 13C-NMR spectroscopy and intrinsic viscosity measurement, Journal of Polymer Science Part A: Polymer Chemistry, 31 (1993) 1871-1877.

[37] D.D. Werstler, Quantitative 13C n.m.r. characterization of aqueous formaldehyde resins: 2. Resorcinol-formaldehyde resins, Polymer, 27 (1986) 757-764.

[38] M. Ide, M. El-Roz, E. De Canck, A. Vicente, T. Planckaert, T. Bogaerts, I. Van Driessche, F. Lynen, V. Van Speybroeck, F. Thybault-Starzyk, P. Van Der Voort, Quantification of silanol sites for the most common mesoporous ordered silicas and organosilicas: total versus accessible silanols, Physical Chemistry Chemical Physics, 15 (2013) 642-650.

[39] X.S. Zhao, G.Q. Lu, A.K. Whittaker, G.J. Millar, H.Y. Zhu, Comprehensive Study of Surface Chemistry of MCM-41 Using 29Si CP/MAS NMR, FTIR, Pyridine-TPD, and TGA, The Journal of Physical Chemistry B, 101 (1997) 6525-6531.

[40] Y.T. Chua, C.X.C. Lin, F. Kleitz, X.S. Zhao, S. Smart, Nanoporous organosilica membrane for water desalination, Chemical Communications, 49 (2013) 4534-4536.

[41] Z. Ding, R. Ma, A.G. Fane, A new model for mass transfer in direct contact membrane distillation, Desalination, 151 (2003) 217-227.

Supplementary Information

Background

MD operates through a phase change mechanism, wherein the membrane acts as barrier, allowing the liquid/vapour interface to form at the hot feed side. The water vaporizes across the membrane due to the transmembrane vapour pressure difference which typically arises from the temperature gradient between the hot feed and cold permeate streams. Hence, the mass transfer of water vapour could be expressed as follows [1],

$$J = C_m (P_{fm} - P_{intf}) = C_g (P_{Tfb} - P_{Tpb}) \quad (1)$$

where J is the permeate flux, C_m is the membrane mass transfer coefficient, P_{fm} and P_{intf} as the water vapour pressure of at the membrane surface of feed and permeate side, respectively. Global mass transfer coefficient C_g is obtained based on the vapour pressure at thermal boundary layer of feed and permeate side, P_{Tfb} and P_{Tpb}, respectively. Here, C_m value correlates to the membrane properties and is more meaningful in assessing the membrane performance [2],

$$C_m \propto \frac{\varepsilon r}{\tau \delta} \quad (2)$$

where ε is the membrane porosity, τ is the pore tortuosity and δ is the membrane thickness. However, it is usually hard to experimentally measure the vapour pressure at both sides of the membrane surface, and thus, global mass transfer coefficient is adapted for the membrane performance assessment, albeit it includes the mass transfer in the boundary layer [2].

According to Wijmans and Baker [3], the transport of membrane with pore size (0.5 to 1.0 nm) could be considered within the transition region of pore-flow and solution-diffusion model. The physical properties of the membrane could be related to the membrane performance by evaluating the activation energy of the permeation using equation as follows,

$$J = J_0 \exp(-E_{aa}/RT) \quad (3)$$

where, J is permeate flux, J_0 is pre-exponential factor, R is gas constant, T is absolute temperature and E_{aa} is the apparent activation energy.

The apparent activation energy, E_{aa} could be calculated from plot of ln J versus $(1/T)$ but this value is usually overestimated and compounded to both the driving force (temperature) and the

membrane permeability [4, 5]. Feng and Huang suggested that driving force-normalized permeation flux ($J/\Delta P$) should be used for Eqn (3) to determine the activation energy of permeation, E_p. Nevertheless, E_p could also be estimated from this equation if the permeate pressure is relatively low compared to the vapour pressure over the feed liquid [6],

$$E_p = E_{aa} - \Delta H_V \quad (4)$$

where, $-\Delta H_V$ is heat of vaporization and ΔP denotes the transmembrane partial pressure difference.

Meanwhile, E_p could also be related to the activation energy of diffusion, E_D and the enthalpy of dissolution ΔH_S of water in the membrane as,

$$E_p = E_D + \Delta H_S \quad (5)$$

Results and Discussion

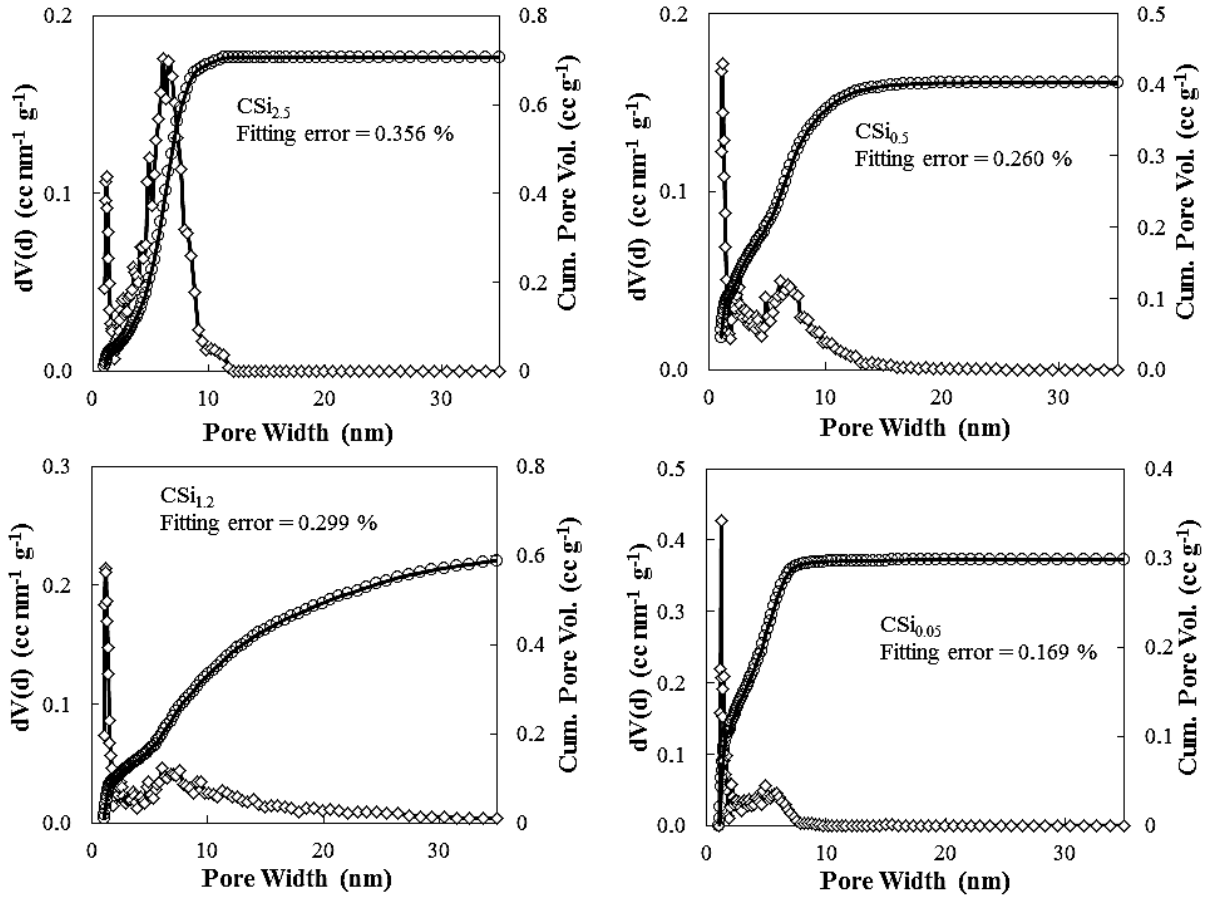

Figure S 7.1 Plot of cumulative pore volume and pore size distribution calculated by NLDFT method.

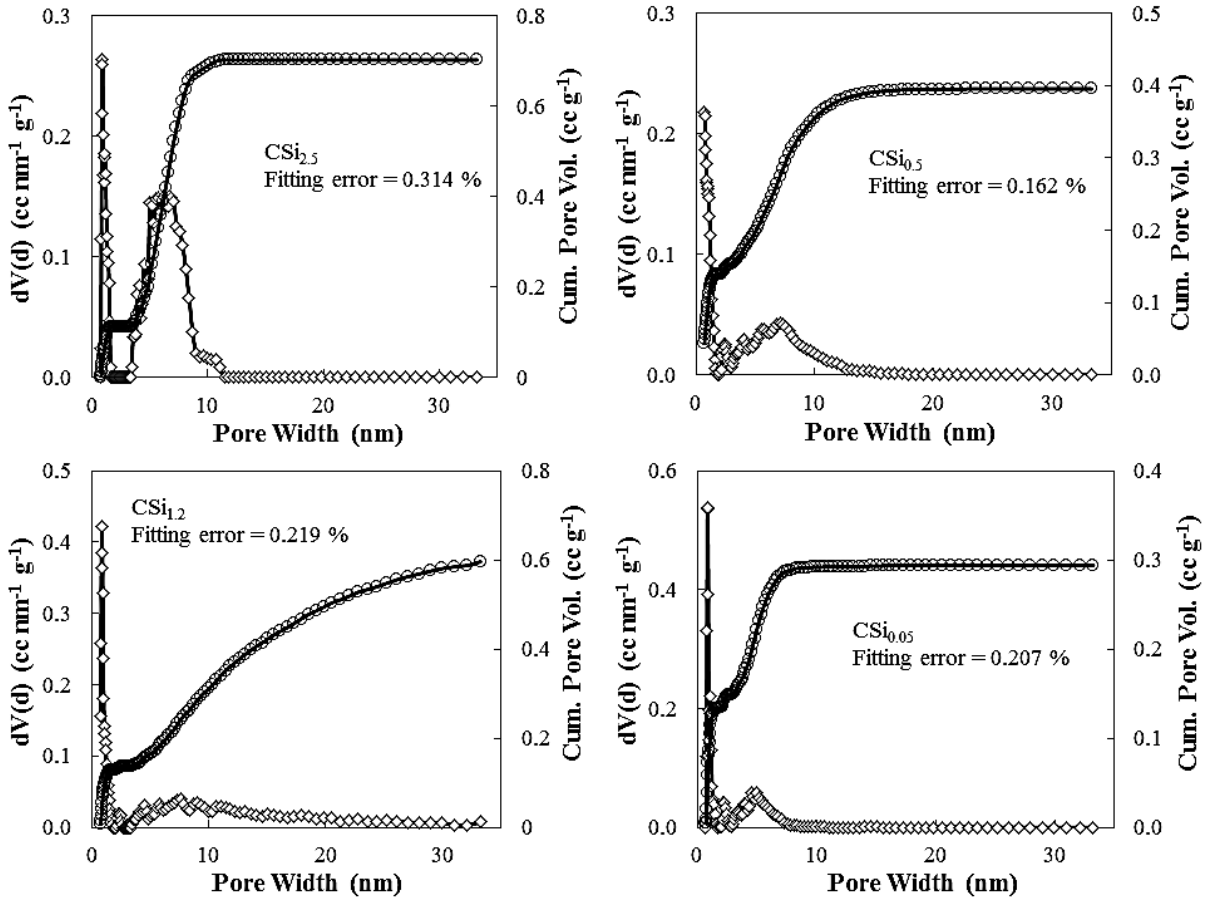

Figure S 7.2 Plot of cumulative pore volume and pore size distribution of polymer-silica nanocomposites calculated by QSDFT method.

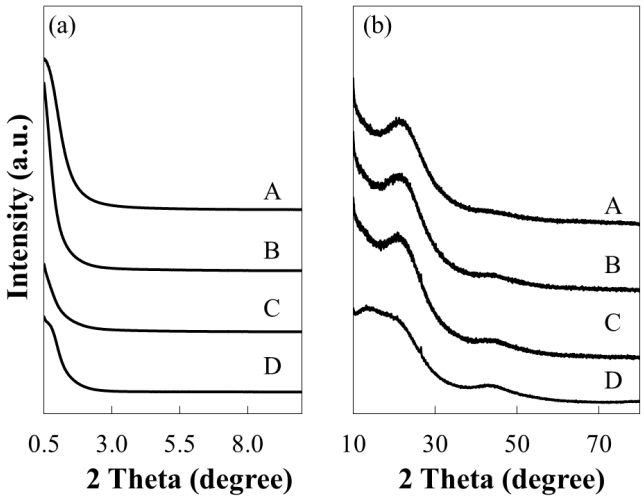

Figure S 7.3 PXRD curves of $CSi_{2.5}$ (trace A), $CSi_{1.2}$ (trace B), $CSi_{0.5}$ (trace C) and $CSi_{0.05}$ (trace D) at (a) low angle diffraction (2 theta of 0.5 to 10 °) and (b) wide angle diffraction.

Table S 7.1 Deconvoluted peaks of the ν_{as}Si-O-Si band in Gaussian components

	$CSi_{2.5}$	$CSi_{1.2}$	$CSi_{0.5}$	$CSi_{0.05}$
v1 (LO)	1306.85	1305.66	1301.71	1326.69
FWHM	43.6926	29.6967	42.8406	31.7729
A(%)	0.68	0.69	0.60	0.20
v2(LO)	1175.92	1185.36	1191.1	1209.89
FWHM	104.44	104.44	104.45	104.44
A(%)	19.68	19.87	20.47	23.68
v3(TO)	1135.2	1124.97	1119.06	1112.29
FWHM	50	50	50	50
A(%)	3.54	3.62	5.91	6.28
v4(TO)	1058.2	1062.63	1061.37	1067.12
FWHM	96	96	96	96
A(%)	54.64	53.04	44.62	27.22
A4/A6	0.057	0.059	0.100	0.127
SiO-	898.843	905.343	908.936	911.325
A(%)	0.48	1.64	3.60	5.09
SiOH	954.548	953.327	953.77	954.266
A(%)	5.09	6.26	7.40	7.30

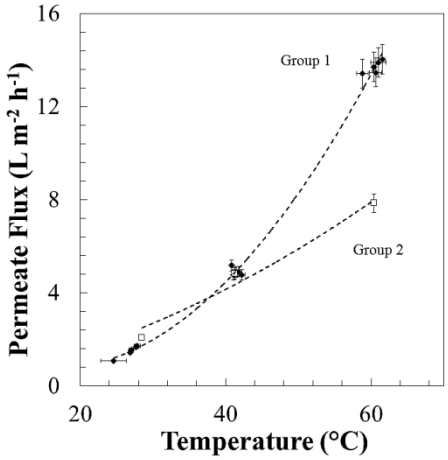

Figure S 7.4 Permeate flux of $CSi_{1.2}$ membrane as a function of feed temperature with horizontal error bars correspond to temperature variation and vertical error bars correspond to ±5 % experimental error. (Data group 1 (0 to 75 g L^{-1}) represented by filled diamond symbols and group 2 (150 g L^{-1}) represented by open square symbols)

References

[1] Z. Ding, R. Ma, A.G. Fane, A new model for mass transfer in direct contact membrane distillation, Desalination, 151 (2003) 217-227.

[2] J. Zhang, J.-D. Li, M. Duke, Z. Xie, S. Gray, Performance of asymmetric hollow fibre membranes in membrane distillation under various configurations and vacuum enhancement, Journal of Membrane Science, 362 (2010) 517-528.

[3] J.G. Wijmans, R.W. Baker, The solution-diffusion model: a review, Journal of Membrane Science, 107 (1995) 1-21.

[4] F. Xianshe, R.Y.M. Huang, Estimation of activation energy for permeation in pervaporation processes, Journal of Membrane Science, 118 (1996) 127-131.

[5] J. Kujawa, S. Cerneaux, S. Koter, W. Kujawski, Highly Efficient Hydrophobic Titania Ceramic Membranes for Water Desalination, ACS Applied Materials & Interfaces, 6 (2014) 14223-14230.

[6] X. Feng, R.Y.M. Huang, Liquid Separation by Membrane Pervaporation: A Review, Industrial & Engineering Chemistry Research, 36 (1997) 1048-1066.

8 CONCLUSIONS AND RECOMMENDATIONS

8.1 Conclusions

The preceding chapters of this thesis outline the development of novel hybrid organic-inorganic membranes in MD desalination, with two different approaches of membrane preparations. This research has demonstrated that the unconventional hydrophilic, nanoporous membranes are potentially applicable in MD, which is in line with the two main hypotheses of this thesis.

The first hypothesis is based on the prevention of pore wetting by employing a membrane with unconventionally small pores and a narrow pore size distribution by using a soft-templating method with an organosilica matrix. The performance of these membranes with pore sizes in the small mesopore region (2-12 nm) was quite comparable with the conventional membranes (pore size ranges from 0.1 to 1 μm). This could be attributed to the narrow pore size distribution that increases the active surface area of separation.

The second hypothesis is related to the incorporation of organic moieties into the silica matrix to improve the membrane stability and flux without compromising pore wetting performance. Two approaches, namely chemical and physical interactions were demonstrated in the preparation of hybrid organic-inorganic membranes. It was proven that either way could maintain the silica mesostructure under humid atmospheres, although pore wetting was evident if the pores were too large and the surface chemistry inappropriate.

The first finding of this work highlights on the nanoporous organosilica membrane with an ordered, narrow pore size distribution (d_p = 2 nm) that was prepared and successfully applied to MD for the first time with good water permeation flux (up to 13 L m^{-2} h^{-1}) and > 99 % salt rejection across an extreme range of salt concentrations (10-150 g L^{-1} NaCl) at moderate temperature (60 °C). The absence of concentration polarization with fluxes effectively unchanged across the entire range of salt concentrations led to the establishment of mathematic modelling for the water transport mechanisms.

The model represents the second major contribution of the thesis demonstrating that the entire system is delicately balanced by the complex relationship between pore size, feed temperature and membrane wettability. The model adapts the Lucas-Washburn equation to an MD setup which, coupled with the behaviour of water in nanoconfined spaces to show that it is the sharp increase in the shear viscosity of water in small mesopores allows the membrane to dramatically resist the capillary force under VMD. As a result, the liquid/vapour interface occurs within the pore channel due to the water intrusion (drawn by the capillary pressure) which is balanced out by the vaporization of water from the interface due to partial pressure difference. The impacts of pore size, membrane thickness, substrate thickness, temperature and concentration polarization, porosity, and contact angle on water flux and pore intrusion depth were quantitatively explored using the model. The results of which are very useful for further inorganic membrane design in VMD. Following this organosilica membranes of different pore size and pore geometries were prepared and most of the outcomes agreed well with the model. This work has advanced the knowledge of water transport in nanoporous, hydrophilic membranes.

The third contribution is the mesoporous carbon-silica nanocomposite membranes being successfully synthesized by a modified triconstituent co-assembly method. This material is comprised of carbon and silica networks that interact physically at the molecular level as opposed to the organosilica membrane where carbon and silicon atoms are covalently bonded. The carbon and silica matrix provide mutual shielding and support effects, in which carbon prevents the migration of mobile silanol groups of silica and therefore resisting hydrothermal densification. The results demonstrated that the use of either inorganic carbon in the CSN membranes or polymeric carbon in the PSN membranes allowed the membranes to perform at a comparable level with organosilica membranes from the earlier work. The PSN membrane series was the most successful, wherein only one layer of coating and lower thermal treatment (450 °C) was needed to produce a suitable membrane. This is a novel approach in membrane development for VMD-based water desalination and paves the way for further development of hybrid organic-inorganic membranes.

8.2 Recommendations for future works

This work has demonstrated the potential of hybrid organic-inorganic membranes in MD but there are more questions that have arisen that require further research but are outside the scope of this thesis. The following recommendations for further work are made:

- The mathematical model is useful in its current state but a version incorporating pore size distributions and complex pore geometries would allow faster development of tailored organosilica or hybrid organic/inorganic membranes. This would allow screening of surfactant/silica/carbon combinations, although caution is advised as the unforeseen tortuosity issues in Chapter 5 would still not have been predicted using the proposed updated model. It would be also useful to better evaluate the impact of pore surface chemistry on membrane performance but this would likely require a complex molecular dynamics simulation.

- The mesoporous carbon-silica or polymer-silica nanocomposite membranes are promising candidates and there are still unexplored area and gaps in the synthesis of this material. For example the materials remain uncharacterised and therefore unoptimized based on precursor and surfactant selection, carbonization conditions and thin film coating techniques.

- It is recommended to initiate a study with free-standing flat-sheet membrane, which is more convenient for the more detail study of the structural characterization, such as membrane wettability and *in situ* ellipsometry for monitoring the membrane thickness, pore structure and even water intrusion.

- The membrane performance study should be expanded to include testing in real brine solutions, containing both a mixture of salt ions with different solubilities (which may cause inorganic scaling) and organic components (which would result in biofouling and biofilm formation). Further, the robustness of the membranes should be studied under conditions that resemble the typical anti-scaling and anti-fouling strategies used in various water industries.

- To demonstrate industrial applicability the MD setup should be scaled up and integrated with either waste or solar energy provision for long term stability tests. This should include an evaluation of the energy efficiency with calculation of the gain to output ratio and the specific thermal energy consumption. Likewise the flow regime should be shifted to the turbulence region to reduce temperature and concentration polarization effects. Further, different membrane configurations, such as hollow fibres should be trialled as a way of reducing module size through increasing packing density. Indeed, it would be interesting from both a fundamental science and applied engineering perspective to produce the mesoporous carbon-silica nanocomposite membranes in a hollow fibre form.

- Finally, it would be interesting to explore the performance of the hybrid membranes in different MD applications for other niche markets such as salt crystal harvesting [1], treatment of produced water from oil and gas extraction which contains phenol, cresol and naphthenic acid (boiling point 165-212 °C) [2-4] or wastewater from acid mine drainage.

References

[1] S. Yoda, M. Ohara, Y. Takebayashi, K. Sue, Y. Hakuta, T. Furuya, M. Yamada, K. Otake, A porous polymer-silica composite with a "vespula-like" structure for thermal insulating materials prepared via high pressure phase control, Journal of Materials Chemistry A, 1 (2013) 9620-9623.

[2] F. Macedonio, E. Curcio, E. Drioli, Integrated membrane systems for seawater desalination: energetic and exergetic analysis, economic evaluation, experimental study, Desalination, 203 (2007) 260-276.

[3] X. Ji, E. Curcio, S. Al Obaidani, G. Di Profio, E. Fontananova, E. Drioli, Membrane distillation-crystallization of seawater reverse osmosis brines, Separation and Purification Technology, 71 (2010) 76-82.

[4] E. Drioli, M. Romano, Progress and New Perspectives on Integrated Membrane Operations for Sustainable Industrial Growth, Industrial & Engineering Chemistry Research, 40 (2001) 1277-1300.